Spring 2021

Analyzing the role of ER membrane biogenesis in mitotic fidelity

Holly Elizabeth Merta
Yale University Graduate School of Arts and Sciences, linkhemzelda@gmail.com

Abstract

Analyzing the Role of ER Membrane Biogenesis in Mitotic Fidelity

Holly Elizabeth Merta

2021

In cell division, chromosomes align and attach to the mitotic spindle with high fidelity in order to limit missegregation of chromosomes that form individual nuclei, termed micronuclei. During cell division, membrane-bound organelles are cleared to the periphery of the cell; lack of clearance of membranes from chromosomes leads to chromosome missegregation. Cells regulate the biogenesis of their membranes throughout the cell cycle. Cancer cells frequently have upregulation of membrane lipid synthesis and micronuclei, but a connection between membrane biogenesis and chromosome missegregation leading to formation of micronuclei has not been established.

In my thesis work, I show that the protein phosphatase CTDNEP1 regulates membrane biogenesis and indirectly the formation of micronuclei in human cell lines. I elucidate how CTDNEP1 controls synthesis of ER membranes through its dephosphorylation and activation of the phosphatidic acid phosphatase lipin 1. I show that ER membrane abundance is increased in mitotic cells lacking CTDNEP1, and endoplasmic reticulum (ER) membranes are less cleared in prometaphase to metaphase. I show that CTDNEP1 has conserved functions for restricting membranes to the surface of the nuclear envelope during nuclear envelope assembly and for maintaining nuclear morphology. Using quantification of mitotic cells in a fixed asynchronous population, I corroborate the results of

previous studies showing that CTDNEP1 is necessary for correct timing of mitotic progression.

Errors in attachment to the mitotic spindle (that may or not be surveilled by the spindle assembly checkpoint) lead to chromosome missegregation that results in formation of micronuclei. Inhibition of the spindle assembly checkpoint in synchronized cells leads to a small increase in micronuclei in CTDNEP1-depleted cells. In contrast, transient spindle disassembly that causes unbalanced attachment errors not sensed by the spindle assembly checkpoint results in severely micronucleated nuclei in CTDNEP1-depleted cells, showing that micronuclei in CTDNEP1-depleted cells form through decreased mitotic error correction.

Lipidomic analysis of total cellular lipids in CTDNEP1-depleted cells reveals that phosphatidylcholine/phosphatidylethanolamine are increased with loss of CTDNEP1. I show that inhibition of fatty acid synthesis suppresses ER membrane expansion in CTDNEP1-depleted cells. I observe that depletion of the fatty acid transcriptional regulators sterol regulatory element binding proteins 1 and 2 and stearoyl Co-A desaturase partially suppress ER membrane expansion, illuminating the role of fatty acid synthesis gene upregulation in expansion of ER membranes in CTDNEP1-depleted cells. Inhibiting fatty acid synthesis rescues severe micronucleation after transient spindle disassembly and the incidence of micronuclei in untreated CTDNEP1-depleted cells. These data elucidate the mechanism for how CTDNEP1 controls ER lipid synthesis in human cells. Together, these data support the conclusion that increased fatty acid synthesis

leads to excess ER membranes that interfere with chromosome segregation in mitosis, leading to formation of micronuclei. This study provides the first connection to misregulation of lipid synthesis to formation of micronuclei, two events that are common in cancer cells. This study thus provides a link between regulation of lipid synthesis and chromosome segregation and informing our understanding of how they are altered in cancer.

Analyzing the Role of ER Membrane Biogenesis in Mitotic Fidelity

A Dissertation

Presented to the Faculty of the Graduate School

Of

Yale University

In Candidacy for the Degree of

Doctor of Philosophy

By Holly Elizabeth Merta

Dissertation Director: Shirin Bahmanyar, PhD

June 2021

Table of Contents

Acknowledgements

I am so thankful to everyone at Yale and beyond who have made all of this possible, and I hope the best for all of you.

I would like to thank Shirin Bahmanyar for excellent mentorship during my time in the Bahmanyar lab. I am thankful for Shirin's striving to bring out the best work from all of us, whether it's conducting experiments or presenting work to others. I am thankful for her encouragement for me to pursue a research project that was challenging yet impactful and for providing support that helped me overcome obstacles in the research. I am so thankful for her commitment to teamwork and building collaborations that have been very beneficial to all involved. I am so thankful for her feedback on my work and discussions that have helped me to frame and understand our research findings. I am thankful for her support, understanding, and reassurance when I was going through personal or research difficulties that sometimes made me think that I wouldn't be able to complete this project. Shirin is truly brilliant and hardworking and navigates life and academia with a smile, confidence, and grace, and this makes Shirin a truly great research supervisor and such an inspiration to all of us.

I am very thankful to members of the Bahmanyar lab for camaraderie and teamwork that contributed to the development of a supportive research environment. Thank you all for always being open to discussion and always offering help and for always being down to celebrate our milestones. I would like to thank Marshall Deline, Tevis Vitale, Jake W. Carrasquillo Rodríguez, Gunta Celma, and Shoken Lee for their experimental contributions and discussions that

helped us better understand the functions of human CTDNEP1. I would also like to thank Lena Schroeder and Joerg Bewersdorf and members of the Bewersdorf lab for allowing me to contribute to the ER nanoholes story and for continued discussion and reagent exchange for the best ways to image live ER. I am very grateful to current Bahmanyar lab members Mike Mauro and Sarah Barger, who have helped a lot with experiment troubleshooting and image analysis and discussions of lipid synthesis and the nuclear envelope that have helped us form this story. I would like to thank past Bahmanyar lab members for help with experiments and discussions that helped move these projects forward, including Lauren Penfield, Mike Martinez, Brian Wysolmerski, Curtis Broberg, Ryan Nguyen, and Razvan Azamfirei. I am also very grateful to our collaborators in the Needleman and Harris labs- Dan Needleman and Maya Anjur-Dietrich, as well as Thurl Harris and Mitch Granade- for their instrumental contributions and discussions to increase our understanding of how CTDNEP1 controls lipid synthesis and mitotic error correction.

I am thankful to members of the Yale Community for valuable discussion and feedback on my research. I am grateful to my committee members, Tom Pollard, Patrick Lusk, and Joerg Bewersdorf, for their guidance on all aspects of my PhD work. I would like to thank members of the LusKing and Schlieker and Breslow labs for their feedback on this research and questions that have helped guide our experiments. I am thankful to core facilities in MCDB that helped make aspects of our work possible, including the microscopy core (and assistance from Joe Wolenski) and the flow cytometry core (and assistance from Kenneth Nelson). I

am also thankful to the department of MCDB as a whole for providing a supportive environment for trainees and for everyone's feedback during research in progress talks.

Finally, I would like to thank my friends and family for their love and support. I thank my parents and sisters for their encouragement and support through difficult times and for their support of my husband and child. I am thankful to my son Anthony, who has been an endless source of inspiration and whose zest for life has kept me going during exceptional challenges. I am most thankful to my husband David, who has made many personal sacrifices, especially during the pandemic, to make sure I always have enough time and resources to keep doing research. David's commitment to support me has been truly unrivaled, and I consider myself exceptionally blessed to have someone who understands so fully that our successes are shared. I am also thankful to my grad student friends from UST and Yale who have been so supportive and a source of solidarity during tough times. I wish you all the best.

Chapter 1

Chapter 2

Chapter 3

Chapter 4

Chapter 5

Chapter 6

List of Tables

List of Abbreviations

ATP: Adenosine triphosphate

CRISPR: Clustered Regularly Interspaced Short Palindromic Repeats

CDP: Cytidine diphosphate

CoA: Coenzyme A

CE: Cholesterol Ester

DAG: Diacylglycerol

DIC: Differential Interference Contrast

DMSO: Dimethyl sulfoxide

DNA: Deoxyribonucleic acid

ER: Endoplasmic Reticulum

ESCRT: Endosomal Sorting Complexes Required for Transport

FA: Fatty acid

GTPase: Guanosine Triphosphate hydrolase

HAD: Haloacid dehalogenase

INM: Inner Nuclear Membrane

LINC: Linker of Nucleoskeleton and Cytoskeleton

LPA: Lysophosphatidic acid

MCC: Mitotic Checkpoint Complex

mRNA: messenger Ribonucleic acid

MT: Microtubule

NE: Nuclear Envelope

NPC: Nuclear Pore Complex

Nups: nucleoporins

ONM: Outer Nuclear Membrane

PA: Phosphatidic acid

PAM: Protospacer-adjacent motif

PAP: Phosphatidic acid phosphatase

PC: Phosphatidylcholine

PE: Phosphatidylethanolamine

PG: Phosphatidylglycerol

PI: Phosphatidylinositol

PIPs: Phosphatidylinositol phosphates

PS: Phosphatidylserine

KO: Knockout

RNAi: Ribonucleic acid interference

SAC: Spindle Assembly Checkpoint

sgRNA: single guide RNA

siRNA: Small interfering ribonucleic acid

SiR: Silicon Rhodamine

SM: Sphingomyelin

TAG: Triacylglycerol

TOFA: 5-(tetradecyloxy)-2-furancarboxylic acid

Chapter 1: General Introduction

Cell and organelle membranes

Cells are the fundamental unit of living things, and they rely on faithful division to propagate all of life. The idea that living things are made of cells was formed in the 1600s-1800s thanks to the invention of light microscopy (Mazzarello, 1999; Ribatti, 2018). Further light and electron microscopy studies identified organelles, or membrane-bound compartments with distinct makeups and functions that are common to all eukaryotic cells (Golgi, 1898; Palade, 1952, 1956; Porter et al., 1945). Organelles were later found to compartmentalize cellular functions, and they have specific populations of proteins to support these functions. Many organelles are encapsulated by membranes with distinct lipid compositions that also support their functions.

Membranes in cells consist primarily of lipids, molecules with hydrocarbon chains or rings that impart hydrophobicity. The hydrophobic nature of lipids causes lipids to self-aggregate within the hydrophilic environment of the cell. Further, the qualities of cellular lipids allow for the formation of different structures. Polar lipids, such as glycerophospholipids, self-aggregate in such a way as to form membranes, which allow the cell to compartmentalize its organelles and to separate itself from its environment.

In cells, membranes take the form of mostly polar lipid bilayers (Nicolson, 2014). The structure of cell membranes has been well described as a fluid mosaic, wherein proteins can span (completely or partially) and diffuse within the lipid bilayer (Nicolson, 2014; Singer and Nicolson, 1975). The lipid makeup of the lipid bilayers has shown to be important for cell physiology, including membrane

properties and cell differentiation (Harayama and Riezman, 2018; Levental et al., 2017).

Types of membrane lipids

The main types of lipids in cells include fatty acids, glycerolipids, sphingolipids, and sterols (Figure 1.1). Within each type of lipid (except for sterols), there are classes defined by their headgroups, and within each class exists hundreds of different possible lipid species based on fatty acid composition (Harayama and Riezman, 2018).

Fatty acids are made up of a carboxylic acid with a hydrocarbon chain typically around 16-22 carbons in length in mammalian cells (Figure 1.1) (Yamashita et al., 2014). These hydrocarbon chains can be saturated (having no double bonds) or unsaturated (having double bonds). The length and saturation of fatty acids within membrane lipids is highly important for the biophysical properties of the membrane (van Meer et al., 2008). Unsaturated fatty acids impart more fluidity to membranes due to less lipid packing (relatively more space between adjacent lipids) (Bigay and Antonny, 2012; van Meer et al., 2008). Longer fatty acids in one leaflet of a bilayer have the potential to interdigitate with the fatty acids of the other leaflet, increasing lipid packing (Murate and Kobayashi, 2016).

Glycerolipids consist of a glycerol backbone, fatty acids connected to the glycerol backbone by an ester linkage, and a head group (in the case of glycerophospholipids) (Figure 1.1). Diacylglycerol (DAG) and triacylglycerol (TAG) consist of the glycerol backbone and 2 or 3 fatty acid chains, respectively.

Glycerophospholipids, such as phosphatidic acid (PA), phosphatidylcholine (PC), phosphatidylethanolamine (PE), phosphatidylserine (PS), and phosphatidylinositol (PI), have two fatty acid chains and a head group on the glycerol backbone connected by a phosphate group. Although their compositions appear similar, the charges and shapes of glycerophospholipids can help or hinder the stabilization membrane curvature and the ability of proteins to associate with the membrane (Harayama and Riezman, 2018). In contrast to glycerolipids, sphingolipids are less saturated and have longer hydrocarbon chains that contribute to a taller profile compared to glycerolipids (van Meer et al., 2008). Sterols, like cholesterol, maintain membrane fluidity at lower temperatures but permit lipid packing to stabilize membranes at higher temperatures as well (Dufourc, 2008). The lipid-condensing effect of cholesterol and long saturated acyl chains of sphingolipids allows them to form relatively-more-solid microdomains of distinct lipid composition within membranes, called lipid rafts, that can preferentially sequester or change the conformation of proteins for signaling purposes (Sezgin et al., 2017). The properties of membrane lipids enable organelles of different lipid compositions to support diverse populations of proteins for different cellular functions.

Organelle membrane lipid compositions

The membranes of organelles have distinct lipid makeups that play a role in organelle morphology, membrane activities and protein localization, and organelle identity. Strides in biochemical and mass spectrometry analysis have generated key insights about how lipid composition of organelle membranes

contribute to their functions. Future analyses making use of lipid probes, species-specific degradation of leaflets, and more sophisticated purification techniques will improve our understanding of organelle composition (Ballweg et al., 2020; Harayama and Riezman, 2018; Lorent et al., 2020; Romanauska and Köhler, 2018).

Generally, the lipid makeup of cells' organelles has been thought to follow a gradient of their involvement in the secretory pathway (Bigay and Antonny, 2012). Most of the cell's lipids are made in the endoplasmic reticulum (ER) (Jacquemyn et al., 2017) (Figure 1.3). The ER consists of mostly PC and PE, PI and PS to a lesser extent, and then very small amounts of sphingolipids and cholesterol (van Meer et al., 2008; Vance, 2015). The nuclear envelope is thought to be similar in composition to the ER, but interconnected nature of the nuclear envelope and ER confounds lipid composition analyses utilizing organelle purification (Bahmanyar and Schlieker, 2020). Recent studies using lipid probes indicate the inner nuclear membrane could have a distinct composition from the ER (Romanauska and Köhler, 2018). In contrast to the ER, the plasma membrane has relatively less PC and greater amounts of PS, sphingolipids, and abundant cholesterol (Horvath and Daum, 2013). The *cis* Golgi is more similar in composition and physical properties to the ER, whereas the *trans* Golgi and endosomes are more similar in composition and physical properties to the cytoplasmic leaflet of the plasma membrane, reflecting how lipids are trafficked from the ER to the plasma membrane and other organelles (Bigay and Antonny, 2012). Organelles' distinct lipid compositions are

established in part by delivery of lipids that are synthesized by the endoplasmic reticulum and contiguous nuclear envelope.

The nuclear envelope and endoplasmic reticulum

The nuclear envelope and endoplasmic reticulum make up a contiguous membrane structure with domains supporting different functions (Watson, 1955) (Figure 1.2). Their structures and functions are outlined below.

The endoplasmic reticulum (ER)

The ER was first identified by electron microscopy as a contiguous structure consisting of perinuclear ribosome-studded “rough ER” sheets and peripheral “smooth ER” tubules (Palade, 1956) (Figure 1.2). We now know that the ultrastructure of the ER in live cells also includes small peripheral sheets with embedded nanoholes (Schroeder et al., 2018). The structure of the ER is supported by ER shaping proteins and interactions with the cytoskeleton (Figure 1.2). Reticulons are tubule-stabilizing proteins that insert a hairpin structure partially into the ER membrane to support membrane curvature (Hu et al., 2008; Voeltz et al., 2006) including inside ER nanoholes (Schroeder et al., 2018). ER sheets are stabilized by ribosomes/translocons and CLIMP-63, which spans the ER lumen in dimers to stabilize a defined lumen width (Klopfenstein et al., 2001; Shibata et al., 2010). Interphase ER structure is also defined by the availability of GTPases that can facilitate ER tubule fusion, such as atlastin and Rab10 (English and Voeltz, 2013; Orso et al., 2009). The fusion activity of atlastin and tubule-stabilizing functions of reticulons and lunapark cooperate to form an extended network of ER tubules (Wang et al., 2016b). The maintenance and

dynamics of peripheral ER structure are also supported by interactions between ER-resident proteins and microtubules (Bola and Allan, 2009; Waterman-Storer and Salmon, 1998). STIM1 on ER tubules interacts with EB1 on microtubule plus ends, leading to ER tubules tracking plus-end microtubule growth (Grigoriev et al., 2008). In general, peripheral ER tubules co-align with microtubules (Waterman-Storer and Salmon, 1998). Movement of organelles to which the ER is tethered also determines its localization and movement (Friedman et al., 2013). The abundance of ribosomes on rough ER and extensive network of the smooth ER support the ER's functions to help maintain other organelles.

The ER performs functions in translation and modification of transmembrane and secreted/luminal proteins and in lipid synthesis. It connects with other organelles to deliver proteins, lipids, and function in signaling.

Early electron microscopy and biochemical studies identified that proteins can be synthesized in the ER and trafficked to other organelles or secreted (Caro and Palade, 1964; Palade and Siekevitz, 1956; Siekevitz and Palade, 1960). Transmembrane proteins and proteins destined for secretion or localization to organelle lumens are translated partially in the cytosol before being targeted to translocons in the ER membrane, where the protein is translated while being shunted into the ER lumen through the translocon (or embedded in the ER membrane) (Rapoport, 2007; Schwarz and Blower, 2015). ER chaperones can assist in folding these proteins, and some posttranslational modifications are also performed in the ER, such as signal peptide cleavage, N-linked glycosylation, and disulfide bond formation (Braakman and Hebert, 2013). The ER also

synthesizes lipids—fatty acids, cholesterol, triglycerides, sphingolipid precursors, and most glycerophospholipids—for the cell.

The ER is also highly interconnected with mitochondria, endosomes, the Golgi apparatus, and the plasma membrane; ER contacts cover up to 5% of mitochondrial and endosomal outer membranes (Phillips and Voeltz, 2015). It is now known that ER contact sites are responsible for exchanging proteins, lipids, and ER-stored Ca^{2+}, and ER contact sites are important for organelle maintenance, such as in endosome maturation (Csordás et al., 2006; Friedman et al., 2013; Phillips and Voeltz, 2015). Finally, the ER is also responsible for organelle biogenesis of peroxisomes and lipid droplets (Hoepfner et al., 2005; Joshi et al., 2017). The ER's structures throughout the cell therefore facilitate its functions in protein and lipid synthesis and delivery of these molecules to other organelles without relying on relatively slow vesicular transport.

The nuclear envelope

The nuclear envelope is a double membrane sheet that encases the nucleus (Figure 1.2). The nuclear envelope was first identified to have a double lipid bilayer by electron microscopy of extracted membranes from *Xenopus laevis* oocyte nuclei (Callan and Tomlin, 1950). These bilayers have since been termed the outer (ONM) and inner (INM) nuclear membranes. Subsequent microscopy studies have identified connections between the outer nuclear membrane and ER (Watson, 1955) as well as invaginations of inner (type I) or outer/inner (type II) nuclear envelope membranes termed nucleoplasmic reticuli (Drozdz and Vaux, 2017). The nuclear envelope contains nuclear pore complexes (NPCs),

~100 nm ring-shaped protein assemblies consisting of nucleoporins (Nups) that span both layers of the nuclear envelope (Bahr and Beermann, 1954; Beck et al., 2004; D'Angelo and Hetzer, 2008; Hetzer, 2010). The structure of the nuclear envelope is supported by a meshwork of intermediate filament-type proteins (lamins) underneath the inner nuclear membrane called the nuclear lamina (Leeuw et al., 2018). The nuclear lamina is connected to the cytoskeleton through LINC complexes that span the nuclear envelope and interact with lamins as well as with actin filaments or microtubules in the cytosol (Sosa et al., 2013).

The nuclear envelope's functions largely entail its protection of the nuclear contents. The nuclear envelope is a semipermeable barrier for the nucleus owing to the nuclear pore complexes' selective permeability. Molecules of size <30-40 kDa can pass through the nuclear pore complexes by diffusion, while large proteins require interaction with importins/exportins to enter and leave the nucleus (Capelson et al., 2010; Hetzer, 2010). This barrier allows the cell to partition transcription from translation, adding a layer of regulation to protein synthesis (Orphanides and Reinberg, 2002). Compartmentalizing the cell's genome allows the nuclear envelope to protect DNA from cytosolic nucleases and the innate immune signaling pathways that allow the cell to detect and rid itself of viral nucleic acids (Ma et al., 2020; Paludan and Bowie, 2013; Semenova et al., 2019). The nuclear envelope also plays an important role in mechanotransduction, as alterations in force applied to a cell lead to nucleus-mediated changes in gene expression (Kaminski et al., 2014).

Though they are contiguous, nuclear envelope functions are thought to be removed from ER functions; however, emergent evidence implicates the nuclear envelope in regulation of lipid synthesis. Studies using nuclear-localized lipid sensors in budding yeast show that the inner nuclear membrane has a distinct lipid composition and that lipid synthesizing enzymes localize to the inner nuclear membrane (Romanauska and Köhler, 2018). In human cells, the nuclear envelope protein lamin B receptor (LBR) catalyzes an intermediate step in cholesterol synthesis from lanosterol and is required for human cell growth in cholesterol-deficient media (Tsai et al., 2016). Nucleoplasmic reticuli have shown to originate from newly synthesized glycerophospholipid incorporation into reticuli at the inner nuclear membrane during interphase (Drozdz et al., 2017; Goulbourne et al., 2011). Nuclear lipid droplets are droplets of mostly triacylglycerol and cholesterol that appear to originate from the ER lumen, nuclear envelope lumen, the inner nuclear membrane, or type I nucleoplasmic reticuli (Lagrutta et al., 2017; Layerenza et al., 2013; Ohsaki et al., 2016; Romanauska and Köhler, 2018; Sołtysik et al., 2019). Altering lipid synthesis at the INM controls nuclear lipid droplet formation in yeast (Romanauska and Köhler, 2018). Recent work showed for the first time that formation of nuclear lipid droplets is conserved in human cells. However, in contrast to budding yeast, they form in the absence of the triglyceride-sequestering lipid droplet maturation protein seipin, indicating that the mechanism of nuclear lipid droplet formation differs from that of ER-derived lipid droplets (Sołtysik et al., 2020; Wang et al., 2016a; Zoni et al., 2020). While the function of nuclear lipid droplets is not fully

known, evidence has implicated them in hepatocyte (liver) lipid homeostasis (Lagrutta et al., 2017; Ohsaki et al., 2016). The nuclear envelope is thus an active player in regulating and performing lipid synthesis in spite of its continuity with the ER.

Many lipid synthesis-regulating functions of the nuclear envelope involve CTP:phosphocholine cytidyltransferase α (CCTα). CCTα localizes to the inner nuclear envelope and catalyzes the synthesis of CDP-choline, which is the rate limiting step of phosphatidylcholine (the most abundant structural glycerophospholipid in metazoan cells) synthesis (Cornell and Antonny, 2018). CCTα does not constitutively localize to the inner nuclear membrane, however. In response to curvature elastic stress of the inner nuclear membrane, the M helices of CCTα move away from an autoinhibitory conformation to insert into the surface of the lipid bilayer, and linkers facilitate close apposition of the catalytic domain to the membrane to provide an anhydrous milieu for its activity (Haider et al., 2018; Knowles et al., 2019; Ramezanpour et al., 2018). Recent evidence suggests that hepatocyte nuclear lipid droplets recruit CCTα to membranes, perhaps in response to bilayer stress (Ohsaki et al., 2016; Sołtysik et al., 2019). Acute induction of nucleoplasmic reticuli formation also depends on the localization and activity of CCTα (Gehrig et al., 2008; Goulbourne et al., 2011). Recent evidence suggests CCTα's localization is regulated posttranslationally, as phosphorylation of CCTα's membrane binding domain limits its localization to the INM and nuclear lipid droplets (Yue et al., 2020). Given its functions in sensing lipid composition of the INM and nuclear lipid droplets, CCTα links the lipid

composition of the nuclear envelope to regulation of lipid synthesis. How the nuclear envelope regulates lipid synthesis through mechanisms other than CCTα has yet to be fully elucidated.

Lipid synthesis in the endoplasmic reticulum

Lipid synthesis pathways in the ER

The bulk of membrane lipids are synthesized in the ER, and this process is controlled by nutritional inputs and uses substrates of nutrient metabolism (Figure 1.3). All lipids that are made in the ER *de novo* are made from acetyl-Coenzyme A (acetyl-CoA), which is produced by conversion of citrate from the Krebs cycle, breakdown of fatty acids, or breakdown of amino acids (Pietrocola et al., 2015). Glycerolipids additionally require glycerol-3-phosphate, which is made from glycerol derived from glyceraldehyde-3-phosphate made during glycolysis (Lunt and Vander Heiden, 2011) or glycerol from glyceroneogenesis (Hanson and Reshef, 2003). In mammalian cells, the decision to synthesize membrane lipids is controlled by pro-growth signaling that is largely controlled by mammalian target of rapamycin (mTOR) (Ben-Sahra and Manning, 2017). Nutrients such as amino acids, glucose, and growth factors lead to downstream mTORC1 activation, which leads to activation of sterol regulatory element binding proteins (SREBPs), transcription factors that lead to upregulation of fatty acid and cholesterol synthesis genes through an unknown mechanism (Ben-Sahra and Manning, 2017). In yeast, transcription of fatty acid synthesis genes mediated by the transcription factors Ino2 and Ino4 occurs during exponential growth and under nutrient conditions that lead to increased ER PA

concentrations (by sequestering the transcriptional repressor Opi1, which binds PA) (Henry et al., 2012; Hofbauer et al., 2018; Loewen et al., 2004). Increased fatty acid synthesis leads to increased *de novo* lipid synthesis in these pro-growth contexts to support cell proliferation.

Additional signals for ER lipid synthesis are changes in intracellular membrane physical properties, such as packing (Jacquemyn et al., 2017). CCTα localizes to the surface of the inner nuclear membrane in response to packing defects to perform the rate-limiting step for PC synthesis (Cornell and Antonny, 2018). The PA phosphatase lipin localizes to membranes more readily with increased PA and PE concentration (Eaton et al., 2013; Karanasios et al., 2010). In yeast, membrane saturation is sensed by Mag2 and controls transcription of the fatty acid desaturase gene Ole1 (Ballweg et al., 2020). SREBPs are additionally regulated by cholesterol in ER membranes (which is usually scarce to begin with); low cholesterol leads to increased SREBP processing that generates mature, functional SREBPs (Shimano and Sato, 2017). Lipid synthesis in the ER thus takes nutrient availability and membrane properties as signaling inputs for generating lipids for cell growth and maintenance.

ER-derived lipids all start from acetyl-CoA (Holthuis and Menon, 2014) (Figure 1.3). Acetyl-CoA is then converted to either malonyl-CoA in the committed step for fatty acid synthesis (feeding into glycerolipid or sphingolipid synthesis) or acetoacetyl-CoA in the committed step for cholesterol synthesis (Holthuis and Menon, 2014; Tong, 2005) (Figure 1.3). In cholesterol synthesis, sequential steps lengthen and cyclize intermediates into cholesterol in ER

membranes. In fatty acid synthesis, malonyl-CoA is elongated by fatty acid synthase into the fatty acid palmitate, which can be elongated and desaturated into other fatty acyl-CoA species (Figure 1.3). For sphingolipid synthesis, fatty acids are formed into long chain bases, then are additionally acylated to form ceramides, and these can be additionally processed in the Golgi to form other sphingolipids such as sphingomyelin (Breslow, 2013) (Figure 1.3).

Committed glycerolipid synthesis begins with formation of lysophosphatidic acid (LPA) from fatty acyl Co-A and glycerol-3-phosphate (Jacquemyn et al., 2017). LPA can be additionally acylated to form PA. In metazoans, PA can form phosphatidylinositol through the CDP-DAG pathway, or it can be dephosphorylated to form diacylglycerol by phosphatidic acid phosphatases (PAPs), including lipins (Zhang and Reue, 2017). DAG can form PC or PE or triglycerides through the Kennedy pathway (Gibellini and Smith, 2010; Kennedy and Weiss, 1956). The synthesis of either PA- or DAG-derived lipids depends on PA phosphatase activity, which is mediated by lipins in mammalian cells.

CTDNEP1 and lipin 1 control of ER lipid synthesis

The phosphatidic acid phosphatase lipin 1 (Pah1 in budding yeast; Ned1 in fission yeast; LPIN-1 in nematodes) and its phosphatase C terminal domain nuclear envelope phosphatase 1 (CTDNEP1) (Nem1 in budding and fission yeast; CNEP-1 in nematodes) regulate the synthesis of PA- and DAG-derived lipids (Figure 2.1A). Lipin is conserved from yeast to humans, and isoforms of lipin are known to be phosphoregulated in yeast, nematodes, flies, mice, and humans (Bahmanyar et al., 2014; Eaton et al., 2013; Grimsey et al., 2008; Harris

et al., 2007; O'Hara et al., 2006; Santos-Rosa et al., 2005; Tange et al., 2002). In budding yeast, Pah1 was found to be a Mg^{2+}-dependent phosphatidic acid phosphatase (PAP) that dephosphorylates PA to form DAG (Han et al., 2006). Nem1 was found to be a haloacid dehalogenase (HAD) superfamily phosphatase that dephosphorylates lipin to activate it (Kim et al., 2007; O'Hara et al., 2006; Santos-Rosa et al., 2005). In mouse cells, the nutrient-sensing kinase complex mTORC1 phosphorylates lipin (Peterson et al., 2011). Because other glycerophospholipid species can be formed from PA and DAG (Figure 2.1A), the activation state of lipin regulated by Nem1/CNEP-1/CTDNEP1 determines which glycerolipid species are made in the ER.

Depletion of Nem1/CNEP-1 in budding yeast and *C. elegans* alters cellular lipid composition and ER and nuclear envelope membrane structures (Bahmanyar et al., 2014; Siniossoglou et al., 1998). In budding and fission yeast, loss of lipin catalytic activity leads to a proliferation of nuclear envelope and ER membranes, drastically altering the nucleus' shape from round to lobed (Siniossoglou et al., 1998; Tange et al., 2002). In LPIN-1- or CNEP-1-deficient *C. elegans* early embryos, PA and PI are increased, resulting in an increase in ER sheets and deficient nuclear envelope breakdown (Bahmanyar et al., 2014; Golden et al., 2009; Gorjánácz and Mattaj, 2009). Cultured mouse cell nuclei become oblong rather than round when exposed to conditions causing lipin dephosphorylation (Peterson et al., 2011). In mice, active lipin is also thought to negatively regulate transcriptional regulation of fatty acid synthesis and positively regulate lipid breakdown and adipocyte maturation, and these mechanisms may

occur through local PA concentration changes or in some cases lipin interaction with transcriptional regulators (Finck et al., 2006; Péterfy et al., 2005; Peterson et al., 2011; Phan et al., 2004; Zhang et al., 2012). The functions of lipin 1 and CTDNEP1 in regulating lipid synthesis in human cells are not well understood. Key features of human diseases involving loss of function of lipin 1 or CTDNEP1 are not seen in mouse models of lipin 1 deficiency, so studies of human CTDNEP1/lipin 1 are warranted (Jones et al., 2012; Pelosi et al., 2017). In what is known so far in all organisms, however, lipin and CTDNEP1 generally act to limit membrane glycerolipid synthesis and abundance.

Lipid synthesis alterations in cancer

Cancer is a disease is caused and aggravated by genetic or epigenetic changes to a cell's DNA that cause a cell to divide continuously in an uncontrolled manner. Cancer is often characterized by hallmarks, common characteristics that facilitate transformation of benign cells into malignant cells and that make malignant cells even more so, all at the expense of surrounding healthy cells (Fouad and Aanei, 2016). Recently redefined hallmarks include alterations within the cell— advantages for growth and proliferation, survival-promoting stress responses, and adaptive metabolic alterations— along with others involving tumor interaction with surrounding tissue to promote metastasis, or spreading to other tissues (Fouad and Aanei, 2016). Changes in lipid synthesis are part of the adaptive metabolic alterations that support growth and proliferation in cancer cells.

Lipid synthesis is necessary for cell division. Cells accumulate membrane lipids prior to mitosis to supply membranes for organelles for both daughter cells (Jackowski, 1994). Cancer cells frequently show increased lipid synthesis to support increased cell proliferation (Currie et al., 2013). Consistent with their role upstream of sphingolipid and glycerolipid synthesis, the components of fatty acid synthesis are highly upregulated in cancer (Cheng et al., 2018). SREBPs, SREBP processing components, and SREBP target genes are all upregulated in a variety of tumors, as are proteins responsible for generating acetyl-CoA, such as ATP citrate lyase and acetyl-CoA synthetases (Cheng et al., 2018). SREBP1 targets fatty acid synthase and stearoyl-CoA desaturase are especially known to be upregulated in cancer (Igal, 2010; Kuhajda et al., 1994). Upregulation of these fatty acid synthesis pathway components bypasses the pro-growth signaling that works through mTOR to lead to SREBP activation and target gene upregulation, all in support of uncontrolled cell proliferation. Because the complex functions and dynamics of organelles are all supported by lipid synthesis, the total impact of increased lipid synthesis in cancer cells is not understood.

Nuclear envelope and endoplasmic reticulum dynamics during cell division

In open mitosis in mammalian cells, the nuclear envelope breaks down; its membranes are absorbed into the ER, while nuclear envelope-resident proteins distribute throughout the ER (if transmembrane) or cytosol (if soluble) (Figure 1.4). During mitotic exit, nuclear envelope membranes are reassembled from ER membranes (Figure 1.4). In this section, nuclear envelope and ER dynamics in mitosis will be discussed.

Nuclear envelope breakdown

In nuclear envelope breakdown, the nuclear pore complexes, nuclear lamina, DNA-associated proteins, and inner nuclear membrane proteins are phosphorylated by mitotic kinases, and nuclear envelope membranes disassemble (Ungricht and Kutay, 2017). Nuclear envelope breakdown begins with phosphorylation and disassembly of nuclear pore complexes in a sequential manner that leads to slow initial inward diffusion of cytosolic molecules (Dultz et al., 2008; Lénárt et al., 2003; Terasaki et al., 2001). Cyclin dependent kinase 1 (Cdk1), Polo-like kinase 1, and NIMA-related kinase 1 phosphorylate the FG (soluble) nucleoporin Nup98 leading it to be disassociated from the nuclear pore complexes first, facilitating disassembly of other Nups in protein complexes (Dultz et al., 2008; Laurell et al., 2011; Macaulay et al., 1995). The nuclear lamina is then phosphorylated by protein kinase C (PKC) and Cdk1-cyclin B, leading to its disintegration (Goss et al., 1994; Mall et al., 2012; Ottaviano and Gerace, 1985; Peter et al., 1990). Dynein pulling forces from the nascent mitotic spindle forming under mammalian cell nuclei also contribute to breakdown of the lamina (Beaudouin et al., 2002). Phosphorylation of proteins that link DNA and the lamina to the inner nuclear membrane leads to dissociation of chromosomes from the nuclear envelope (Hirota et al., 2005; Molitor and Traktman, 2014; Tseng and Chen, 2011).

Nuclear envelope clearance from mitotic spindle and chromosomes

After disassembly of nuclear envelope-associated proteins by mitotic phosphorylation, the nuclear envelope membranes are removed from the vicinity

of chromosomes to ensure that the assembling mitotic spindle can access chromosomes. Multiple mechanisms appear to play a role in removing membranes from chromatin. Depletion of LINC complex components or NudE/EL (which promotes dynein association to the nuclear envelope during mitotic entry) reduces the removal of nuclear envelope membranes from chromatin (Turgay et al., 2014). ER-associated proteins REEP3/REEP4 also limit membranes from being associated with mitotic chromosomes (Schlaitz et al., 2013). Nuclear envelope breakdown is also influenced by mitotic ER structure or ER/nuclear envelope membrane composition. Maintenance of mitotic ER structure by reticulon expression or expression of the membrane fusion GTPase Rab5 is required for proper nuclear envelope breakdown in the *C. elegans* early embryo (Audhya et al., 2007). Depletion of lipin or CNEP-1/CTDNEP1 in *C. elegans* and human cells leads to defective or delayed nuclear envelope breakdown (Bahmanyar et al., 2014; Golden et al., 2009; Gorjánácz and Mattaj, 2009; Mall et al., 2012). After nuclear envelope breakdown and removal of membranes from chromatin, the nuclear envelope membranes are absorbed into ER membranes (Yang et al., 1997). The nuclear envelope and ER in mitosis are a contiguous membrane system, with nuclear envelope transmembrane proteins being distributed throughout the ER (Ellenberg et al., 1997; Yang et al., 1997).

ER and endomembrane exclusion from mitotic spindle and chromosomes

During prometaphase through mitotic exit, the mitotic ER localizes primarily to the cell cortex, and this localization is important for mitotic fidelity. In *Drosophila* S2 cells, the membranes are thought to form a “spindle matrix” that

concentrates factors critical for building the mitotic spindle (Schweizer et al., 2015). Disruption of the spindle matrix causes disorganized spindle formation that leads to chromosome missegregation (Schweizer et al., 2015). The ER-resident protein STIM1 is phosphorylated in mitosis to abolish its association with the microtubule plus end-interacting protein EB1 (Smyth et al., 2012). REEP3/4 on ER membranes also facilitate removal of ER membranes from chromatin; though REEP3/4 interact with microtubules and ER membranes exhibit minus-ward movement, REEP3/4 do not interact with the minus-ward motor dynein (Schlaitz et al., 2013). It is not known how REEP3/4 drive membrane dissociation from mitotic chromosomes along microtubules. What remains to be described for mitotic ER localization is how lateral contacts between ER membranes and spindle microtubules are avoided, as ER membranes interact with microtubules (MTs) along their lengths by ER-resident MT-binding proteins and interactions with cargo motors (Bola and Allan, 2009). Other membranous organelles also localize to the cell cortex during mitosis to facilitate coordinated division and organelle inheritance (Carlton et al., 2020). Persistence of membranes on chromosomes during mitosis leads to chromosome segregation errors, highlighting the importance of the cortical localization of ER membranes in mitosis (Champion et al., 2019; Schlaitz et al., 2013). It is not known how membrane biogenesis by the ER is coordinated with membrane dynamics during cell division, although clearance of membranes to the cell periphery in mitosis may ensure proper mitotic progression.

In addition to abolition of ER-MT contacts, ER membranes restructure during mitosis. Some have observed transition of ER structure to mainly sheet-like cisternae (Lu et al., 2009; Wang et al., 2013), while others have observed a transition to tubule-like structures, dependent on cell type (Puhka et al., 2007, 2012). REEP3/4 have shown to be important for maintaining ER structure in mitosis independently from their function to clear ER membranes from metaphase chromatin. Cells upregulate REEP4 expression by 50% in mitosis compared to interphase, and mitotic cells lacking REEP3/4 have large extended ER sheets instead of a network of tubules and sheets (Kumar et al., 2019). Abundance of ER-shaping proteins (specifically reticulons) has shown to influence the rate of reestablishment of the nuclear permeability barrier during mitotic exit, showing how ER structure in mitosis may regulate the progression of mitotic events (Anderson and Hetzer, 2008).

Nuclear envelope reassembly

During mitotic exit, the nuclear envelope reassembles from ER membranes (Figure 1.4). After anaphase onset and cyclin B degradation, protein phosphatases reverse phosphorylation of nuclear envelope proteins to facilitate nuclear envelope reformation (Asencio et al., 2012; Schmitz et al., 2010). Transmembrane INM proteins in ER membranes interact with DNA directly or through DNA-binding proteins like barrier to autointegration factor (BAF) or heterochromatin protein 1 to initiate nuclear envelope reassembly (Anderson and Hetzer, 2007; Schellhaus et al., 2015; Ulbert et al., 2006). ER membranes are recruited to chromatin in distinct regions based on spindle microtubule

localization (Haraguchi et al., 2008; Liu et al., 2018) (Figure 1.4). In the “non-core” region that is distal from spindle microtubules, almost all nuclear envelope proteins are present on the reforming nuclear envelope, including the nuclear pore complexes that assemble during mitotic exit (Clever et al., 2012; Haraguchi et al., 2000, 2008; Lee et al., 2001; Liu et al., 2018). In contrast, the “core” region where spindle microtubules are located possesses inner nuclear membrane proteins and most of the proteins involved in nuclear sealing but is bereft of NPCs (Haraguchi et al., 2000, 2008; Lee et al., 2001; Liu et al., 2018). Lamin A is associated with the “core” region, whereas lamin B is associated with the “noncore” region (Haraguchi et al., 2008). BAF, a traditionally “core” protein, localizes to the entire reforming nuclear envelope but is enriched close to the spindle later on in the reassembly process, indicating that “core” regions could correspond to all surfaces of chromatin, with only “non-core” proteins being spatially restricted by the spindle (Samwer et al., 2017). In agreement with this idea, missegregating chromosomes located close to the spindle inherit only “core” proteins when they form micronuclei, while micronuclei forming from chromosomes in the cell periphery have the full complement of nuclear proteins (Liu et al., 2018).

During and after recruitment of ER membranes, the membranes spread and nuclear pore complexes assemble (Anderson and Hetzer, 2007; Schooley et al., 2012). ER membranes progressively cover the surface of chromatin; in the presence of an intact ER network, membrane fusion by GTPases is not necessary for reforming the nuclear envelope (Anderson and Hetzer, 2007).

Local lipid synthesis at the nuclear envelope could also provide the substrate for nuclear envelope reassembly, as newly synthesized phosphatidylcholine is selectively incorporated into the nascent nuclear envelope (Henry and Hodge, 1983; Rodriguez Sawicki et al., 2019). It is not fully understood how lipid synthesis before and during mitosis are coordinated to allow proper nuclear assembly. A combination of preexisting membranes spreading and local synthesis of new lipids could contribute to the rapid formation of a nuclear envelope, which is performed on the order of 10 minutes in mammalian cells (Anderson and Hetzer, 2008; Lu et al., 2011).

Nuclear pore complexes also assemble in a mechanism distinct from interphase NPC insertion (Schooley et al., 2012). First, soluble MEL28/ELYS interacts with chromatin and recruits NUP107-160 (Franz et al., 2007). Then, POM121 on ER membranes interacts with NUP160 (Mitchell et al., 2010). Additional soluble nucleoporins are incorporated to form the functional NPC (Schooley et al., 2012). The membrane topology of this process is such that NPCs are built into holes in the nuclear envelope membrane that shrink and then dilate to accommodate the nucleoporins (Otsuka et al., 2018). Nuclear pore complexes are transport-competent before they are fully built and begin importing from the “non-core” regions before the nuclear envelope is completely assembled (Lu et al., 2011; Otsuka et al., 2018). The nuclear envelope is not sealed at this point, preventing a spatially uniform increase in imported material in the reforming nucleus.

Toward the end of nuclear envelope reassembly, the nuclear envelope is sealed, and DNA-bound microtubules are severed. Nuclear sealing is performed by ESCRT-III complexes (Olmos et al., 2015; Vietri et al., 2015). LEM2 on ER membranes interacts with BAF on chromatin and recruits the ESCRT component CHMP7 (Gu et al., 2017), which also binds membrane PA (Thaller et al., 2021). LEM2 has shown to condense to a separated liquid phase around spindle microtubules that will be severed, creating a ring-like seal (von Appen et al., 2020). This seal facilitates assembly of ESCRT-III spiral filaments that constrict and lead to membrane fusion by VPS4 and hole resolution (von Appen et al., 2020; Olmos et al., 2015; Vietri et al., 2015). The spindle microtubule is severed by spastin (Vietri et al., 2015). Coordination of membrane lipid synthesis by CNEP-1/CTDNEP1 facilitates proper nuclear sealing (Penfield et al., 2020). After completion of nuclear sealing, the daughter nuclei are transport-competent and fully sealed, and the nuclei expand to their interphase size as additional pores are incorporated (Carlton et al., 2020; Ungricht and Kutay, 2017). The coordination of membrane dynamics from nuclear envelope breakdown to nuclear sealing are crucial for limiting abnormal nuclear formation.

Micronuclei

Micronuclei are small nuclei that form from missegregated chromosomes or chromosome fragments that form their own nuclear envelope separate from the primary nucleus (Fenech et al., 2011) (Figure 1.5). Micronuclei are commonly found in cancer and serve as prognostic markers for cancer progression (Adhikari, 2019). Micronuclei are also used as a biomarker for exposure to

genotoxic agents suspected to cause DNA damage or chromosomal instability (Adhikari, 2019; Nikolouzakis et al., 2019). Therefore, understanding the mechanisms by which micronuclei form is important for understanding cancer progression and underlying chromosomal instability.

Mechanisms of formation of micronuclei

Chromosome fragments can form micronuclei (Figure 1.5). Chromosome fragments form when non-homologous end joining repairs DNA double strand breaks in such a way that two breaks that do not belong together are joined; these fragments can subsequently have zero or two centromeres (Fenech et al., 2011). Erroneous repair leads to chromosome fragmentation in other situations as well. Chromosome fragmentation resulting in micronuclei can also occur in chromosome bridges, wherein a chromatid or chromosome attached to two sides of the spindle spans and links the segregating chromosome masses (Fenech et al., 2011; Gisselsson, 2008; Janssen et al., 2011). However, chromosome bridges do not form micronuclei if the missegregated chromosome is incorporated into one or both primary nuclei (Pampalona et al., 2016). Chromosome fragments can also arise from chromothripsis, a catastrophic genetic event in which 3 or more double strand breaks rearrange at once to lead to randomly strung together fragments (Leibowitz et al., 2015). These are not mutually exclusive, as chromosome bridges from dicentric chromosomes can also undergo chromothripsis (Maciejowski et al., 2015).

Micronuclei can also occur from missegregation of whole chromosomes and chromatids (Figure 1.5). Micronuclei caused by chromosome missegregation

occur when the lagging chromosomes are excluded from primary nuclei before the nuclear envelope reassembles. Lagging chromosomes can be caused by defective spindle assembly checkpoint activity, merotelic (unbalanced) kinetochore-microtubule attachments, or faulty chromosome alignment. Spindle assembly checkpoint proteins limit chromosome missegregation by surveying attachments of spindle microtubules to kinetochores. Chromosomes attached to one spindle pole (or neither spindle pole) are sensed by the spindle assembly checkpoint. Deficiency in the surveillance parts of the spindle assembly checkpoint permits the cell to progress from metaphase to anaphase before all chromosomes are attached (Fenech et al., 2011). Defects in centromere or kinetochore architecture can also contribute to chromosome missegregation by causing misattachments to not be surveilled properly by the spindle assembly checkpoint (Fenech et al., 2011). Merotely is another major mechanism that generates lagging chromosomes (Cimini et al., 2001). Merotelic attachments occur when a kinetochore of a chromosome is attached to microtubules from both spindle poles, leading to a tug-of-war instead of poleward movement for that chromatid at anaphase onset (Gregan et al., 2011). It is important to note that although the spindle assembly checkpoint surveils for unattached kinetochores, merotelic attachments satisfy the checkpoint. Because the attachment is imbalanced, merotelically attached chromosomes lag in anaphase and form micronuclei (Figure 1.5, “Merotely”). Merotely can be recovered during prometaphase and metaphase, indicating that lack of recovery is part of the mechanism for lagging chromosome formation (Cimini, 2003; Wang et al., 2017).

The extent to which the number of microtubules attached to a merotelically attached kinetochore from each side is unbalanced also influences whether or not the chromosome will missegregate during anaphase (Cimini et al., 2004; Thompson and Compton, 2011).

Chromosome misalignment is another mechanism by which micronuclei can form through chromosome missegregation. Alignment occurs during chromosome congression in prometaphase, when chromosomes attached to the mitotic spindle move toward the metaphase plate. Congression is performed by chromokinesins, kinesin motor proteins that interact with chromosomes and spindle microtubules and generate chromosome movement (Almeida and Maiato, 2018). Loss of kinesin KIF18A, which suppresses kinetochore dynamics to promote congression, leads to increased formation of micronuclei (Fonseca et al., 2019). The micronuclei form from missegregated but normally attached chromosomes that arise from having to travel longer distances during anaphase (Fonseca et al., 2019). These data suggest that having chromosomes lined up at the metaphase plate allows all chromosomes to travel together upon anaphase onset so that all chromosomes can be incorporated into primary nuclei before the nuclear envelope reassembles. Consistent with this idea, it has been proposed that late-aligning chromosomes are more likely to become lagging chromosomes after anaphase onset (Kuniyasu et al., 2019).

It is important to note that p53, a tumor suppressor very frequently lost in cancer, is thought to arrest the cell cycle of cells with aneuploidy resulting from chromosome fragments (Soto et al., 2017). In contrast, aneuploidy from

missegregation of whole chromosomes is tolerated by p53 with regards to cell cycle progression (Soto et al., 2017). p53 is mutated in 42% of cancers overall, though the frequency ranges from 2.2% to 95% depending on the tissue of origin (Bykov et al., 2018). Therefore, in cases where cells have intact p53, whole chromosome missegregation may contribute further to chromosomal instability.

Consequences of formation of micronuclei

Nuclear envelope reassembly in micronuclei differs from in the main nucleus, and this has consequences for nuclear envelope integrity. It has been proposed that nuclear envelope reassembly occurs more slowly (by NUP107 fluorescence tracking) on lagging chromosomes due to a limiting Aurora B gradient in the spindle midzone (Afonso et al., 2014). Live and fixed cell imaging with more nuclear envelope markers has since revealed that the nuclear envelope reforms on micronuclei at the same time as the main nucleus, (Liu et al., 2018). However, in lagging chromosomes in the spindle midzone, only “core” nuclear envelope proteins are recruited, in contrast to recruitment of the full complement of nuclear envelope proteins, including NPCs, in lagging chromosomes located in the cell periphery (Liu et al., 2018). The mechanism for two modes of nuclear assembly is due to presence of tightly-bundled spindle microtubules in the midzone restricting membrane access, as opposed to an Aurora B gradient restricting protein localization (Liu et al., 2018).

This finding might shed light on a discrepancy in findings regarding the fate of micronuclei depending on how the lagging chromosome formed. Chromatids in micronuclei generated by merotely do not replicate DNA and have

shown to missegregate often in future divisions (Crasta et al., 2012; Soto et al., 2018), whereas chromatids in micronuclei generated by misalignment may missegregate less often (Fonseca et al., 2019). Merotelic chromosomes can be seen as lagging chromosomes within the spindle midzone (Cimini, 2003; Cimini et al., 2004), whereas this is not always the case with misaligned chromosomes (Fonseca et al., 2019). Micronuclei generated by misaligned chromosomes away from the spindle midzone may be more likely to have functioning NPCs and may thereby be able to import factors that allow DNA replication and functional kinetochore assembly. Further studies will illuminate whether different mechanisms of chromosome missegregation lead to micronuclei that contribute to aneuploidy more or less due to different levels of completeness in nuclear envelope reassembly. This is especially important to understand because micronuclei are additionally subject to adverse events that may lead to mutations.

DNA within micronuclei is subject to damage, innate immune detection, deficient replication, and missegregation. It has been shown that micronuclei can undergo a loss in compartmentalization characterized by infiltration of the chromosome by ER membranes and increased DNA damage; this collapse is influenced by lamin B levels in micronuclei (Crasta et al., 2012; Hatch et al., 2013; Vietri et al., 2020). Chromothripsis has also shown to occur in micronuclei, leading to complex rearrangements and indels in the chromosome contained in the micronucleus (Zhang et al., 2015). Collapse of the nuclear envelope in micronuclei leads to recognition of micronuclear cytosolic DNA by cGAS, which leads to downstream upregulation of type I interferon response genes

(MacKenzie et al., 2017). Nuclear rupture in micronuclei also cannot be repaired in a coordinated manner as in primary nuclei (Vietri et al., 2020). Finally, as mentioned previously, DNA in micronuclei may not replicate properly and often missegregates during mitosis (Crasta et al., 2012; Soto et al., 2018). Even if the DNA is incorporated into a primary daughter nucleus in the subsequent division, the cell runs the risk of damaged DNA from the micronucleus being propagated in future divisions (Giam and Rancati, 2015). The high prevalence of micronuclei in aggressive cancers likely reflects their role in increasing genome instability.

Role of membrane dynamics in formation of micronuclei

Membrane dynamics have been implicated in chromosome missegregation that can lead to formation of micronuclei. Preventing clearance of ER membranes from chromatin by knocking down REEP3 and REEP4 leads to chromosome missegregation, including lagging chromosomes and chromosome bridges (Schlaitz et al., 2013). Artificially tethering ER membranes to chromatin prior to anaphase onset likewise prevents proper chromosome segregation (Champion et al., 2019). These data support the idea that membranes can impede proper chromosome segregation and raise the question of how membrane abundance and dynamics in mitosis regulate mitotic progression.

Despite the importance of membrane dynamics in mitosis influencing chromosome segregation, the role of lipid synthesis regulation of membrane abundance in regulation chromosome segregation has not been studied. Mammalian cells accumulate lipids prior to entry into mitosis (Jackowski, 1994), but it is not known if limiting membrane lipid synthesis impacts mitotic fidelity.

Here, I identify a link between regulation of ER membrane biogenesis and formation of micronuclei through the lipin phosphatase CTDNEP1. In Chapter 2, I characterize ER and nuclear envelope protein localization and functions using CRISPR-Cas9 gene editing in human cell lines, and I use a CRISPR-edited cell line to show that CTDNEP1 limits ER membrane abundance through its catalytic activity on lipin 1 and limits formation of micronuclei. In Chapter 3, I use live cell imaging time lapses to characterize the membrane dynamics of CTDNEP1-depleted cells during cell division. I show that membranes are more abundant and less cleared in mitotic cells depleted of CTDNEP1. In Chapter 4, I investigate specific mechanisms of chromosome missegregation in CTDNEP1-depleted cells using small molecule inhibitors to show that specific errors that are not sensed by the spindle assembly checkpoint are less corrected in CTDNEP1-depleted cells. In Chapter 5, I elucidate the mechanism by which CTDNEP1 limits membrane biogenesis using lipidomic analysis, small molecule inhibition of fatty acid synthesis, and RNAi modulation of fatty acid synthesis gene expression. I show that CTDNEP1 limits flux into fatty acid and ER membrane lipid synthesis to limit membrane biogenesis. I additionally show that inhibition of fatty acid synthesis suppresses formation of micronuclei in CTDNEP1-depleted cells, which links the excess membranes in mitosis to error correction defects seen with loss of CTDNEP1. In Chapter 6, I discuss remaining questions and possibilities for future experiments.

Together, these show that the protein phosphatase CTDNEP1 restricts ER membrane biogenesis through lipin 1 to facilitate mitotic error correction that

limits the formation of micronuclei in human cell lines. These data link regulation of lipid synthesis to chromosome segregation errors resulting in micronuclei, which can inform as to how chromosomal instability can occur in cancer cells with increased lipid synthesis.

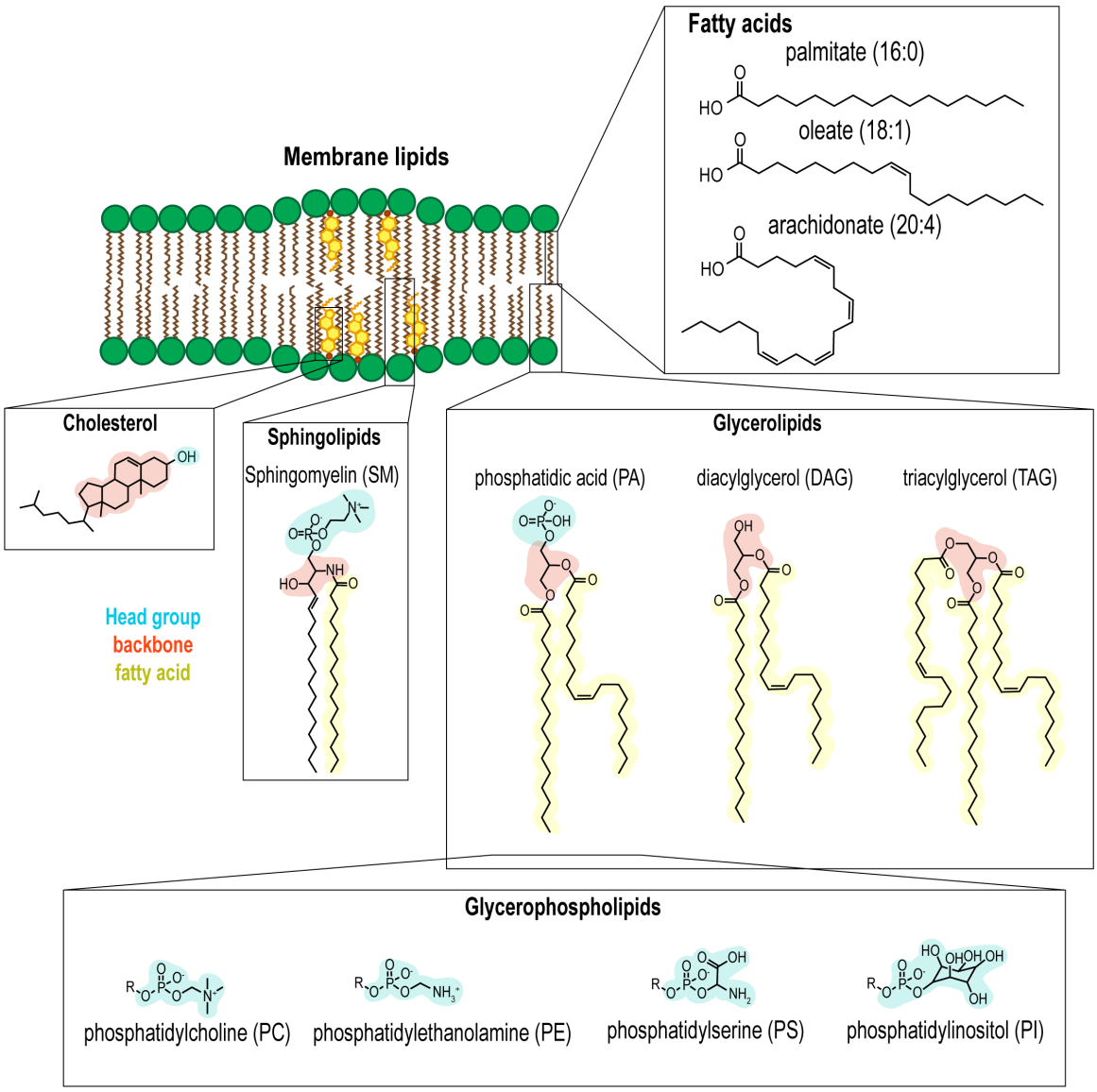

Figure 1.1 Types of cellular lipids and their properties
Schematic of types of membrane lipids. Organization of glycerolipids, sphingolipids and cholesterol into membrane microdomains shown. Head groups of lipids are shown in blue, backbones are shown in red, and fatty acid chains are shown in yellow.

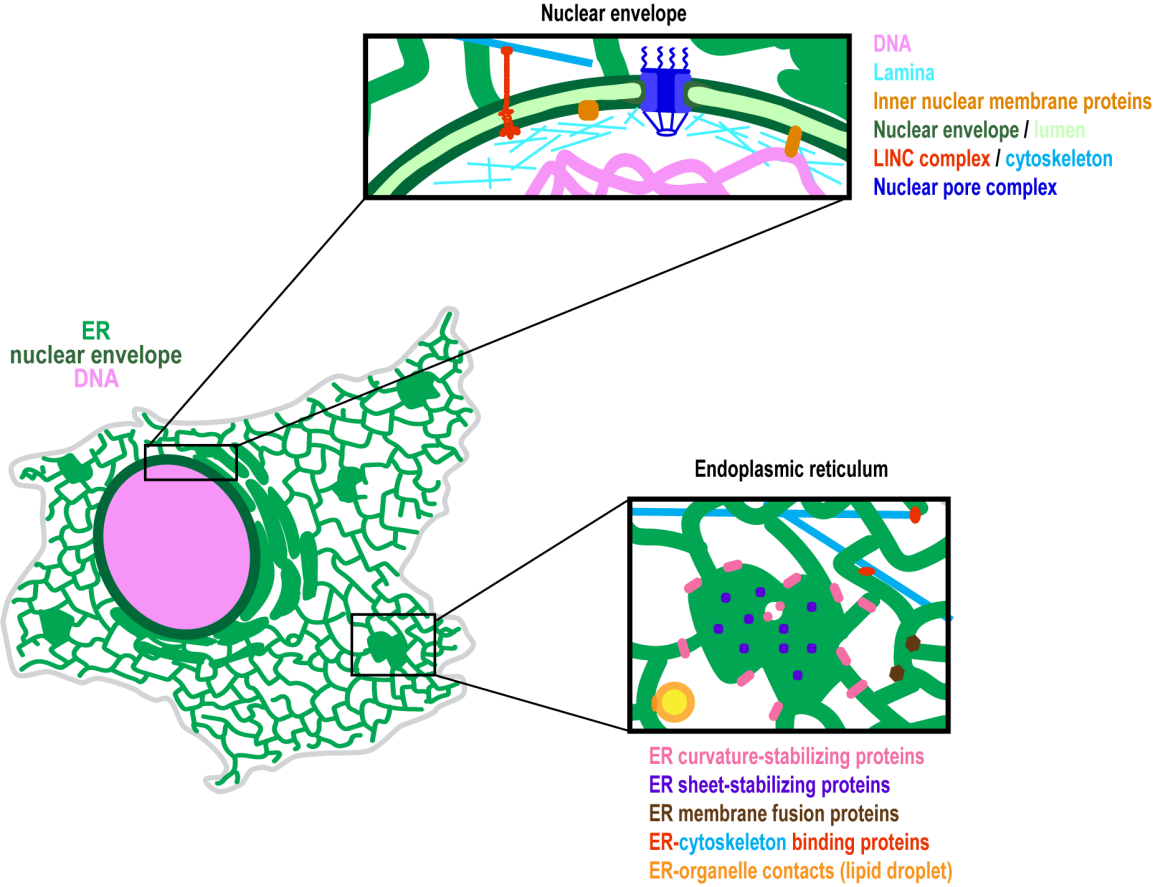

Figure 1.2 The nuclear envelope and endoplasmic reticulum
Organization of nuclear envelope and ER (focusing on peripheral ER) is shown. The nuclear lamina and chromatin are anchored to the inner nuclear membrane through inner nuclear membrane proteins. Nuclear pore complexes span the inner and outer nuclear membrane, and the LINC complex spans the nuclear membranes and connects the nuclear envelope to the cytoskeleton. In the ER, curvature-stabilizing proteins stabilize curvature at tubules, tubule junctions, sheet edges, and on ER nanohole edges. Sheet-stabilizing proteins localize to the center of sheets and stabilize the luminal width. ER structure is also dependent on contacts with the cytoskeleton and contact sites with other organelles (tethered lipid droplet shown).

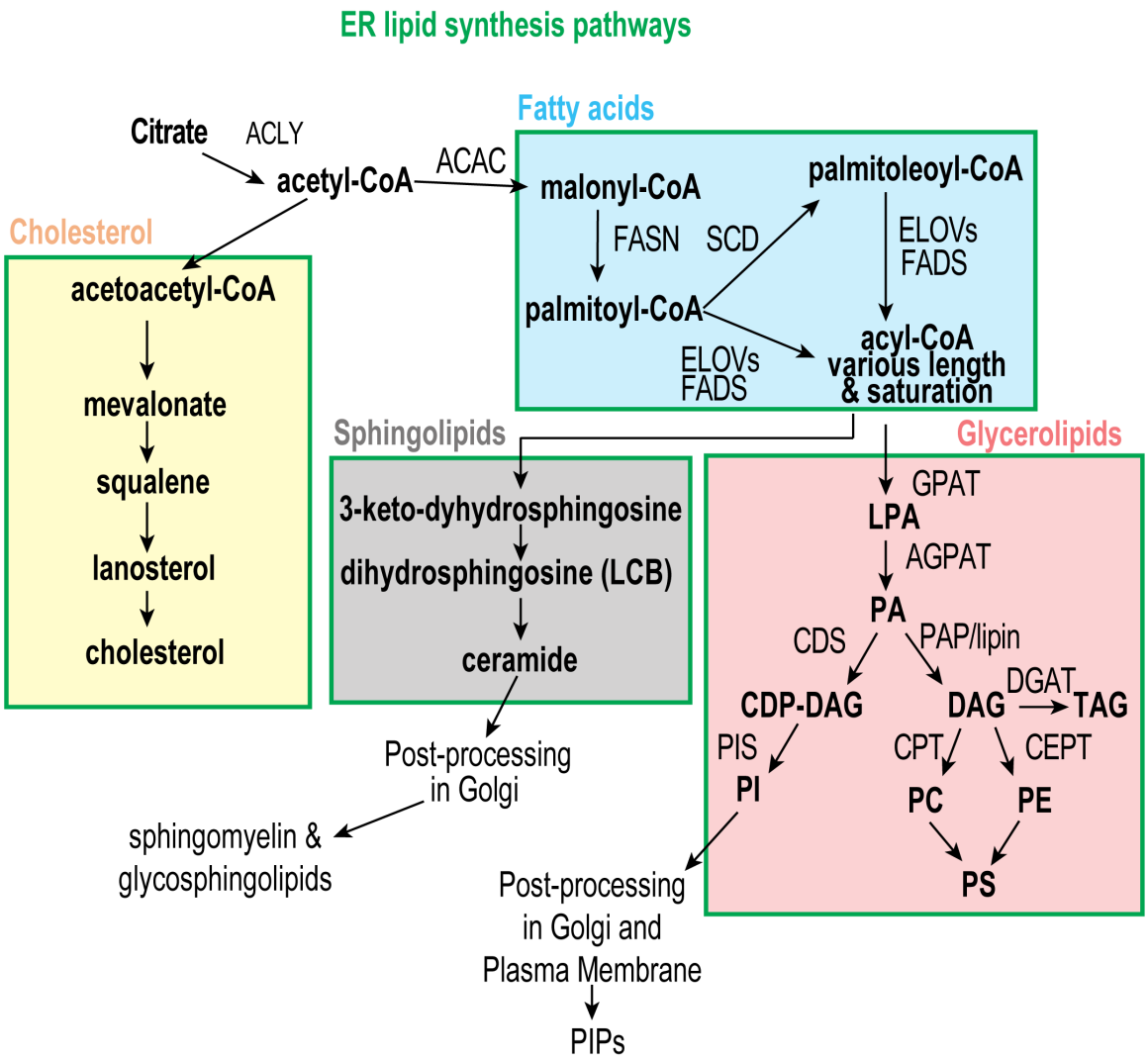

Figure 1.3 Lipid synthesis pathways in the ER
Schematic of lipid synthesis pathways in the ER (steps occurring in the ER are outlined in green). Citrate is converted to acetyl-CoA by ATP citrate lyase (ACLY). Acetyl-CoA is converted to acetoacetyl-CoA, and subsequent steps result in synthesis of cholesterol. Acetyl-CoA is also formed into fatty acids starting with conversion to malonyl Co-A by acetyl-CoA carboxylase (ACAC). Fatty acid synthase (FASN) elongates malonyl-CoA to palmitate, which is then converted to palmitoyl-CoA. Fatty acids are desaturated at the Δ9 position by stearoyl-CoA desaturase (SCD) and/or additionally desaturated by fatty acid desaturases (FADs) or elongated by ELOVs (Elongation of very long chain fatty acids proteins). These acyl-CoAs can be incorporated into sphingolipids or glycerolipids. Acyl-CoA is combined with glycerol-3-phosphate by glycerol-3-phosphate acyltransferase (GPAT) to form LPA. LPA can be additionally acylated by 1-acylglycerol-3-phosphate-O-acyltransferase (AGPAT) to form PA. PA can be converted to CDP-DAG by CDP-DAG synthase (CDS) and then PI by PI synthase (PIS). PI can be phosphorylated to form phosphatidylinositol phosphate derivatives (PIPs). PA can

be dephosphorylated by PAPs (including lipins) to DAG. DAG can be formed to TAG by diacylglycerol acyltransferase (DGAT) or PC or PE by choline or choline/ethanolamine phosphotransferase (CPT, CEPT); PC and PE can be converted to PS.

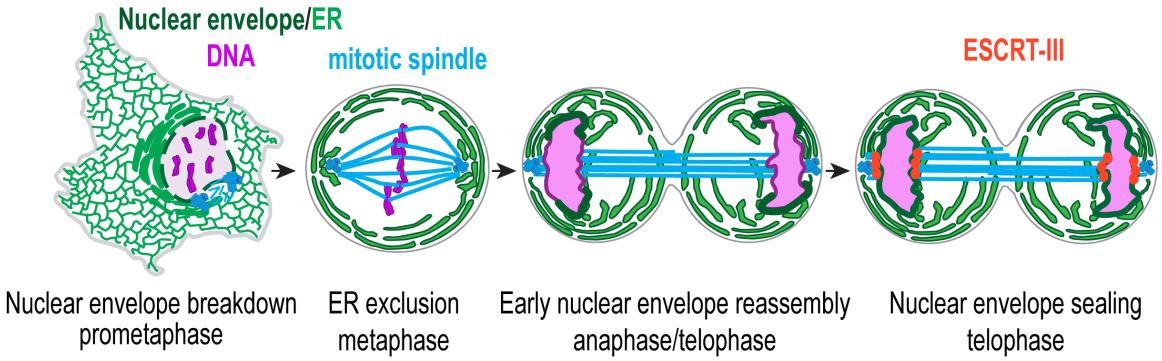

Figure 1.4 Nuclear envelope and ER dynamics in mitosis
Schematic of ER and nuclear envelope dynamics from nuclear envelope breakdown through mitotic exit. The nuclear envelope is intact in interphase, and centrosomes are unduplicated. During prometaphase, the nuclear envelope breaks down, and the nuclear envelope membranes are absorbed into ER membranes. Membranes are cleared from chromosomes and cleared to the cell periphery, excluded from the spindle. After anaphase, nuclear membranes contact chromosomes and reform the nuclear envelope. The membranes are sealed by the ESCRT-III complex.

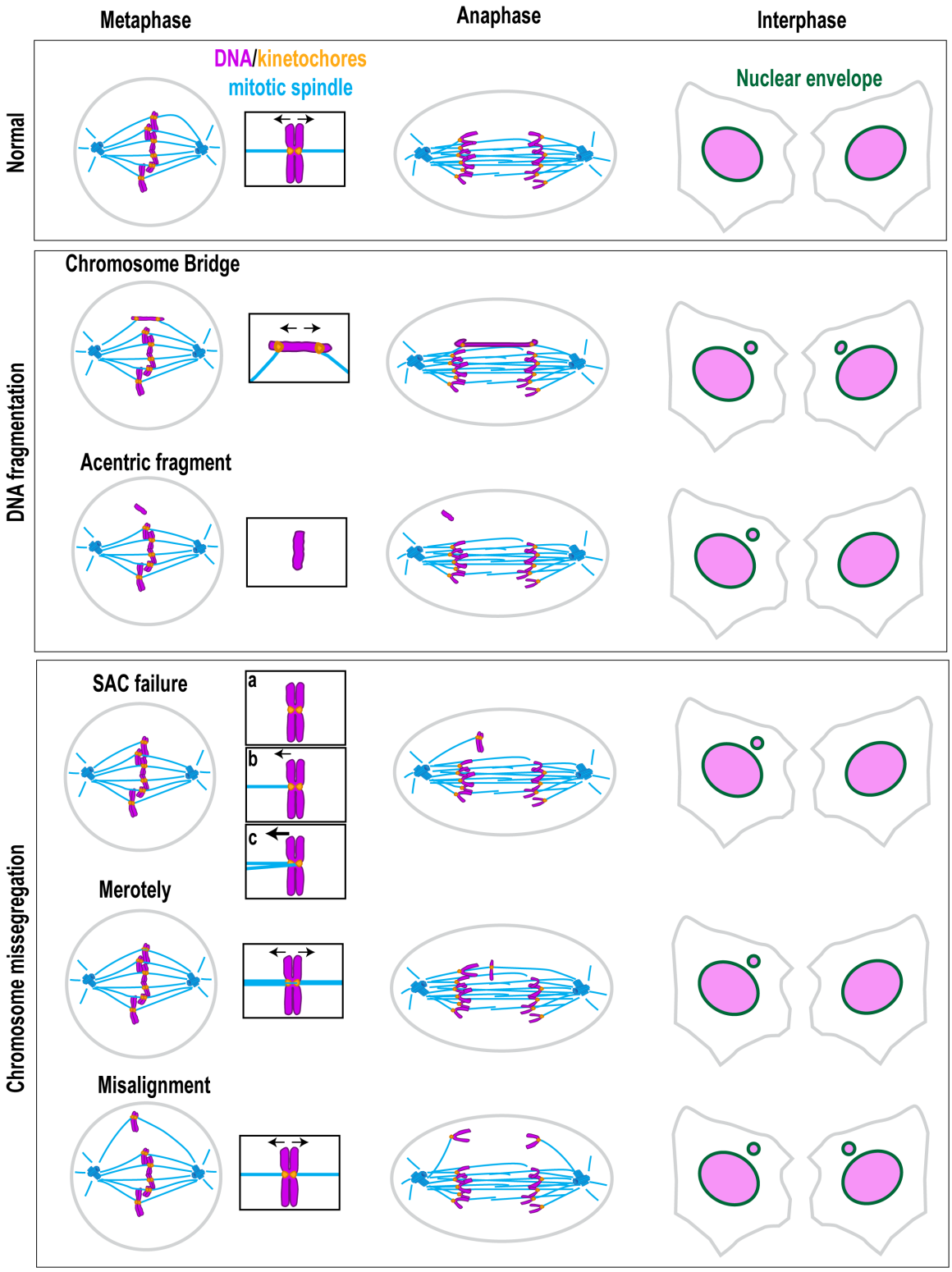

Figure 1.5 Mechanisms of formation of micronuclei
Schematic of mechanisms for how micronuclei can form. Chromosome abnormalities and attachment abnormalities in metaphase are shown with insets showing kinetochore-microtubule attachments and tension/pulling forces (black

arrows). The result for chromosome segregation in anaphase is shown, as well as the consequence for interphase primary and micro-nuclei. In “SAC failure,” insets show a) no attachment, b) monotely, and c) syntely.

Chapter 2: Nuclear envelope-localized human CTDNEP1 regulates ER membrane biogenesis, nuclear morphology and formation of micronuclei

Some of this work is included and/or modified from this publication and manuscript:

Lena K. Schroeder, Andrew E.S. Barentine[#], Holly Merta[#], Sarah Schweighofer[#], Yongdeng Zhang, David Baddeley, Joerg Bewersdorf[+], Shirin Bahmanyar[+]. Dynamic nanoscale morphology of the ER surveyed by STED microscopy. *J Cell Biol* 218(1):83-96 (2018). doi: https://doi.org/10.1083/jcb.201809107.

Holly Merta[*], Jake W. Carrasquillo Rodríguez[*], Maya I. Anjur-Dietrich, Mitchell E. Granade, Tevis Vitale, Thurl E. Harris, Dan Needleman, Shirin Bahmanyar. A CTDNEP1-lipin 1-mTOR regulatory network restricts ER membrane biogenesis to Enable Chromosome Motions Necessary for Mitotic Fidelity. *bioRxiv* (2021). doi: https://doi.org/10.1101/2021.03.02.433553

[*] Co-first authors
[#] Co-second authors
[+] Co-corresponding authors

Introduction

The structure of organelle membranes is important for organelle function. Tissue-specific functions rely on unique and highly adapted organelle structures, such as long ER tubules in neurons (Yalçın et al., 2017) or multilobed, flexible nuclei in some immune cells (Skinner and Johnson, 2017). Maintenance of organelle structure is shown to be specifically disrupted in many human diseases, highlighting the importance of understanding how organelle structure is established and maintained.

Organelle structure can be maintained by membrane-shaping proteins. In the ER, reticulons stabilize membrane curvature through insertion of two hydrophobic helices (Voeltz et al., 2006). Reticulons oligomerize and cooperate with other ER-shaping proteins to stabilize new and existing curvature, including sheet edges and nanoholes (Hu et al., 2008; Schroeder et al., 2018; Shibata et al., 2010; Wang et al., 2016b). Ectopic reticulon overexpression causes formation of long, unbranched peripheral ER tubules, whereas knockdown of reticulons leads to an increase in ER sheets and decrease in tubules (Anderson and Hetzer, 2008; Schroeder et al., 2018; Shibata et al., 2010; Voeltz et al., 2006). Both reticulon overexpression and downregulation can be observed in neurodegenerative diseases, reflecting how tuning ER structure is important for cell function (Chiurchiù et al., 2014).

Organelle structure is also determined by ER lipid synthesis. Overabundance of membranes through increased fatty acid synthesis without increased reticulon expression leads to ER sheet formation (Shibata et al., 2010).

Increased synthesis of PI, PC, and PE in yeast and PA and PI in *C. elegans* by deletion of the lipin phosphatase CTDNEP1 leads to ER membrane expansion and sheet formation, respectively, while nuclear envelope structure is also affected (Bahmanyar et al., 2014; Kim et al., 2007; Siniossoglou et al., 1998). For this study, we primarily focused on the function of human CTDNEP1 for maintaining ER and nucleus morphology through lipin 1 dephosphorylation.

In metazoans, lipin's catalytic activity determines whether glycerolipid species derived from PA or DAG are made in the ER. Lipin has also shown to have transcriptional regulation activities, in some cases indirectly through regulation of PA levels. In mice, lipin 1 has shown to positively regulate PPARα and PPARγ-dependent transcription to activate lipid breakdown and adipocyte differentiation (through transcription factor or repressor binding) (Finck et al., 2006; Phan et al., 2004; Zhang et al., 2012). Nuclear lipin 1 represses SREBP-dependent fatty acid synthesis gene transcription through an unknown mechanism (Peterson et al., 2011). Lipin 1 is sensitive to metabolic status through insulin-dependent phosphorylation by the nutrient-sensing kinase mTOR (Huffman et al., 2002; Peterson et al., 2011). Lipin 1 isoforms α and β transcriptional regulation permits differentiation of adipocytes through modulating PA levels (Grimsey et al., 2008; Koh et al., 2008; Phan et al., 2004; Zhang et al., 2012), and consistent with this role, lipin 1-deficient mice and flies exhibit lipodystrophy (Péterfy et al., 2001; Ugrankar et al., 2011). Lipin 1's transcriptional regulation activity is dependent on its localization; dephosphorylated lipin

localizes to the nucleus, while phosphorylated lipin is retained in the cytoplasm and degraded (Peterson et al., 2011; Shimizu et al., 2017).

CTDNEP1 and lipin 1 are both HAD superfamily phosphatases with canonical DXDX(T/V) active sites (Seifried et al., 2013) (Figure 2.1B-2.1C). CTDNEP1 has an N-terminal transmembrane domain and localizes to nuclear envelope and ER membranes (Bahmanyar et al., 2014; Han et al., 2012; Siniossoglou et al., 1998), while Pah1/lipin 1 is a cytosolic/nuclear protein that binds to PA in membranes for its PAP activity (Eaton et al., 2013; Han et al., 2006). Lipin's polybasic domain is important for its PA binding and is thought to serve as its nuclear localization signal (Eaton et al., 2013; Ren et al., 2010) (Figure 2.1C). CTDNEP1 localization and activity is allowed through interaction with its obligate binding partner, NEP1R1 (ySpo7) (Han et al., 2012; Siniossoglou et al., 1998). While CTDNEP1 and lipin 1 are HAD superfamily phosphatases, the phosphatase domain of lipins was recently found to be split into the NLIP and CLIP domains, which fold together to form the functional phosphatase domain (Khayyo et al., 2020) (Figure 2.1B-2.1C). Lipin 1 linker phosphorylation is now thought to prevent functional assembly of the phosphatase domain (Khayyo et al., 2020).

The functions of human CTDNEP1 and lipin 1 are not fully known. Unlike the mouse model of lipodystrophy, human patients with lipin 1-inactivating mutations do not have lipodystrophy but instead present with rhabdomyolysis, episodic breakdown of muscle tissue leading to myoglobinuria, during childhood (Michot et al., 2010; Zeharia et al., 2008). Truncating mutations in CTDNEP1 are

found in Group 3/4 and uncharacterized medulloblastomas, cancers of the cerebellum (Jones et al., 2012; Northcott et al., 2017). Patients in these subgroups of medulloblastoma frequently have loss of heterozygosity at Chr17p where *CTDNEP1* (and prominent tumor suppressor *TP53*) are located, while *TP53* is unaltered, making CTDNEP1 a tumor suppressor candidate in this region (Jones et al., 2012). The disease mechanisms for loss of function of CTDNEP1 and lipin 1 are not understood. Unlike in lipin-deficient mice, adipose tissue of patients lacking functional lipin 1 has normal composition, though lipid droplets are smaller, and adipogenic gene expression is upregulated (Pelosi et al., 2017). Human adipose tissue may have compensatory mechanisms in place that are not present in mice, or lipin's functions in human adipose tissue may not be fully conserved. These differences warrant study of lipin 1 and CTDNEP1 to further understand their regulation of lipid synthesis in human cells.

Here, I show that CTDNEP1 is required for limiting ER membrane biogenesis in a human cancer cell line. I establish methods for quantifying ER membrane abundance and qualitatively assessing changes in ER structure through modulating reticulon levels versus ER abundance through CTDNEP1 and lipin. I also demonstrate that CTDNEP1 and lipin 1 catalytic activity are required for limiting ER membrane abundance. I also show that CTDNEP1 has a conserved role for maintaining nuclear shape. These data show that regulation of ER membrane biogenesis and nuclear morphology in human cells through CTDNEP1 and lipin 1 converges with limiting ER biogenesis in other model organisms, despite differences in lipid synthesis pathways and lipid synthesis

regulation between organisms. These data also uncover a previously unknown role for CTDNEP1 in regulating formation of micronuclei.

Results

CRISPR-Cas9 strategies for targeting nuclear envelope and ER proteins reveals role for reticulons in ER nanohole formation/stability

To determine the role of reticulons in the formation or stabilization of curvature within ER sheets in ER nanoholes, I generated a CRISPR knockout cell line of all isoforms of reticulon 4 (Figure 2.2A-B). The sgRNA targeted the sequence corresponding to a hydrophobic region within the reticulon homology domain, in order to disrupt the synthesis of stable reticulon 4 isoforms (Figure 2.2A). Consistent with the depletion of reticulon isoforms, reticulon 4 B/D were unable to be detected by immunoblot in RTN4^{KO} U2OS cells (Figure 2.2B). Immunostaining RTN4^{KO} cells with an antibody targeting the reticulon 4 N terminus (targeting RTN4A/B/D) did not show any specific staining unlike in unmodified U2OS cells (data not shown). Triple knockdown of reticulons 1,3, and 4 induces ER sheet formation (Anderson and Hetzer, 2008). With L. K. Schroeder, I imaged U2OS or RTN4^{KO} U2OS cells treated with control or RTN1/3-targeting siRNA by confocal and stimulated emission depletion (STED) nanoscopy (Figure 2.2C). Nanoholes can be seen in ER sheets in control cells (Figure 2.2C, above inset and arrows), whereas sheets in reticulon-depleted cells are devoid of nanoholes (Figure 2.2C, below inset). On the population level, control U2OS cells have more small peripheral sheets that are non-uniform in appearance, whereas reticulon-depleted cells have extended ER sheets that are

uniform in appearance throughout (Schroeder et al., 2018). Thus, reticulons are involved in ER nanohole formation or maintenance.

To determine nanohole size relative to other membrane features by live STED nanoscopy, a homozygous endogenous marker of a well-defined feature was needed. Nuclear pore complexes have a defined size of ~100 nm and vary little in size, making them an ideal candidate. I targeted the Y complex nucleoporin NUP160 because NUP160 fusion proteins are functional in multiple model organisms, which is particularly important in the case where every copy of the gene is tagged. Using homology-directed repair with CRISPR-Cas9, I tagged all alleles of endogenous NUP160 with the coding sequence for the dye ligand covalent binding partner HaloTag7 (Figure 2.3A-2.3B). Endogenously-tagged NUP160 localized to the nuclear envelope in a punctate localization, as expected (Figure 2.3C). A coverslip-level section highlights the punctate localization of the protein (Figure 2.3C). STED nanoscopy of NUP160-Halo revealed a consistent ~100 nm size of nuclear pore complex membrane holes, which contrasts with a large range of ER nanohole sizes (Schroeder et al., 2018).

CRISPR-Cas9 strategies for targeting human CTDNEP1

To understand the cellular functions of human lipin 1 and CTDNEP1 in this study, I targeted human CTDNEP1 for generation of tagging knock-in and knockout cell lines (Figure 2.4, Figure 2.6). Targeting CTDNEP1 is preferable to targeting lipin due to the presence of 3 lipins in human cells with some functional redundancy, and targeting lipin activation is less detrimental to cell health than lipin deletion to permit functional studies (Bahmanyar et al., 2014; Donkor et al.,

2007; Gorjánácz and Mattaj, 2009). Depleting cells of CTDNEP1 also allows us to study the roles of lipin's S/T phosphorylation state, as there are post-translational modifications of lipin not regulated by CTDNEP1 that cannot be ruled out by targeting lipin alone (Liu and Gerace, 2009; Song et al., 2020).

I generated a CTDNEP1 knockout clonal U2OS human osteosarcoma cell line using CRISPR-Cas9 (Figure 2.4A). This knockout cell line has a homozygous truncating single-nucleotide insertion in exon 3 just past the DLDET active site (Figure 2.4B). Although the active site is intact, this truncating mutation makes CTDNEP1 transcripts in this cell line candidates for nonsense-mediated decay, as CTDNEP1 mRNA levels in CTDNEP1^{KO} U2OS cells are decreased by >80%, similar to knockdown of CTDNEP1 in U2OS and RPE-1 cells (Figure 2.5A). This cell line is deficient in CTDNEP1 phosphatase activity, as J. W. Carrasquillo Rodríguez found that lipin 1 in CTDNEP1^{KO} cells is hyperphosphorylated and less abundant (Merta et al., 2021).

Localization of endogenous CTDNEP1

The localization of CTDNEP1 in human cells is not known but has the potential to inform the mechanism for how lipin 1's localization to the nucleus is regulated – Nem1 in yeast localizes to nuclear envelope/ER membranes, but CNEP-1 in *C. elegans* is enriched at the nuclear envelope (Bahmanyar et al., 2014; Siniossoglou et al., 1998). Generation of a CTDNEP1-specific antibody has proven difficult (S. Bahmanyar, G. Celma, T. Vitale, Y. Kim, correspondence). A commercial CTDNEP1 peptide antibody, a commissioned commercial peptide antibody, and an antibody made using CTDNEP1 with 3

internal deletions to improve solubility all failed to show specific staining by immunoblot or immunofluorescence (data not shown; with Tevis Vitale and Gunta Celma). To determine the localization of endogenous human CTDNEP1, I generated a CRISPR knock-in U2OS cell line in which all copies of *CTDNEP1* are tagged with GFP (Figure 2.6). Live spinning disk confocal imaging of GFP signal in U2OS CTDNEP1^{EN}-GFP cells reveals that CTDNEP1 localizes to the nuclear envelope with some cytoplasmic localization likely corresponding to ER membranes (Figure 2.7A, left). Knockdown of CTDNEP1 in U2OS CTDNEP1^{EN}-GFP cells abrogates GFP fluorescence at the nuclear envelope (data not shown). Fluorescent punctae are also seen in the perinuclear region of cells (Figure 2.7A, left). Imaging immunostained GFP in U2OS CTDNEP1^{EN}-GFP cells shows nuclear envelope localization and perinuclear diffuse staining, perhaps localizing to ER membranes (Figure 2.7A, right). The perinuclear punctate fluorescence seen in live imaging of CTDNEP1-GFP is not seen in immunostained cells, indicating that this could be an artifact of high exposure needed to visualize low-expressing CTDNEP1. If not, this localization could correspond to lipid droplets, which CTDNEP1 has shown to localize to in yeast (Choudhary et al., 2020). Future colocalization studies will reveal if CTDNEP1 in human cells localizes to compartments other than the nuclear envelope, as well as what face of the nuclear envelope CTDNEP1 localizes to, to further enlighten its functions.

CTDNEP1 controls ER membrane abundance in human cells

Deletion of CTDNEP1 in yeast (yNem1) leads to a proliferation of ER and nuclear envelope membranes (Kim et al., 2007; Siniossoglou et al., 1998). I transiently expressed GFP-KDEL in U2OS CTDNEP1^{KO} cells to visualize ER morphology. Control U2OS cells have an ER morphology consisting of dense ER sheets close to the nucleus and a peripheral network of mostly tubules arranged in 3-way junctions (Figure 2.8A, top and top inset). In contrast, CTDNEP1^{KO} U2OS ER appears to be expanded and dense uniformly throughout the cell, extending to the periphery (Figure 2.8A, bottom). ER tubules and sheets can be seen in the cell periphery (Figure 2.8A, bottom inset). This phenotype is highly penetrant, occurring in 93.7 ± 3.9 % of cells (Figure 2.8B). To rule out the possibility that this "expanded ER" phenotype is exclusive to GFP-KDEL overexpression, I fixed U2OS cells with formaldehyde and glutaraldehyde to preserve membrane structure and stained them with a calnexin antibody to mark ER membranes. Staining of this endogenous ER marker also revealed that the ER is more packed and denser in CTDNEP1^{KO} U2OS cells compared to control cells (Figure 2.8C).

Two subsequent attempts to generate of a second clonal CTDNEP1^{KO} cell line using a different guide RNA sequence (targeting exon 1) were unsuccessful. To control for the possibility that the expansion of ER membranes in CTDNEP1^{KO} cells could be due to non-CTDNEP1 mutations in the clonal cell line, I knocked down CTDNEP1 in unmodified U2OS cells (Figure 2.5A, right; Figure 2.9). Cells subject to CTDNEP1 RNAi showed expanded ER membranes (Figure 2.9A). With a knockdown to 9.3 ± 0.43% of CTDNEP1 mRNA transcript levels

determined by qRT-PCR, 77.5 ± 6.42% of cells treated with CTDNEP1 siRNA had expanded ER, closely resembling the phenotype penetrance in CTDNEP1^{KO} U2OS cells (Figure 2.5A, right; Figure 2.9B).

To determine if the effect of depleting CTDNEP1 leading to expansion of ER membranes is cell line-specific, I chose RPE-1 cells to replicate this phenotype. Although U2OS cells are amenable to imaging organelles due to their size and spread-out shape, U2OS is a cancer cell line, and cancer cell lines can have upregulated expression of fatty acid synthesis genes (Cheng et al., 2018). This could possibly sensitize them to alterations in lipid synthesis pathways. RPE-1 cells are non-transformed, non-cancer, and mostly karyotypically normal, and they are ideal for ruling out the possibility of cancer cell specificity for CTDNEP1 depletion phenotypes. RPE-1 cells have a smaller ER tubular network per cell area compared to U2OS cells (Figure 2.10A, left), but expansion of ER membranes can still be seen when CTDNEP1 is knocked down (Figure 2.10A, right). This presents as a disappearance of the peripheral tubular network and bright ER filling the cell to the cell edge, obscuring individual ER features, like tubules (Figure 2.10A, right). This phenotype was also highly penetrant in RPE-1 cells (Figure 2.10B). In addition to replicating expansion of ER membranes with CTDNEP1 depletion in RPE-1 cells, E. Guinn and S. Lee have found that depletion of CTDNEP1 leads to ER expansion in COS-7 (African green monkey kidney) and DLD-1 (human colorectal adenocarcinoma) cells (data not shown). These data support the conclusion that CTDNEP1 limits the abundance of ER membranes in human cells from multiple tissue types and origins.

Quantitative and qualitative assessment of ER membrane morphology and abundance

To assess penetrance of the expanded ER phenotype in cell lines, I used scoring and incidence of the phenotype to report our findings. However, quantification of ER membrane expansion is needed to confirm the findings and to assess if a continuum of phenotypes exists. Segmentation of fluorescent ER signal has been used to discern the percentage of ER-positive pixels belonging to ER tubules or sheets to show which how a membrane fusion-regulating protein is required for tubule fusion and reducing ER sheets (English and Voeltz, 2013). In this study, the authors made maximum projections of ER signal, reduced the bit depth from 16-bit to 8-bit, and segmented both total ER and sheet-like ER using the Renyi entropy thresholding algorithm before quantifying sheet-like ER versus total ER (English and Voeltz, 2013). The advantage of this approach is that reducing the bit depth and making the image a maximum projection of ER signal makes it easier to segment total ER, which takes on a variety of morphologies of different brightnesses due to different thicknesses and, in some cases, non-uniform distribution of fluorescent markers or ms-scale ER movement (Nixon-Abell et al., 2016; Schroeder et al., 2018). I sought to adapt this technique to quantify changes in ER membrane overall abundance rather than structure.

To quantify changes in the amount of membranes in cells with altered lipid synthesis by depletion of CTDNEP1, I measured the area fractions of cells that are taken up by ER membranes. Starting with 16-bit spinning disk confocal image stacks of GFP-KDEL (live) or calnexin (fixed) signal that encompassed the

entire cell volume, I reduced the bit depth to 8-bit and made maximum intensity projections of the image stacks. To ensure that peripheral tubules would be segmented as well as brighter ER features, I applied an unsharp masking filter to the maximum projection images, which subtracts a Gaussian blurred image (here with a radius of 0.2 and mask of 0.6) from the unaltered image to sharpen it (Figure 2.11A). I then thresholded the image using the Huang algorithm, which relies on measures of image fuzziness (Huang and Wang, 1995) (Figure 2.11A). Fuzziness in images refers to the extent of lack of belonging to the object or the background (Huang and Wang, 1995). The Huang algorithm in ImageJ finds the threshold at which fuzziness is minimized. I rationalized using the Huang algorithm for segmenting total ER because there is a wide dynamic range of maximum projection ER brightness due to morphology differences throughout the cell, and maximizing object-belonging is desirable to segment dim tubules with bright perinuclear ER. In practice, this thresholding segments total ER well (Figure 2.11A, images). I then manually drew outlines of the cell border and nucleus and then measured the percent area of the cytoplasm occupied by ER membranes (Figure 2.11A). Using this method, I show that CTDNEP1^{KO} U2OS cells have higher occupancy of the cytoplasm with ER membranes compared to control U2OS cells (Figure 2.11B). Cells depleted of CTDNEP1 by RNAi also have a higher percentage of ER-positive pixels taking up the cytoplasm area compared to cells treated with control siRNA (Figure 2.11B). The spread of individual values in control U2OS cells is large compared to the spread of values in CTDNEP1^{KO} cells (~55-85% in control cells versus ~85-100% in CTDNEP1^{KO}

cells) reflecting how CTDNEP1^{KO} cells' ER takes up a large proportion of the cytoplasm (Figure 2.11B). Cells treated with CTDNEP1 siRNA also have a larger spread of individual values and lower overall occupancy of ER in the cytoplasm compared to CTDNEP1^{KO} cells, likely due to a lesser extent of CTDNEP1 depletion with RNAi knockdown (Figure 2.11B).

To distinguish between expansion of ER membranes due to increased membrane abundance and alteration of ER morphology, I compared cells depleted of CTDNEP1 to cells depleted of reticulons 1, 3, and 4 (Figure 2.12). Depletion of reticulons 1, 3, and 4 causes the ER to form more membrane sheets that lack nanoholes, as well as thicker ER tubules (Anderson and Hetzer, 2008; Schroeder et al., 2018) (Figure 2.2C; Figure 2.12A, below, yellow arrow). In all cells, perinuclear ER is brightest and appears most dense (Figure 2.12A, blue arrows). In control U2OS and reticulon-depleted U2OS, peripheral ER tubules can be seen at the edge of cells, and ER sheets of roughly the same brightness as tubules can be seen in reticulon-depleted cells (Figure 2.12, left and below, yellow arrows). In contrast, the ER in CTDNEP1^{KO} cells is more uniformly bright in all areas of the cell, reflecting increased membranes rather than a shift in structure of existing membranes (Figure 2.12, right, yellow arrow). Thus, the appearance of expanded ER membranes in CTDNEP1^{KO} cells can be distinguished from a change in ER membrane structure by assessment of uniform ER brightness through the whole cell.

CTDNEP1 and lipin 1 phosphatase activities are required for limiting ER membrane abundance

To determine if the expansion of ER membranes in CTDNEP1^{KO} cells is due to loss of CTDNEP1 phosphatase activity, I transiently overexpressed CTDNEP1-HA wild type and mutant constructs with and without its obligate binding partner NEP1R1 (Figure 2.13A-B). Overexpressed CTDNEP1 and NEP1R1 localize to the nuclear envelope and ER membranes (Figure 2.13A). Expression of wild type CTDNEP1-HA alone (Figure 2.13A-B, "WT") partially suppressed the incidence of expansion of ER membranes in CTDNEP1^{KO} cells (Figure 2.13B). Consistent with its role in stabilizing CTDNEP1 localization and activity, NEP1R1 overexpression with expression of catalytically active CTDNEP1 rescued expansion of ER membranes to a greater extent (Santos-Rosa et al., 2005) (Figure 2.13B). CTDNEP1 in which the DLDET active site is mutated to ELDET (D67E; "PD") to render it phosphatase dead does not rescue ER expansion when co-expressed with NEP1R1, indicating that it is loss of active CTDNEP1 that is responsible for expansion of ER membranes in CTDNEP1^{KO} cells (Figure 2.13A-B).

Transient overexpression of CTDNEP1 in U2OS cells leads to localization that is not consistent with localization of endogenous CTDNEP1 (Figure 2.7; Figure 2.13A). Therefore, I quantified the incidence of ER expansion and occupancy of ER membranes in CTDNEP1^{KO} cells stably expressing wild type CTDNEP1 (Figures 2.13C-D, "WT (stable)"). Stable overexpression of CTDNEP1-HA substantially reduced the incidence of expanded ER in CTDNEP1^{KO} cells (Figure 2.13C). Stable overexpression of CTDNEP1-HA also reduced the occupancy of ER membranes in the cytoplasm of CTDNEP1^{KO} cells

(Figure 2.13D). Together, these data support the conclusion that expansion of ER membranes in CTDNEP1^{KO} cells is due to loss of CTDNEP1 catalytic activity.

CTDNEP1's primary known substrate for dephosphorylation is the phosphatidic acid phosphatase lipin (Santos-Rosa et al., 2005). Since lipin controls ER membrane lipid synthesis (Figure 2.1A), I sought to determine if the expansion of ER membranes in CTDNEP1^{KO} cells is caused by loss of lipin 1 control of lipid synthesis. I overexpressed lipin 1 in CTDNEP1^{KO} cells (Figure 2.14A). Mouse lipin 1β is the most well-studied mammalian lipin and has a variety of known mutants for studying its activity and localization (Harris et al., 2007; Peterson et al., 2011). Further, unlike in humans, the S/T phospho-sites of lipin 1 in mouse are confirmed by multiple mass spectrometry studies and are well-characterized (Harris et al., 2007; Peterson et al., 2011). I overexpressed FLAG-lipin 1β constructs in CTDNEP1^{KO} cells and visualized ER morphology with calnexin staining (Figure 2.14A). Wild type lipin 1β overexpression partially suppressed the incidence of expanded ER in CTDNEP1^{KO} U2OS cells (Figure 2.14A-B). This rescue is likely partial because CTDNEP1 is not present to dephosphorylate the overexpressed lipin. Therefore, I overexpressed a mutant form of lipin 1β in which 19 of the S/T sites identified by mass spectrometry as being known or probable insulin-dependent phosphosites are mutated to alanine ("19S/T to A", Figure 2.1A/B). This construct drives nuclear localization of lipin 1β in mouse cells (Peterson et al., 2011). Consistent with this finding, lipin 1β 19S/T to A localizes more to the nucleus than wild type lipin 1β in U2OS cells (Figure 2.14A, 2.15C). In order to determine if the loss of membrane biogenesis

regulation in CTDNEP1^{KO} cells is specifically due to loss of lipin 1 phosphatidic acid phosphatase activity, I overexpressed a mutant form of mouse lipin 1β that has 19 S/T residues mutated to A but also has two mutations in the DXDXT active site (DIDGT>EIEGT) that renders it phosphatase dead (Figure 2.14A-2.14B, “19S/T to A PAP dead”). Overexpression of this construct does not suppress the incidence of ER expansion in CTDNEP1^{KO} cells (Figure 2.14B). Based on these data, I conclude that the expansion of ER membranes is due to loss of CTDNEP1 dephosphorylation of lipin 1 to potentiate its catalytic activity.

Lipin 1 is known to regulate multiple transcription-based mechanisms of lipid homeostasis in a manner that is dependent on its localization to either the nucleus or cytoplasm (Finck et al., 2006; Peterson et al., 2011; Phan et al., 2004; Zhang et al., 2012). PPAR-mediated gene transcription is thought to be activated by lipin 1 binding a transcription factor or binding and sequestering a nuclear repressor (Finck et al., 2006; Phan et al., 2004; Zhang et al., 2012). Conversely, SREBP-mediated gene transcription is negatively regulated by nuclear lipin 1, although the mechanism for this is not clear (Peterson et al., 2011). To determine the impact of localization of lipin on the abundance of ER membranes in CTDNEP1^{KO} U2OS cells, I transiently expressed constructs of mouse lipin 1β with either a nuclear localization signal or nuclear export signal appended to the C terminus (Figure 2.15A). These signals were introduced to the C termini of the lipin constructs to minimize interference with the endogenous NLS located near the N terminus (that is also important for PA binding and thus lipin activity) (Eaton et al., 2013) (Figure 2.1C). In contrast to wild-type lipin 1β, which localizes to

mostly the cytoplasm, lipin 1β-NES localized more to the cytoplasm, and lipin 1β-NLS localized more to the nuclear compartment (Figure 2.15C).

Overexpression of wild type lipin 1β partially suppressed the incidence of expanded ER in CTDNEP1^{KO} cells (54.6 ± 8.1% in transfected cells vs 93.2 ± 4.4% in untransfected cells; Figure 2.14B). Appending either an NLS or NES to lipin 1β did not increase the extent of rescue of expanded ER in CTDNEP1^{KO} cells (64.2 ± 0.1% in lipin 1β-NLS-transfected cells vs 83.3 ± 2.5% in untransfected cells; 58.9 ± 3.7% in lipin 1β-NES-transfected cells vs 83.5 ± 1.5% in untransfected cells; Figure 2.15B). This finding is surprising given that lipin's localization has shown to be important for mediating transcription of fatty acid synthesis genes (Peterson et al., 2011). These data suggest that restoring lipin 1β activity overall in the cell is what is important for regulating ER abundance rather than localization of lipin alone. Alternatively, minor pools of lipin in cellular compartments may be sufficient to limit the synthesis of ER membranes.

An alternative mechanism for the etiology of ER membrane expansion in CTDNEP1-depleted cells is that PPARα activation by lipin is lowered, leading to decreased lipid breakdown (Finck et al., 2006). There is a known PPARα-binding motif, LXXIL, in lipin 1β, and mutation of this motif to LXXFF reduces the interaction with PPARα (Finck et al., 2006). This mutation also greatly reduces lipin 1β PAP activity, likely because the LXXIL motif is 6 residues away from the active site (Finck et al., 2006). We reasoned that if ER expansion is mediated through PPARα activation, overexpression of the binding mutant lipin would not rescue ER expansion to any extent, despite the PAP activity being reduced.

Unexpectedly, overexpression of lipin 1β with 19 S/T residues mutated to A and the LXXIL motif mutated to LXXFF partially suppressed ER membrane expansion in CTDNEP1^{KO} cells (Figure 2.15B), indicating that lack of PPARα transcriptional regulation is not the major mechanism of ER expansion in CTDNEP1^{KO} cells. Since phosphatase-deficient lipin 1β does not rescue ER membrane expansion at all, we conclude that lipin 1β 19xA LXXFF is at least partially functional. Mutation of S/T residues to alanine greatly increases PAP activity because dephosphorylation increases PAP activity (Eaton et al., 2013); the 19xA mutations may have a larger positive effect on the PAP activity of lipin 1β than the negative effect of the LXXFF mutation. These data together support the conclusion that ER membrane expansion in CTDNEP1^{KO} U2OS cells is due to loss of lipin 1β catalytic activity that is not dependent on lipin 1β localization and may not involve PPARα-dependent transcription. Thus, when CTDNEP1 is present, dephosphorylated, active lipin 1β limits ER membrane biogenesis.

Expression of endogenous ER proteins in CTDNEP1^{KO} cells

The expansion of ER membranes in CTDNEP1^{KO} cells raises the question of whether CTDNEP1-depleted cells contain more ER-resident proteins. Further, a mouse model of lipin 1 depletion in only muscle tissue exhibits accumulation of neutral lipids and ER stress of the sarcoplasmic reticulum (muscle cell ER), with consistently increased expression of the ER protein folding chaperone Binding immunoglobulin Protein (BiP) (Rashid et al., 2019). To establish whether ER-resident protein levels are increased in CTDNEP1^{KO} cells, I determined the expression of ER-resident proteins calnexin, calreticulin, and BiP by immunoblot

(Figure 2.16). Calnexin and calreticulin are protein folding chaperones that bind and stabilize glycosylated proteins to facilitate folding and oligosaccharide processing (Williams, 2006). Levels of calnexin and calreticulin in CTDNEP1^{KO} U2OS cells are not increased relative to control levels (Figure 2.16A). BiP levels are also not increased in CTDNEP1^{KO} cells (Figure 2.16B). Thus, ER-resident protein levels appear to not be increased with loss of CTDNEP1. Future studies will clarify if other ER stress pathways are upregulated with loss of CTDNEP1.

As stated previously, it has been hypothesized that the morphology of the ER depends on membrane abundance and concentration of curvature/morphology-stabilizing proteins (Shibata et al., 2010). To determine reticulon expression in CTDNEP1^{KO} cells, I immunoblotted for reticulon 4B/D (Figure 2.16C). In immunoblotted control cell lysates, two bands can be seen (Figure 2.16C). Surprisingly, a third, higher molecular-weight species was present in CTDNEP1^{KO} lysates, and the RTN4B/D species that were also in control cells were less abundant (Figure 2.16C). This higher molecular weight species is unlikely to be a reticulon oligomer due to its size (~55 kDa vs 50 kDa). RTN4B can be phosphorylated on S16 by cyclin-dependent kinases and on S107 with oxidative stress induction (Rodríguez-Feo et al., 2015; Schweigreiter et al., 2007), so these species might represent phosphorylated RTN4B or RTN4B/D with other post-translational modifications. Future studies will clarify if reticulon levels or post-translational modifications are altered with loss of CTDNEP1 and how these changes interact with lipid synthesis alterations to regulate ER morphology.

CTDNEP1 has a conserved function for maintaining nuclear shape

Loss of CTDNEP1 leads to altered nuclear morphology in multiple model systems. Expansion of ER and nuclear envelope membranes in budding and fission yeast with loss of Nem1 leads to lobulated nuclear structures (Siniossoglou et al., 1998; Tange et al., 2002). I sought to determine if regulation of nuclear structure by CTDNEP1 is conserved in human cells. Nuclear shape was measured by assessing solidity of DAPI-stained nuclei (Figure 2.17A). Solidity is defined as the area fraction of a convex hull for an object; more circular nuclei have solidity values closer to 1.0, whereas highly lobulated nuclei have solidity values less than 1 and decreasing with lobulation (Figure 2.17A). Nuclei of CTDNEP1^{KO} cells have lower solidity compared to nuclei from control U2OS cells (Figure 2.17B). An established measure for the percentage of nuclei in a population that have low solidity is the percentage of nuclei that have solidity values less than one standard deviation from the mean control solidity value (Fonseca et al., 2019). By this standard, a higher percentage of CTDNEP1^{KO} cells have low nuclear solidity values compared to control cells (31.7 ± 14.3 % of CTDNEP1^{KO} cells compared to 12.9 ± 5.3 % of control cells; Figure 2.17C). To determine if this change in nuclear shape is due to loss of CTDNEP1, I measured nuclear solidity in CTDNEP1^{KO} cells stably overexpressing CTDNEP1-HA (Figure 2.18). Overexpression of CTDNEP1 suppresses the low solidity of CTDNEP1^{KO} cells, both by measuring the population averages and percentage of nuclei with low solidity (12.8 ± 1.3 % of CTDNEP1-overexpressing CTDNEP1^{KO} cells compared to 39.3 ± 5.5 % of CTDNEP1^{KO} cells; Figure 2.18A-2.18B). These data

support the conclusion that CTDNEP1 has a conserved function for maintaining nuclear morphology.

CTDNEP1 limits formation of micronuclei

While observing nuclear morphology, I noticed that nuclei of CTDNEP1^{KO} cells frequently had micronuclei (Figure 2.19A, arrow in inset). I quantified the percentage of nuclei with micronuclei and found that more CTDNEP1^{KO} cells had micronuclei than control cells (10.2 ± 2.9 % of CTDNEP1^{KO} cells compared to 4.3 ± 0.8% of control cells; Figure 2.19B, above). To determine if the increase in micronuclei in CTDNEP1^{KO} cells is due to loss of CTDNEP1 function, I quantified the incidence of micronuclei in CTDNEP1^{KO} cells stably overexpressing CTDNEP1-HA. Overexpression of CTDNEP1 suppressed formation of micronuclei in CTDNEP1^{KO} cells (2.6 ± 1.3 % of CTDNEP1-expressing CTDNEP1^{KO} cells compared to 13.2 ± 5.1 % of CTDNEP1^{KO} cells; Figure 2.19B). Thus, CTDNEP1 limits formation of micronuclei.

Discussion

This work defines the roles of CTDNEP1 and lipin 1 in regulating ER membrane biogenesis (Figure 2.20) and nuclear structure (Figure 2.21) in human cells. Using human cell lines edited using CRISPR-Cas9 to tag endogenous CTDNEP1 loci with GFP, we show that CTDNEP1 is enriched at the nuclear envelope as CNEP-1 is in *C. elegans* early embryos (Bahmanyar et al., 2014). Using RNAi depletion of CTDNEP1 and a U2OS cell line in which CTDNEP1 was knocked out using CRISPR-Cas9, we show that CTDNEP1 limits the abundance of ER membranes. Quantitation of ER membrane segmentation confirms this

finding and provides a tool for future assessment of genetic modifications that alter lipid synthesis to determine if ER membrane abundance is affected. Qualitative comparison of CTDNEP1-depleted cells to ER shaping protein-depleted cells reveals that densely packed ER in CTDNEP1-depleted cells appears different from ER with more sheets. Overexpression of CTDNEP1 constructs in CTDNEP1^{KO} cells confirms a role for NEP1R1 in human cells for stabilizing CTDNEP1 as in yeast (Han et al., 2012; Santos-Rosa et al., 2005) and confirms that expansion of ER membranes in CTDNEP1^{KO} cells is due to loss of CTDNEP1 catalytic activity. Overexpression of mouse lipin 1β constructs in CTDNEP1^{KO} cells reveals that ER membrane expansion is due to loss of lipin 1 catalytic activity. Together, these data show that CTDNEP1 and lipin 1 control ER membrane biogenesis in human cells.

The finding that lipin 1 localizing to either the nucleus or cytoplasm partially rescue ER expansion in CTDNEP1^{KO} cells to a similar extent as non-specifically localized lipin is surprising given the nuclear envelope localization of endogenous CTDNEP1, which suggests local regulation of lipin. One consequence of CTDNEP1 depletion is that lipin levels are reduced (Merta et al., 2021) (finding by J.W. Carrasquillo Rodríguez). It is possible that overexpressed catalytically active lipin satisfies a requirement of raising levels of lipin in the cell to raise overall cellular PA, which then re-balances ER lipid synthesis (Figure 2.20A-B). In yeast, lipin localizes to the nuclear envelope (to the nuclear-vacuolar junction) under starvation conditions and produces DAG for TAG synthesis (Barbosa et al., 2015), so a similar mechanism may be in place for lipin and

CTDNEP1 localization to control lipid synthesis. We additionally found that a PPARα binding site mutant of dephospho-mimic 19xA lipin 1β appears to be catalytically active in that it partially suppresses ER expansion with loss of CTDNEP1, in contrast to previous findings. As previously mentioned, the dephosphorylation-mimic mutations may counteract the effects of reducing PAP activity that is caused by mutating the PPARα binding site. Future studies will illuminate the specific effects of lipin localization and post-translational modification in regulating its catalytic activity and ER lipid synthesis in human cells.

An open question that remains is whether the catalytic activity of lipin 1 limits ER membrane biogenesis by limiting synthesis of certain lipids, or shifting flux of lipid synthesis toward triglycerides and away from membrane biogenesis, or by influencing a combination of these (Bahmanyar et al., 2014; Grillet et al., 2016). In transcriptionally quiescent *C. elegans* early embryos, loss of CNEP-1 leads to an increase in PA and PI and increased ER sheets (Bahmanyar et al., 2014). In yeast, depletion of Nem1p leads to increased nuclear envelope and ER membrane biogenesis (Barbosa et al., 2015; Santos-Rosa et al., 2005; Siniossoglou et al., 1998). Loss of lipin 1 (yPah1) catalytic activity alone can explain the expansion of ER membranes in yeast, because yeast can utilize the CDP-DAG pathway to make PC and PE in addition to PI (the major membrane glycerophospholipid in yeast) (Barbosa et al., 2015). It has been hypothesized that lipin activity balances energy storage (as triglycerides) and membrane biogenesis (as PC and PE synthesis) in mammalian cells (Grillet et al., 2016). In

this model, increased lipin activity leads to greater DAG stores and higher TAG synthesis. Loss of lipin activity leads to increased synthesis of CDP-choline to in turn form PC because increased PA leads to increased CCTα activation (Grillet et al., 2016). In *Arabidopsis*, lipin (PAH1) depletion leads to increased ER sheets, and this occurs through increased PA activating CCTα to upregulate PC synthesis (Craddock et al., 2015). Evidence of PA activating CCTα in mammalian cells is lacking. It is known in multiple organisms, however, that CCTα senses membrane packing to increase CDP-choline synthesis (Cornell and Ridgway, 2015). DAG is also required for PC synthesis through the Kennedy pathway; in *Arabidopsis*, DAG levels in lipin mutants are not limiting for PC synthesis (Craddock et al., 2015), though it is not known if this is the case in mammals. Thus, the contribution of CCTα to increasing PC synthesis in human cells lacking lipin 1 catalytic activity is unclear. In all organisms, however, CTDNEP1 and lipin 1 orthologues limit ER membrane biogenesis through limiting synthesis of certain glycerolipids, though the mechanism appears to differ between yeast, worms, and plants. In human cells, CTDNEP1 (with its obligate binding partner NEP1R1) dephosphorylates lipin 1 (Figure 2.20A). CTDNEP1 regulates lipin 1 activation to control ER lipid synthesis, and multiple levels of lipin 1 regulation of lipid synthesis could contribute to limiting ER membrane biogenesis (Figure 2.20B-C). Whether lipin 1 limits ER membrane biogenesis through enzymatic, transcriptional, or indirect enzymatic regulation remains to be seen.

CTDNEP1 has a conserved function of maintaining nuclear structure (Figure 2.21). In yeast, loss of Pah1 catalytic activity leads to increased PA that feeds

into upregulation of fatty acid synthesis through Ino2/Ino4 derepression, and PA can form membrane glycerophospholipids that feed into membrane synthesis as opposed to TAG production (Figure 2.21A-B). This leads to an expansion of ER membranes but also a proliferation of nuclear envelope membranes (Siniossoglou et al., 1998). In human cells, despite differences in lipid synthesis pathways, CTDNEP1's function of controlling nuclear structure is conserved (Figure 2.21C-D).

CTDNEP1 also limits formation of micronuclei in human cells (Figure 2.19). CTDNEP1 has not been implicated in regulating formation of micronuclei in other organisms. CTDNEP1's role in limiting formation of micronuclei may be part of why it is commonly mutated in medulloblastoma subgroups associated with chromosomal instability, as micronuclei are a common consequence of chromosomal instability in cancer (Giam and Rancati, 2015; Jones et al., 2012). The remainder of this work will investigate the mechanism for formation of micronuclei with loss of CTDNEP1. The next chapter will describe investigation of the dynamics of expanded ER membranes during cell division to uncover how CTDNEP1 controls nuclear shape and limits formation of micronuclei.

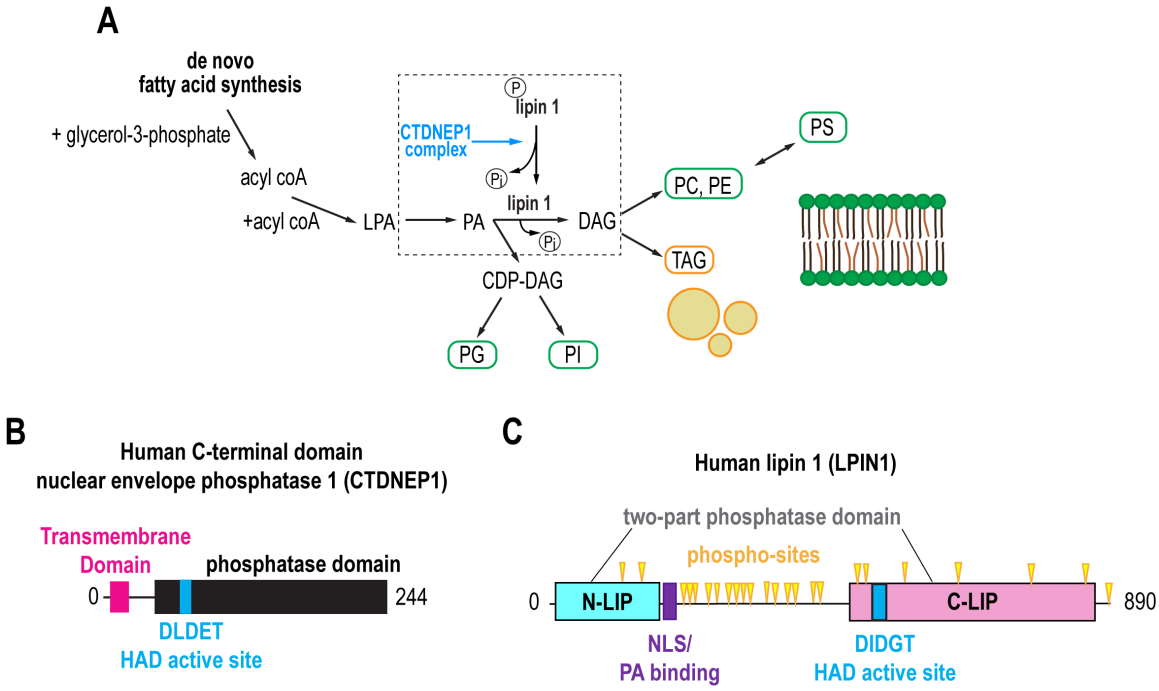

Figure 2.1 CTDNEP1 and lipin 1 control of lipid synthesis
A) Overview of CTDNEP1/lipin 1-controlled ER lipid synthesis. Direct activities of CTDNEP1 and lipin 1 are outlined with a dashed box. Membrane glycerophospholipids are circled in green, and lipid droplet glycerolipids are circled in orange. P, phosphate; Pi, inorganic phosphate. B) Domain architecture of human CTDNEP1. HAD, haloacid dehalogenase. C) Domain architecture of human lipin 1. NLS, nuclear localization sequence.

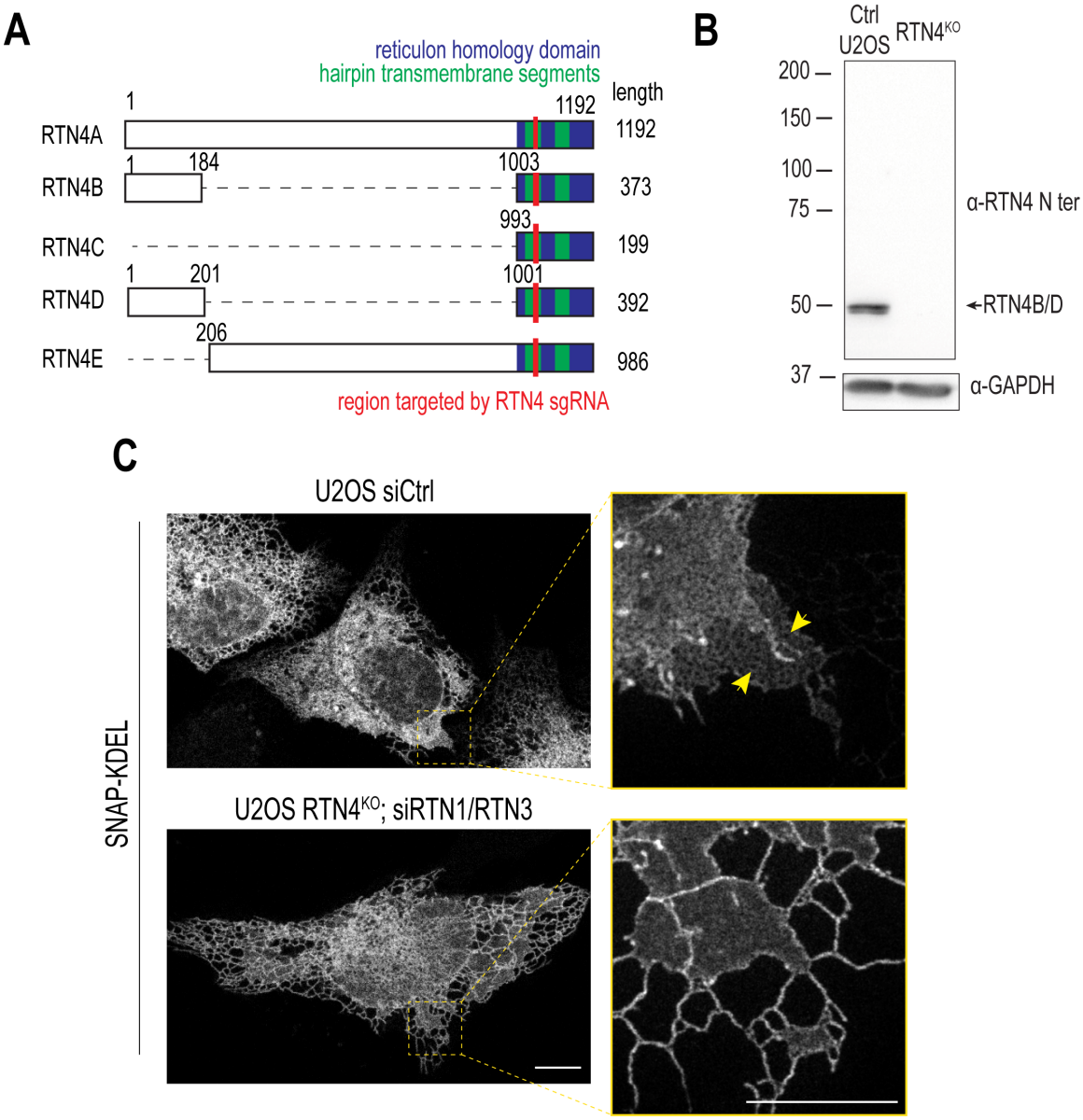

Figure 2.2 depletion of reticulons 1,3, and 4 reveals role for formation/stabilization of ER nanoholes

A) Domain architecture of reticulon 4 isoforms, with the region targeted by the RTN4 sgRNA to generate a RTN4^{KO} cell line shown. B) Immunoblot of endogenous RTN4B/D from whole cell lysates derived from control and RTN4^{KO} U2OS cells. C) Scanning confocal (left) and stimulated emission depletion (STED) (inset, right) images of SNAP-KDEL signal in cell lines treated as indicated. Scale bars, 10 μm (left) and 2 μm (inset).

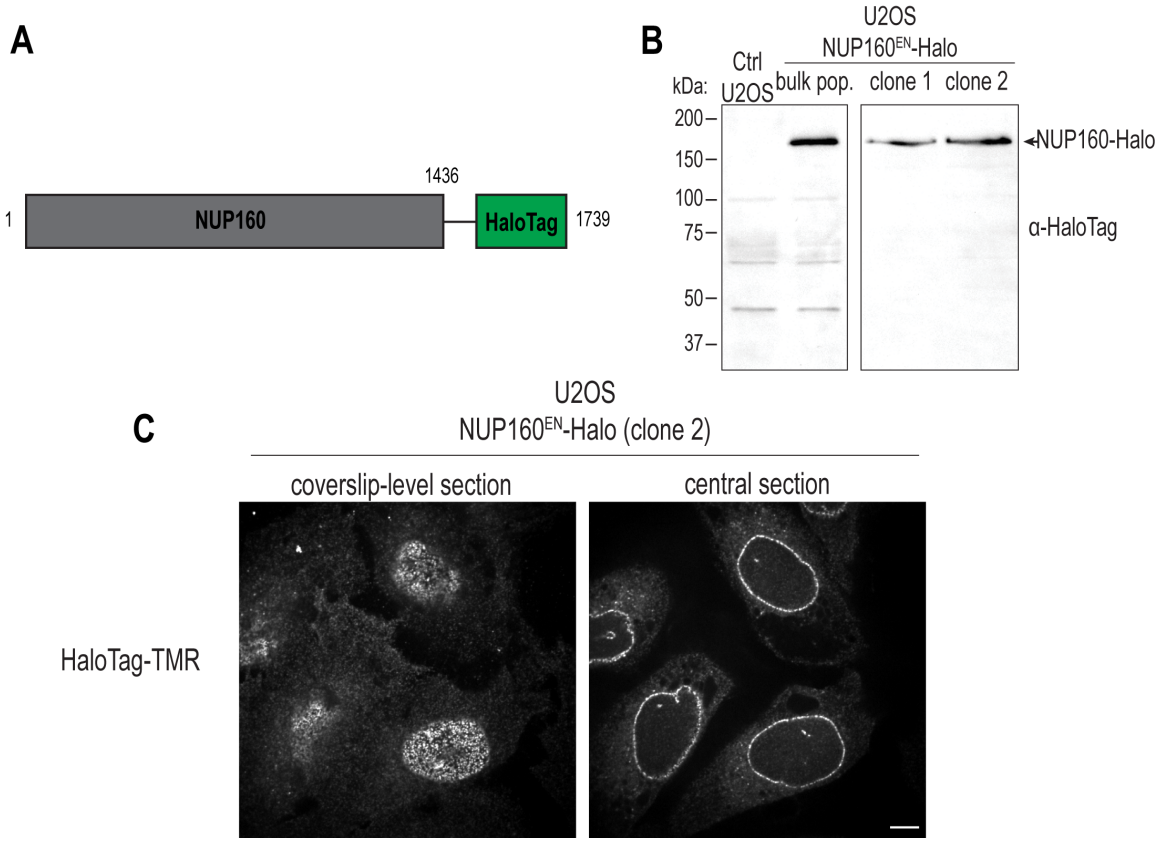

Figure 2.3 Localization of endogenous NUP160 in human cells
A) Domain architecture of endogenous NUP160-Halo. B) Immunoblot of HaloTag in whole cell lysates derived from indicated cell lines. “Bulk pop.” refers to a bulk population of Cas9/guide/homology repair template-transfected cells. C) Spinning disk confocal images of HaloTag-TMR signal in NUP160^{EN}-Halo U2OS cells. Scale bar, 10 μm.

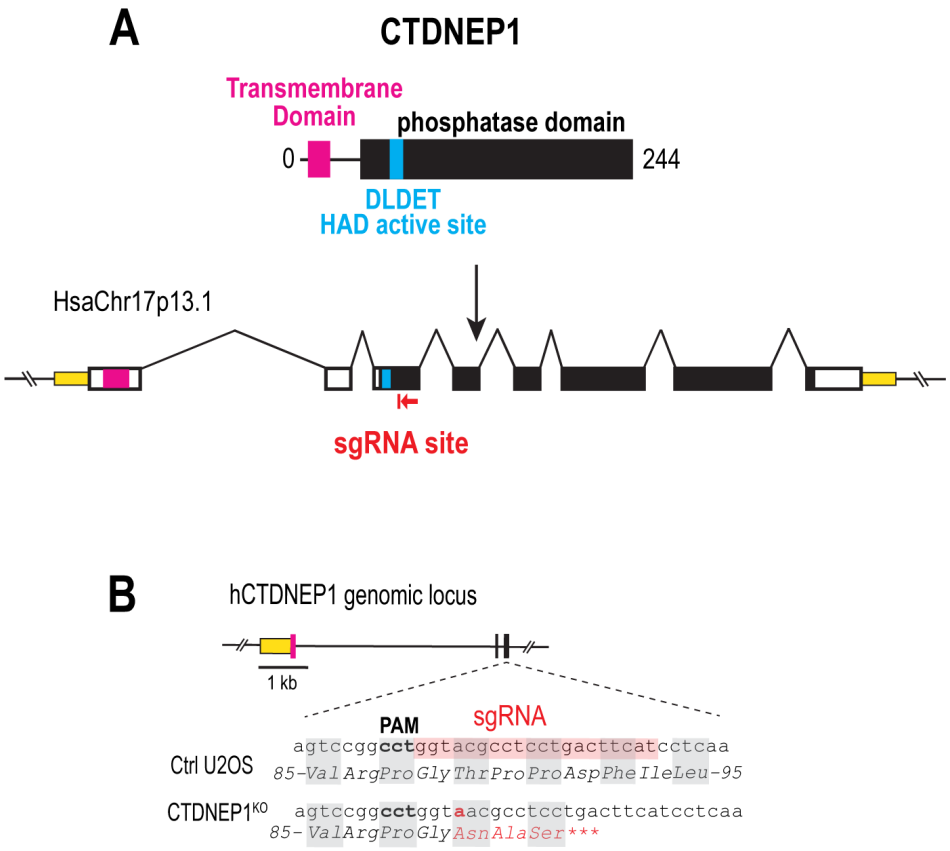

Figure 2.4 Generation of CTDNEP1^{KO} U2OS cells
A) Domain architecture of CTDNEP1 mapped to the gene architecture of *CTDNEP1*. sgRNA, single guide RNA. 5' and 3' untranslated regions marked in yellow, exons as white or marked boxes, and introns as lines. Colors indicate exons coding for parts of domains. B) Schematic of single nucleotide insertion and subsequent consequence for the CTDNEP1 protein sequence induced by CRISPR-Cas9 in CTDNEP1^{KO} U2OS cells. Untranslated regions and exons marked in colored bars as in (A).

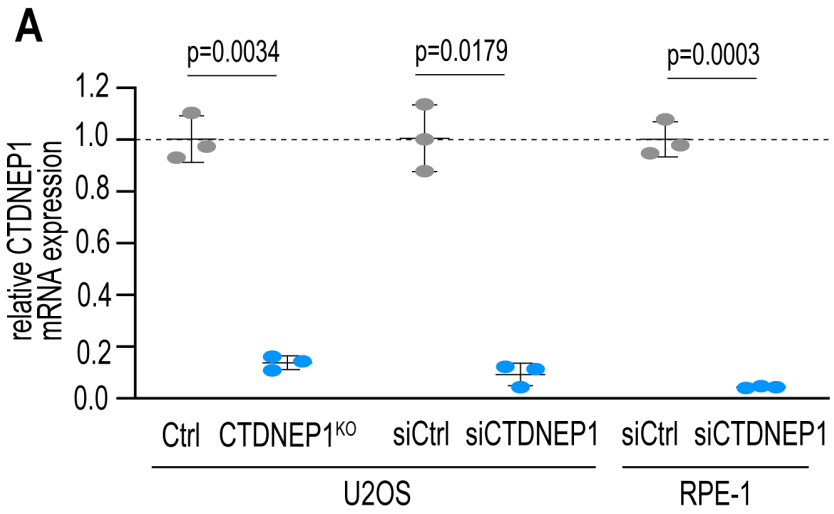

Figure 2.5 CTDNEP1^{KO} U2OS cells and CTDNEP1 siRNA-treated cells have reduced levels of CTDNEP1 mRNA

A) qRT-PCR of CTDNEP1 transcript levels in human cell lines with indicated treatments. U2OS siRNA-treated cells are overexpressing GFP-KDEL and are from the same experiment as Figures 2.9 and 2.11. RPE-1 siRNA-treated cells are overexpressing GFP-KDEL and are from the same experiment as Figure 2.10. Values are normalized to GAPDH expression. Results are expressed as the fold change in expression and relative to mean of control U2OS or siCtrl-treated U2OS or RPE-1 values. Expression data from control U2OS and CTDNEP1^{KO} U2OS collected by J. W. Carrasquillo Rodríguez. P values, paired t tests of ΔCt values. Means ± SDs shown. N = 3 experimental repeats.

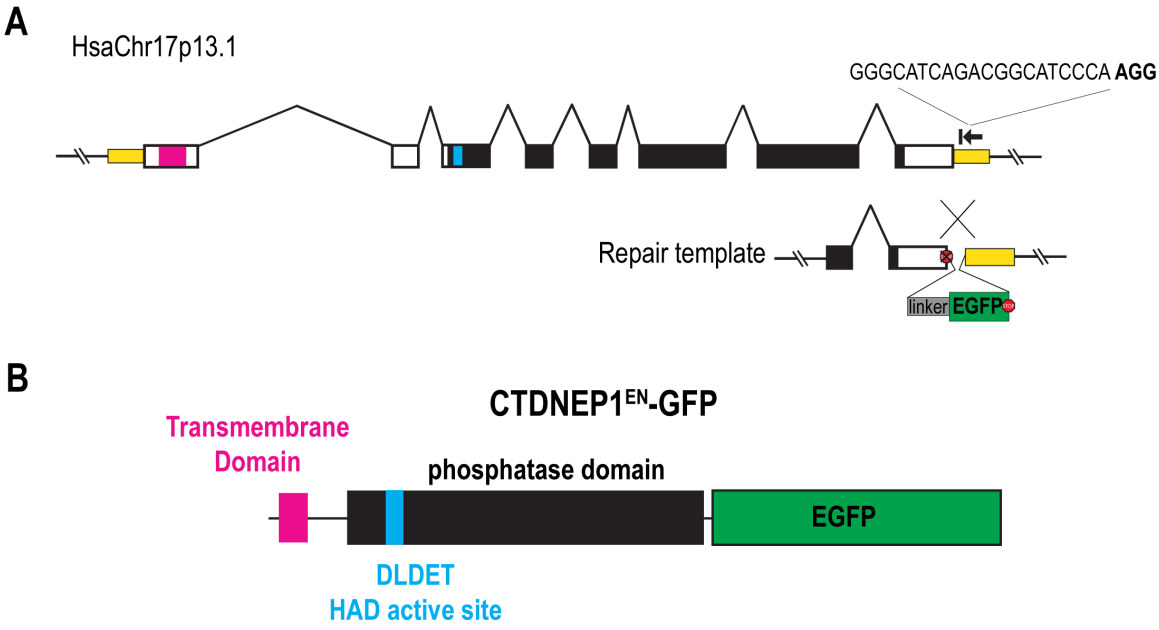

Figure 2.6 Generation of endogenously-tagged CTDNEP1^{EN}-GFP cells
A) Schematic of strategy for homology-directed repair by CRISPR-Cas9 to tag endogenous CTDNEP1 with a C-terminal GFP tag. 5' and 3' untranslated regions marked in yellow, exons as white or marked boxes, and introns as lines. Colors indicate exons coding for parts of domains. B) Domain architecture of CTDNEP1^{EN}-GFP in U2OS cells.

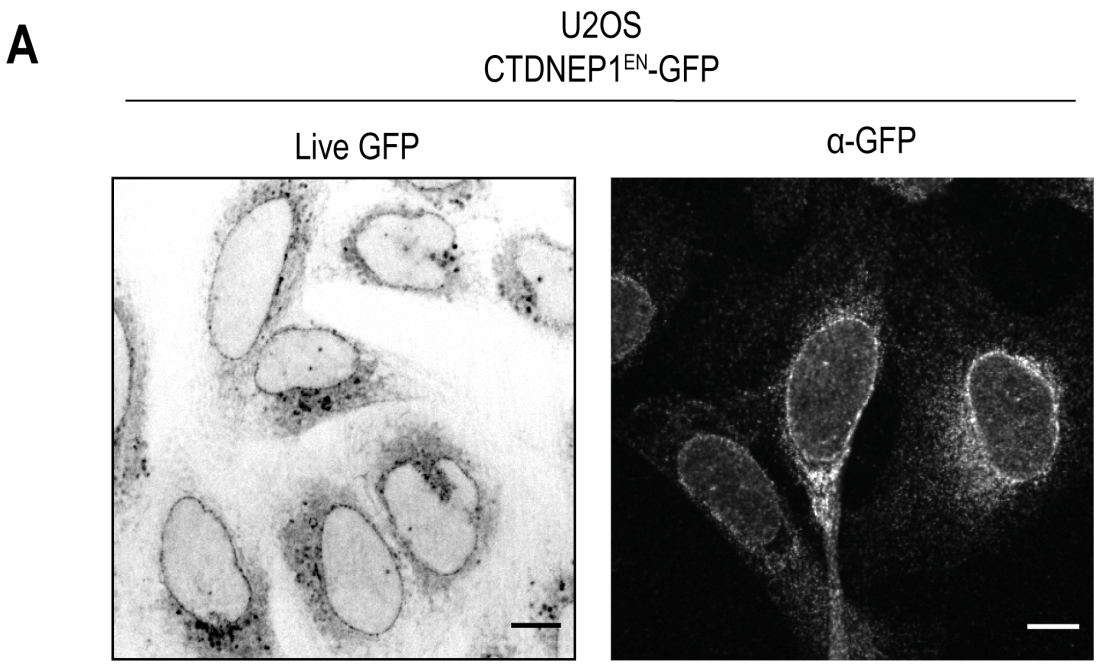

Figure 2.7 Endogenous localization of human CTDNEP1
A) Left, live spinning disk confocal microscopy image of GFP in live U2OS CTDNEP1^{EN}-GFP cells. Right, confocal microscopy image of GFP staining in fixed U2OS CTDNEP1^{EN}-GFP cells. Scale bars, 10 μm.

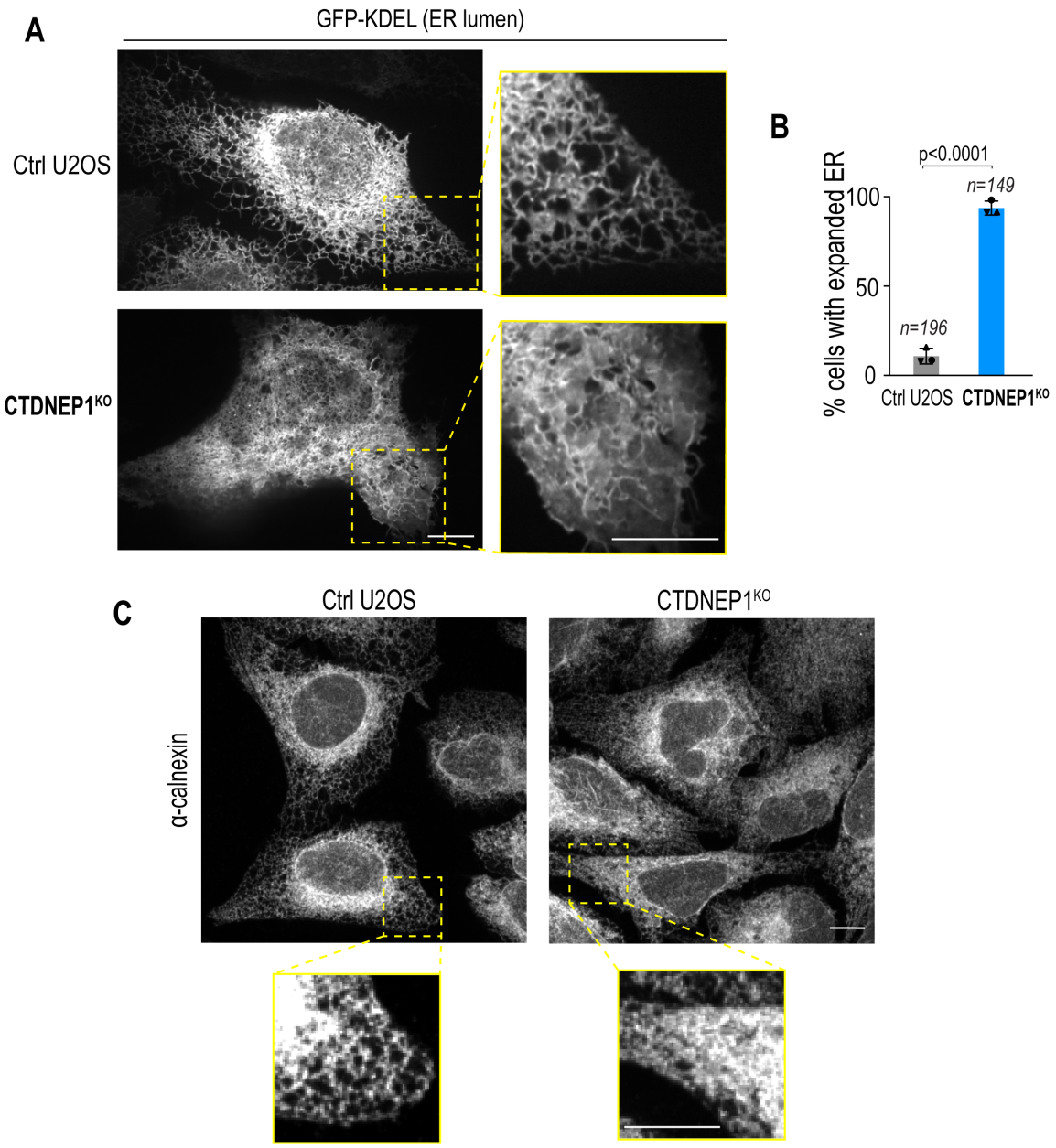

Figure 2.8 Expansion of ER membranes in CTDNEP1^{KO} U2OS cells
A) Spinning disk confocal microscopy images of GFP-KDEL transiently expressed in U2OS cells. Scale bars, 10 μm. B) Quantification of incidence of expanded ER phenotype in cells from (A). n = number of cells, N = 3 experimental repeats. Mean ± SD shown. P value, Fisher's exact test of total incidences. C) Spinning disk confocal microscopy image of calnexin signal in immunostained U2OS cells. Inset brightness adjusted relative to uncropped image to highlight fine ER morphology. Scale bars, 10 μm.

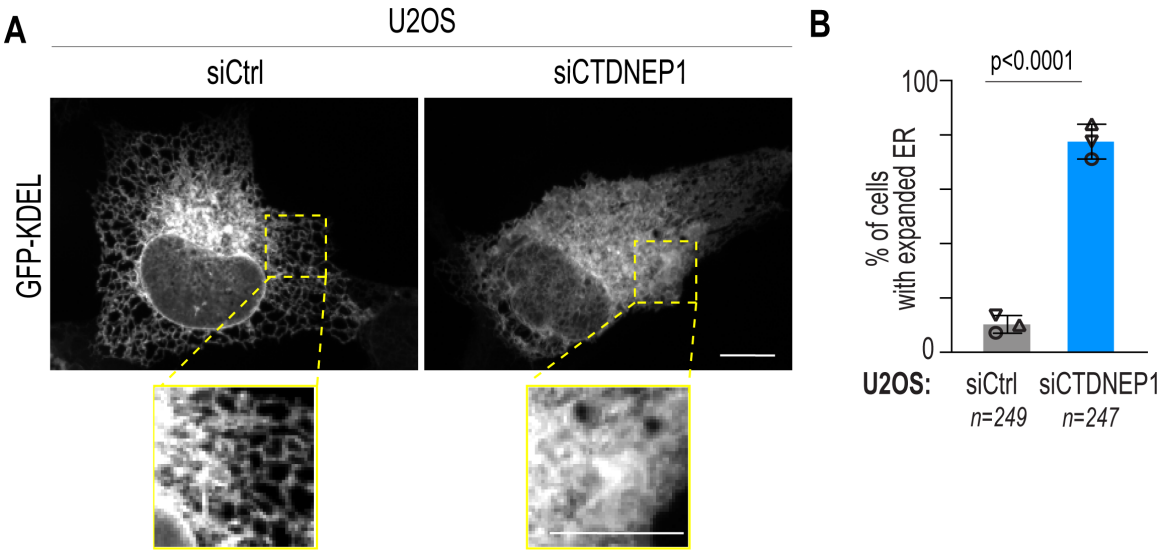

Figure 2.9 Expansion of ER membranes in U2OS cells treated with CTDNEP1 siRNA

A) Spinning disk confocal microscopy images of GFP-KDEL transiently expressed in U2OS cells. Scale bars, 10 µm. Inset brightness adjusted relative to uncropped image to highlight fine ER morphology. Scale bars, 10 µm. B) Quantification of incidence of expanded ER phenotype in cells from (A). n = number of cells, N = 3 experimental repeats. Mean ± SD shown. P value, Fisher's exact test of total incidences.

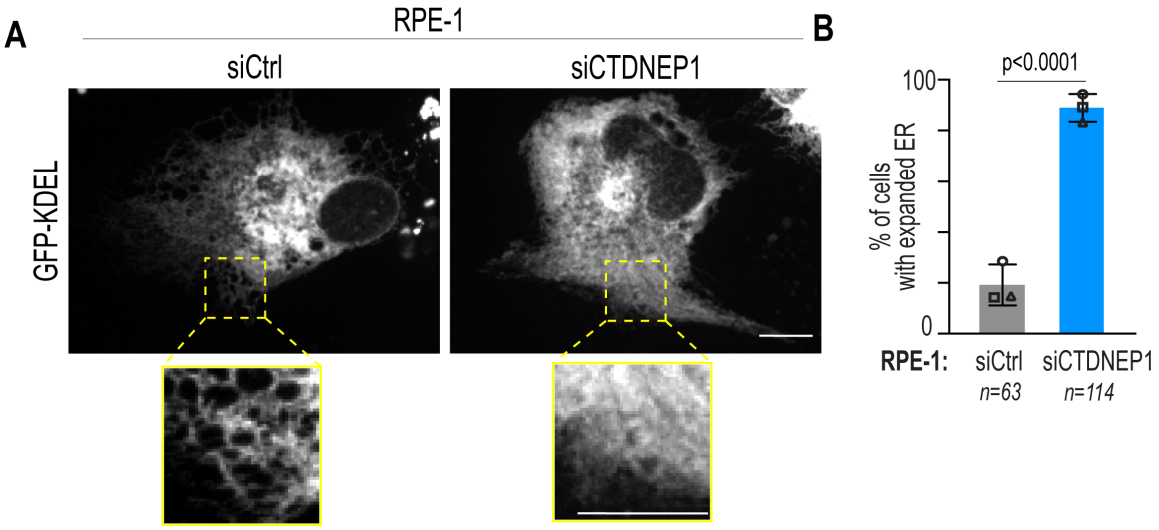

Figure 2.10 Expansion of ER membranes in RPE-1 cells treated with CTDNEP1 siRNA

A) Spinning disk confocal microscopy images of GFP-KDEL in transiently-expressing RPE-1 cells treated with indicated siRNAs. Inset brightness adjusted relative to uncropped image to highlight fine ER morphology. Scale bars, 10 μm. B) Quantification of incidence of expanded ER phenotype in cells from (A). n = number of cells, N = 3 experimental repeats. Mean ± SD shown. P value, Fisher's exact test of total incidences.

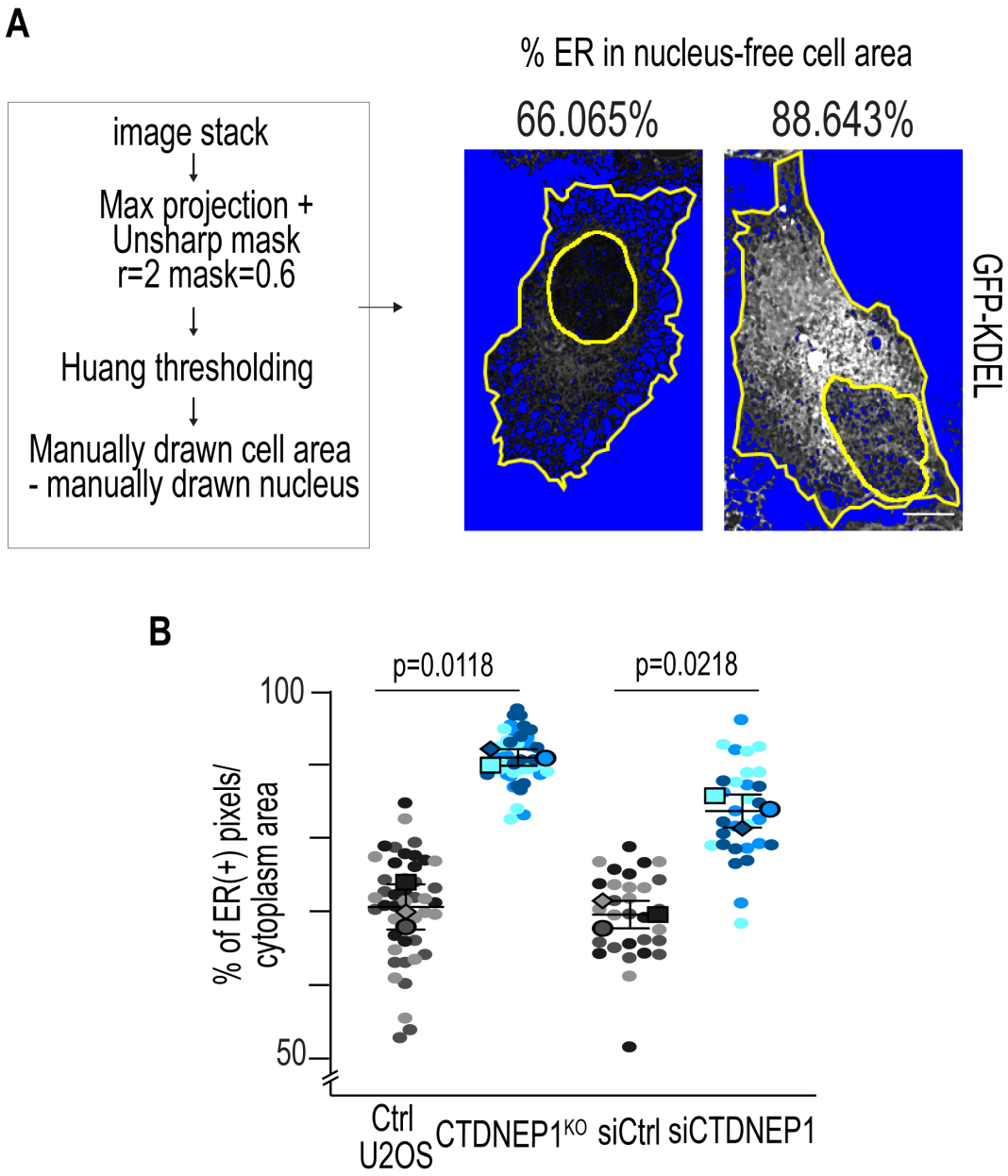

Figure 2.11 Quantification of ER membrane abundance using ER fluorescent signal segmentation

A) Spinning disk confocal mages of GFP-KDEL in transiently-expressing cells were processed as described and quantified for percent of pixels in cytoplasm area positive for segmented ER signal pixels. Scale bar, 10 μm. B) Plot of percentage of ER-positive pixels in cytoplasm area in cells (n) under the indicated conditions. N = 3 experimental replicates. Means ± SDs shown. P values, paired t tests of replicate means. Note y axis truncation.

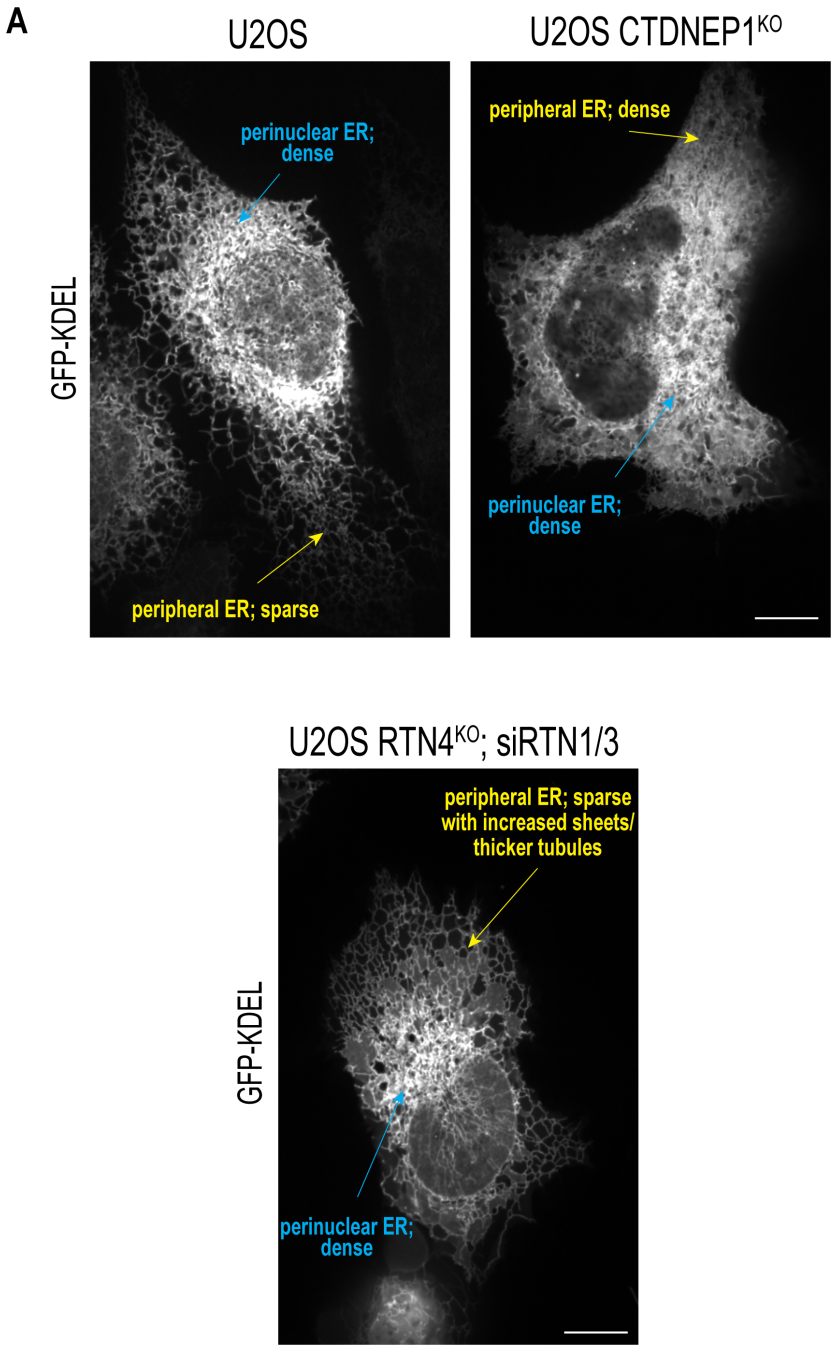

Figure 2.12 Qualitative comparison of ER morphology between CTDNEP1-depleted and reticulon 1,3,4-depleted U2OS cells

A) Spinning disk confocal microscopy images of transiently-expressed GFP-KDEL in cells in the indicated conditions. Blue arrows point to morphologies in the perinuclear ER, and yellow arrows point to morphologies in the peripheral ER. Lower image is from a separate experiment from the left 2 images. In all images, brightness is adjusted so that perinuclear ER is slightly saturated.

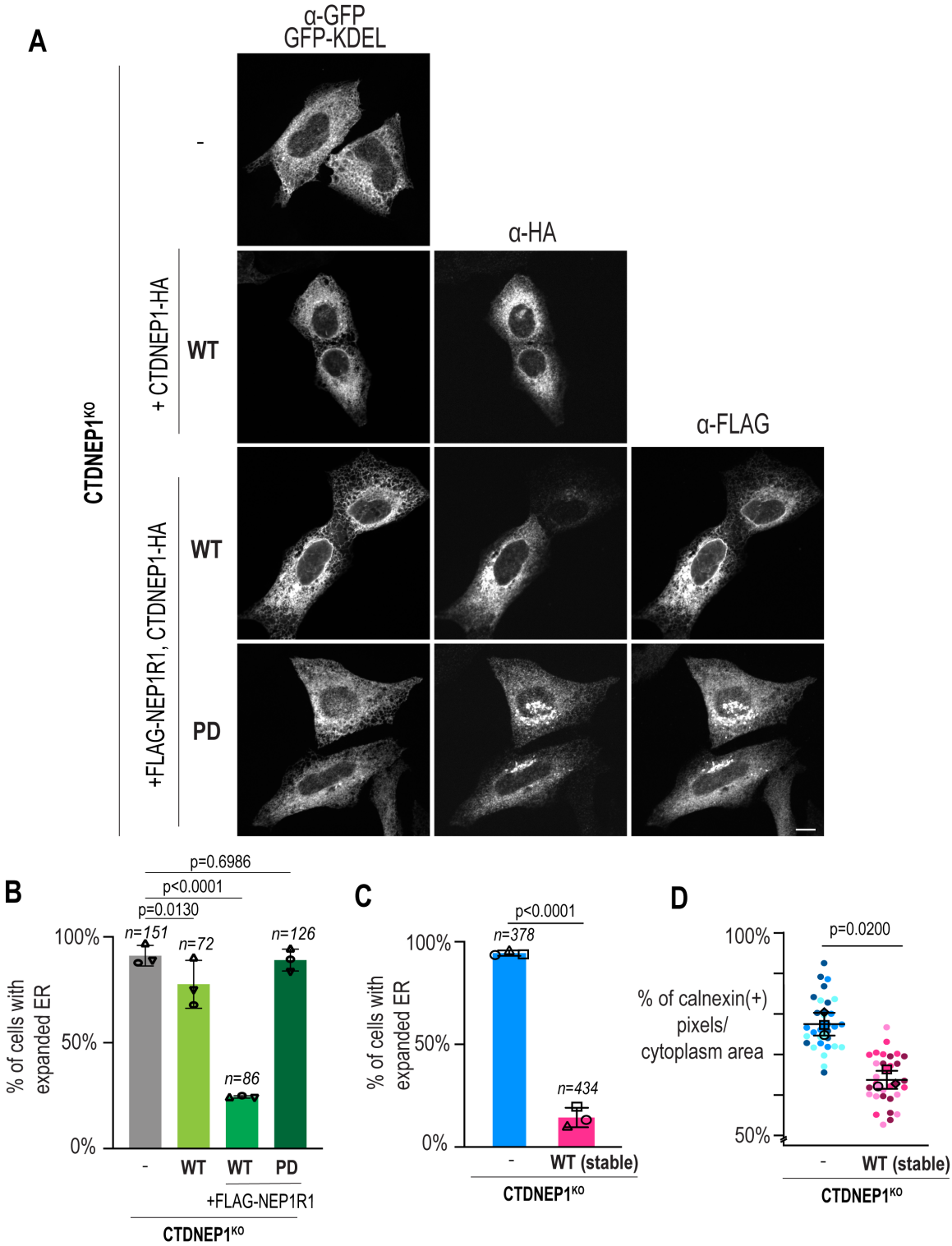

Figure 2.13 Stable or transient overexpression of catalytically active CTDNEP1 suppresses ER membrane expansion in CTDNEP1^{KO} cells

A) Spinning disk confocal microscopy images of GFP (KDEL), HA (CTDNEP1), and FLAG (NEP1R1) staining in U2OS cells overexpressing the indicated constructs, including empty vector (-), wild-type CTDNEP1-HA (WT), or

phosphatase dead D67E CTDNEP1 (PD). Scale bar, 10 μm. B) Quantification of incidence of expanded ER phenotype in cells from (A). n = number of cells, N = 3 experimental repeats. Mean ± SD shown. P values, Fisher's exact tests of total incidences. C) Quantification of incidence of expanded ER phenotype in cells with indicated conditions. WT (stable) refers to stable cell line overexpressing CTDNEP1-HA. N = number of cells, N = 3 experimental repeats. Mean ± SD shown. P value, Fisher's exact test of total incidences. D) Plot of percentage of ER-positive pixels in cytoplasm area in cells (n) under the indicated conditions. N = 3 experimental replicates. P value, paired t test of replicate means. Note y axis truncation.

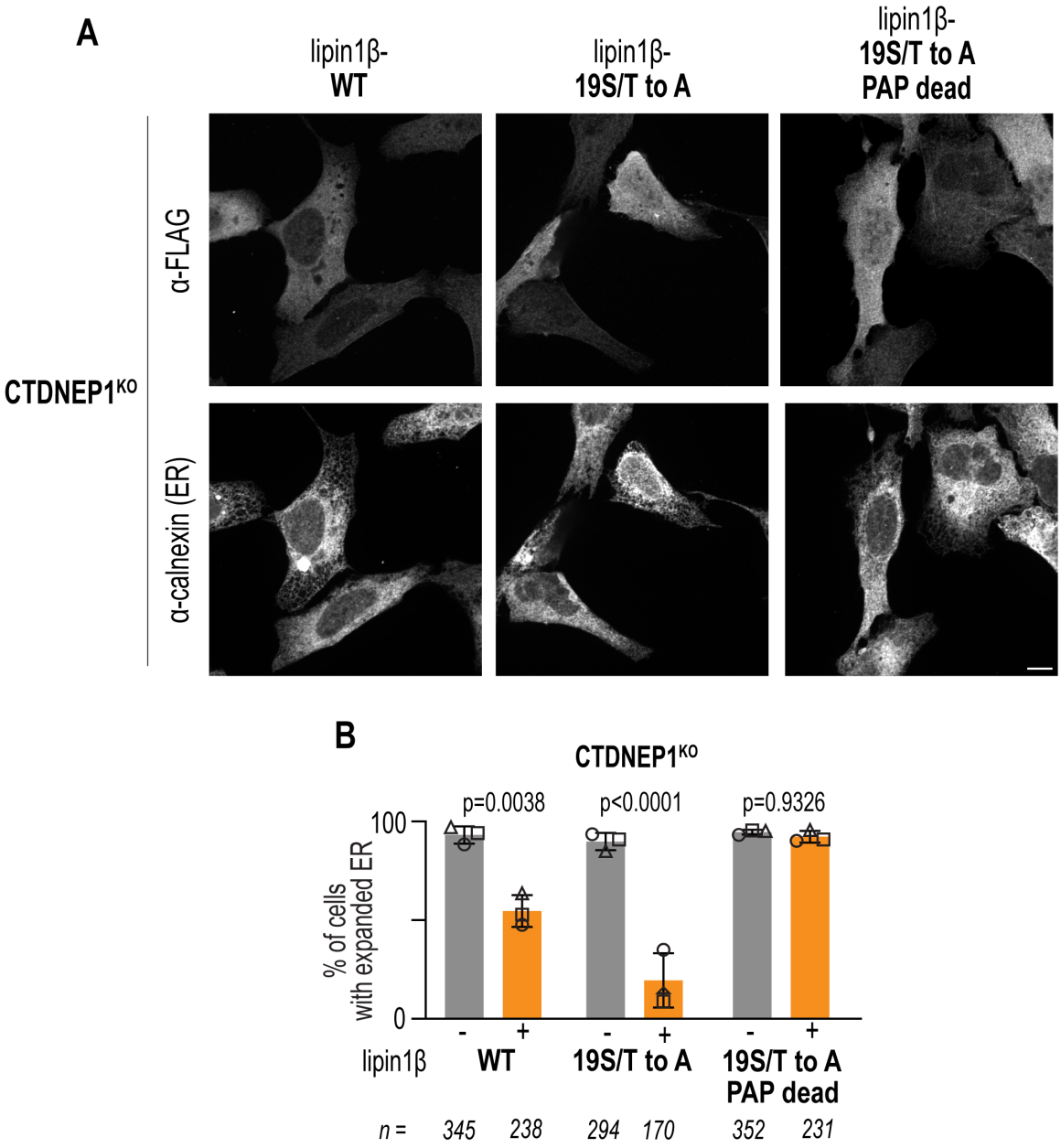

Figure 2.14 Transient overexpression of catalytically active lipin 1 suppresses ER membrane expansion in CTDNEP1^{KO} cells

A) Spinning disk confocal microscopy images of calnexin and FLAG staining in U2OS cells overexpressing the indicated constructs and GFP-KDEL as a co-transfection marker (not shown). 19 S/T to A refers to 19 serine/threonine sites mutated to dephospho-mimic alanine residues. PAP dead refers to phosphatase dead lipin 1. Scale bar 10 µm. B) Quantification of incidence of expanded ER phenotype in cells from (A). "-" and "+" refer to cells not expressing and expressing lipin 1 and the co-transfection marker in the same experiment, respectively. n= number of cells, N = 3 experimental repeats. Mean ± SD shown. P values, Fisher's exact tests of total incidences.

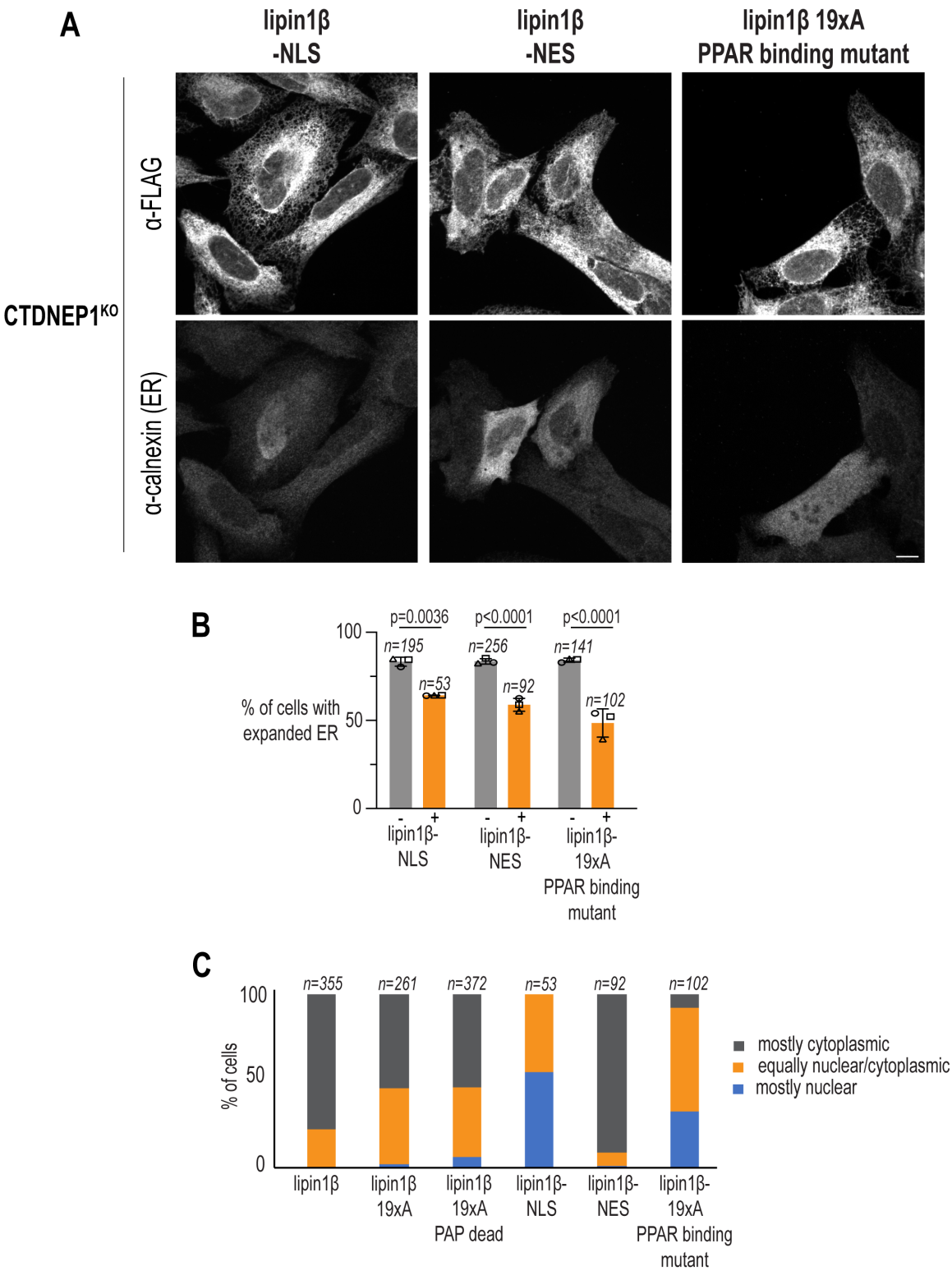

Figure 2.15 Localization of lipin 1 and suppression of ER membrane expansion in CTDNEP1^{KO} cells

A) Spinning disk confocal microscopy images of calnexin and FLAG staining in U2OS cells overexpressing the indicated constructs and GFP-KDEL as a co-transfection marker (not shown). 19 S/T to A refers to 19 serine/threonine sites

mutated to dephospho-mimic alanine residues. NLS = nuclear localization signal and NES = nuclear export signal. PPAR binding mutant has LXXIL PPARα binding motif mutated to LXXFF (Finck et al., 2005). Scale bar 10 µm. B) Quantification of incidence of expanded ER phenotype in cells from (A). "-" and "+" refer to cells not expressing and expressing lipin 1 and the co-transfection marker in the same experiment, respectively. n = cells, N = 3 experimental repeats. Mean ± SD shown. P values, Fisher's exact tests of total incidences. C) Incidence of nuclear localization phenotypes for indicated FLAG constructs. n = number of cells from N = 3 experimental repeats.

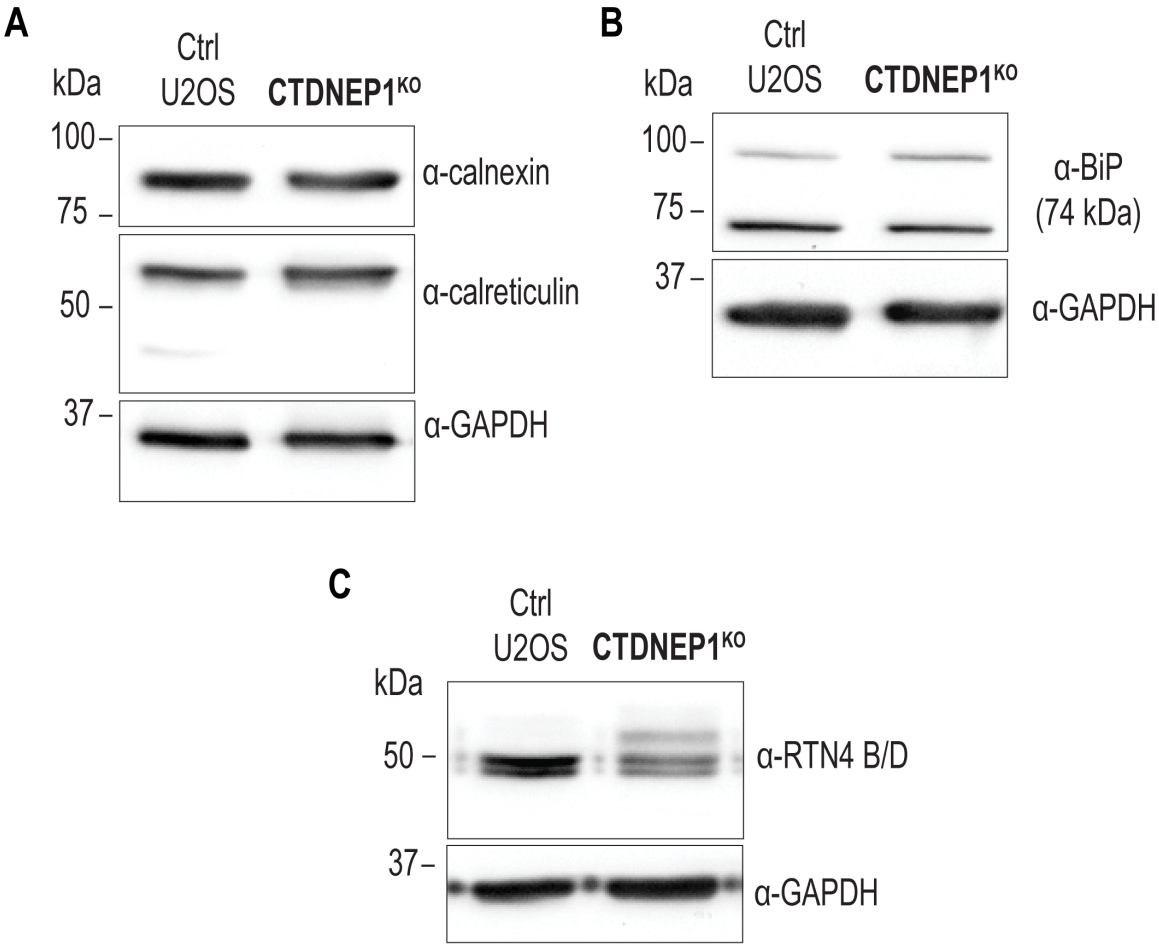

Figure 2.16 Expression of ER-resident proteins in CTDNEP1^{KO} cells
A, B, C) Immunoblot (using indicated antibodies) from whole cell lysates derived from control and CTDNEP1^{KO} U2OS cells.

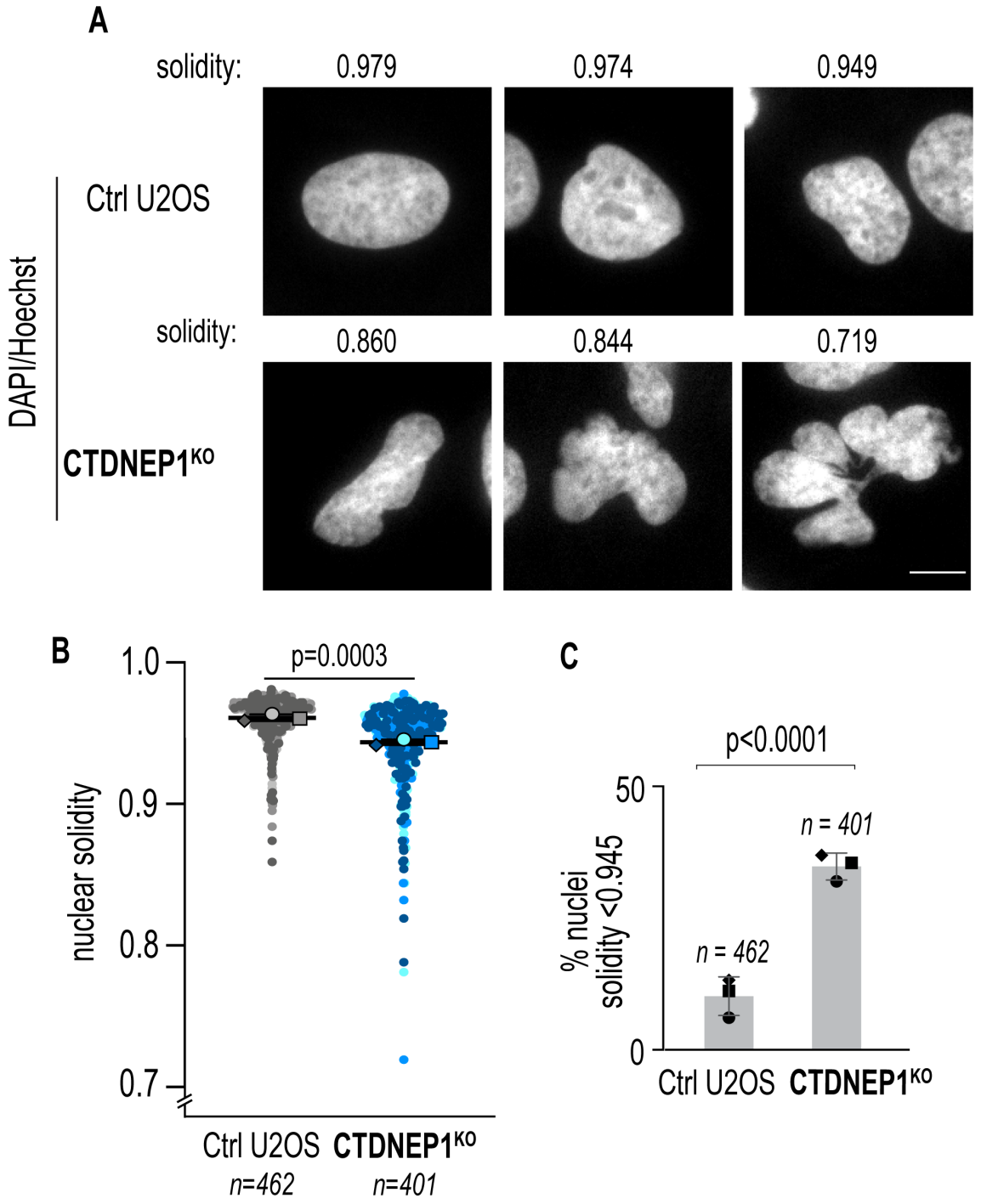

Figure 2.17 CTDNEP1^{KO} cells have decreased nuclear solidity
A) Epifluorescence images of DAPI/Hoechst staining in control and CTDNEP1^{KO} cells showing nuclear morphologies and their corresponding solidity values. Scale bar 10 µm. B) Plot of solidity of nuclei (n) from cells as in (A). N = 3 experimental repeats. Individual values and means ± SDs shown. P value, paired t test of replicate means. C) Quantification of incidence of solidity less than 1 SD from the mean of control nuclei solidity (0.944). n = number of nuclei, N = 3 experimental repeats. Mean ± SD shown. P value, Fisher's exact test of total incidences.

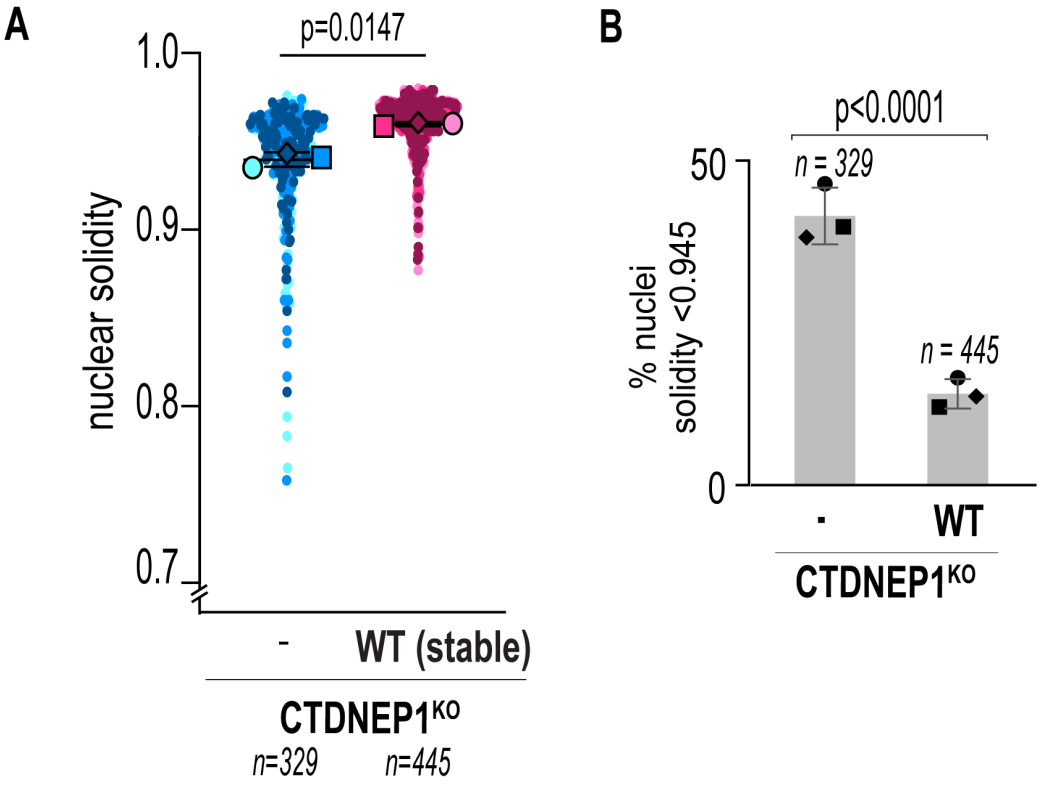

Figure 2.18 Stable overexpression of CTDNEP1 rescues nuclear solidity of CTDNEP1^{KO} cells

A) Plot of solidity of nuclei (n) of cells from indicated conditions. "WT (stable)" refers to cells stably overexpressing CTDNEP1-HA. N = 3 experimental repeats. Means ± SDs shown. P value, paired t test of replicate means. B) Quantification of incidence of solidity less than 1 SD from the mean of control nuclei solidity n = number of nuclei, N = 3 experimental repeats. Mean ± SD shown. P value, Fisher's exact test of total incidences.

A

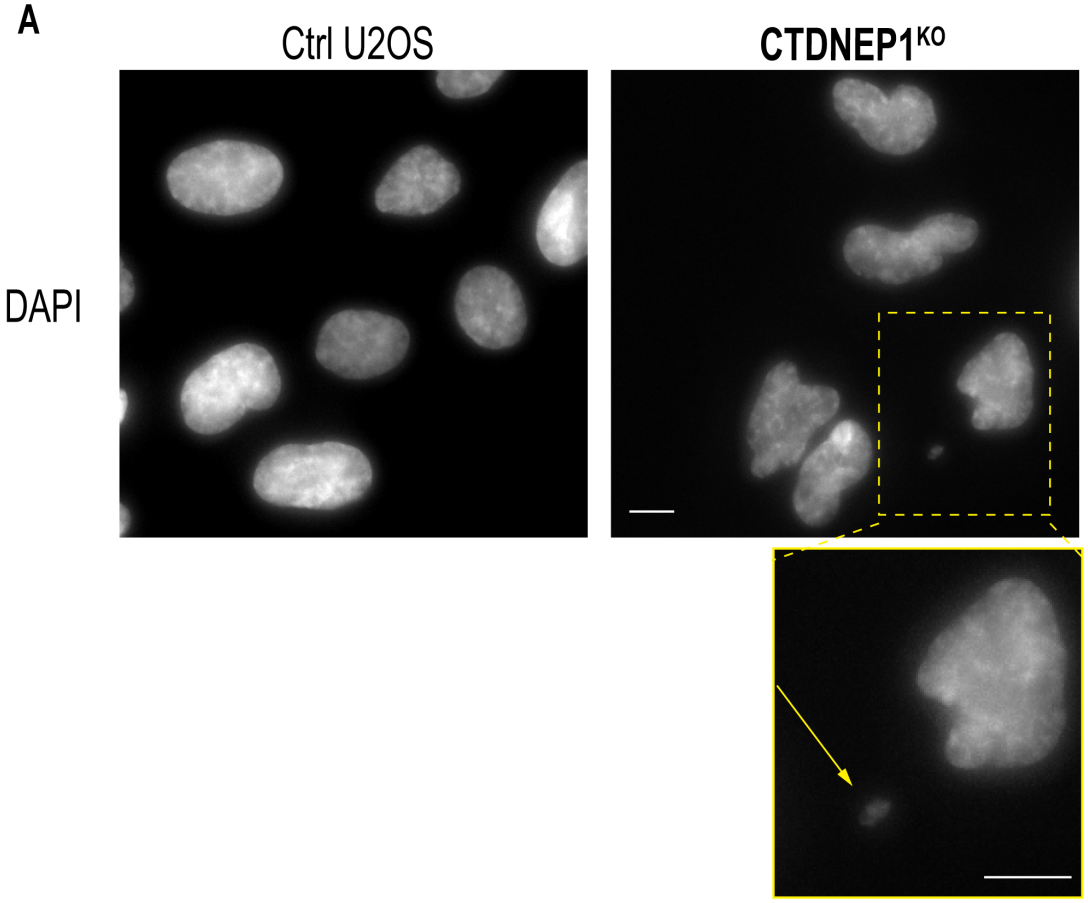

B

	% micronuclei	p value
Ctrl U2OS *n=544*	4.3 ± 0.8%	0.0006
CTDNEP1KO *n=514*	**10.2 ± 2.9%**	
**CTDNEP1KO - ** *n=415*	**13.2 ± 5.1%**	<0.0001
CTDNEP1KO WT *n=494*	2.6 ± 1.3%	

Figure 2.19 CTDNEP1 limits formation of micronuclei, and stable overexpression of CTDNEP1 in CTDNEP1^{KO} cells suppresses formation of micronuclei

A) Epifluorescence images of DAPI/Hoechst in cells from indicated conditions. Scale bars, 10 μm. B) Quantification of incidence of micronuclei in cells in indicated conditions. WT refers to stable overexpression of CTDNEP1-HA. n = number of cells from N = 3 experimental repeats. Means ± SDs shown. P values, Fisher's exact tests of total incidences. Top two and bottom two rows are from separate experiments.

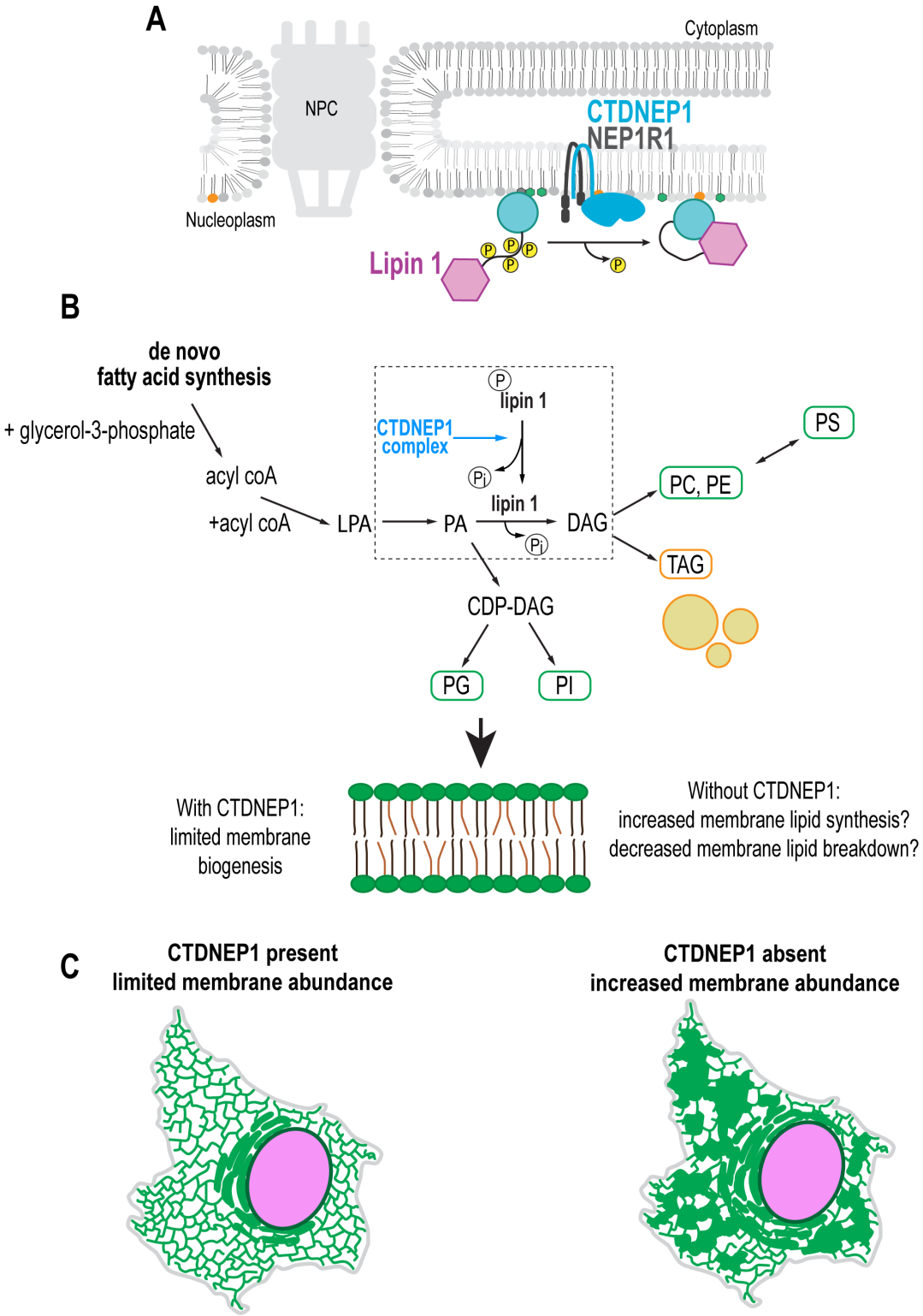

Figure 2.20 Role of CTDNEP1 in limiting expansion of ER membranes
A) Schematic of proposed lipin 1 dephosphorylation and activation at the nuclear envelope by CTDNEP1/NEP1R1 (dark gray). B) Schematic of potential mechanisms for how CTDNEP1 control of lipid synthesis could lead to increased

membrane abundance. C) Schematic showing how membrane abundance is impacted by loss of CTDNEP1.

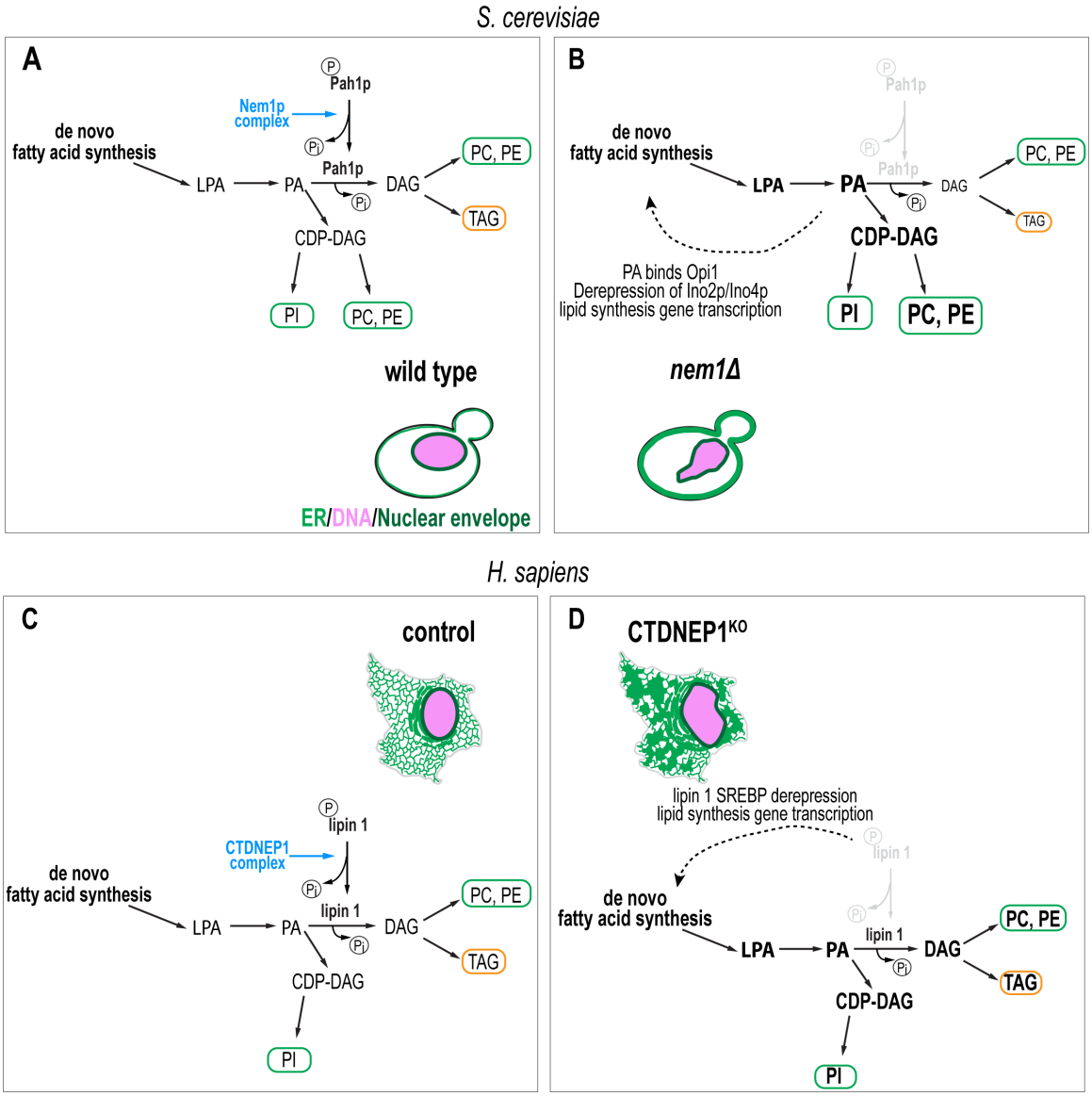

Figure 2.21 Roles of CTDNEP1 in maintaining nuclear shape
A,C) Lipid synthesis pathways in yeast and human cells and nuclear shape during lipid homeostasis. B,D) Lipid synthesis alterations with loss of Nem1p and CTDNEP1 and concomitant changes in nuclear shape resulting from increased membrane biogenesis.

Chapter 3: Characterization of ER and nuclear envelope dynamics in CTDNEP1-deleted cells

Some of this work is included and/or modified from the manuscript:

Holly Merta[*], Jake W. Carrasquillo Rodríguez[*], Maya I. Anjur-Dietrich, Mitchell E. Granade, Tevis Vitale, Thurl E. Harris, Dan Needleman, Shirin Bahmanyar. A CTDNEP1-lipin 1-mTOR regulatory network restricts ER membrane biogenesis to Enable Chromosome Motions Necessary for Mitotic Fidelity. *bioRxiv* (2021). doi: https://doi.org/10.1101/2021.03.02.433553

[*] Co-first authors

Introduction

Membrane biogenesis and dynamics are tightly controlled throughout the cell cycle (Storck et al., 2018). Coordination of phosphatidylcholine synthesis with ramping down glycerophospholipid breakdown leads to an accumulation of glycerophospholipids during S phase (Jackowski, 1994). ER membranes are cleared to the cell periphery during mitosis; limiting clearance from mitotic chromosomes throughout mitosis leads to chromosome segregation defects (Champion et al., 2019; Schlaitz et al., 2013).

In *C. elegans* early embryos, CNEP-1 is known to regulate membrane dynamics in mitosis and mitotic progression. Loss of lipin or CNEP-1 activity leads to deficient nuclear envelope breakdown that leads to lack of mixing of parental genomes and the persistence of two 'twinned' nuclei or oblong single nuclei (Bahmanyar et al., 2014; Golden et al., 2009; Gorjánácz and Mattaj, 2009). In *cnep-1*Δ embryos, this is accompanied with an increase in ER sheets, and the nuclear envelope at nuclear envelope breakdown has an additional membrane layer enwrapping the nuclear envelope (Bahmanyar et al., 2014). During nuclear reformation in meiosis II, membrane extensions can be seen in nuclei of *cnep-1*Δ embryos, and the nuclei are more permeable than those of control embryos (Penfield et al., 2020). The nuclear envelope and ER phenotypes in *cnep-1*Δ embryos can be rescued by suppression of PI synthesis (Bahmanyar et al., 2014; Penfield et al., 2020). Thus, flux of ER lipid synthesis controlled by lipin limits membrane clearance and limits abnormal localization of membranes in and around nuclei in mitosis.

In human cells, depletion of lipin or CTDNEP1 by RNAi leads to delayed lamin B1 disassembly and delayed mitotic progression (including delayed chromosome congression) (Mall et al., 2012). The delay in nuclear envelope breakdown can be rescued by exogenous supplementation with lipin's product, DAG, and the delay in mitotic progression is partially rescued with DAG supplementation (Mall et al., 2012). The authors conclude that lack of DAG limits protein kinase C activation to phosphorylate lamin and facilitate nuclear envelope breakdown. It is unclear if any other consequences of lipin inactivation, such as flux toward PI synthesis, affect mitotic progression. The role of human CTDNEP1 and lipin 1 in regulating mitotic progression after nuclear envelope breakdown, especially during chromosome congression in prometaphase, is unclear.

Here, we show that CTDNEP1 regulates membrane abundance and clearance during mitosis to facilitate mitotic progression during prometaphase. We show that CTDNEP1^{KO} cells have a higher percentage of prometaphase cells within the mitotic cell population, and membranes are more abundant and less cleared in prometaphase and metaphase CTDNEP1^{KO} cells. ER membranes can be seen enwrapping aligning chromosomes in prometaphase to metaphase, and ER membranes are not restricted from the nuclear interior upon mitotic exit. We show that CTDNEP1-depleted cells additionally show increased nuclear size and faster reestablishment of nuclear import upon mitotic exit. These data show that CTDNEP1-controlled membrane biogenesis limits abnormal membrane localization in mitosis in mammalian cells.

Results

Higher incidence of prometaphase cells in mitotic CTDNEP1-deleted cells

Previous work showed that depletion of CTDNEP1 or lipins in human cells leads to delayed mitotic progression, including delayed nuclear breakdown and delayed chromosome congression (Mall et al., 2012). To determine if mitotic progression is altered in CTDNEP1^{KO} cells, I imaged a fixed asynchronous population of control or CTDNEP1^{KO} U2OS cells and quantified the incidence of cells in each mitotic stage from prometaphase to telophase within the mitotic cell population (Figure 3.1A). Consistent with the previous findings, CTDNEP1^{KO} cells had a higher proportion of mitotic cells in prometaphase and lower proportion in other stages, which suggests that prometaphase could be lengthened (Figure 3.1B). Live imaging of CTDNEP1^{KO} cells can determine the timing by which loss of CTDNEP1 delays mitotic progression, which is not able to be determined with imaging an asynchronous cell population. These results are consistent with the previous finding that depletion of loss of CTDNEP1 delays mitotic progression.

Prometaphase ER membrane localization and relation to chromosomes

I next sought to determine if ER membrane clearance in CTDNEP1-depleted human cells is delayed and to investigate the dynamics of ER membranes during prometaphase. I imaged a population of control and CTDNEP1^{KO} cells expressing the ER marker GFP-KDEL, enriched for prometaphase and metaphase cells by drugless mitotic shakeoff and using DIC to determine mitotic staging and chromosome localization (Figure 3.2A). I blindly scored these images with categories based on the prevalence of intracellular ER membranes (“cleared”, “partially cleared”, and “not cleared”, Figure 3.2) and

found that a higher proportion of CTDNEP1^{KO} cells lacked GFP-KDEL clearance from the region occupied by chromosomes compared to control cells (47.4 ± 6.8 % of CTDNEP1^{KO} cells compared to 25.4 ± 11.4 % of cells categorized as “not cleared”, Figure 3.2B). To assess whether chromosomes interact with ER membranes during chromosome congression, I imaged control and CTDNEP1^{KO} cells transiently expressing GFP-KDEL/H2B-mCherry after washout from a Cdk1 inhibitor-mediated G2/M arrest (Figure 3.3A). We observed that, over the course of chromosome congression, unaligned chromosomes could be seen within peripheral ER of control and CTDNEP1^{KO} cells before aligning to the metaphase plate (Figure 3.3A, yellow arrows). In CTDNEP1^{KO} prometaphase cells, ER tubules could also be seen within the spindle region leading up to chromosomes at the metaphase plate (Figure 3.3A, cyan arrows). These data show that CTDNEP1 activity facilitates clearance of membranes after nuclear envelope breakdown.

Excess ER membranes fill mitotic cytoplasm in CTDNEP1^{KO} cells and CTDNEP1-depleted cells

I previously showed that CTDNEP1 limits ER membrane abundance in human cells. To determine if expansion of ER membranes persists in CTDNEP1-depleted cells in mitosis, I imaged U2OS cells stably expressing the ER transmembrane marker GFP-Sec61β and chromatin marker H2B-mCherry treated with control or CTDNEP1 siRNA from anaphase onset through telophase (Figure 3.4A). Membranes are largely cleared to the cell periphery by anaphase onset (“0 min”, Figure 3.4A), so measurement of relative ER membrane

abundance in mitotic cells can be performed by measuring the thickness of the cortical ER membranes at a consistent location in the cells. I measured the percent of the cell diameter at the metaphase plate that is occupied by Sec61β signal by measuring the full width at half max of Sec61β signal (Figure 3.4B). Consistent with our findings in interphase cells, a greater percentage of the cell diameter was taken up by ER membranes in mitotic CTDNEP1-depleted cells compared to cells treated with control siRNA (Figure 3.4B-C). Individual traces of ER and chromatin marker signal additionally revealed that greater occupancy by ER membranes at the metaphase plate leaves less space for chromosomes to localize (Figure 3.4B).

To confirm these findings in cells in which every cell is depleted of CTDNEP1, I imaged control and CTDNEP1^{KO} cells transiently expressing GFP-KDEL and stained with the live Hoechst dye SiR-DNA to mark chromosomes from anaphase onset (Figure 3.5A; SiR not shown). I measured the percentage of cell diameter occupied by GFP-KDEL and found that CTDNEP1^{KO} cells had a greater occupancy of the cell diameter by ER membranes (Figure 3.5B-3.5C).

M. I. Anjur-Dietrich (under the supervision of D. Needleman) introduced magnetic beads about the size of a mitotic chromosome (~2-3 μm) into CTDNEP1^{KO} cells and measured bead displacement upon pulling with defined force using magnetic tweezers and found that the cytoplasm is more viscous in CTDNEP1^{KO} cells than in control cells (Merta et al., 2021). Further, chromosomes in prometaphase have a lower average velocity in CTDNEP1^{KO} cells compared to control cells (Merta et al., 2021) (finding by M. I. Anjur-

Dietrich). Because uncleared membranes occur more frequently in prometaphase CTDNEP1^{KO} cells, these data suggest that expanded ER membranes can limit chromosome movements. The decreased space taken up by chromosomes at the metaphase plate because of increased space taken up by ER membranes in CTDNEP1^{KO} cells supports this idea (Figure 3.4B).

Together, these data support the conclusion that more abundant and uncleared ER membranes in mitosis in CTDNEP1^{KO} cells contribute to viscous forces exerted on mitotic chromosomes to limit chromosome motions. With CTDNEP1, membrane biogenesis is limited to maintain mitotic membrane clearance, contain cytoplasmic viscosity, and facilitate chromosome movement.

Conserved function for CTDNEP1 in limiting membrane extensions into post-mitotic nuclei

In meiosis II of *C. elegans* early embryos deleted of CNEP-1, membrane extensions can be seen inside of newly reformed nuclei; these extensions are exacerbated by additional depletion of the ESCRT-III sealing factor CHMP7 and can be rescued by suppressing PI synthesis (Penfield et al., 2020). I thus sought to determine if human CTDNEP1 restricts membrane localization from the nuclear interior following mitotic exit. I imaged control and CTDNEP1^{KO} cells transiently expressing GFP-KDEL and enriched for mitotic cells by drugless mitotic shakeoff from anaphase onset through telophase (Figure 3.6A). After nuclear envelope reformation, at 25 min after anaphase onset, CTDNEP1^{KO} cell nuclei had more membrane extensions as determined by GFP-KDEL fluorescence (Figure 3.6A, inset and arrows; Figure 3.6B). These membrane

extensions were fainter than nuclear envelope signal, which is consistent with findings in *C. elegans* embryo post-meiotic nuclei (Penfield et al., 2020).

I next sought to determine if nuclear membrane extensions formed in mitosis persist in interphase cells. I imaged CTDNEP1^{KO} and control U2OS cells transiently expressing GFP-KDEL in long-term (8-12 hr) time-lapse format (Figure 3.7A). A greater proportion of CTDNEP1^{KO} cells in early G1 had nuclear membrane extensions compared to control cells (Figure 3.7A, pink arrows; Figure 3.7B). Unlike invaginations of the outer and inner nuclear membranes, which are as bright as the rest of the nuclear envelope and are common in control U2OS cells (Figure 3.7A, green arrows), nuclear membrane extensions are fainter than the rest of the nuclear envelope (Figure 3.7A, pink arrows). Future studies will determine if the nuclear membrane extensions in CTDNEP1-depleted human cells are derived from the inner nuclear membrane. Together, these data support the conclusion that human CTDNEP1 has a conserved role for limiting membrane extensions from forming inside of newly reassembled nuclei.

CTDNEP1 limits reestablishment of nuclear import and nuclear size during mitotic exit

To determine if altered membrane dynamics during nuclear envelope reassembly impacts nuclear import or growth, I imaged U2OS cells stably expressing a single importin β binding domain of importin α fused to GFP (IBB-GFP) and H2B-mCherry, treated with control or CTDNEP1 siRNA. IBB localizes to the nucleus during interphase, then to the cytoplasm after nuclear envelope

breakdown, then to the nucleus again as nuclear pores are rebuilt and import is re-established (Figure 3.8A). Cells treated with CTDNEP1 siRNA appeared to have faster colocalization of IBB with chromatin after anaphase onset, and nuclei appeared slightly larger (Figure 3.8B). I measured the integrated intensity of IBB signal in the nucleus and expressed it as fold increase over integrated intensity 3 min after anaphase onset (a time point >5 min prior to initiation of nuclear import) (Lu et al., 2011) (Figure 3.8C). The integrated intensity of IBB signal in nuclei was higher in CTDNEP1-depleted cells compared to control cells starting at around 15 min after anaphase onset, which corresponds to when membranes are finished wrapping around chromosomes by visualization of Sec61β fluorescence (Lu et al., 2011) (Figure 3.8C). Measurements of H2B signal surface area revealed a similar timing for CTDNEP1-depleted cell nuclei expanding faster than control cell nuclei (Figure 3.8D). One caveat of these results is that the images were taken at low resolution and with low signal to noise. IBB is not imported uniformly in the reforming nucleus but is imported at “non-core” regions before “core” regions (Lu et al., 2011), so higher magnification imaging with better signal to noise is needed to confirm these findings. Another notable caveat of these results is that the a single IBB domain fused to GFP (~33 kDa) is small enough to freely diffuse through the nuclear pore and likely through unsealed nuclear envelope holes, so the reestablishment of nuclear import being measured in this study is of net nuclear import. Additionally, postmeiotic nuclei of *C. elegans* early embryos lacking CNEP-1 are leaky most likely due to unsealed nuclear envelope holes (Penfield et al., 2020); leakiness of nuclei in this cell line

would not be detected due to the size of the IBB reporter. To address these caveats, a triple-GFP IBB reporter can be used, as it is large enough to be retained in the nucleus without diffusing back through pores (Hatch et al., 2013). Together, these results suggest that CTDNEP1 limits reestablishment of nuclear import and nuclear growth during mitotic exit.

Discussion

These data reveal multiple roles for CTDNEP1-controlled membrane biogenesis in regulating mitotic events. We confirmed that CTDNEP1 limits mitotic progression during prometaphase and found that CTDNEP1 limits excess membranes in mitosis and regulates membrane clearance during prometaphase and metaphase. Excess membranes can contribute to viscous forces exerted on chromosomes, and chromosome movements are dampened in CTDNEP1^{KO} cells. We additionally show that CTDNEP1 limits reestablishment of nuclear import and nuclear growth and restricts membrane localization from the nuclear interior during mitotic exit.

The finding that depletion of CTDNEP1 limits reestablishment of nuclear import and nuclear growth suggests that ER membrane access might be limiting for postmitotic nuclear pore complex assembly. Overexpression of CTDNEP1 or its obligate binding partner NEP1R1 in fly fat body cells leads to less fluorescence labeling of FG-Nups by the nucleoporin antibody mAb414, although pore density appears to be unaffected; the authors conclude that CTDNEP1 limits pore maturation (Jacquemyn et al., 2020). Future studies will determine the mechanisms by which CTDNEP1 limits nuclear pore complex assembly or

maturation to regulate nuclear import following mitosis. In sea urchin embryos, availability of perinuclear ER membranes allows nuclear expansion (Mukherjee et al., 2020). Nuclear growth also scales with nuclear import (Levy and Heald, 2010). Because CTDNEP1 limits ER membranes and also appears to limit nuclear pore complex assembly/maturation, it is unclear what is the mechanism for how CTDNEP1 regulates nuclear growth. Future studies uncoupling import from membrane availability will illuminate how these factors regulate nuclear size with loss of CTDNEP1.

CTDNEP1 has a conserved role for restricting ER membranes to the surface of the nuclear envelope during and after mitotic exit. Membrane extensions are likely not seen earlier in nuclear envelope reformation because chromosomes are crosslinked together by barrier to autointegration factor (BAF) which does not crosslink chromosomes during mitotic exit (Samwer et al., 2017). The mechanism for how nuclear membrane extensions are made or persist in the nucleus is not fully understood. CTDNEP1 interacts genetically with the ESCRT-III sealing factor CHMP7, revealing that coordination of lipid synthesis acts with nuclear envelope sealing to keep membranes from the nuclear interior (Penfield et al., 2020). These data support the idea that nuclear extensions could be produced during nuclear sealing by uncoordinated lipid synthesis with ESCRT-III activity. Other cases exist in which uncoordinated ESCRT-III activity leads to nuclear membrane abnormalities. Micronuclei lack the ability to spatially restrict ESCRT-III sealing and often have several membrane intrusions upon nuclear rupture (Vietri et al., 2020). CHMP7 has shown to bind PA in the inner nuclear

membrane in yeast (Thaller et al., 2021). Future studies will illuminate if lipid flux by lipin controlled by CTDNEP1 serves to regulate targeting of CHMP7 to the inner nuclear membrane to coordinate sealing and limit the formation of nuclear envelope extensions.

CTDNEP1 regulation of membrane biogenesis facilitates prometaphase and metaphase ER membrane clearance from the region around chromosomes in human cells (Figure 3.2; Figure 3.9). Expansion of ER membranes of CTDNEP1-depleted cells persists into mitosis, leading to an excess of membranes that are not cleared as fast as membranes in control cells. It is not clear if the membranes are less cleared because of the sheer amount of membranes overwhelming clearing mechanisms like REEP3/4, but future studies can determine if this is the case. Together, these data support the idea that uncleared membranes can impede proper mitotic progression.

ER membranes appear to contribute to the viscosity of the mitotic cytoplasm. These results show that ER lipid synthesis is limited to contain cytoplasmic viscosity in mitosis. Prometaphase chromosome velocity is also dampened in CTDNEP1^{KO} U2OS cells. High cytoplasmic viscosity due to increased ER membranes may limit the movements of chromosomes being pushed and pulled by the mitotic spindle in prometaphase.

Micronuclei are not observed in *S. cerevisiae* or *C. elegans* depleted of CTDNEP1, despite alterations in ER membrane biogenesis present in these cells (Bahmanyar et al., 2014; Siniossoglou et al., 1998). We hypothesize that differences in mitoses may account for the differences in chromosome

segregation (Figure 3.10). *S. cerevisiae* have closed mitosis, in which the spindle assembles and chromosome segregation occurs inside of the nucleus (Figure 3.10, above). *C. elegans* have semi-open mitosis, in which nuclear envelope membranes become permeable and are detached from chromosomes, but the spindle assembles inside of nuclear envelope (Figure 3.10, middle). In human cells, membranes are totally cleared from chromosomes and the mitotic spindle (Figure 3.10, below). In the absence of membrane clearance, interference by membranes may inhibit proper chromosome segregation, leading to formation of micronuclei (Figure 3.10, below). This suggests that nuclear envelope breakdown and membrane clearance may be coordinated to occur before the spindle assembles in human cells to allow unimpeded spindle assembly to promote proper chromosome segregation.

It is unclear exactly how excess membranes in mitosis in CTDNEP1^{KO} cells could lead to formation of micronuclei, given that error correction mechanisms are in place to limit chromosome missegregation in human cells. The next chapter will discuss data that assess chromosome segregation in CTDNEP1^{KO} with respect to multiple aspects of mitotic error correction to determine how micronuclei can form.

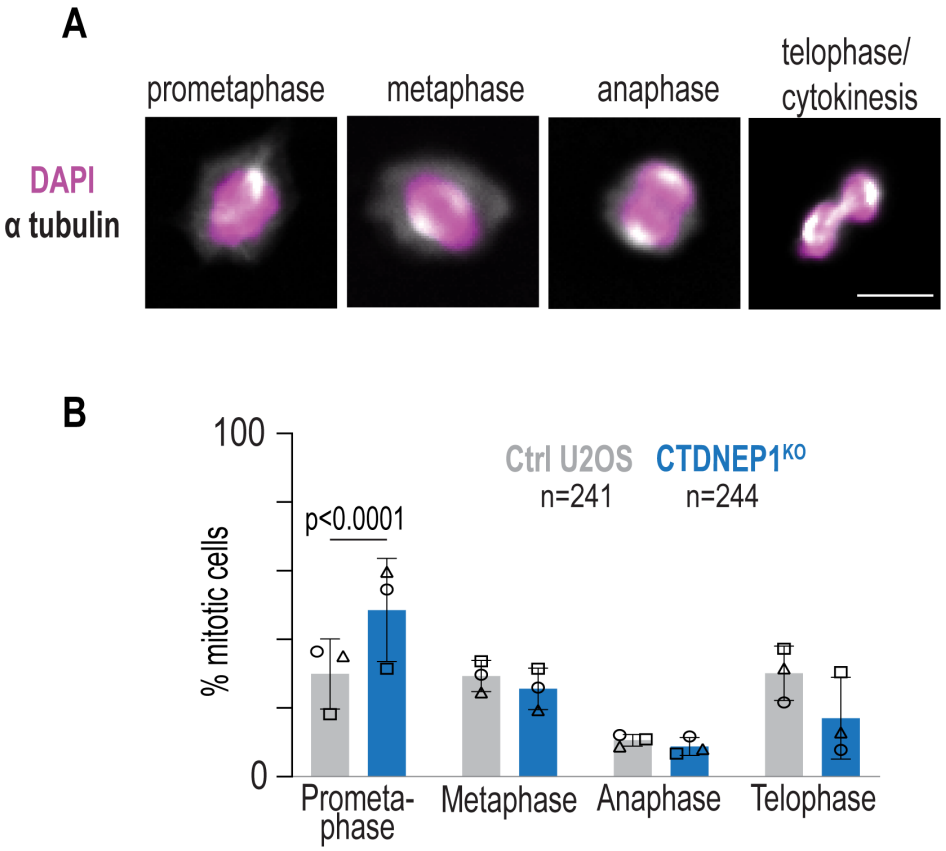

Figure 3.1 CTDNEP1^{KO} cells have a higher incidence of prometaphase cells
A) Confocal images of DAPI/Hoechst and tubulin staining in U2OS cells used for mitotic staging. Scale bar = 10 μm. B) Plot of quantification of percent of mitotic cells in each stage of mitosis in control and CTDNEP1^{KO} U2OS cells. Means ± SDs of proportions shown. n = number of cells, N = 3 experimental repeats. P value, Fisher's exact test of incidences of prometaphase cells vs incidences of cells in other mitotic stages.

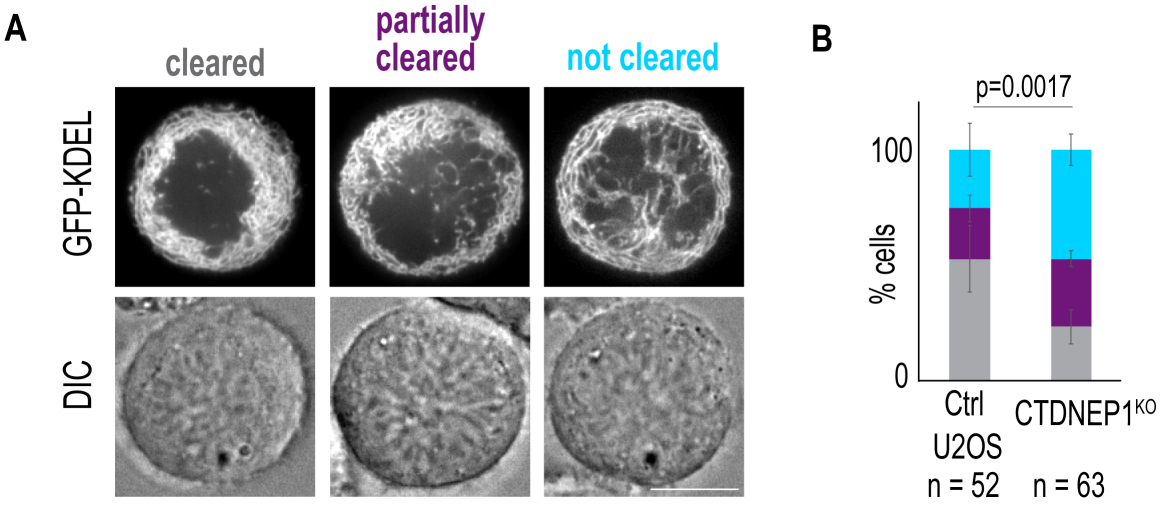

Figure 3.2 Prometaphase and metaphase CTDNEP1^{KO} cells have more uncleared membranes in proximity to chromosomes

A) Confocal image of GFP-KDEL or DIC in transiently-expressing U2OS CTDNEP1^{KO} cells subject to mitotic shakeoff, with phenotypic categorization. Scale bar 10 μm. B) Plot of incidence of indicated phenotypes in cells imaged as in (A). Means ± SDs shown. n = number of cells, N = 3 experimental repeats. P value, Chi squared test of total incidences.

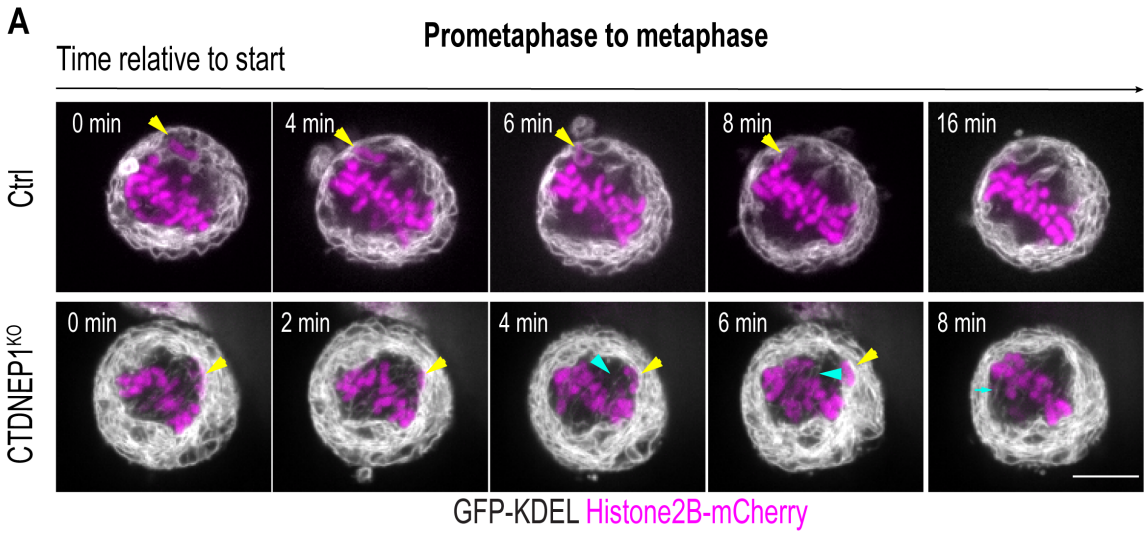

Figure 3.3 Chromosomes in prometaphase cells can be embedded in ER membranes during mitotic progression in control and CTDNEP1^{KO} cells

A) Select images from confocal time lapse of GFP-KDEL and H2B-mCherry in transiently-expressing U2OS CTDNEP1^{KO} cells subject to Cdk1 inhibitor washout. Yellow arrows point to unaligned chromosomes; cyan arrows point to ER tubules extending into the metaphase plate. Scale bar, 10 μm.

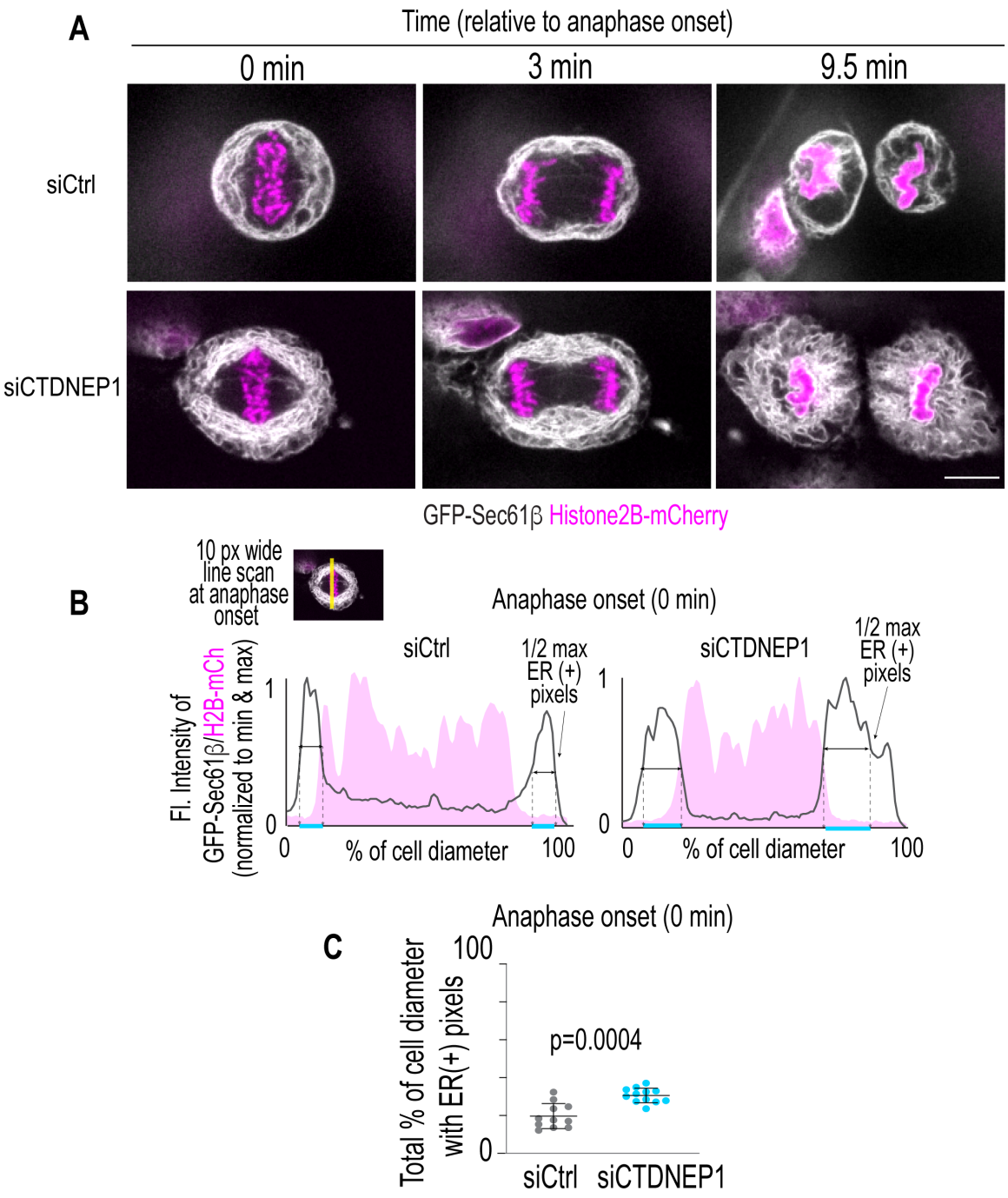

Figure 3.4 Excess ER membranes fill mitotic cytoplasm in CTDNEP1-depleted U2OS cells, and chromosomes take up less space

A) Selected spinning disk confocal images of GFP-Sec61β and H2B-mCherry from a time lapse movie of U2OS cells treated with indicated siRNAs. Scale bar 10 μm. B) Graphs plotting fluorescent intensities of GFP-Sec61β (gray) and mCherry-H2B (magenta) along a 10-pixel line profile drawn along the equatorial region at anaphase onset for indicated conditions. Values are normalized to minimum and maximum values for each channel and to the percentage of the cell diameter. Blue

lines indicate percentage of the cell diameter at the half maximum value for GFP-Sec61β. C) Plot of percent of cell diameter occupied by Sec61β-positive pixels in cells treated with indicated siRNA as in (A) and (B). Means ± SDs shown. n = number of cells, N = 7 experimental repeats. P value, Mann-Whitney 2-tailed unpaired t test.

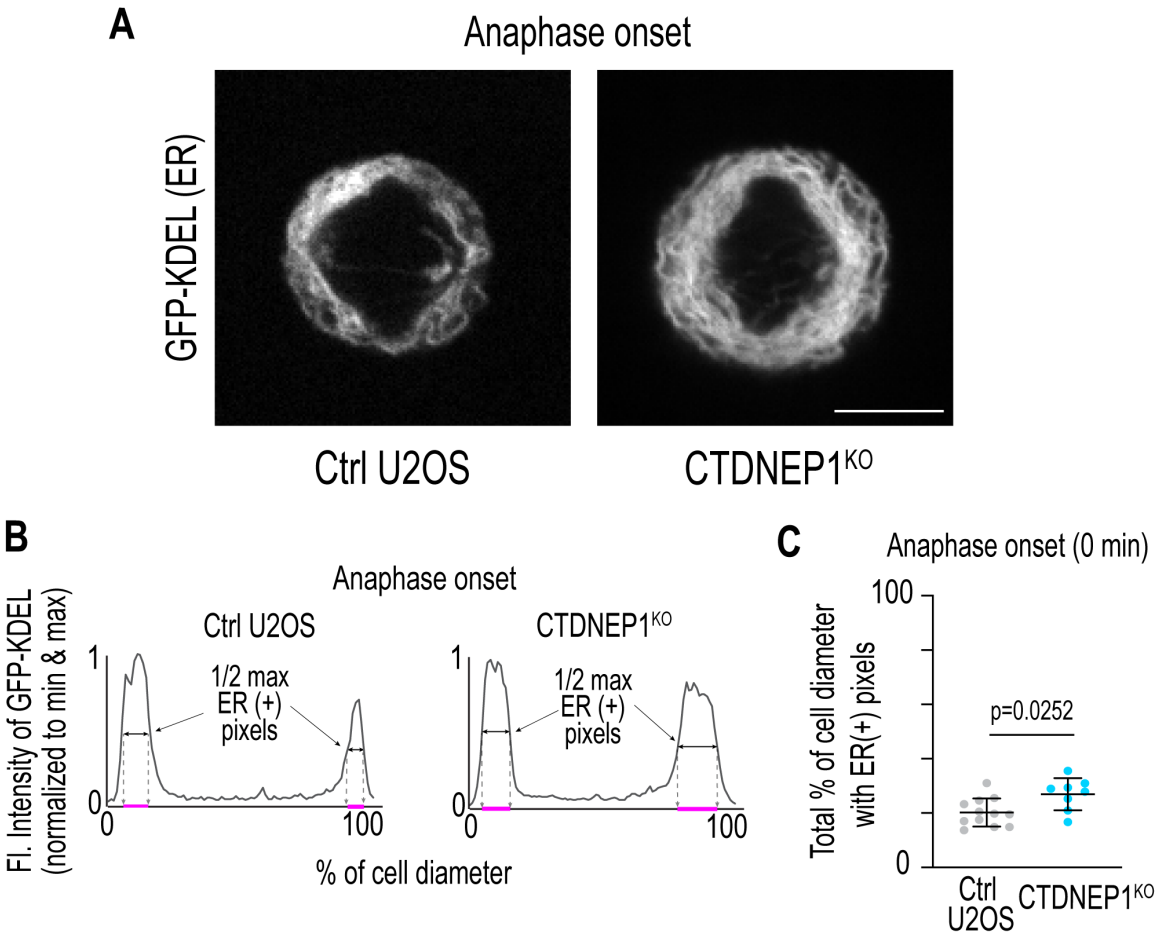

Figure 3.5 Excess ER membranes fill mitotic cytoplasm in CTDNEP1^{KO} U2OS cells

A) Confocal images of GFP-KDEL signal from a time lapse movie of U2OS cells at anaphase onset as determined by SiR-DNA staining (not shown). Scale bar 10 μm. B) Graphs plotting fluorescent intensities of GFP-KDEL along a 10-pixel line profile drawn along the equatorial region at anaphase onset for indicated conditions. Values are normalized to minimum and maximum values for each channel and to the percentage of the cell diameter. Blue lines indicate percentage of the cell diameter at the half maximum value for GFP-Sec61β. C) Plot of percent of cell diameter occupied by KDEL-positive pixels in cells treated with indicated siRNA as in (A). Means ± SDs shown. n = number of cells, N = 3 experimental repeats. P value, Mann-Whitney 2-tailed unpaired t test.

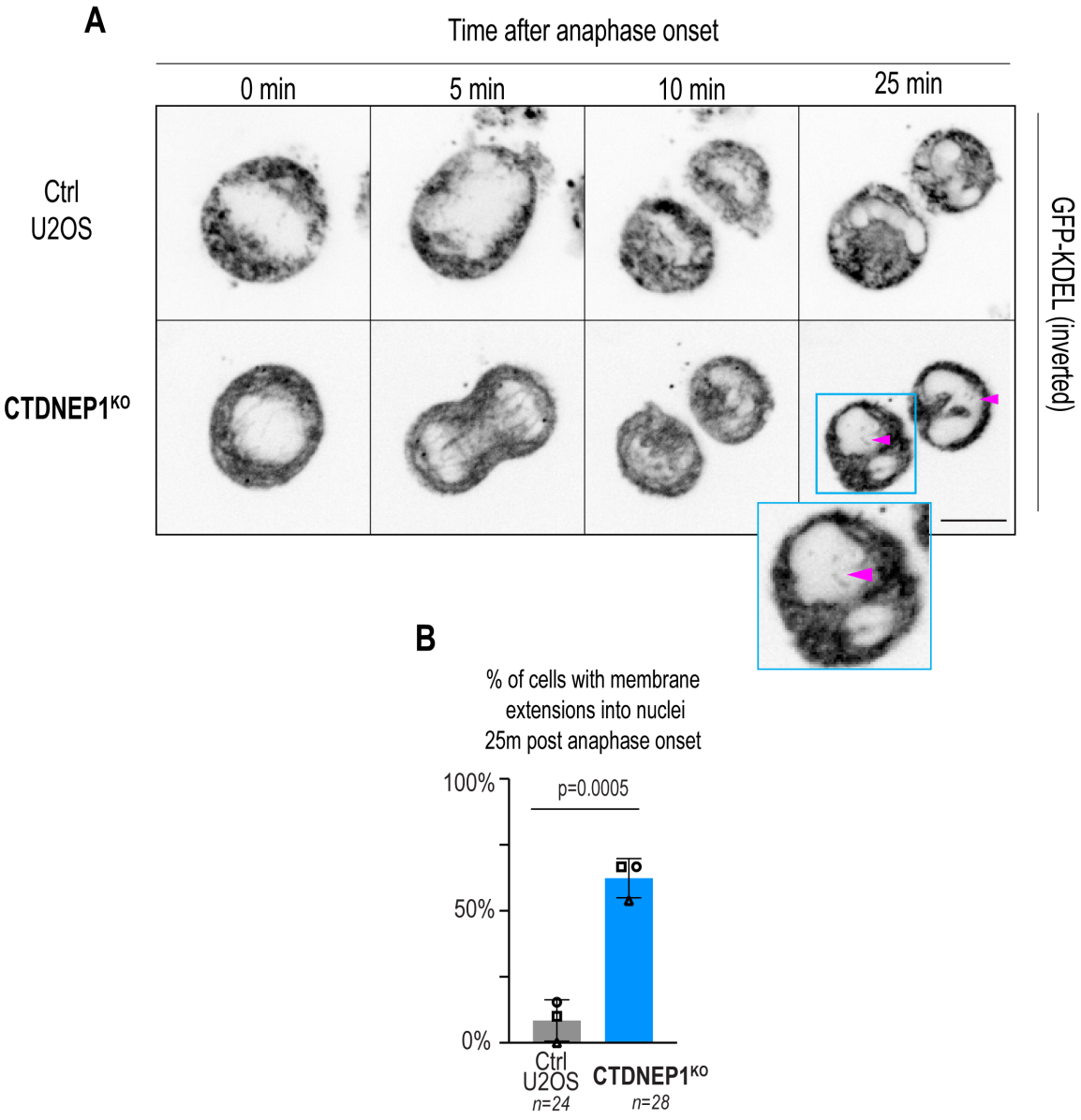

Figure 3.6 Membrane extensions in CTDNEP1^{KO} U2OS cells during mitotic exit

A) Selected spinning disk confocal images of GFP-KDEL signal (inverted) from a time lapse movie of U2OS cells after mitotic shakeoff. Mitotic staging determined by SiR-DNA staining (not shown). Arrows point to intranuclear membrane extensions. Scale bar 10 µm. B) Plot of incidence of membrane extensions in postmitotic nuclei. Means ± SDs shown. n = number of daughter cell pairs, N = 3 experimental repeats. P value, Fisher's exact test of total incidences.

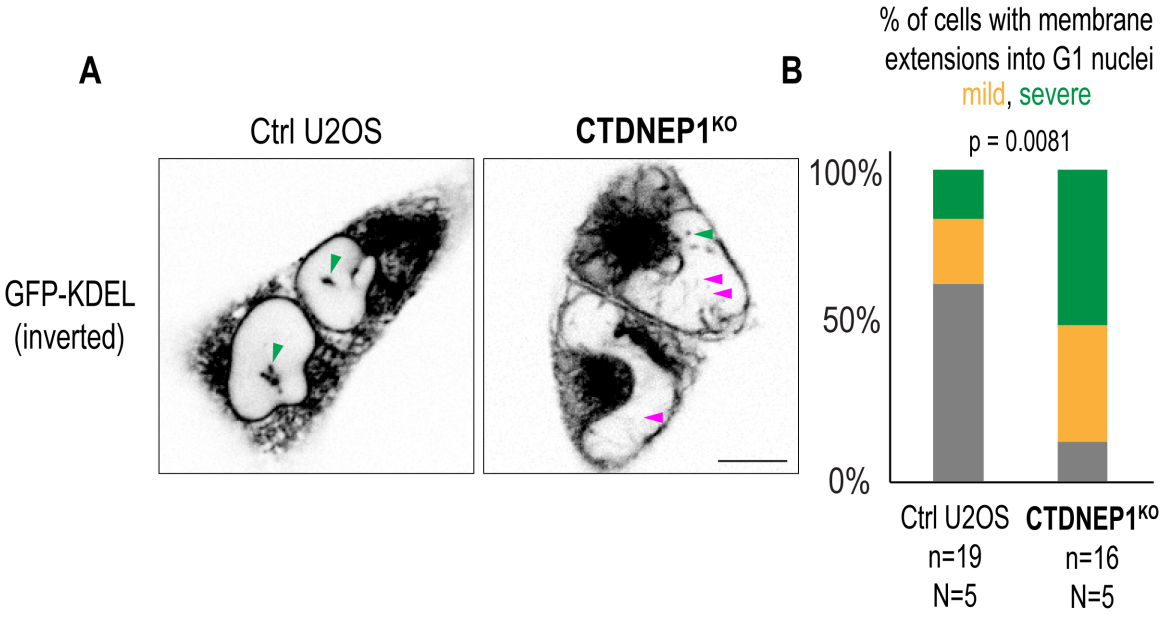

Figure 3.7 Persistence of membrane extensions in early G1 CTDNEP1^{KO} U2OS cells

A) Selected spinning disk confocal images of GFP-KDEL (inverted) from a time lapse movie of U2OS cells in early G1. Mitotic staging determined by SiR-DNA staining (not shown). Arrows point to intranuclear membrane extensions. Scale bar 10 µm. B) Plot of incidence of membrane extensions in post-mitotic G1 nuclei. Means ± SDs shown. n = number of daughter cell pairs from N = 5 experimental repeats. P value, Chi squared test of total incidences.

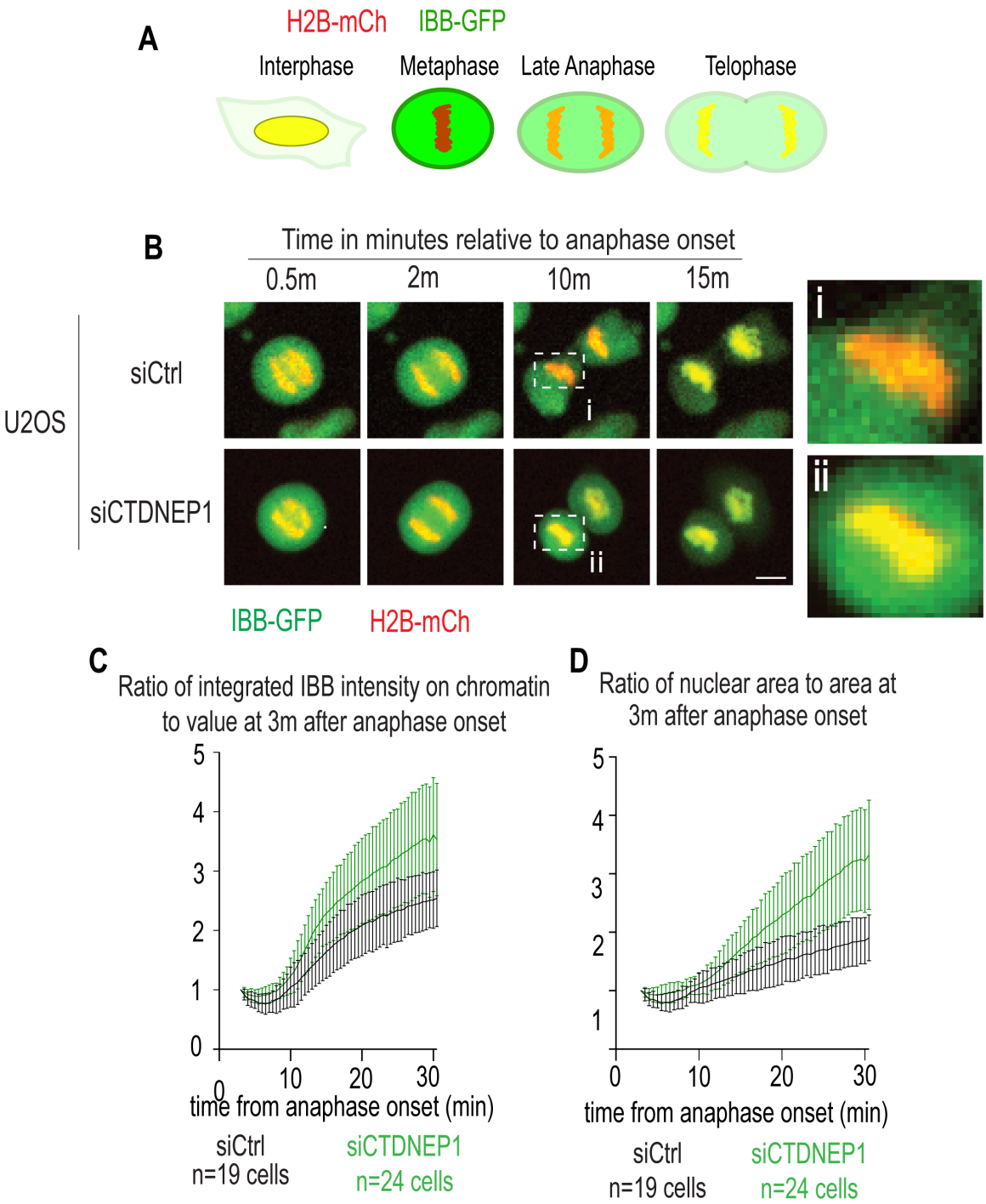

Figure 3.8 siCTDNEP1-treated cells show faster reestablishment of net nuclear import and faster nuclear growth during mitotic exit

A) Schematic of importin β-binding domain of importin α (IBB) localization with chromatin (H2B) during the cell cycle. B) Images from spinning disk confocal time lapse movie of IBB and H2B signal during mitotic exit. Scale bar, 10 μm. C) Plot of fold increase of integrated IBB intensity in the chromatin-containing region over time in cells treated with the indicated siRNA. Fold increase is compared to value at t = 3 min. Means ± SD shown. D) Plot of fold increase in nuclear surface area

over time in cells treated with the indicated siRNA. Fold increase is compared to value at t = 3 min. Means ± SD shown. For all, N = 4 experimental repeats.

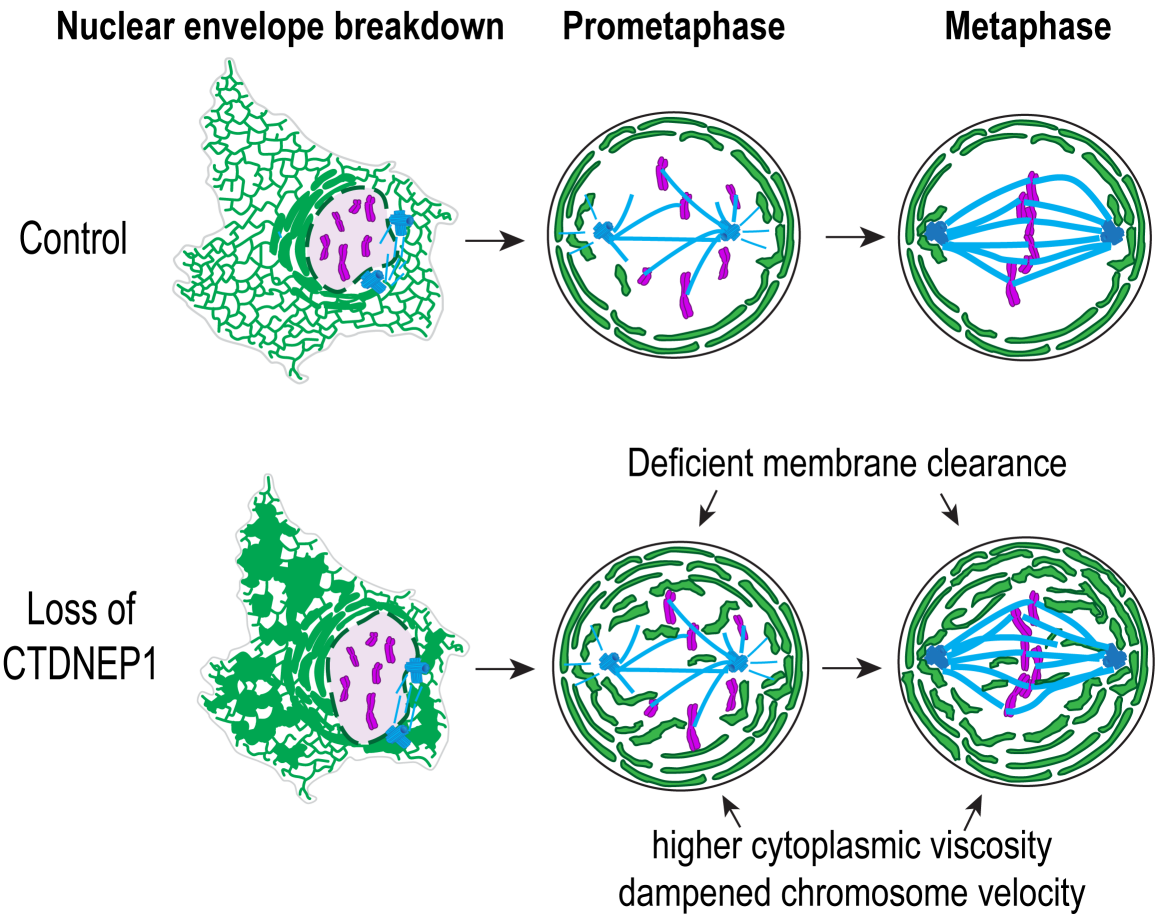

Figure 3.9 Coordination of membrane clearing is obfuscated by increased lipid synthesis controlled by CTDNEP1

A) Schematic for how membranes are cleared to the cell periphery after nuclear envelope breakdown and cell rounding. This process is disrupted with excess ER membranes in CTDNEP1^{KO} cells, leading to persistence of uncleared membranes in prometaphase to metaphase cells. Light green = ER, dark green = nuclear envelope; pink = DNA, and blue = mitotic spindle.

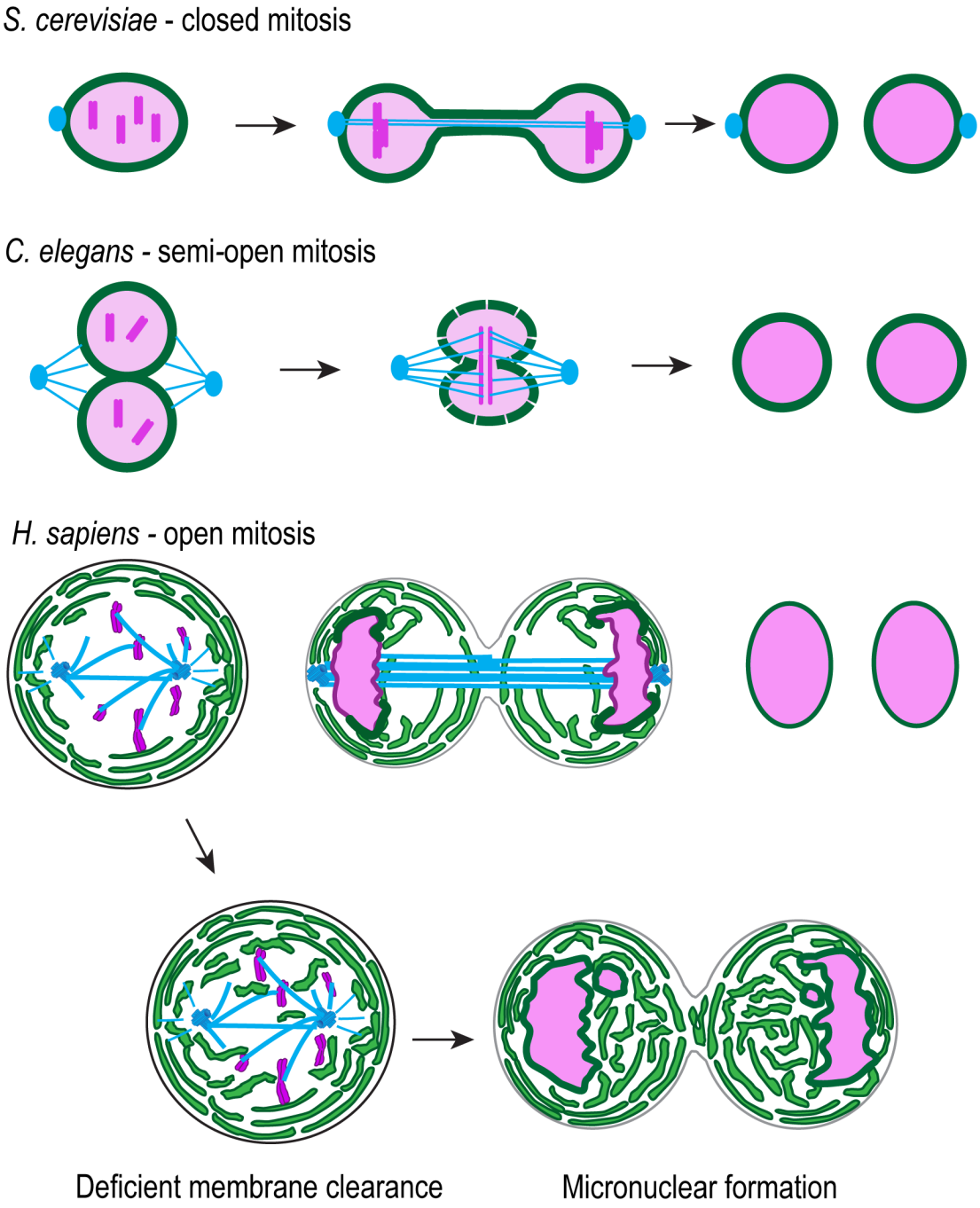

Figure 3.10 Comparison of closed vs semi-open vs open mitosis and implications for improper membrane clearance for chromosome segregation

A) Schematic showing differences between nuclear envelope membrane dynamics during mitosis in yeast, worm, and human cells. Dark green = nuclear envelope; pink = DNA, and blue = mitotic spindle. ER (light green) also shown in human cell to demonstrate membrane clearing to cell periphery. Bottom, deficient membrane clearance leads to formation of micronuclei in open mitosis.

Chapter 4: CTDNEP1 is required for correction of errors in mitosis

Some of this work is included and/or modified from the manuscript:

Holly Merta[*], Jake W. Carrasquillo Rodríguez[*], Maya I. Anjur-Dietrich, Mitchell E. Granade, Tevis Vitale, Thurl E. Harris, Dan Needleman, Shirin Bahmanyar. A CTDNEP1-lipin 1-mTOR regulatory network restricts ER membrane biogenesis to Enable Chromosome Motions Necessary for Mitotic Fidelity. *bioRxiv* (2021). doi: https://doi.org/10.1101/2021.03.02.433553

[*] Co-first authors

Introduction

We have shown that CTDNEP1 limits ER membrane biogenesis to limit membrane abundance and clearance in mitosis. We have also shown that mitotic cells without CTDNEP1 have higher cytoplasmic viscosity and lower prometaphase average chromosome velocity. What remains to be shown is how micronuclei can form in CTDNEP1-depleted cells. In this chapter, I investigate known mechanisms of chromosome missegregation in CTDNEP1-depleted cells to determine how CTDNEP1 limits formation of micronuclei.

Micronuclei can form from either missegregation of non-centromere-containing chromosome fragments induced by DNA damage/breaks or missegregation of whole chromosomes (Fenech et al., 2011). We have found that CTDNEP1^{KO} U2OS cells exhibit excess ER membranes and less ER membrane clearance in mitosis. Previous studies implicating membrane clearance in chromosome segregation have found that poor clearance of membranes from chromatin resulted in anaphase bridges and chromosome missegregation (Schlaitz et al., 2013), both of which involve chromosomes with intact centromeres (Pampalona et al., 2016). Therefore, we hypothesize that missegregation of whole chromosomes is more likely to be the culprit than missegregation of chromosome fragments.

Missegregation of whole chromosome fragments can occur by failed congression, merotely, or premature spindle assembly checkpoint (SAC) inactivation, or a combination of these (Fenech et al., 2011). Failed chromosome congression can occur by chromosomes not aligning on the metaphase plate,

then being unable to reach the main chromosome mass to reform into the main nucleus after anaphase onset (Fonseca et al., 2019). Merotely occurs when one or both kinetochores of a chromosome are attached to microtubules emanating from both spindle poles, instead of only one (Cimini et al., 2001). If the abnormal attachment is strong enough to sufficiently counter the tension from the correct attachments, the chromosome lags and does not incorporate with the main chromosome mass during anaphase (Cimini et al., 2004). Merotely can occur when spindle geometry is altered; for example, multipolar spindles that cluster centrosomes to become bipolar later (transient multipolarity) frequently have merotelic attachments biased toward the spindle pole with two centrosomes (Silkworth and Cimini, 2012). Cells with delayed spindle pole separation also have more merotelically attached chromosomes (Cimini, 2003; Silkworth and Cimini, 2012). Altered kinetochore architecture has also been shown to contribute to merotely (Gregan et al., 2011). Merotely is a common occurrence in prometaphase cells, and merotelic attachments are typically repaired before anaphase onset (Cimini et al., 2004). Prolonging metaphase reduces the proportion of wrongly attached microtubules to correctly attached microtubules and decreases the overall incidence of merotelic attachments (Cimini et al., 2004). Aurora B has been implicated in mediating merotelic attachment correction; an Aurora B-generated phosphorylation gradient around centrosomes allows spatially controlled motor protein and attachment-regulating protein activities to promote correct attachments and destabilize incorrect ones (Cimini et al., 2006; DeLuca et al., 2006; Gregan et al., 2011). Merotelic attachments are

not sensed by the spindle assembly checkpoint (Gregan et al., 2011), making these distinct mechanisms contributing to formation of micronuclei.

Premature inactivation of the spindle assembly checkpoint also leads to formation of micronuclei (Liu et al., 2018). The spindle assembly checkpoint monitors for unattached and improperly attached kinetochores and prevents sister chromatids from separating and cell cycle progression into anaphase (Musacchio, 2015). Broadly, the spindle assembly checkpoint prevents cyclin B (part of the cyclin dependent-kinase 1/cyclin B kinase complex) and securin (a protein that inhibits separase, which mediates chromatid dissociation through cohesin dissociation) from being degraded (Musacchio, 2015). At unattached kinetochores, the mitotic checkpoint complex (MCC) inhibits the anaphase promoting complex/cyclosome (APC/C), which would otherwise ubiquitinate cyclin B and securin (Hayward et al., 2019; Musacchio, 2015). MCC assembly and recruitment to unattached kinetochores appears to be a tunable response based on the frequency of unattached kinetochores (Collin et al., 2013), yet one unattached kinetochore is sufficient to activate the spindle assembly checkpoint (Dick and Gerlich, 2013). Aurora B recruits the checkpoint kinase MPS1 to kinetochores, and MPS1 phosphorylates kinetochore proteins to create a docking site for spindle assembly checkpoint players that make up or support the MCC (Hayward et al., 2019; Musacchio, 2015). When all kinetochores are properly attached, these steps are reversed; and passive and active SAC silencing mechanisms facilitate MCC dissociation from the kinetochore and from APC/C (Hayward et al., 2019; Musacchio, 2015). APC/C then ubiquitinates cyclin B and

securin to allow chromatids to separate and anaphase to proceed (Musacchio, 2015). Premature inactivation of the spindle assembly checkpoint occurs in some cancer cells and contributes to aneuploidy and formation of micronuclei (Bharadwaj and Yu, 2004; Fenech et al., 2011).

Here we show that CTDNEP1 is required for mitotic error correction. We show that CTDNEP1-depleted cells have more lagging chromosomes and have longer spindles. Prematurely inactivating the spindle assembly checkpoint modestly increases the number of micronuclei in CTDNEP1^{KO} cells compared to control cells. On the other hand, increasing merotelic attachments by subjecting cells to transient spindle disassembly causes severe micronucleation in CTDNEP1^{KO} cells and CTDNEP1-depleted cells. This severe micronucleation is suppressed by CTDNEP1/NEP1R1 or catalytically active lipin 1 overexpression. These data show that CTDNEP1 limits correction of merotelic errors, illuminating the mechanism for how chromosome segregation changes can lead to formation of micronuclei in cells lacking CTDNEP1 and informing how CTDNEP1 mutations might contribute to chromosomal instability in cancer.

Results

Lagging chromosomes in CTDNEP1-depleted cells

To confirm that CTDNEP1-depleted cells have increased rates of chromosome missegregation that can contribute to formation of micronuclei, I sought to quantify kinetochore or centromere localization during anaphase relative to chromosome and spindle markers. I used a U2OS cell line stably expressing GFP-Centrin 2 (centrosome marker), GFP-CENPA (centromere

marker), and mCherry-α tubulin (Yu et al., 2019) and RNAi-depleted of CTDNEP1 (Figure 4.1). To enrich for mitotic cells for live imaging, I performed a drugless mitotic shakeoff and plated and imaged cells immediately. In mid-late anaphase and early telophase cells, lagging chromosomes could be visualized as GFP punctae localized away from the segregating chromosomes, either in the spindle midzone or in the cell periphery, (Figure 4.1A, yellow arrow). One caveat of this experiment is that the cells had CENPA and Centrin 2 fluorescing at the same wavelength. However, Centrin 2 punctae were brighter than CENPA punctae and had associated bright tubulin signal that occurs at centrosomes (Figure 4.1A, cyan arrow), making them easily distinguishable for this analysis. By blind categorization, I quantified the percentage of anaphase/telophase cells with GFP-CENPA punctae apart from chromosome masses and found that cells treated with CTDNEP1 siRNA had significantly more lagging chromosome punctae than control cells (32.6 ± 5.2 % in CTDNEP1 RNAi-depleted cells vs 9.6 ± 6.5 % of cells treated with control siRNA; Figure 4.1B). These results show that depletion of CTDNEP1 results in an increase in lagging chromosomes, which can contribute to formation of micronuclei.

Bypassing the spindle assembly checkpoint in CTDNEP1-depleted cells increases formation of micronuclei

An increase in lagging chromosomes can indicate that errors that are sensed by the spindle assembly checkpoint are increased in CTDNEP1-depleted cells. To determine the rate of attachment errors, one can use an inhibitor of the spindle assembly checkpoint on a synchronized cell population; cells will enter

anaphase with improperly attached kinetochores, and the cells will form micronuclei in the subsequent interphase (Liu et al., 2018) (Figure 4.2A). To test if CTDNEP1 depletion leads to increased erroneous kinetochore attachments, I synchronized control and CTDNEP1^{KO} cells at the G2/M transition using a Cdk1 inhibitor, RO-3306 (K_i = 35 nM for Cdk1/cyclin B1 and K_i = 110 nM for Cdk1/cyclin A (Calbiochem)), and released the cells from the G2 block in the presence of an inhibitor of the checkpoint kinase MPS1 (NMS-P715, K_i = 0.99 nM (Calbiochem)) (Liu et al., 2018) (Figure 4.2A-4.2B). CTDNEP1^{KO} cells had a higher incidence of micronuclei compared to control cells with MPS1 inhibition (43.3 ± 4.9 % of CTDNEP1^{KO} cells compared to 39.9 ± 1.9 % of control cells; Figure 4.2C). Although significant, the small magnitude of this difference led us to conclude that increased kinetochore attachment errors sensed by the SAC is likely not the major mechanism that contributed to lagging chromosomes and formation of micronuclei in cells lacking CTDNEP1, and so we assessed other mechanisms that cause lagging chromosomes.

Recovery from transient spindle disassembly leads to abnormal hyper-micronucleation in CTDNEP1-depleted cells that is suppressed with CTDNEP1/lipin expression

Increased formation or decreased correction of merotelic attachments is another mechanism by which lagging chromosomes and micronuclei can form. Transient disassembly of the mitotic spindle is known to increase merotelic attachments and is used to enrich for micronuclei (Cimini, 2003; Cimini et al., 2001; Liu et al., 2018) (Figure 4.3). During recovery from spindle

depolymerization, a delay in establishing spindle bipolarity and stretching of kinetochores leads to increased merotelic attachments that persist into anaphase (Cimini, 2003). To determine if correction of merotelic errors is deficient in CTDNEP1-deleted cells, I treated cells with a low dose of nocodazole and performed mitotic shakeoff, then allowed cells to recover from nocodazole treatment ("nocodazole washout") (Liu et al., 2018); I then performed immunofluorescence processing on the cells in interphase to score cells for the presence of micronuclei (Figure 4.3A; Figure 4.4A). In control cells, recovery from spindle depolymerization by nocodazole washout led to an increase in micronuclei (Figures 4.4A-4.4B; compare 10.6 ± 2.0 % in Figure 2.19B to 4.3 ± 0.8 % in Figure 4.4B). In CTDNEP1^{KO} cells, a significant proportion of nuclei appeared severely multilobed/micronucleated, a phenotype we refer to as "hyper-micronucleated" nuclei (40.0 ± 8.5 % in CTDNEP1^{KO} cells compared to 4.3 ± 1.2 % of control cells; Figure 4.4A-4.4B). To confirm that this phenotype is not exclusive to U2OS cells, I also performed nocodazole washout on RPE-1 cells RNAi-depleted of CTDNEP1 (Figure 4.5A). Consistent with the previous results, RPE-1 cells depleted of CTDNEP1 exhibited more hyper-micronucleated nuclei (21.5 ± 2.6 % in CTDNEP1-depleted cells compared to 9.2 ± 2.4 % of control cells; Figure 4.5B). To determine if loss of CTDNEP1 is responsible for controlling formation of hyper-micronucleated nuclei in CTDNEP1^{KO} cells, I transiently overexpressed CTDNEP1-HA and FLAG-NEP1R1 and subjected cells to nocodazole washout and found that CTDNEP1/NEP1R1 expression reduces the number of hyper-micronucleated nuclei compared to overexpression of a

control vector (Figure 4.6A-4.6B). Together, these data show that CTDNEP1 is required for the correction of merotelic attachment errors.

I next sought to determine if CTDNEP1 control of lipin 1 plays a role in regulating correction of merotelic attachments, because CTDNEP1 dephosphorylation of other unknown substrates could also control this regulation. I transiently expressed the mouse lipin 1β construct with 19 S/T sites mutated to alanine, which rescues ER expansion in CTDNEP1^{KO} cells (Figure 2.14A-2.14B), as well as the PAP dead version of this construct, and performed nocodazole washout. Overexpression of lipin 1β 19xA suppressed formation of hyper-micronucleated nuclei, whereas overexpression of the PAP dead construct did not (8.7 ± 1.0 % with FLAG-lipin 1β 19xA compared to 30.7 ± 1.4 % in control; 26.2 ± 2.8 % with phosphatase-dead FLAG-lipin 1β 19xA compared to 25.3 ± 3.4 % in control, Figure 4.7A-4.7B). Thus, loss of lipin 1 catalytic activity upon CTDNEP1 depletion allows hyper-micronucleated nuclei formation with nocodazole washout. These data show that CTDNEP1 control of lipin 1 phosphorylation allows correction of merotelic attachments in mitosis.

Mitotic exit in CTDNEP1^{KO} cells recovering from transient spindle disassembly

The appearance of multiple large micronuclei in hyper-micronucleated cells is suggestive of multiple chromosomes segregating into micronuclei during recovery from spindle depolymerization in CTDNEP1^{KO} cells. I performed nocodazole washout on control and CTDNEP1^{KO} U2OS cells and fixed cells 45-60 min after mitotic shakeoff and release from nocodazole to capture cells in mitotic exit (Liu et al., 2018) (Figure 4.8A). Consistent with previous results that

CTDNEP1 depletion leads to a prometaphase delay, a larger proportion of CTDNEP1^{KO} cells were still in prometaphase after 1 hour of nocodazole washout compared to control cells (Figure 4.8B). Among anaphase and telophase cells, CTDNEP1^{KO} cells recovering from nocodazole treatment frequently had masses of chromosomes and concomitant tubulin staining in the periphery of cells (55.2 ± 5.0 % of CTDNEP1^{KO} cells compared to 7.8 ± 7.9 % of control cells, Figure 4.9A). These data support the conclusion that lack of CTDNEP1 control of lipin 1 allows merotelic attachments to persist and lead to chromosome missegregation that results in severe micronucleation.

Longer spindle lengths in CTDNEP1-depleted U2OS mitotic cells

I previously showed that CTDNEP1-depleted cells exhibit sensitivity to spindle depolymerization and dampened prometaphase chromosome movements. These findings prompted us to observe chromosome dynamics and mitotic spindles in CTDNEP1-depleted cells stably expressing Centrin-2, CENPA, and mCherry-α tubulin in metaphase (Figure 4.10A, left). Chromosome alignment was not significantly decreased in CTDNEP1-depleted metaphase cells compared to control cells (data not shown). I found that the pole-pole distance of mitotic spindles in CTDNEP1-depleted metaphase cells was increased compared to the spindle lengths in control cells (Figure 4.10A, right).

Discussion

These data show that CTDNEP1 is required for mitotic error correction and proper chromosome segregation. We show that kinetochore attachment errors that are sensed by the spindle assembly checkpoint are not greatly increased in

CTDNEP1^{KO} cells. CTDNEP1-deleted cells are greatly sensitized to merotelic kinetochore attachment errors that are brought about by transient spindle disassembly, and this sensitization is due to loss of lipin 1 catalytic activity.

I previously described data showing that CTDNEP1 controls membrane abundance and clearing during mitosis. In CTDNEP1^{KO} cells, the cytoplasmic viscosity is increased, and prometaphase chromosome movements are decreased. Merotelic errors are resolved by detaching microtubules from the incorrect spindle pole, which involves rotation of the chromosome to keep microtubules from the same incorrect spindle pole from reattaching (Cimini, 2003). Thus, dampened chromosome movements in CTDNEP1^{KO} cells could contribute to reduced mitotic error correction.

It is not clear why metaphase spindles appear longer in CTDNEP1-depleted cells. A previous computational modeling study has shown that an elastic, deformable membrane around the spindle can assist with focusing minus ends of microtubules by forming pockets for filaments to gather, promoting longer spindle length (Poirier et al., 2010). Future studies can determine if expanded membranes are more elastic (more able to retain their shape) in CTDNEP1^{KO} cells and whether this might contribute to spindle microtubule focusing. Alternatively, a membranous spindle matrix has been proposed to surround the mitotic spindle and concentrate components of the spindle (Schweizer et al., 2014, 2015). I previously showed that CTDNEP1-depleted mitotic cells have a greater occupancy by ER membranes, with less room for chromosomes to occupy (Figure 3.4B). The expanded membranes and increased cytoplasmic

viscosity in the region where membranes are present in mitotic CTDNEP1^{KO} cells could lead to higher concentration of spindle components that allows spindles to grow longer. Future studies can confirm these results and test these hypotheses to determine how lipid synthesis regulation by CTDNEP1 might control mitotic spindle length.

Another remaining question is to what extent mitotic errors that are not related to merotelic attachments could be impacted by CTDNEP1 depletion. For example, the possibility of missegregation of chromosome fragments in CTDNEP1-depleted cells still needs to be ruled out. In nocodazole washout, transient spindle multipolarity is more common, and this leads to more merotelic attachments. Longer spindles in CTDNEP1-depleted cells, slower chromosome movement, and the peripheral localization of lagging chromosomes and tubulin in CTDNEP1^{KO} cells during telophase after nocodazole washout hint that spindle dynamics are altered with loss of CTDNEP1, while persistence of merotelic attachments could result from this. Future studies can determine if spindle architecture is challenged by the presence of excess membranes in mitosis and what additional mechanisms can contribute to formation of micronuclei.

These data show that CTDNEP1 promotes proper chromosome segregation by permitting merotelic attachment correction. What remains to be seen is how regulation of lipid synthesis by CTDNEP1 plays a role in regulating mitotic error correction.

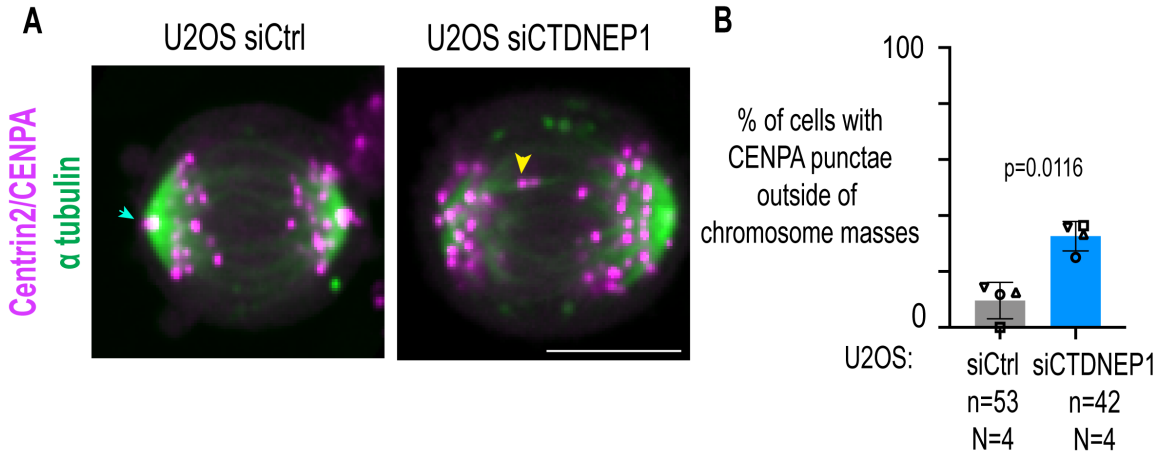

Figure 4.1 CTDNEP1-depleted cells have a higher incidence of lagging chromosomes

A) Spinning disk confocal images of Centrin2/CENPA/α tubulin fluorescence signal in stably-expressing live cells treated with indicated siRNAs. Scale bar, 10 μm. B) Quantification of incidence of lagging CENPA punctae in cells in indicated conditions. Means ± SDs shown. n = number of cells, N = number of experimental repeats. P value, Fisher's exact test of total incidences.

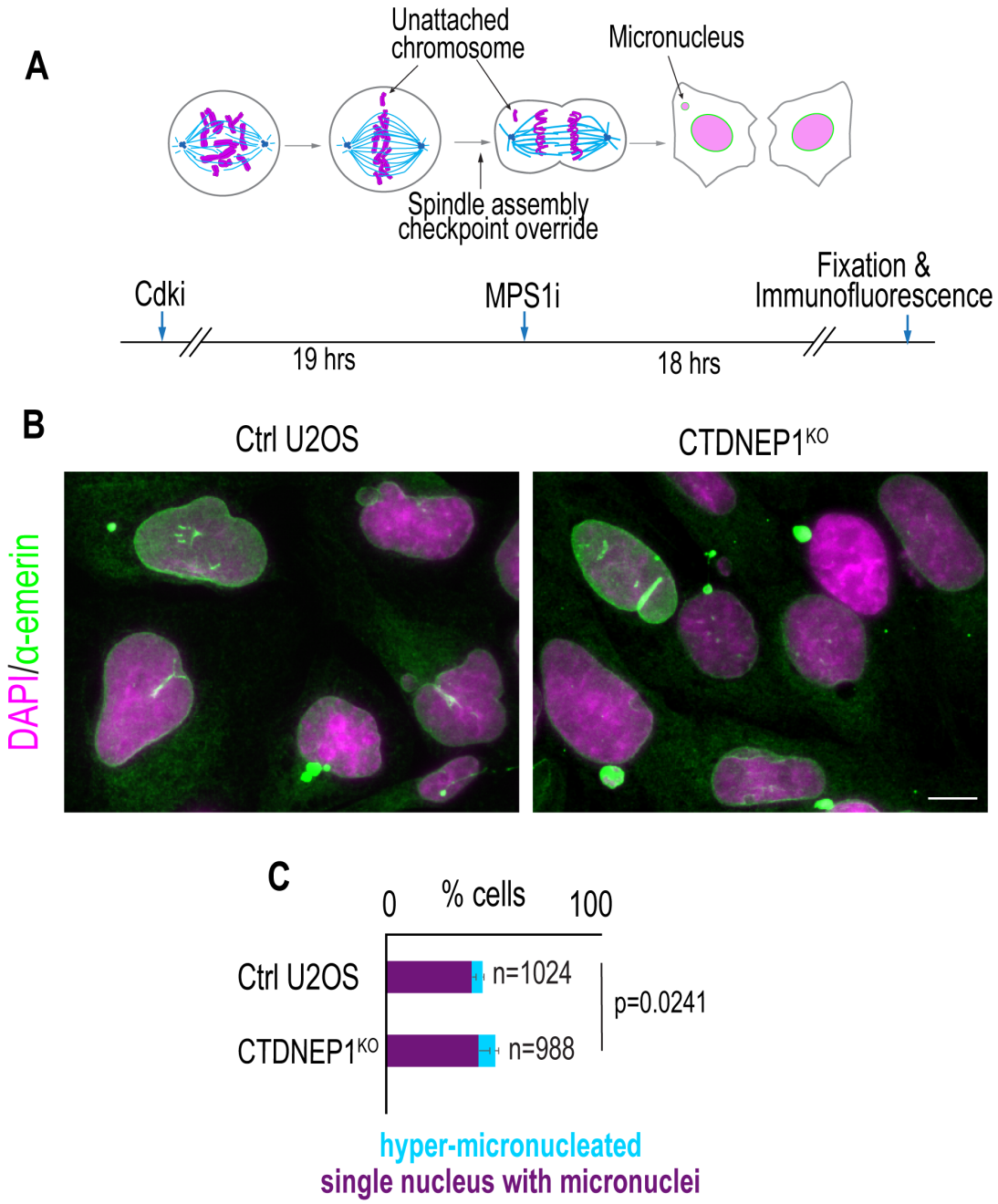

Figure 4.2 Bypassing the spindle assembly checkpoint in CTDNEP1^{KO} cells does not highly increase formation of micronuclei compared to control cells

A) Schematic of generating micronuclei using synchronization with RO-3306 (Cdki) and spindle assembly checkpoint bypass with NMS-P719 (MPS1i). DNA is pink, mitotic spindle is in blue, and nuclear envelope is in green. B) Confocal images of emerin and DAPI/Hoechst staining in fixed cells treated as in (A). Scale bars, 10 μm. C) Quantification of incidence of indicated phenotypes in cells treated as shown. n = number of cells, N = 3 experimental repeats. Means + SDs shown. P value, Chi squared test of total incidences.

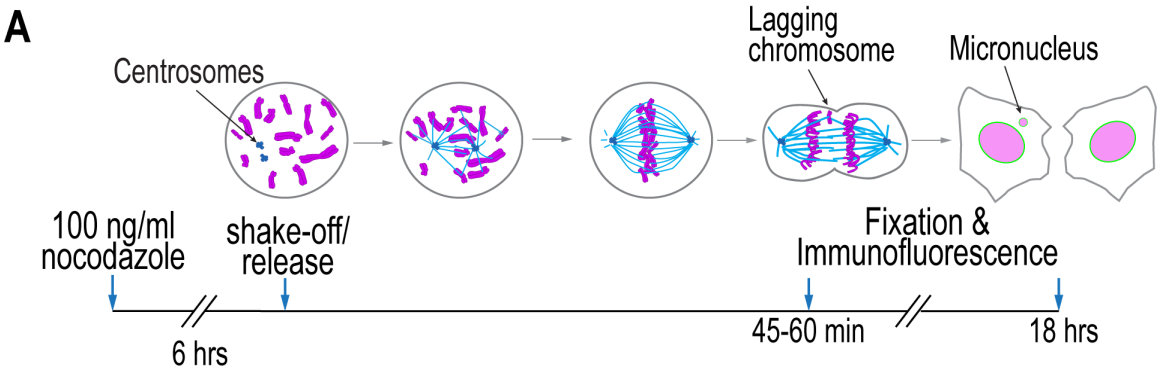

Figure 4.3 Using recovery from nocodazole treatment to assess sensitivity to acute spindle depolymerization for formation of micronuclei

A) Schematic of generating micronuclei using transient spindle disassembly with nocodazole. DNA is pink, mitotic spindle is in blue, and nuclear envelope is in green.

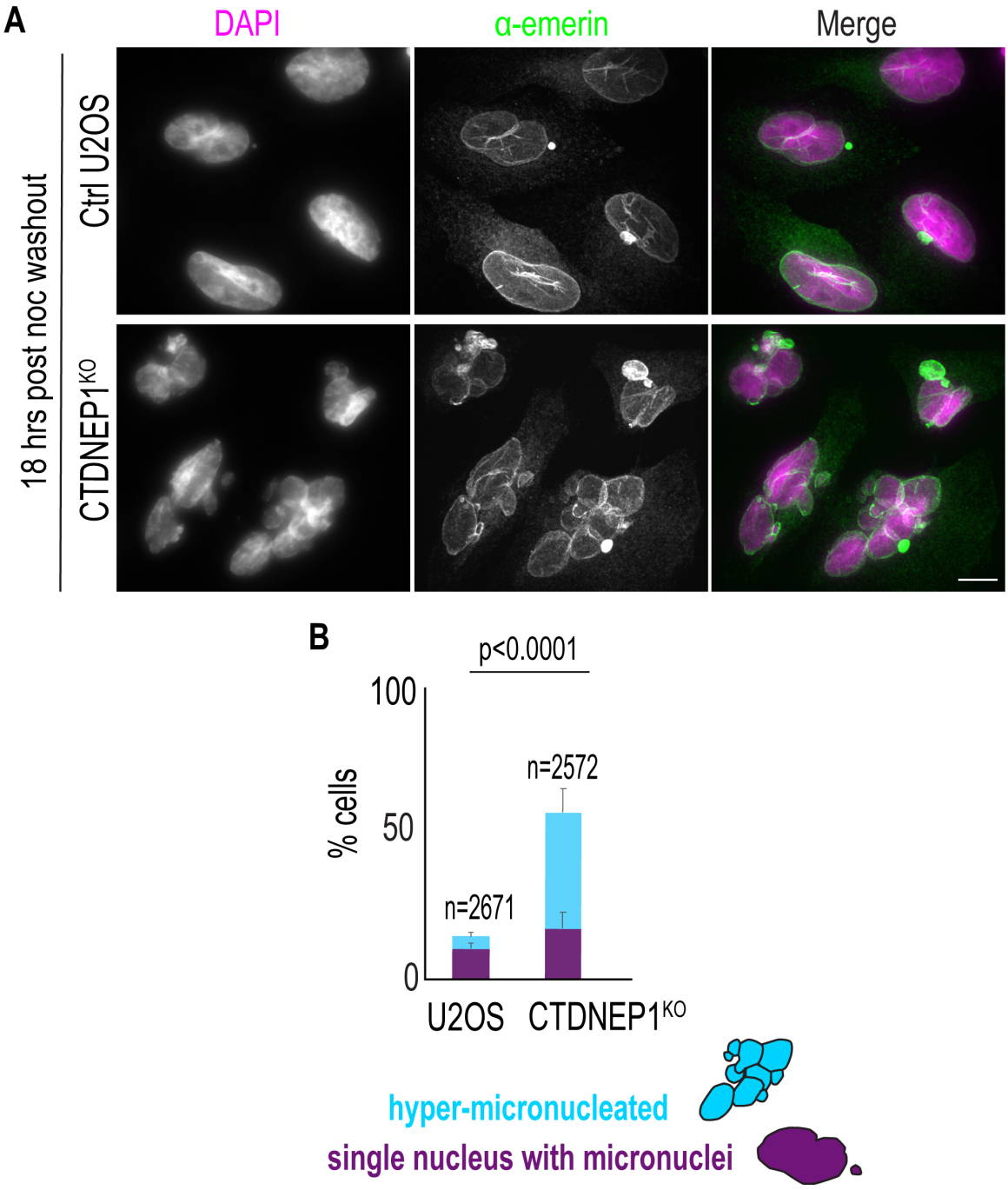

Figure 4.4 Recovery from transient spindle disassembly leads to abnormal hyper-micronucleation in CTDNEP1^{KO} U2OS cells

A) Epifluorescence (DAPI/Hoechst) and confocal (emerin) images of immunostained cells treated as in Figure 4.3A. Scale bar 10 μm. B) Quantification of incidence of indicated phenotypes in cells treated as shown. n = number of cells, N = 3 experimental repeats. Means + SDs shown. P value, Chi squared test of total incidences.

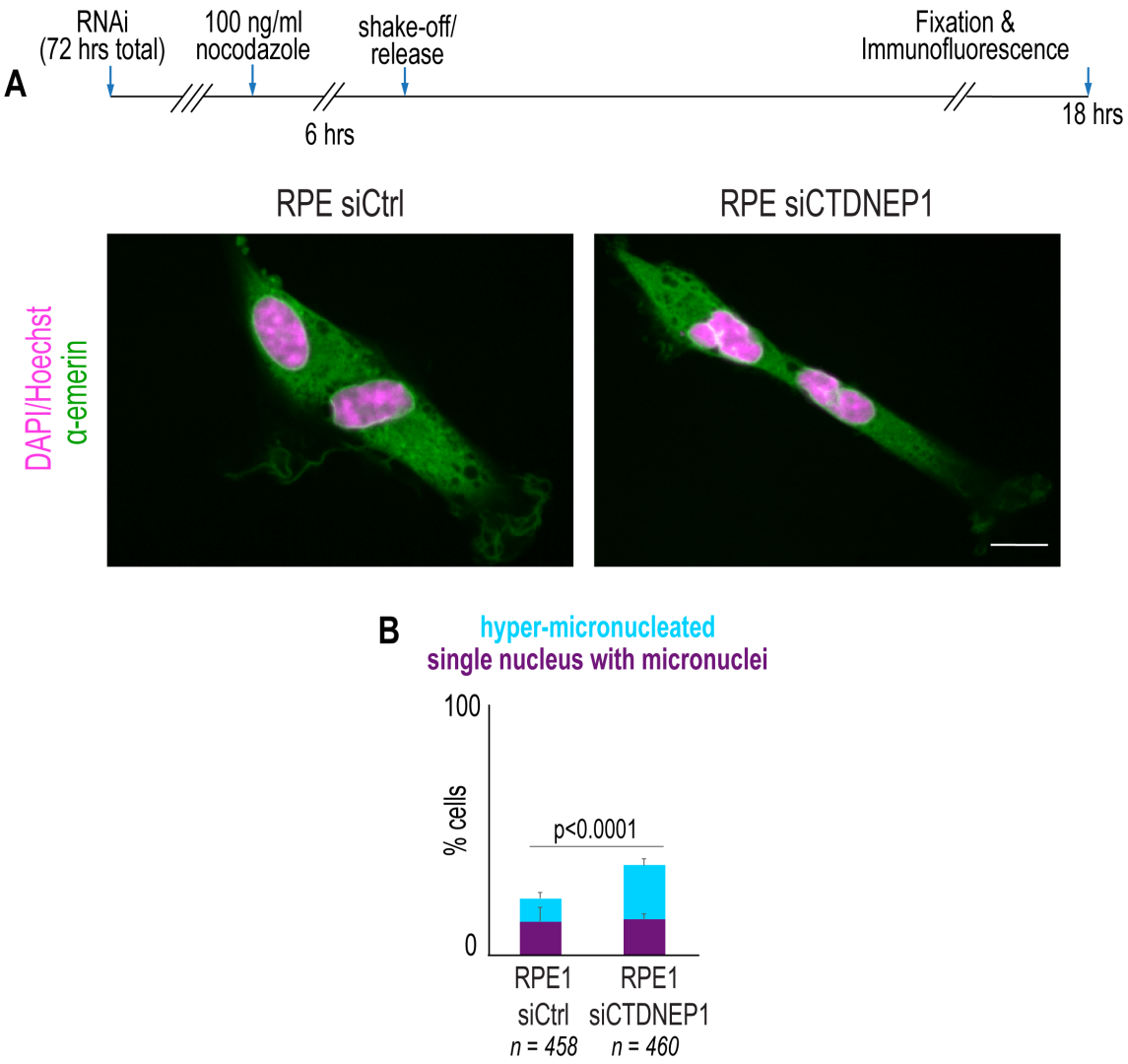

Figure 4.5 Recovery from transient spindle disassembly leads to abnormal hyper-micronucleation in CTDNEP1-depleted RPE-1 cells

A) Schematic of combined nocodazole washout and RNAi; epifluorescence (DAPI/Hoechst) and confocal (emerin) images of immunostained cells treated as shown in the schematic. Scale bar 10 μm. B) Quantification of incidence of indicated phenotypes in cells treated as shown. n = number of cells, N = 3 experimental repeats. Means + SDs shown. P value, Chi squared test of total incidences.

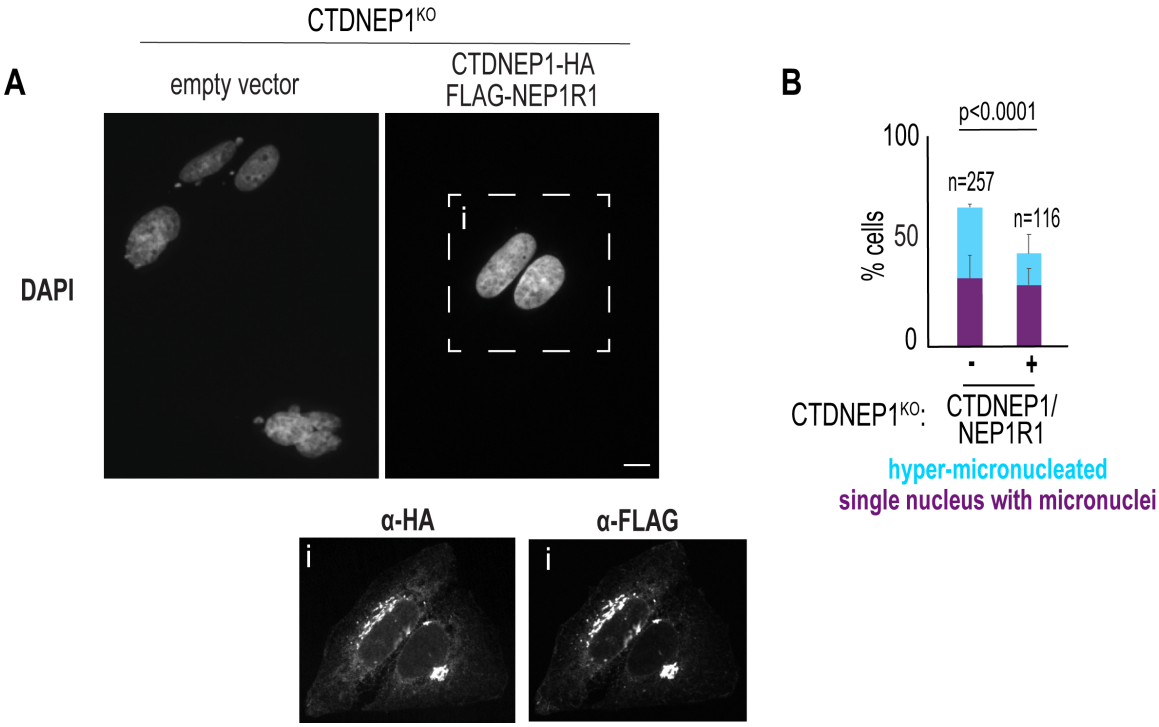

Figure 4.6 Overexpression of CTDNEP1/NEP1R1 suppresses hyper-micronucleation in CTDNEP1^{KO} cells upon recovery from transient spindle disassembly

A) Epifluorescence (DAPI/Hoechst) and confocal (FLAG, HA) images of immunostained cells transfected with indicated vectors and subject to nocodazole washout for 18 hrs as in Figure 4.3A. Scale bar 10 μm. B) Quantification of incidence of indicated phenotypes in cells treated as shown. n = number of cells, N = 3 experimental repeats. Means + SDs shown. P value, Chi squared test of total incidences.

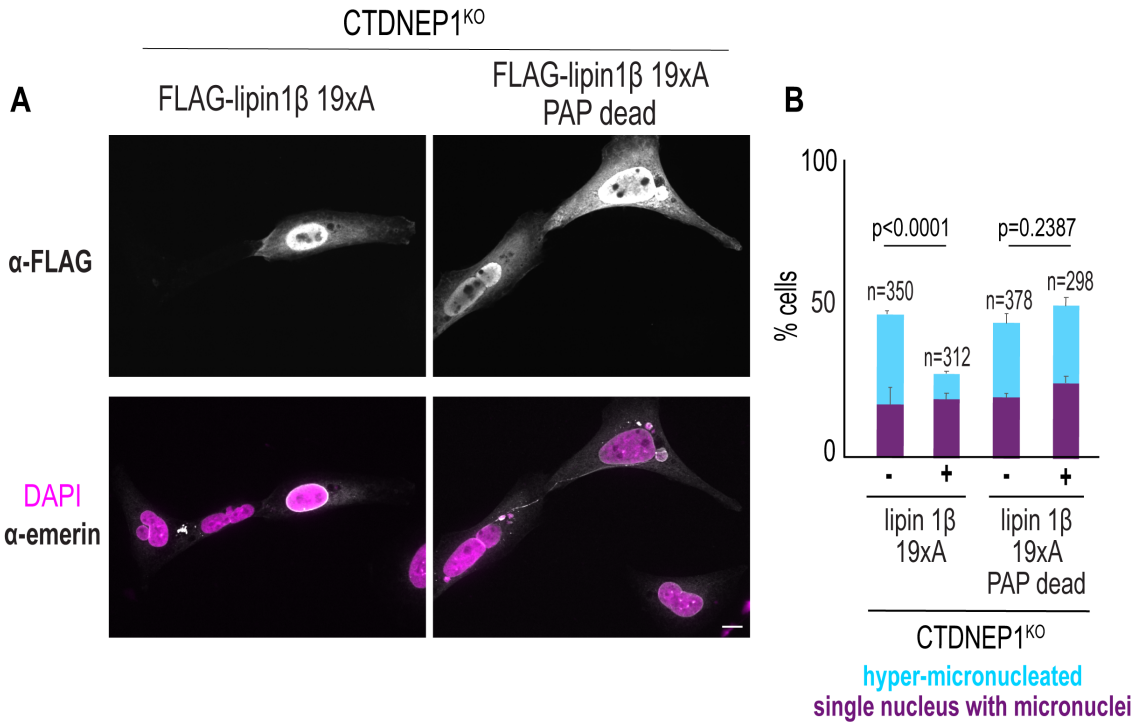

Figure 4.7 Overexpression of catalytically active lipin 1 suppresses hyper-micronucleation in CTDNEP1^{KO} cells upon recovery from transient spindle disassembly

A) Epifluorescence (DAPI/Hoechst) and confocal (FLAG, emerin) images of immunostained cells transfected with indicated vectors and subject to nocodazole washout for 18 hrs as in Figure 4.3. Scale bar 10 μm. 19 S/T to A refers to 19 serine/threonine sites mutated to dephospho-mimic alanine residues. PAP dead refers to phosphatase dead lipin 1. B) Quantification of incidence of indicated phenotypes in cells treated as shown. "-" refers to non-construct-expressing, and "+" refers to construct-expressing cells in the same experiment. n = number of cells, N = 3 experimental repeats. Means + SDs shown. P values, Chi squared tests of total incidences.

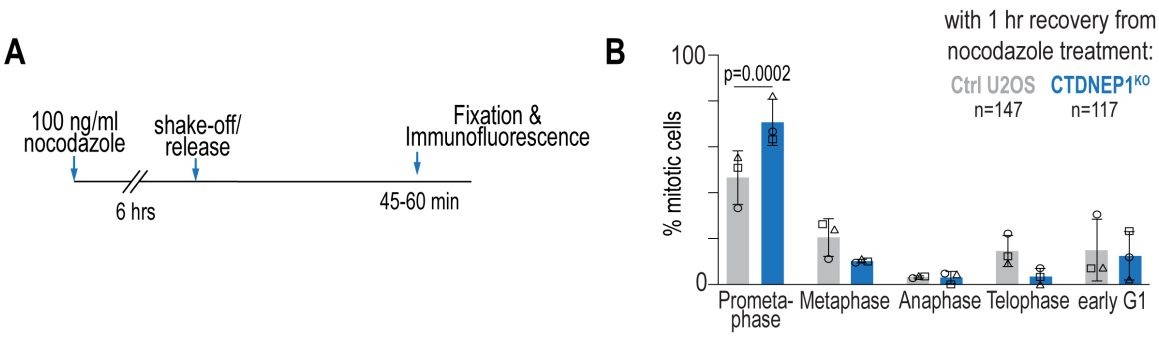

Figure 4.8 CTDNEP1^{KO} cells have a higher incidence of prometaphase cells upon recovery from transient spindle disassembly

A) Schematic for transient spindle disassembly with washout from acute nocodazole treatment. B) Plot of quantification of percent of mitotic cells in each stage of mitosis in control and CTDNEP1^{KO} U2OS cells treated as shown. Means ± SDs shown. n = number of cells, N = 3 experimental repeats. P value, Fisher's exact test of total incidences of prometaphase cells.

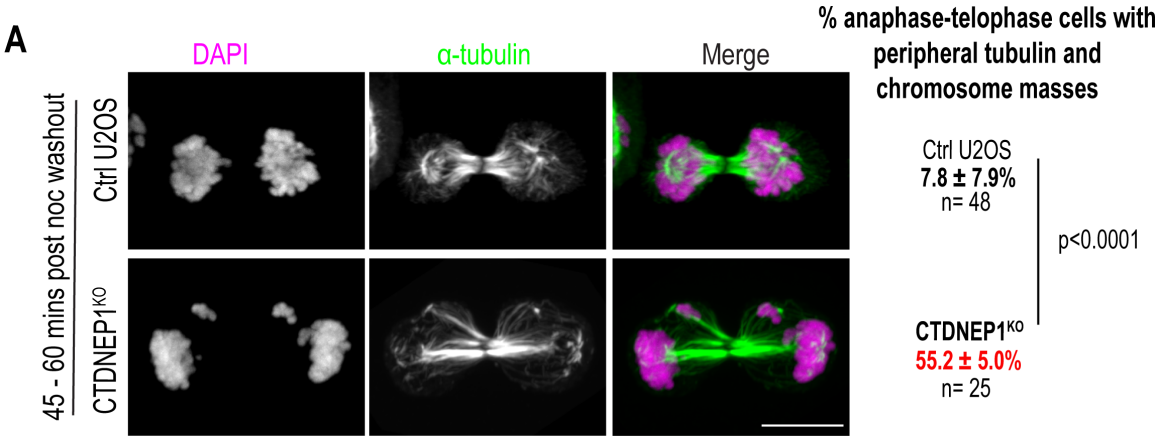

Figure 4.9 Anaphase and telophase CTDNEP1^{KO} cells recovering from transient spindle disassembly have more frequent chromosome masses and tubulin apart from the main nuclei and spindle

A) Spinning disk confocal images of DAPI/Hoechst and tubulin-stained telophase cells subject to nocodazole washout for 45-60 min as in Figure 4.3. Cells were treated with Ca^{2+}-buffer to depolymerize non-kinetochore microtubules just before fixation. Quantification of indicated phenotype shown. n = number of cells from N = 3 experimental repeats. Means ± SDs shown. P value, Fisher's exact test of total incidences.

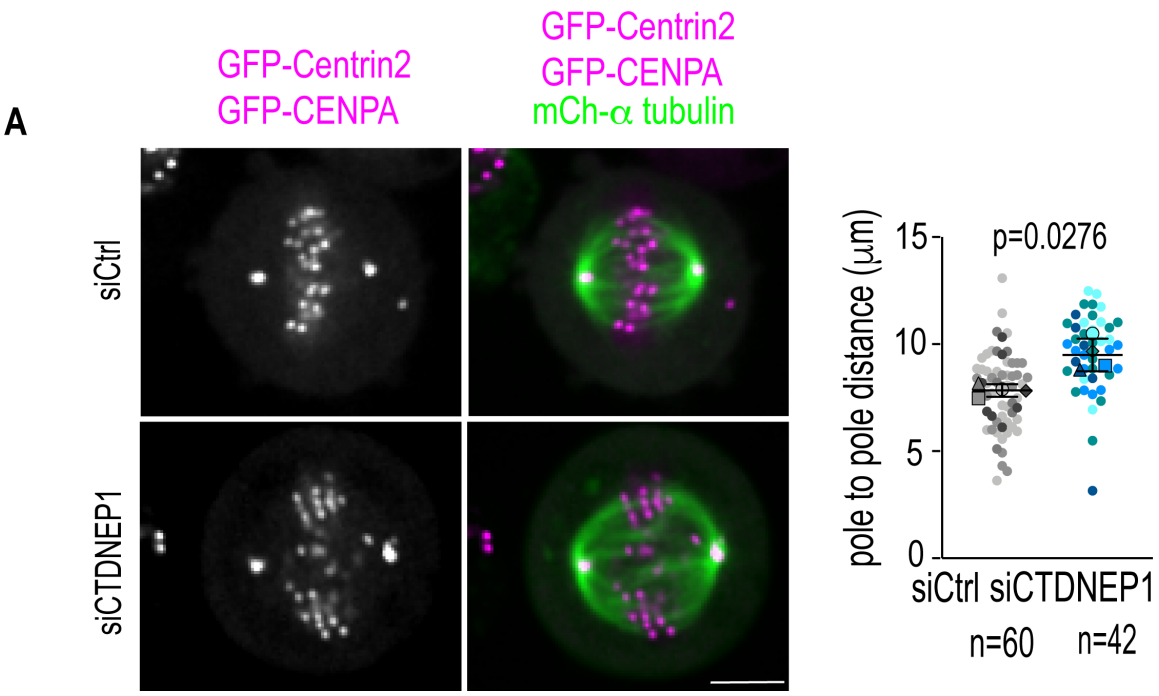

Figure 4.10 Longer spindle lengths in CTDNEP1-depleted U2OS prometaphase-metaphase cells

A) Confocal images of Centrin2, CENPA, and α tubulin signal in metaphase U2OS cells treated with the indicated siRNAs and subject to mitotic shakeoff. Scale bar, 5 μm. B) Plot of spindle pole-pole distance in cells as in (A). n = number of cells. N = 4 experimental repeats. Individual data points and means ± SDs shown. P value, paired t test of replicate means.

Chapter 5: A CTDNEP1-lipin 1 regulatory network controls fatty acid synthesis to limit ER membrane biogenesis, nuclear morphology defects, and formation of micronuclei

Some of this work is included and/or modified from the manuscript:

Holly Merta[*], Jake W. Carrasquillo Rodríguez[*], Maya I. Anjur-Dietrich, Mitchell E. Granade, Tevis Vitale, Thurl E. Harris, Dan Needleman, Shirin Bahmanyar. A CTDNEP1-lipin 1-mTOR regulatory network restricts ER membrane biogenesis to Enable Chromosome Motions Necessary for Mitotic Fidelity. *bioRxiv* (2021). doi: https://doi.org/10.1101/2021.03.02.433553

[*] Co-first authors

Introduction

We have shown that CTDNEP1 limits ER membrane biogenesis and controls membrane dynamics in mitosis. CTDNEP1 additionally limits cytoplasmic viscosity, allows prometaphase chromosome movements, and promotes mitotic error correction to limit formation of micronuclei. Major questions that remain are the mechanism by which CTDNEP1 limits ER membrane synthesis, as well as the connection between CTDNEP1's control of lipid synthesis and regulation of chromosome segregation.

One possibility for how CTDNEP1 can control ER membrane biogenesis is through regulation of sterol regulatory element binding protein (SREBP)-dependent transcription, mediated through lipin. The primary mechanism of controlling fatty acid synthesis in human cells is through SREBP-dependent transcription (Figure 5.1). SREBPs change cellular localization from ER membrane-bound to soluble and nuclear in response to changes in ER membrane cholesterol levels (Inoue and Sato, 2013) (Figure 5.1A). At normal ER membrane cholesterol levels, SREBP cleavage-activating protein (SCAP) remains bound to cholesterol and Insulin-sensitive gene (Insig) (Inoue and Sato, 2013). When cholesterol levels in the ER are reduced, SCAP binds to SREBP via its basic helix-loop-helix (bHLH) domain and causes it to be taken up for anterograde trafficking to the Golgi through COPII proteins Sec23/24 and Sar1 (Inoue and Sato, 2013). In the Golgi, SREBP is cleaved by proteases S1P and S2P to free the bHLH domain to enter the nucleus and activate SREBP-dependent transcription (Inoue and Sato, 2013). SREBP1 target genes control

fatty acid synthesis (Figure 5.1B, above), while SREBP2 target genes control steps in cholesterol synthesis (Figure 5.1B, below).

Lipin has shown to control fatty acid pools on multiple fronts, including synthesis (regulated by mTOR and mediated through SREBP transcriptional regulation) and breakdown (mediated through PPARα transcriptional regulation) (Finck et al., 2006; Peterson et al., 2011). Lipin has repeatedly been shown to be phosphoregulated with insulin and nutrient stimulation, demonstrating that it responds to metabolic inputs (Harris et al., 2007; Huffman et al., 2002; Peterson et al., 2011). mTOR (specifically, mTORC1) has been identified as the insulin and nutrient-sensitive kinase complex that phosphorylates lipin 1 (Harris et al., 2007; Peterson et al., 2011). In response to serum and glucose/amino acid stimulation, lipin 1 is phosphorylated by mTOR on phosphosites known to be regulated upon insulin stimulation (Peterson et al., 2011).

Lipin has shown to control SREBP-dependent gene expression. Inhibition of mTOR reduces SREBP target gene expression, including SREBP1c target genes fatty acid synthase (FASN), acetyl-CoA carboxylase alpha (ACACA), and stearoyl-CoA decarboxylase (SCD), as well as SREBP2 targets 3-hydroxy-3-methylglutaryl-coenzyme A reductase (HMGCR) and farnesyl diphosphate synthase (FDPS) (Peterson et al., 2011). Lipin 1-deficient mice do not have elevated SREBP target gene expression in a basal state, but SREBP target gene expression is unresponsive to mTOR inhibition (Peterson et al., 2011). On the other hand, expression of dephospho-mimic lipin 1 is sufficient to restore SREBP response to mTOR inhibition in lipin 1-deficient mouse cells (Peterson et al.,

2011). These data indicate that lipin 1 represses SREBP-dependent gene transcription when dephosphorylated. While the mechanism of this repression is not understood, it is known that phosphorylated lipin is retained in the cytoplasm and is degraded (Shimizu et al., 2017). It remains to be seen if hyper-phosphorylated lipin increases SREBP-dependent gene transcription through derepression to positively regulate fatty acid synthesis. In CTDNEP1-depleted cells, derepression of SREBPs by hyperphosphorylated, low-abundance lipin could lead to increased fatty acid synthesis to feed into membrane biogenesis.

Here, I show that increased fatty acid synthesis and flux of lipid synthesis into membrane biogenesis increase ER membrane abundance in CTDNEP1-depleted cells. I report that CTDNEP1-depleted cells have elevated levels of membrane glycerophospholipids. I show that inhibition of a SREBP1 target gene to shut off fatty acid synthesis partially suppresses ER membrane expansion in CTDNEP1^{KO} cells. I additionally show that supplementation with free fatty acids restores ER membrane expansion in CTDNEP1^{KO} cells in the absence of fatty acid synthesis, showing that flux into ER lipid synthesis is also increased. I explore the contributions of SREBPs 1 and 2 and SREBP1 target gene SCD to ER membrane expansion in CTDNEP1^{KO} cells to reveal a partial role for SREBPs in mediating fatty acid synthesis to control ER membrane abundance through lipin and CTDNEP1. I show that inhibition of fatty acid synthesis suppresses formation of micronuclei in CTDNEP1^{KO} cells. These findings reveal multiple mechanisms for CTDNEP1 control of ER membrane abundance via lipid

synthesis and flux and connect control of fatty acid synthesis to regulation of mitotic error correction to limit formation of micronuclei.

Results

Lipidomic analysis of total cellular lipids in CTDNEP1^{KO} cells

Depletion of CNEP-1 in *C. elegans* and PAH1 (lipin) in *A. thaliana* cells leads to increased cellular PA/PI and PC, respectively (Bahmanyar et al., 2014; Craddock et al., 2015). CTDNEP1 has known roles in limiting glycerolipid synthesis in all organisms tested (Bahmanyar et al., 2014; Craddock et al., 2015; Siniossoglou et al., 1998; Tange et al., 2002). We sought to determine the lipid profiles in CTDNEP1-depleted human cells by mass spectrometry lipidomic analysis. We submitted samples of U2OS cells to Lipotype GmbH, who performed lipid extraction, sample infusion, mass spectrometry and/or tandem mass spectrometry analysis, and lipid identification using Lipotype Xplorer. Data were reported to us as pmols of lipid species per sample (with sample volume utilized), with species reported in species class-combined chain length-combined desaturation format (e.g. PC with 18:1 and 16:0 side chains reported as PC (34:1). Using this information, we were able to extrapolate molar percentage of lipid classes and, with sample protein concentration, pmols lipid class per mg protein (Figure 5.2, Figure 5.3).

We first examined molar percentage of lipid classes in control and CTDNEP1^{KO} U2OS cells to determine if lipid flux favored formation of certain species over others (Figure 5.2A). From this analysis, in CTDNEP1^{KO} cells, PC appeared to be increased in its contribution to the lipid profile, and TAG was also

increased, while cholesterol esters (CE) and sphingomyelin (SM) were decreased (Figure 5.2A). These results indicated to us that overall the lipidome was not shifted toward PI/PA accumulation in CTDNEP1-depleted cells as in *C. elegans* and brought up the possibility that TAG may be increased in addition to membrane glycerolipids. To confirm these results, I resubmitted a new set of samples of control and CTDNEP1^{KO} cells (Figure 5.2B, "-"), this time also with a sample of CTDNEP1^{KO} cells stably overexpressing wild-type CTDNEP1-HA (Figure 5.2B, "WT") to determine what lipidome changes are rescued by overexpressing CTDNEP1. PC was modestly increased in representation in CTDNEP1^{KO} cells compared to control cells and the rescue cell line, while other glycerophospholipid species appeared unchanged in representation (Figure 5.2B). Triglycerides were no longer lower in control cells compared to CTDNEP1^{KO} cells with analysis of the second submission (Figure 5.2B). CE and SM molar percentages remained lower in CTDNEP1^{KO} cells relative to control cells, and these were partially rescued in CTDNEP1^{KO} cells stably expressing CTDNEP1-HA (Figure 5.2B). These data indicate that representation of lipid classes is overall similar in CTDNEP1^{KO} cells relative to control except for PC and lipids that are not synthesized in the ER.

To determine if absolute levels of lipid classes are elevated in CTDNEP1-depleted cells, I normalized pmol of lipid classes to mg of protein in samples (Figure 5.3). This analysis revealed that PC levels (and, to a lesser extent, PE levels) are higher in CTDNEP1^{KO} cells, and this is rescued by stable expression of CTDNEP1 (Figure 5.3A). Cholesterol ester and SM levels were lower in

CTDNEP1^{KO} cells compared to control cells, and CE levels were rescued by CTDNEP1 expression, whereas lower sphingomyelin levels were not rescued (Figure 5.3A). These data show that loss of CTDNEP1 leads to increased cellular PC/PE and decreased cholesterol esters. These data point to a conserved mechanism for increased PC synthesis in human cells with loss of CTDNEP1 activation of lipin. The similar molar percentage profiles of CTDNEP1^{KO} and control cells and elevated pmol of lipid classes point to control of fatty acid synthesis as a possible mechanism for CTDNEP1 regulation of ER membrane biogenesis.

Inhibition of fatty acid synthesis reduces ER membranes in control cell and suppresses ER expansion in CTDNEP1^{KO} cells

Acetate incorporation into lipids is increased in CTDNEP1^{KO} cells, indicating that fatty acid synthesis may be increased with loss of CTDNEP1 (Merta et al., 2021) (finding by M.E. Granade, supervised by T. Harris). I targeted fatty acid synthesis to determine if increased fatty acid synthesis feeds into ER membrane biogenesis in CTDNEP1-depleted cells (Figure 5.4). I used a small molecule inhibitor of acetyl coenzyme-A carboxylase (ACAC) forms α and β, 5-(tetradecyloxy)-2-furancarboxylic acid (TOFA) (IC_{50} 4.5-5.0 μg/ml, (Wang et al., 2009)) (Figure 5.4). ACAC catalyzes the conversion of acetyl-CoA into malonyl-CoA in the rate-limiting and committing step for fixation of cellular acetate into fatty acids in mammalian cells (Tong, 2005). M. E. Granade found that TOFA reduced acetate incorporation into lipids in control U2OS and CTDNEP1^{KO} U2OS cells, reflecting reduced acetyl-CoA fixation into lipids (Merta et al., 2021).

Inhibiting ACAC limits malonyl-CoA formation, which limits fatty acid synthesis and incorporation into PA, which should decrease ER membrane lipid synthesis (Figure 5.4). Supplementation with exogenous fatty acids would bypass ACAC, serving as a control to help determine if changes in ER membranes are due to altered flux of fatty acid synthesis into ER membrane biogenesis (Figure 5.4).

Treatment of U2OS cells with 10 μM TOFA for 24 hours severely reduces ER membranes (Figure 5.5A, above). In contrast to DMSO-treated cells, which have sheet-like perinuclear ER membranes and peripheral reticular ER, TOFA-treated U2OS cells have thin ER tubules with wide spaces in between or completely lack a peripheral ER network (Figure 5.5A, red arrows). The remaining ER in these cells is concentrated around the nucleus and appears thinner than perinuclear ER in control cells (Figure 5.5A, above). TOFA also suppresses ER membrane expansion in CTDNEP1^{KO} cells (Figure 5.5A, below). The appearance of the ER in TOFA-treated CTDNEP1^{KO} cells more closely resembles control U2OS cells' ER than DMSO-treated CTDNEP1^{KO} cells or TOFA-treated U2OS cells (Figure 5.5A). A peripheral ER network is apparent in the majority of TOFA-treated CTDNEP1^{KO} cells (Figure 5.5A, blue arrows). These data show that fatty acid synthesis feeds into ER membrane synthesis to control ER membrane abundance, and that fatty acid synthesis may be increased in CTDNEP1^{KO} cells.

To quantify the extent to which ER membranes were reduced in control and CTDNEP1^{KO} cells, I measured the percent area of cytoplasm taken up by ER membranes as in Figure 2.11 and compared it to previously determined phenotypic categorization of TOFA-treated control U2OS and CTDNEP1^{KO} cells

(Figure 5.6A). I found that the percent area of ER of cells categorized as having "normal ER" is similar in U2OS cells and CTDNEP1^{KO} cells treated with TOFA (Figure 5.6A). CTDNEP1^{KO} cells categorized as having "reduced" ER have percent area of ER that falls within the range of areas of cells categorized as having "reduced" ER, but in line with qualitative findings, the extent of reduced ER could be much more severe in control U2OS cells (Figure 5.6A). These findings reflect that the phenotypic categorization is accurate to the abundance of ER membranes in TOFA-treated cells.

I next sought to determine the time scales at which ACAC inhibition could cause ER membranes to be reduced in both control and CTDNEP1^{KO} cells (Figure 5.7). I treated cells with TOFA for 5 hours, 24 hours, and 48 hours (Figure 5.7A). Treatment with TOFA for 72 hours showed no effect, reflecting that the drug may be metabolized or degraded around that time (data not shown). After 5 hours of TOFA treatment, 16.0 ± 10.3 % of U2OS cells have reduced ER (Figures 5.7A-5.7B). In contrast, after 5 hours, 8.9 ± 1.9 % of DMSO-treated and 77.4 ± 4.5 % of TOFA-treated CTDNEP1^{KO} cells show suppression of ER membrane expansion to a "normal"-looking ER (Figures 5.7A, 5.7C). This finding suggests that the ER membranes of CTDNEP1^{KO} cells respond faster to TOFA treatment than unmodified U2OS cells – either fatty acid synthesis is upregulated to the extent that ACAC inhibition causes a more pronounced effect faster, or fatty acid breakdown could be faster in CTDNEP1-depleted cells. In both unmodified U2OS cells and CTDNEP1^{KO} U2OS cells, the maximum effect of TOFA treatment is observed after 24 hours (Figures 5.7A-5.7C).

Fatty acid supplementation restores ER appearance in cells with fatty acid synthesis inhibition

To determine if reduction of ER membranes in TOFA-treated cells was indeed caused by lack of fatty acid incorporation into membrane lipids, I treated cells with TOFA with or without exogenous fatty acid supplementation (Figure 5.8A). To treat cells with exogenous fatty acids, I used a total concentration of 100 μM and a makeup of 1:2:1 palmitic:oleic:linoleic acid, which were conjugated to 0.5% fatty acid-free bovine serum albumin (BSA) to facilitate solubilization of fatty acids into the media. The concentration and makeup of fatty acids more closely resembles physiological extracellular conditions as opposed to mixes containing only palmitate or oleate (Watt et al., 2012).

Treatment of control U2OS cells with TOFA and exogenous fatty acids restores the appearance of the peripheral ER compared to cells treated with TOFA and fatty acid-free BSA (Figures 5.8A-B). Similarly, supplementation with exogenous fatty acids restores the expanded appearance of the ER in CTDNEP1^{KO} cells treated with TOFA (Figures 5.8A-B). Treating control or CTDNEP1^{KO} cells with exogenous fatty acids in the absence of TOFA does not change ER appearance (Figure 5.9A), so there appears to be a mechanism in place to keep exogenous fatty acids from being incorporated into excess membranes that appears to not be as active in CTDNEP1^{KO} cells. Together, these data support the conclusion that CTDNEP1^{KO} cells have increased fatty acid synthesis and flux of fatty acids into ER lipid synthesis, and this feeds into ER membrane biogenesis. Thus, CTDNEP1 limits fatty acid synthesis and

incorporation of fatty acids into membranes to limit the abundance of ER membranes.

Depletion of SREBPs and SREBP target genes to assess contribution to SREBP-controlled fatty acid synthesis to ER membrane expansion

Since it is known that SREBP-mediated transcription is regulated by lipin depending on its phosphorylation state, we next sought to determine the contribution of SREBP-dependent transcription on ER membrane biogenesis in CTDNEP1^{KO} cells. Jake W. Carrasquillo Rodríguez found that mRNAs of SREBP1 target genes ACACA and SCD are upregulated ~1.3-fold and ~1.5-fold, respectively, in CTDNEP1^{KO} cells compared to control cells (Merta et al., 2021). The SREBP1 targets FASN and SREBP2 targets FDPS and HMGCR are not upregulated (Merta et al., 2021). Although modest, the upregulation of these SREBP targets could explain the apparent increase in fatty acid synthesis in CTDNEP1^{KO} cells.

Since ACACA and SCD are SREBP1 target genes, I first sought to deplete SREBP1 by RNAi in control U2OS and CTDNEP1^{KO} cells to determine if SREBP1 depletion impacts ER morphology in unmodified U2OS cells or suppresses ER membrane expansion in CTDNEP1^{KO} cells (Figures 5.10A-B). U2OS cells did not appear to have altered ER morphology with SREBP1 depletion (Figure 5.10B). Some CTDNEP1^{KO} cells appeared to have suppression of ER membrane expansion such that the peripheral ER network was visible in SREBP1 siRNA-treated cells (Figure 5.10B). SREBP1 depletion reduces the incidence of ER membrane expansion in CTDNEP1^{KO} cells from 98.2 ± 1.6 % of

cells to 93.4 ± 1.6 % (Figure 5.10C). SREBP1-dependent transcription appears to at least partially contribute to fatty acid synthesis that feeds into ER membrane expansion in CTDNEP1-depleted cells. Future experiments to determine if knockdown of SREBP1 decreases levels of nuclear SREBP1 and decreases SREBP1-dependent gene transcription will confirm these findings.

Studies in transgenic mice with deletion of either *Srebp1* or *Srebp2* show that Srebp1 and Srebp2 can compensate for each other to some extent (Horton et al., 2002; Vergnes et al., 2016). To determine if SREBP2 upregulation in SREBP1-depleted cells could be masking an effect of SREBP1 depletion on ER expansion in CTDNEP1^{KO} cells, I co-depleted SREBP1 and SREBP2 with RNAi (Figures 5.11A-B). Like with RNAi depletion of SREBP1 alone, some CTDNEP1^{KO} cells depleted of SREBP1/2 show suppression of ER membrane expansion and restoration of the reticular peripheral ER (Figure 5.11B). The incidence of the expanded ER phenotype in CTDNEP1^{KO} cells decreased from 99.7 ± 0.5 % to 96.2 ± 1.2 % with SREBP1/2 knockdown (Figure 5.11C). This reduction is of similar magnitude as the suppression of ER membrane expansion with depletion of SREBP1 alone, suggesting that cross-talk between SREBP1/2 does not limit suppression of ER membrane expansion in CTDNEP1^{KO} cells depleted of SREBP1. Together, these data support the conclusion that SREBP-mediated fatty acid synthesis gene transcription is at least partially responsible for increased fatty acid synthesis and ER membrane expansion in CTDNEP1^{KO} cells.

CTDNEP1^{KO} U2OS cells exhibit increased SCD expression relative to control U2OS cells and is the most upregulated SREBP target gene (Merta et al., 2021) (finding by Jake W. Carrasquillo Rodríguez). SCD catalyzes the desaturation of saturated fatty acyl-CoAs like palmitoyl- and stearoyl-CoA at the carbon 9 position to produce Δ9 destaurated fatty acyl-CoAs like palmitoleoyl-CoA and oleoyl-CoA. While this step is not rate-limiting or committing for fatty acid synthesis as a whole, it is the rate limiting step for synthesis of monounsaturated fatty acids that make up a large portion of side chains in cellular glycerolipids (ALJohani et al., 2017). Thus, upregulation of SCD specifically in CTDNEP1-depleted cells could lead to expansion of ER membranes through increased availability of monounsaturated fatty acids to feed into membrane lipid synthesis. I depleted SCD in control U2OS and CTDNEP1^{KO} U2OS cells with RNAi (Figure 5.12A-B). Knockdown of SCD reduced the incidence of the expanded ER phenotype from 88.9 ± 1.7 % of cells to 72.3 ± 4.1 % (Figures 5.12B-C). Thus, we conclude that expansion of ER membranes in CTDNEP1^{KO} is at least partially due to specific upregulation of SCD increasing synthesis of fatty acids for membrane biogenesis. I also observed bright punctae ~1 μm in diameter in the perinuclear ER of control and CTDNEP1^{KO} U2OS cells depleted of SCD (Figure 5.12B, 5.12D). In cells treated with high concentrations of palmitate, the rough ER appears distended, and this is thought to be caused by a combination of changes in membrane properties (membrane stiffening) as palmitate is incorporated into ER neutral lipids and increased ER stress in response to the membrane packing defects (Borradaile et al., 2006). Perhaps decreased SCD in

U2OS cells leads to punctae formation in rough ER because of decreased overall desaturation of fatty acids in membranes leading to packing defects. These data show that CTDNEP1 limits fatty acid synthesis and membrane biogenesis partly through limiting SCD activity to produce monounsaturated fatty acids for membranes.

Inhibition of fatty acid synthesis restores nuclear shape in CTDNEP1-depleted cells

It is not known if the role CTDNEP1 plays in limiting fatty acid synthesis mediates its conserved function for maintaining nuclear morphology. I suppressed fatty acid synthesis in CTDNEP1^{KO} cells with ACAC inhibition and found that nuclei appear more round and that nuclear solidity is increased (Figure 5.13A). The proportion of nuclei characterized as having low solidity is reduced from 20.9 ± 2.3 % in DMSO-treated CTDNEP1^{KO} cells to 2.5 ± 2.6 % in TOFA-treated cells (Figure 5.13B). In control U2OS cells, however, TOFA treatment does not significantly increase nuclear solidity (Figure 5.14A, 5.14B). This data supports the conclusion that nuclear shape is at its maximum solidity when CTDNEP1 is intact, such that limiting membrane lipid synthesis does not take away from the nucleus' ability to maintain its shape.

In CTDNEP1^{KO} cells, increased fatty acid synthesis and flux of existing fatty acids into membranes could result in more membranes feeding into the nuclear envelope, causing its morphology to take on a more lobed shape. Upon treatment with the ACAC inhibitor TOFA, decreased fatty acid synthesis could limit the fatty acid pool that is available to incorporate into the nuclear

membranes. To confirm that this is the case, I treated CTDNEP1^{KO} cells with TOFA or DMSO with or without 100 μM exogenous fatty acids (1:2:1 palmitic:oleic:linoleic acid) for 24 hours (Figure 5.14A). As before, TOFA treatment increases nuclear solidity in CTDNEP1^{KO} cells compared to untreated cells; in TOFA- and fatty acid-treated cells, however, nuclear solidity is not significantly changed, though the population values trend toward the solidity of untreated CTDNEP1^{KO} cells (Figure 5.14B). The incidence of nuclei with solidity < 1 SD from the control mean is significantly lower in cells treated with TOFA with exogenous fatty acids compared to cells treated with TOFA alone (Figure 5.14C). We interpret that this result could be a partial rescue by fatty acid treatment of the suppression of decreased nuclear solidity that occurs with ACAC inhibition in CTDNEP1^{KO} cells. This result is somewhat surprising given that fatty acid supplementation appears to restore ER membrane expansion in TOFA-treated CTDNEP1^{KO} cells (Figure 5.8). Together, these data show that CTDNEP1 limits fatty acid synthesis and ER membrane lipid synthesis to control nuclear shape.

Inhibition of fatty acid synthesis decreases formation of micronuclei in CTDNEP1-depleted cells

To determine if the role CTDNEP1 plays in limiting fatty acid synthesis controls formation of micronuclei, I quantified the incidence of micronuclei in CTDNEP1^{KO} cells treated with DMSO or TOFA (5.15A). I measured the doubling time of U2OS cells to be 20-22 hours (data not shown). To account for the time needed for a cell cycle to pass after limiting membrane synthesis, I treated CTDNEP1^{KO} cells with TOFA for 48 hours, a timeframe during which cells

continue to show suppression of ER membrane synthesis (Figure 5.7). After 48 hours of ACAC inhibition, the incidence of micronuclei was decreased (3.3 ± 1.4 % of CTDNEP1^{KO} cells treated with TOFA compared to 10.3 ± 2.3 % of cells treated with DMSO; Figure 5.15). Additionally, I sought to determine if CTDNEP1's role in limiting fatty acid synthesis and ER membrane biogenesis mediates its role in permitting mitotic error correction. I subjected TOFA-treated CTDNEP1^{KO} cells to nocodazole washout as shown (Figure 5.16A-5.16B). TOFA treatment reduced the incidence of hyper-micronucleated nuclei (20.1 ± 4.2 % of TOFA-treated CTDNEP1^{KO} cells compared to 38.8 ± 3.3% of DMSO-treated cells; Figure 5.16C). Together, these data support the conclusion that CTDNEP1's role in permitting mitotic error correct to limit formation of micronuclei occurs through its roles in limiting fatty acid synthesis and ER membrane biogenesis.

Discussion

Here, we have identified that CTDNEP1 and lipin 1 limit ER membrane biogenesis by limiting PC/PE formation and restricting fatty acid synthesis and flux of fatty acids into ER membrane lipids. We show that this control of membrane biogenesis by CTDNEP1 permits mitotic error correction to limit formation of micronuclei.

In *C. elegans* early embryos, ER sheet formation was found to be due to loss of LPIN-1 conversion of PA to DAG, resulting in a buildup of PA that then is synthesized into PI through the CDP-DAG pathway (Bahmanyar et al., 2014). Knockdown of CDP-DAG synthase, which catalyzes the conversion of PA to

CDP-DAG, or PI synthase, which catalyzes the conversion of CDP-DAG to PI, rescues abnormal nuclear shapes caused by depletion of CNEP-1 or LPIN-1 (Bahmanyar et al., 2014). Depletion of CDP-DAG synthase also restores PI and PA abundance and ER sheet formation in CNEP-1-depleted embryos (Bahmanyar et al., 2014). Using mass spectrometry lipidomic analysis, we have found that PI and PA levels are not increased in U2OS CTDNEP1^{KO} cells and that PE and PC levels are increased. This suggests that loss of lipin's PA to DAG conversion alone is not sufficient to explain ER membrane expansion with loss of CTDNEP1 in human cells. We have found that transcriptional control of fatty acid synthesis is altered in CTDNEP1^{KO} U2OS cells. Since *C. elegans* early embryos are transcriptionally quiescent, CNEP-1 deletion does not lead to upregulated fatty acid synthesis as in human cells.

Our data support a mechanism of CTDNEP1 limiting ER membrane biogenesis through multiple modes of regulation (Figure 5.17A-B). First, expression of SREBP1 target genes ACACA and SCD, which catalyze rate-limiting steps of total fatty acid and monounsaturated fatty acid synthesis, is limited by CTDNEP1 to limit fatty acid synthesis (Figure 5.17B, "1."). Addition of exogenous fatty acids with inhibition of fatty acid synthesis revealed that flux of fatty acids into membrane lipids is also limited by CTDNEP1 (Figure 5.17B, "2."). Different rates of response to fatty acid inhibition raise the question of whether the rate of fatty acid breakdown is also modulated by CTDNEP1 (Figure 5.17B, "3."). The combined effects limit synthesis of ER membrane lipids, especially PC and PE, to limit membrane biogenesis (Figure 5.17B, "4." and "5.").

It is not clear why fatty acid supplementation does not fully reverse the suppression of nuclear solidity changes that occurs when CTDNEP1^{KO} cells are treated with an ACAC inhibitor to shut off fatty acid synthesis, despite fatty acid supplementation reversing suppression of ER membrane expansion with ACAC inhibitor treatment. Perhaps the ER's morphology is responsive to changes in fatty acid synthesis on a faster time scale than the nuclear envelope. Another possibility is that exogenously supplied fatty acids are not incorporated into nuclear envelope lipids as easily as into ER membrane lipids to influence nuclear shape. The nuclear envelope has shown to be a metabolic territory of lipid synthesis (Drozdz et al., 2017; Goulbourne et al., 2011; Romanauska and Köhler, 2018); perhaps its lipid metabolic capacity relies more on fatty acids synthesized *de novo* in the interconnected ER. Live imaging studies with acute ACAC inhibition will help establish whether nuclear envelope shape with regards to lipid availability is established during mitosis or can be changed during interphase, the latter of which would lend some support for the hypothesis that nuclear envelope lipid synthesis plays a role in determining its own shape.

This work has established a role for CTDNEP1 and lipin 1 for limiting ER membrane biogenesis in human cells through limiting fatty acid synthesis at least partly through SREBP-mediated gene transcription. This work has additionally connected control of fatty acid synthesis by CTDNEP1 to controlling formation of micronuclei (Figure 5.18). CTDNEP1 counteracts the nutrient-sensing kinase mTOR's phosphorylation of lipin to stabilize a nuclear pool of active lipin 1 (Merta et al., 2021) (findings by J. W. Carrasquillo Rodríguez and T. Vitale). This activity

limits ER membrane biogenesis in interphase and mitosis. Less abundant membranes are more able to be cleared in mitosis, and cytoplasmic viscosity is maintained. We hypothesize that limiting cytoplasmic viscosity and limiting the presence of uncleared membranes permits chromosome movements that are necessary for mitotic error correction, especially correction of merotelic errors, which involve rotation of the chromosome (Cimini, 2003) (Figure 5.18). We propose that membrane clearance and containing cytoplasmic viscosity allows these error-correcting chromosome movements to occur (Figure 5.18). Finally, CTDNEP1 limiting mitotic error correction leads to restriction of formation of micronuclei during mitotic exit (Figure 5.18).

One important future direction for this work will be to determine how reduction of fatty acid synthesis leads to a reduction in formation of micronuclei in CTDNEP1^{KO} cells. According to our model, restricting fatty acid synthesis in CTDNEP1-depleted cells will reduce excess uncleared membranes in mitosis and maintain cytoplasmic viscosity to allow chromosome movements. An alternative possibility that remains to be excluded is that reducing fatty acid synthesis in any context reduces cellular division and thereby limits the opportunity for cells in a population to form micronuclei. The finding that TOFA treatment with nocodazole washout in cells subject to mitotic shakeoff reduces formation of hyper-micronucleated cells suggests that this is not the case. Still, imaging of membranes in mitosis in TOFA-treated cells can confirm that control of membrane abundance and localization in mitosis limits formation of micronuclei.

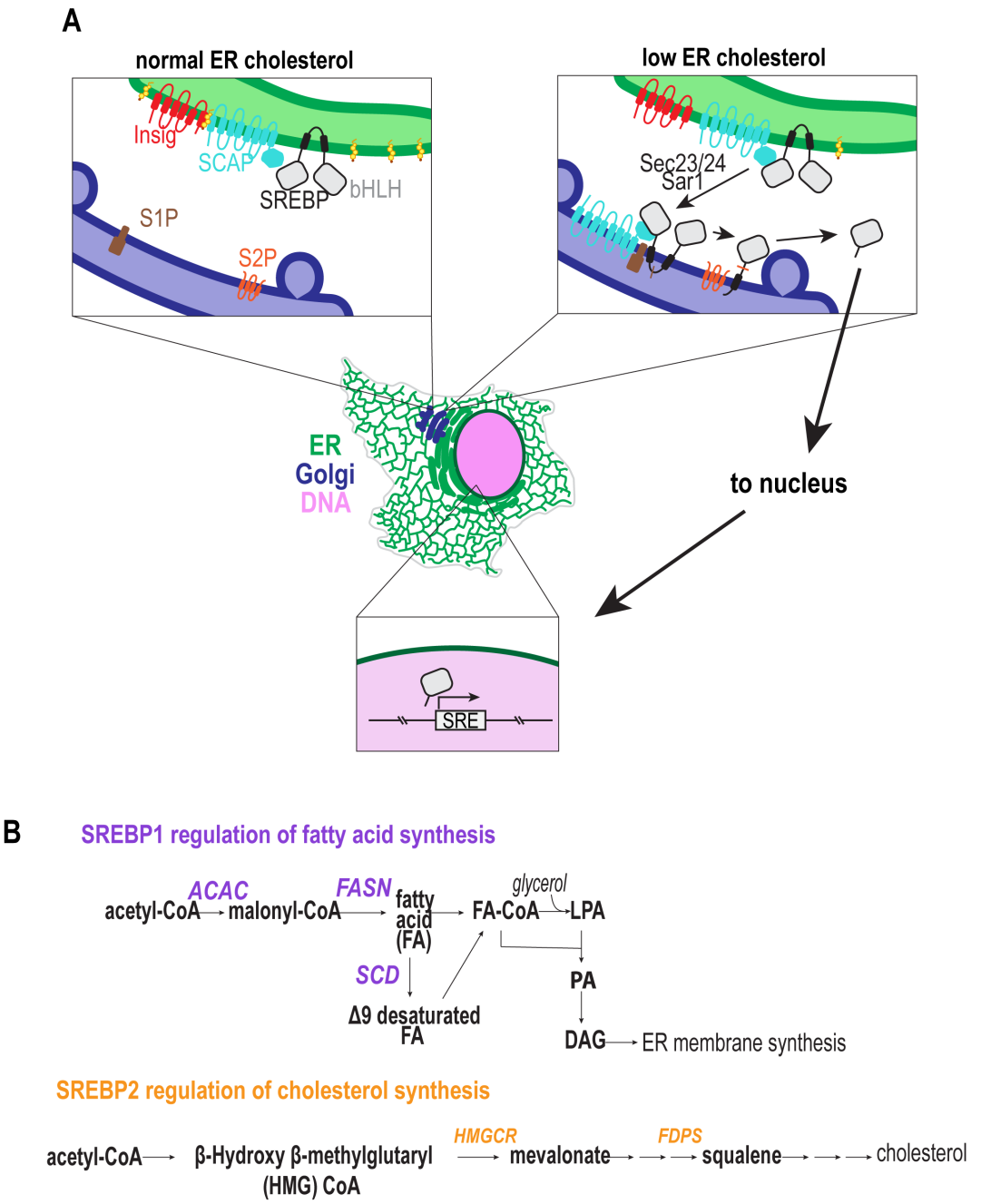

Figure 5.1 SREBP transcriptional control of lipid synthesis
A) Schematic of processing of SREBP from ER membranes to the nucleus in response to cholesterol and membrane packing sensing to upregulate lipid synthesis gene expression. SREBP, serum response element binding protein; Insig, Insulin induced gene; SCAP, SREBP cleavage-activating protein; bHLH, basic helix loop helix; S1P, signal peptidase 1; S2P, signal peptidase 2; SRE, sterol regulatory element. B) Schematic of how SREBP target genes control lipid synthesis. SREBP1 target genes (purple) control fatty acid synthesis, while SREBP2 target genes (orange) control cholesterol synthesis.

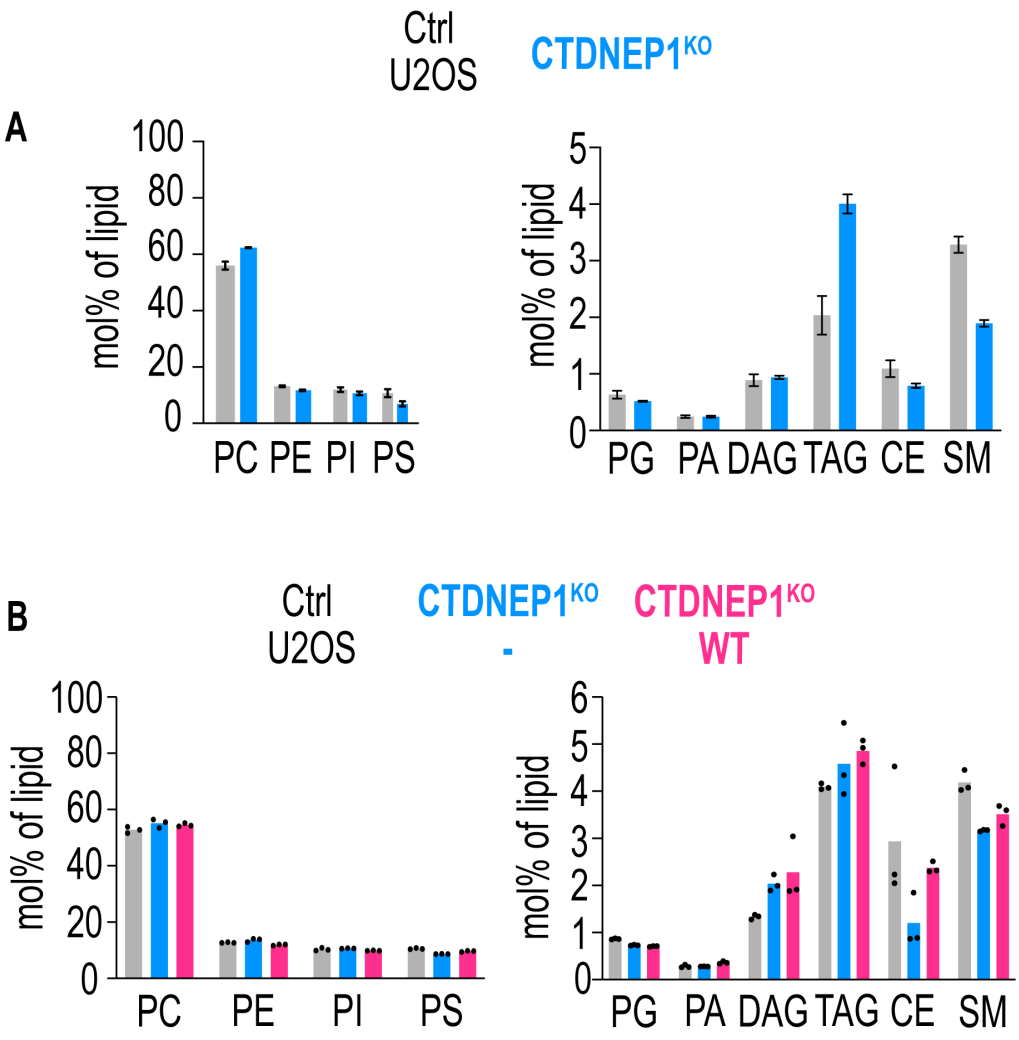

Figure 5.2 Lipidome mole percent composition in CTDNEP1^{KO} cells compared to control and CTDNEP1-overexpressed cells

A, B) Plots of molar percentage of lipid classes as determined by mass spectrometry lipid profiling in indicated cell lines. n = 3 technical repeats per condition. WT refers to stable overexpression of CTDNEP1-HA. Plots in (A) and (B) are from samples submitted and analyzed on different days.

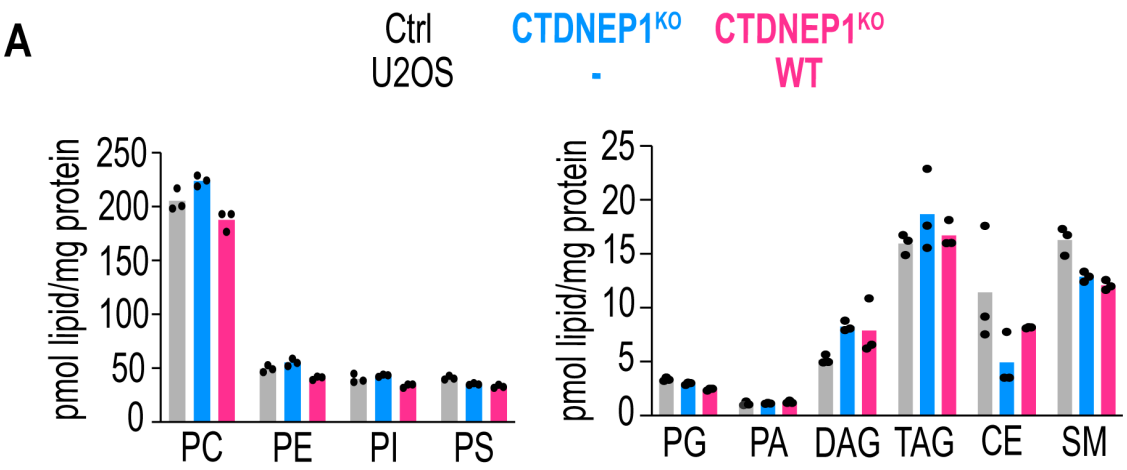

Figure 5.3 Lipidome pmol/mg protein lipid makeup in CTDNEP1^{KO} cells compared to control and CTDNEP1-overexpressed cells

A) Plots of pmol lipid per mg of protein as determined by mass spectrometry lipid profiling. n = 3 technical repeats per condition. WT refers to stable overexpression of CTDNEP1-HA.

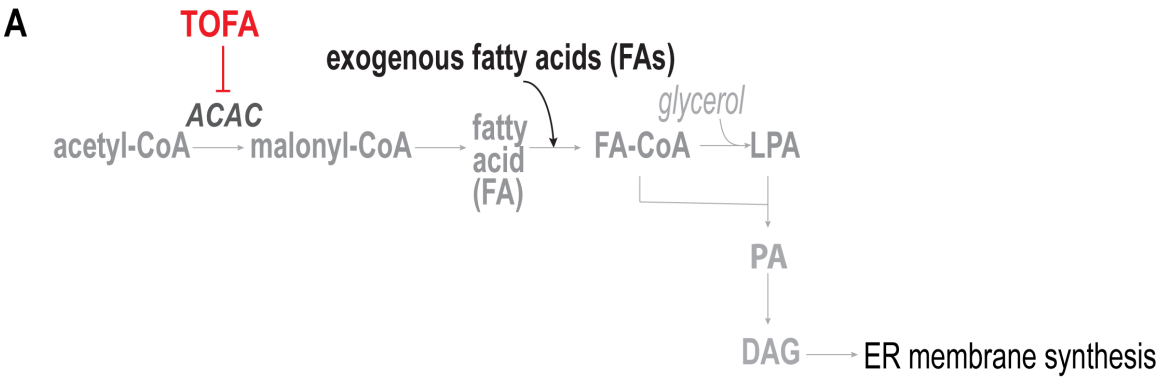

Figure 5.4 Control of fatty acid synthesis with small molecule inhibition of acetyl-CoA carboxylase

A) Schematic of how fatty acid synthesis feeds into ER membrane biogenesis and how it can be modulated using small molecule inhibitors and fatty acid supplementation. ACAC, acetyl-CoA carboxylase; TOFA, 5-(Tetradecyloxy)-2-Furoic Acid; LPA, lyso-phosphatidic acid. Acetyl-CoA is converted to fatty acyl-CoA by sequential carbon additions and can be additionally desaturated and elongated. 2 fatty acyl-CoAs can be formed into PA with glycerol, and PA/DAG can be made into membrane glycerophospholipids.

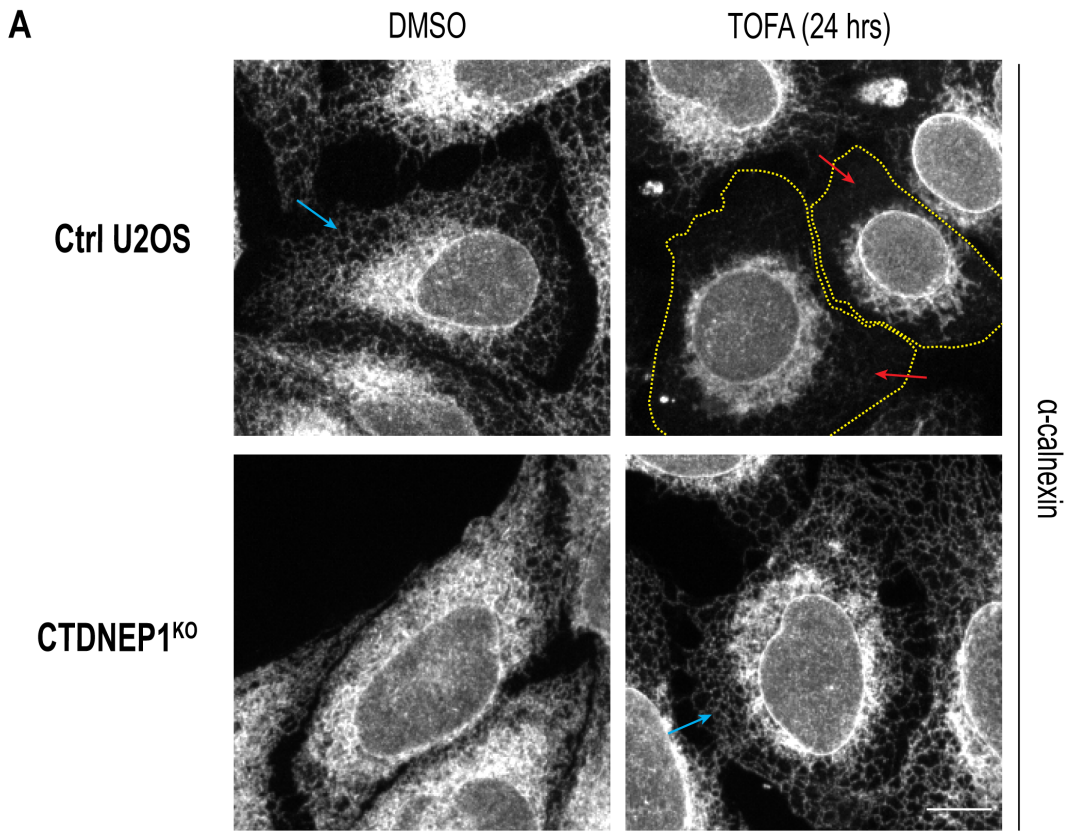

Figure 5.5 Inhibition of acetyl-CoA carboxylase suppresses ER expansion in CTDNEP1^{KO} cells and reduces ER membranes in control U2OS cells

A) Spinning disk confocal microscopy images of calnexin in immunostained U2OS cells treated as indicated. Yellow outlines show cell outlines as determined by manual outline of high-brightness ER signal. Blue arrows point to peripheral ER tubular networks, and red arrows point to thin or absent tubular networks. Scale bar 10 μm.

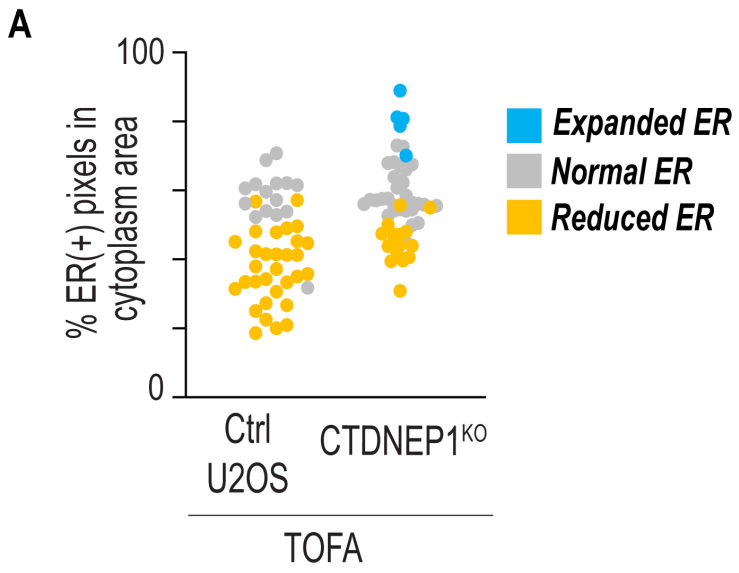

Figure 5.6 Validation of ER phenotype categorization using ER fluorescent signal segmentation

A) Plot, percent area quantification of ER signal segmentation from images of fatty acid-free BSA and DMSO or TOFA (24 hrs)-treated cells with phenotypic characterization for comparison. Values per cell (n) and phenotypic categorization are taken from the same dataset as Figure 5.8.

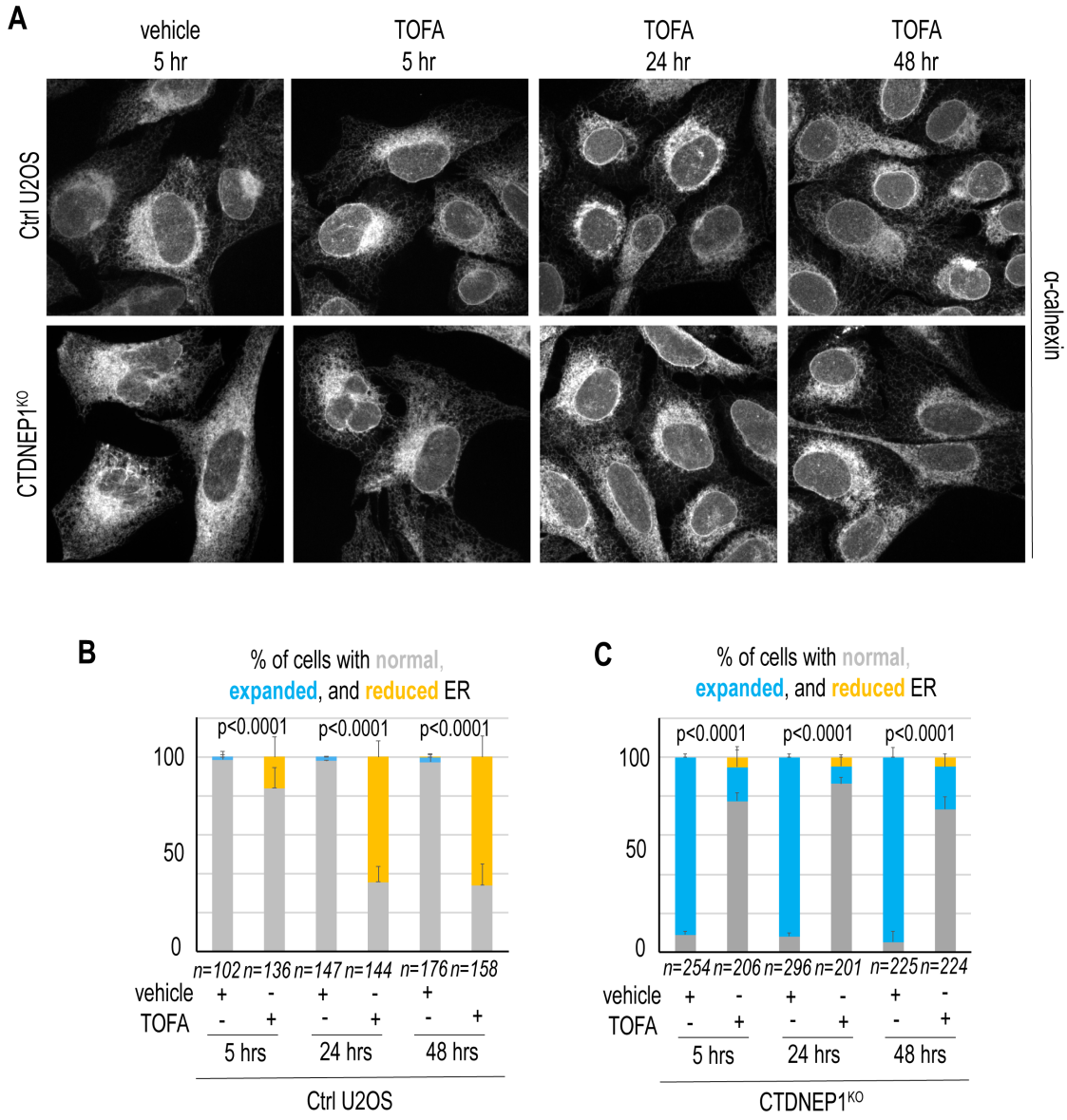

Figure 5.7 Reduction of ER membranes by acetyl-CoA carboxylase inhibition over time

A) Spinning disk confocal microscopy image of calnexin in immunostained U2OS cells treated as indicated. B,C) Quantification of incidence of indicated ER phenotypes in cells treated as indicated. n = number of cells, N = 3 experimental repeats. Mean + SD shown. P values, Chi squared tests of total incidences.

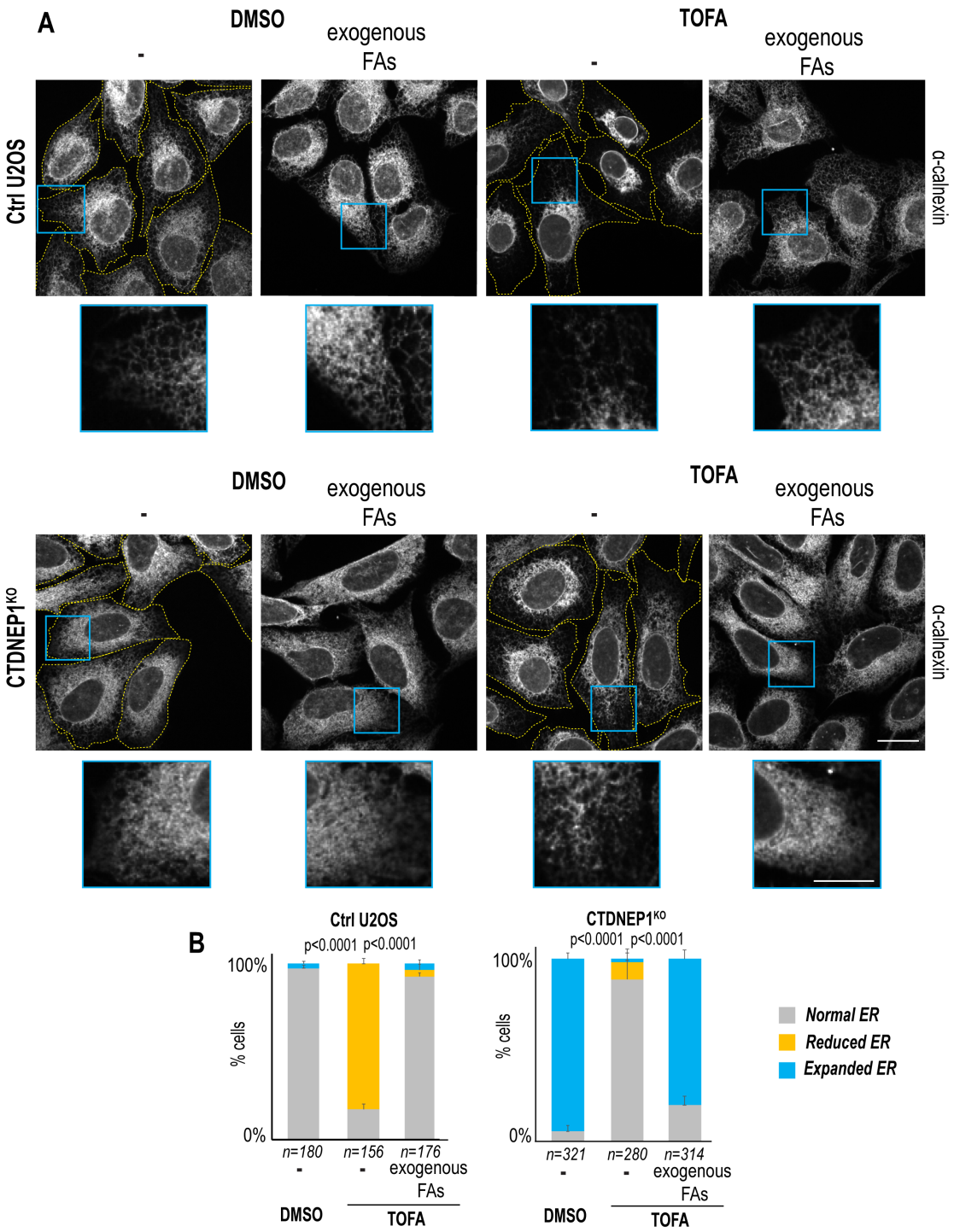

Figure 5.8 Supplementation with exogenous fatty acids restores ER appearance in cells with acetyl-CoA carboxylase inhibition

A) Spinning disk confocal microscopy images of calnexin in immunostained U2OS cells treated as indicated. Yellow outlines show cell outlines as determined by manual outline of high-brightness ER signal. B,C) Quantification of incidence of indicated ER phenotypes in cells treated as indicated. n = number of cells, N = 3

experimental repeats. Mean + SD shown. P values, Chi squared tests of total incidences.

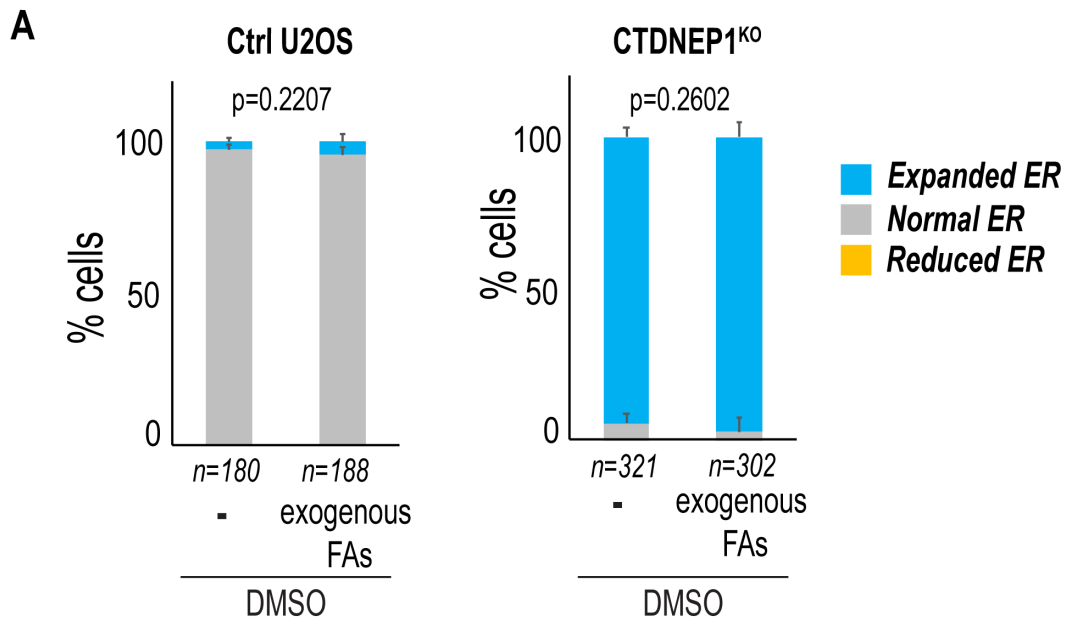

Figure 5.9 Supplementation with exogenous fatty acids does not change ER appearance in untreated cells

A) Quantification of incidence of indicated ER phenotypes in cells treated as indicated. n = number of cells, N = 3 experimental repeats. Mean + SD shown. P values, Chi squared tests of total incidences. Data are taken from the same dataset as Figure 5.8A-B, including the DMSO controls from 5.8B.

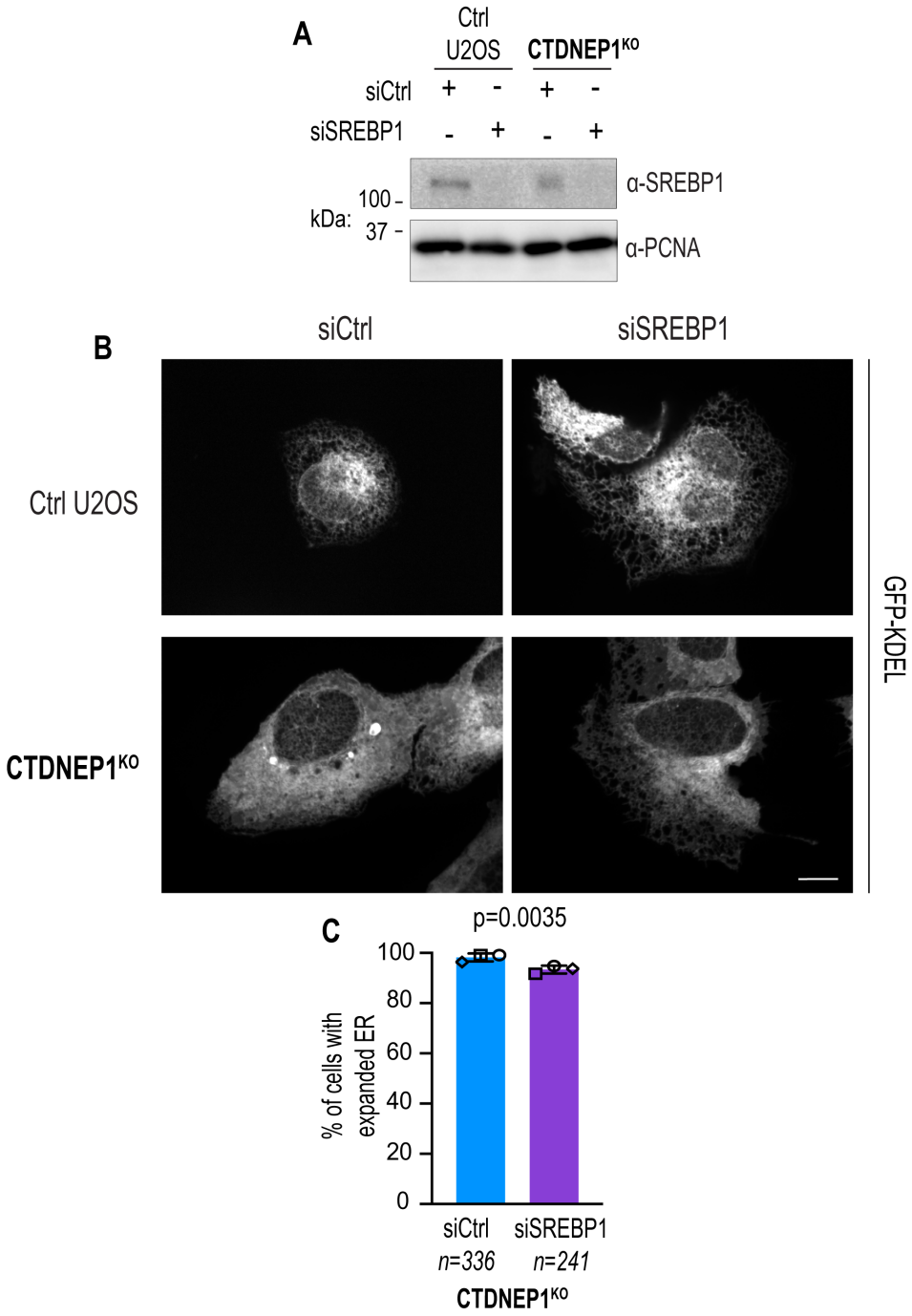

Figure 5.10 Depletion of SREBP1 partially suppresses expansion of ER membranes

A) Representative immunoblot of whole cell lysates from cells treated as indicated with indicated antibodies. Unprocessed SREBP1 is shown. B) Spinning disk confocal microscopy images of GFP-KDEL transiently expressed in U2OS cells treated with the indicated siRNAs. Scale bars, 10 μm. C) Quantification of incidence of expanded ER phenotype in cells from (B). n = number of cells, N = 3 experimental repeats. Mean ± SD shown. P value, Fisher's exact test of total incidences.

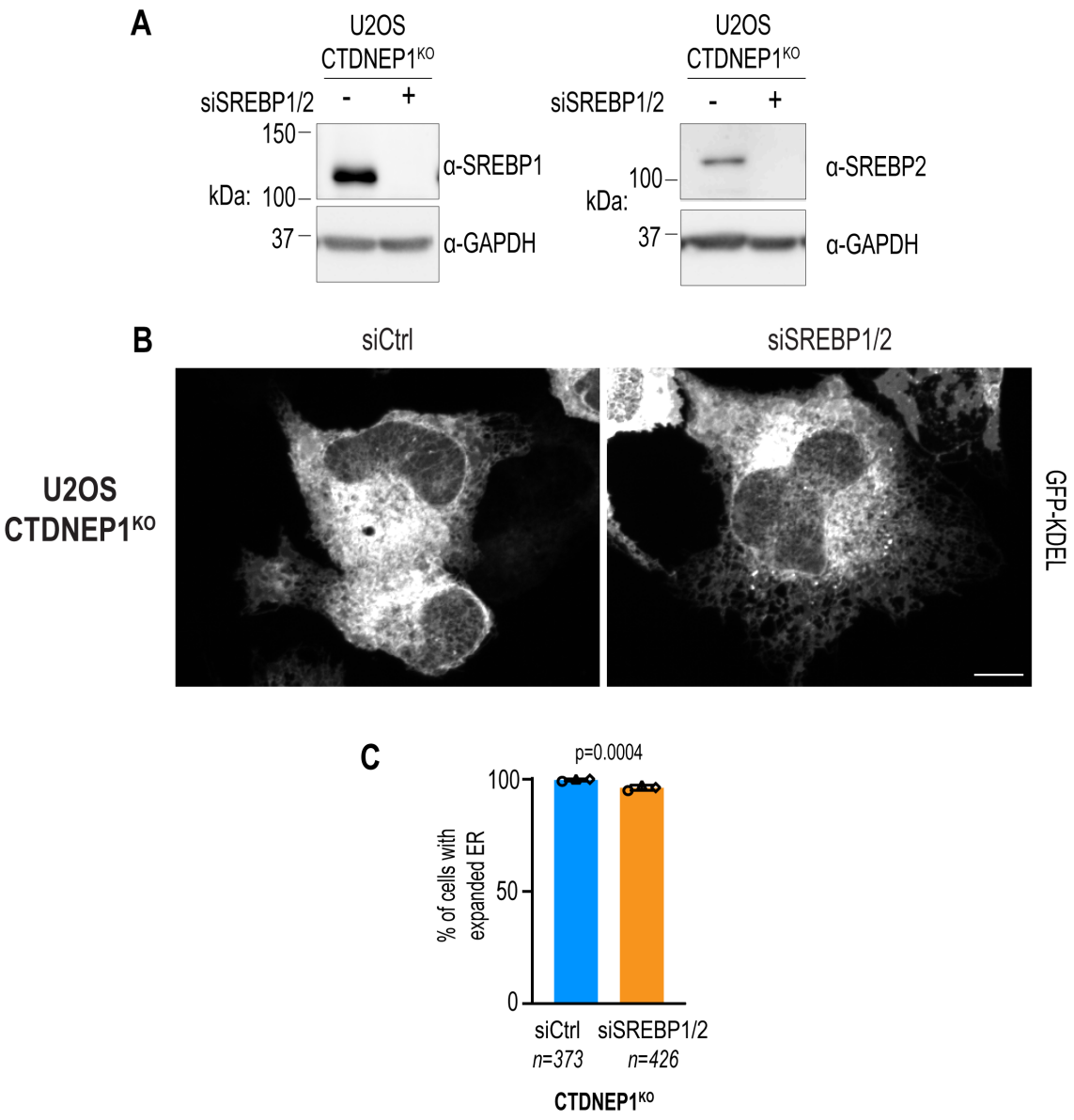

Figure 5.11 Depletion of SREBP1/2 partially suppresses expansion of ER membranes

A) Representative immunoblots of whole cell lysates from cells treated as indicated with indicated antibodies. Unprocessed SREBP1 and SREPB2 are shown. B) Spinning disk confocal microscopy images of GFP-KDEL transiently expressed in U2OS cells treated with the indicated siRNAs. Scale bars, 10 μm. C) Quantification of incidence of expanded ER phenotype in cells from (B). n = number of cells, N = 3 experimental repeats. Mean ± SD shown. P value, Fisher's exact test of total incidences.

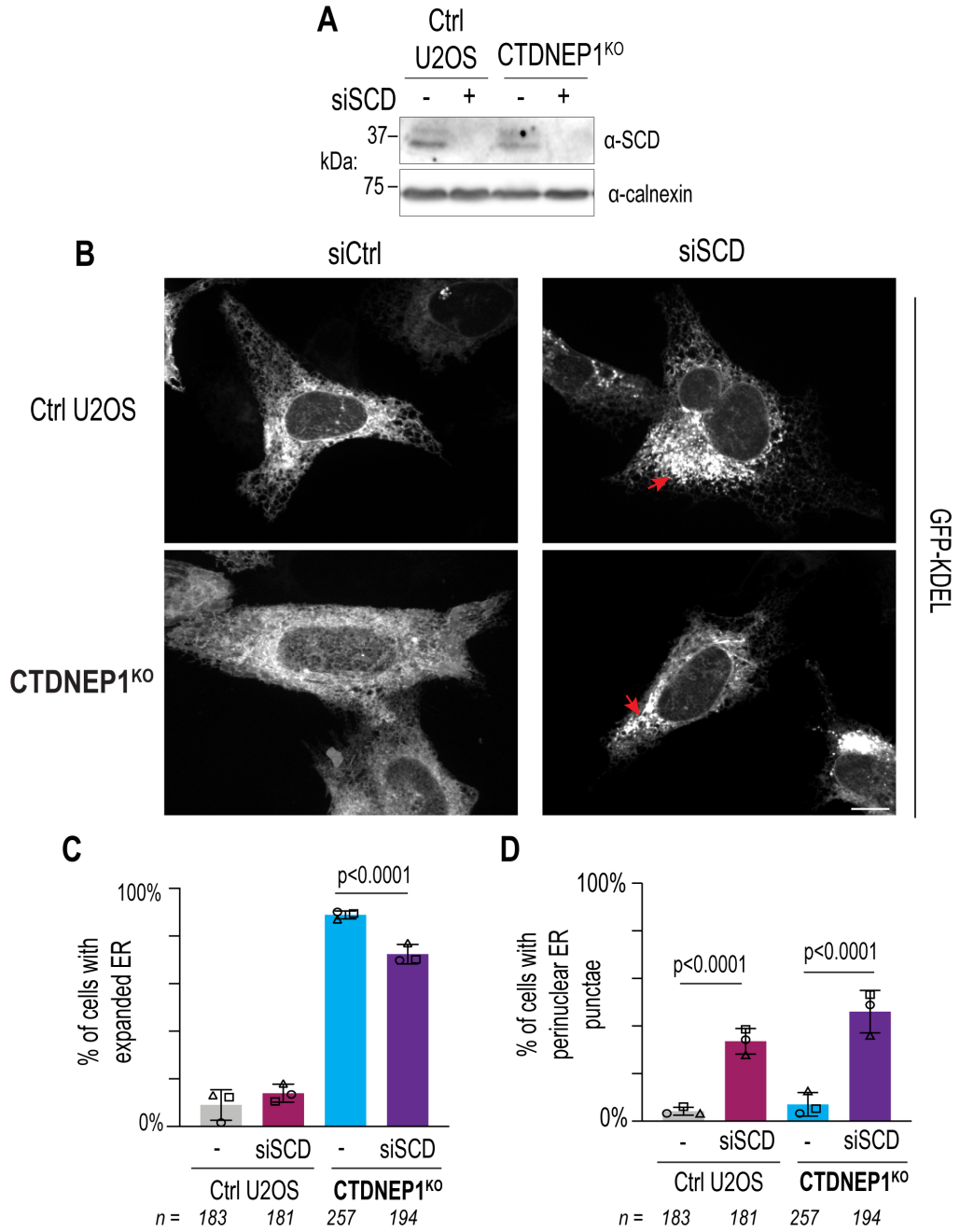

Figure 5.12 Depletion of SCD partially suppresses expansion of ER membranes and leads to perinuclear ER puncta formation

A) Immunoblot of whole cell lysates from cells treated as indicated with indicated antibodies. B) Spinning disk confocal microscopy images of GFP-KDEL transiently expressed in U2OS cells treated with the indicated siRNAs. Scale bars, 10 μm. Perinuclear ER punctae are shown with red arrows. C) Quantification of incidence of expanded ER phenotype in cells from (B). n = number of cells, N = 3 experimental repeats. Mean ± SD shown. P value, Fisher's exact test of total incidences. D) Quantification of incidence of perinuclear ER punctae phenotype in cells from (B). n = number of cells, N = 3 experimental repeats. Mean ± SD shown. P values, Fisher's exact tests of total incidences.

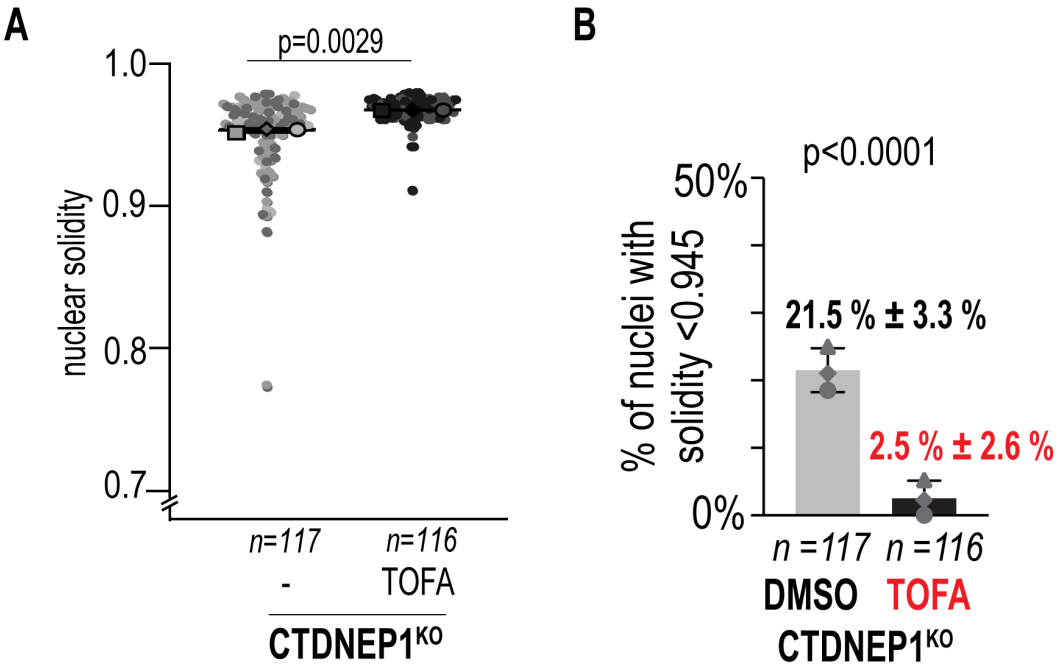

Figure 5.13 Inhibition of acetyl-CoA carboxylase rescues nuclear solidity of CTDNEP1^{KO} cells

A) Plot of solidity of nuclei (n) of cells treated with DMSO or 10 μM TOFA for 24 hrs. N = 3 experimental repeats. Individual values and means ± SD shown. P value, paired t test of replicate means. B) Quantification of incidence of solidity less than 1 SD from the mean of control nuclei solidity. n = number of nuclei, N = 3 experimental repeats. Mean ± SD shown. P value, Fisher's exact test of total incidences.

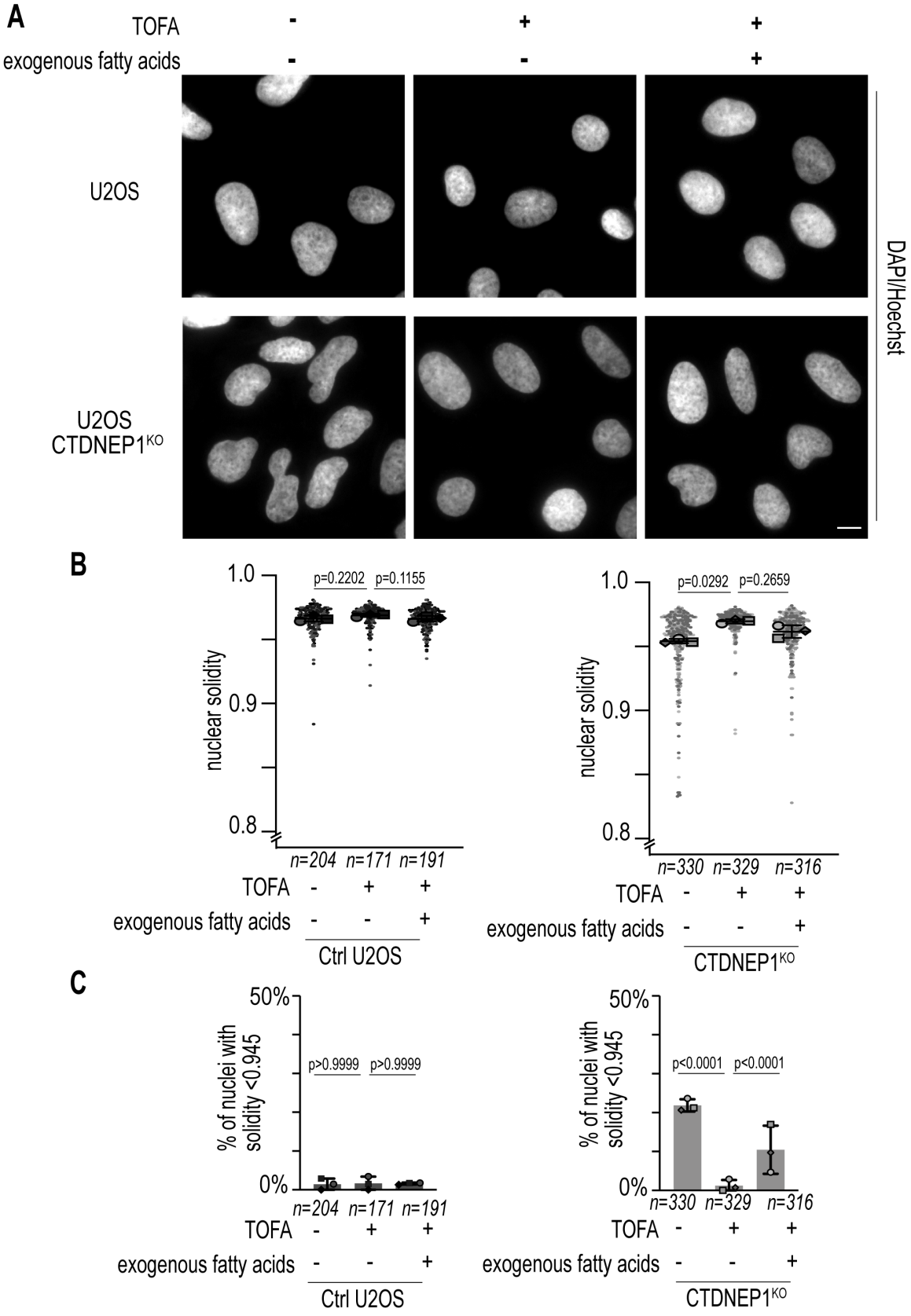

Figure 5.14 Partial suppression of nuclear solidity rescue with acetyl-CoA

carboxylase inhibition in CTDNEP1^{KO} cells with fatty acid supplementation
A) Epifluorescence images of DAPI/Hoechst staining in cells treated as indicated with fatty acid-free BSA or fatty acid-free BSA conjugated to 100 μM 1:2:1 palmitic:oleic:linoleic acid and DMSO or 10 μM TOFA for 24 hrs. Scale bar 10 μm. B) Plots of solidity of nuclei (n) of cells treated as indicated. N = 3 experimental repeats. Individual values and means ± SD shown. P values, repeated measures ANOVA with post-hoc Šidák's multiple comparisons test. C) Quantification of incidence of solidity less than 1 SD from the mean of control U2OS nuclei solidity. n = number of cells from N = 3 experimental repeats. Means ± SDs shown. P values, Fisher's exact tests of total incidences.

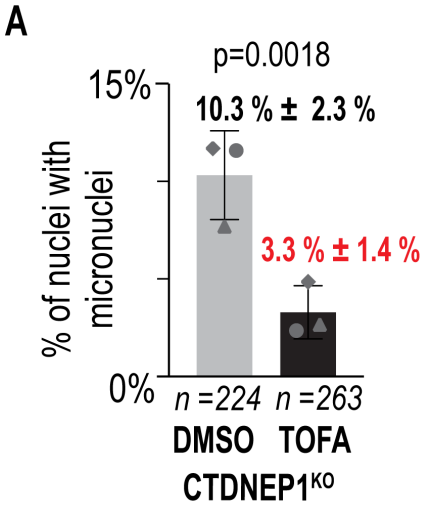

Figure 5.15 Inhibition of acetyl-CoA carboxylase suppresses formation of micronuclei in CTDNEP1^{KO} cells
A) Quantification of incidence of micronuclei in cells treated with DMSO or 10 μM TOFA for 48 hrs. n = number of cells from N = 3 experimental repeats. Means ± SDs shown. P value, Fisher's exact test of total incidences.

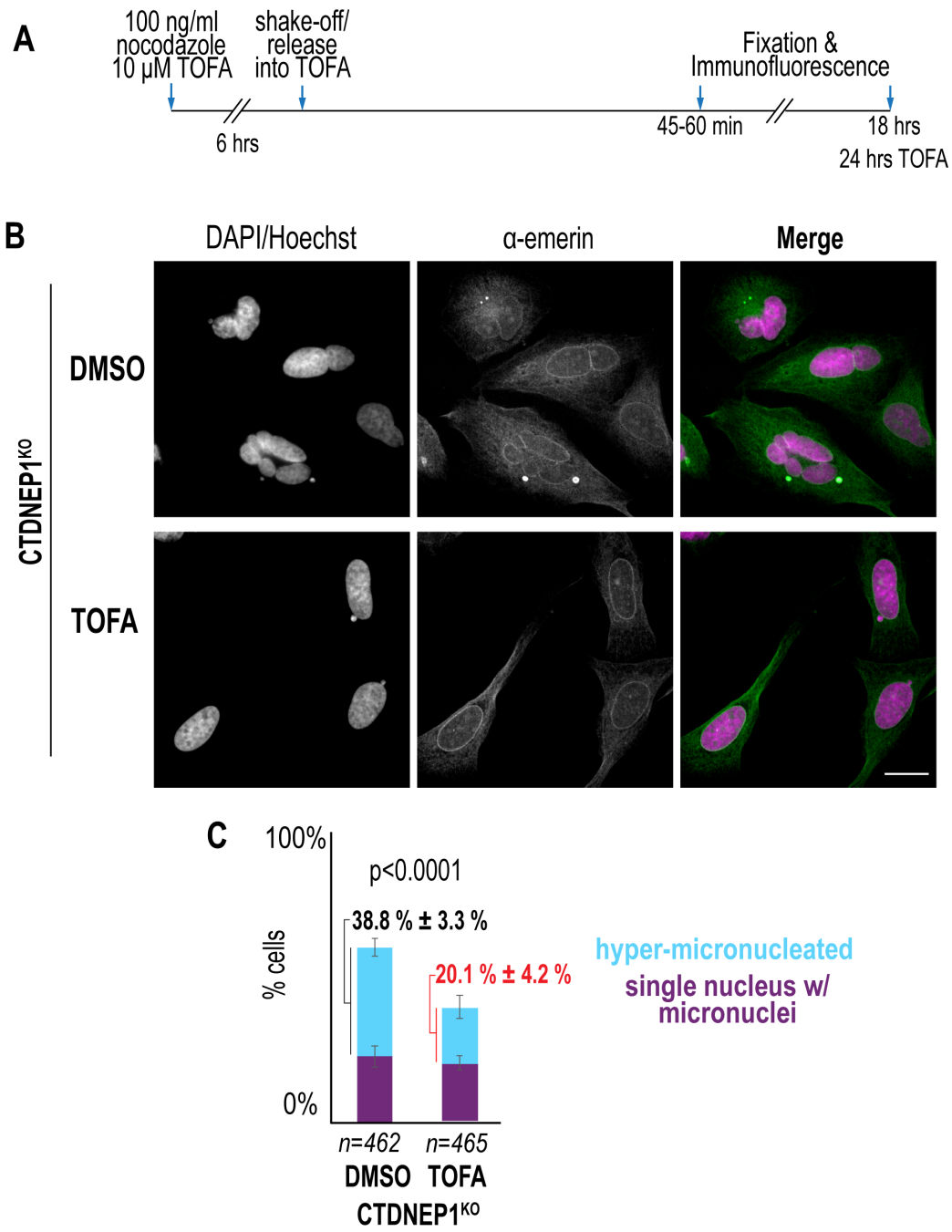

Figure 5.16 Inhibition of acetyl-CoA carboxylase suppresses hyper-micronucleation in CTDNEP1^{KO} cells upon recovery from transient spindle disassembly

A) Schematic detailing nocodazole washout with TOFA treatment. B) Epifluorescence (DAPI/Hoechst) and confocal (emerin) images of immunostained cells treated with 10 μM TOFA or DMSO for 24 hrs (total) and subjected to nocodazole washout as shown. Scale bar 10 μm. C) Quantification of incidence of indicated phenotypes in cells treated as shown. n = number of cells from N = 3 experimental repeats. Means ± SDs shown. P value, Chi squared test of total incidences

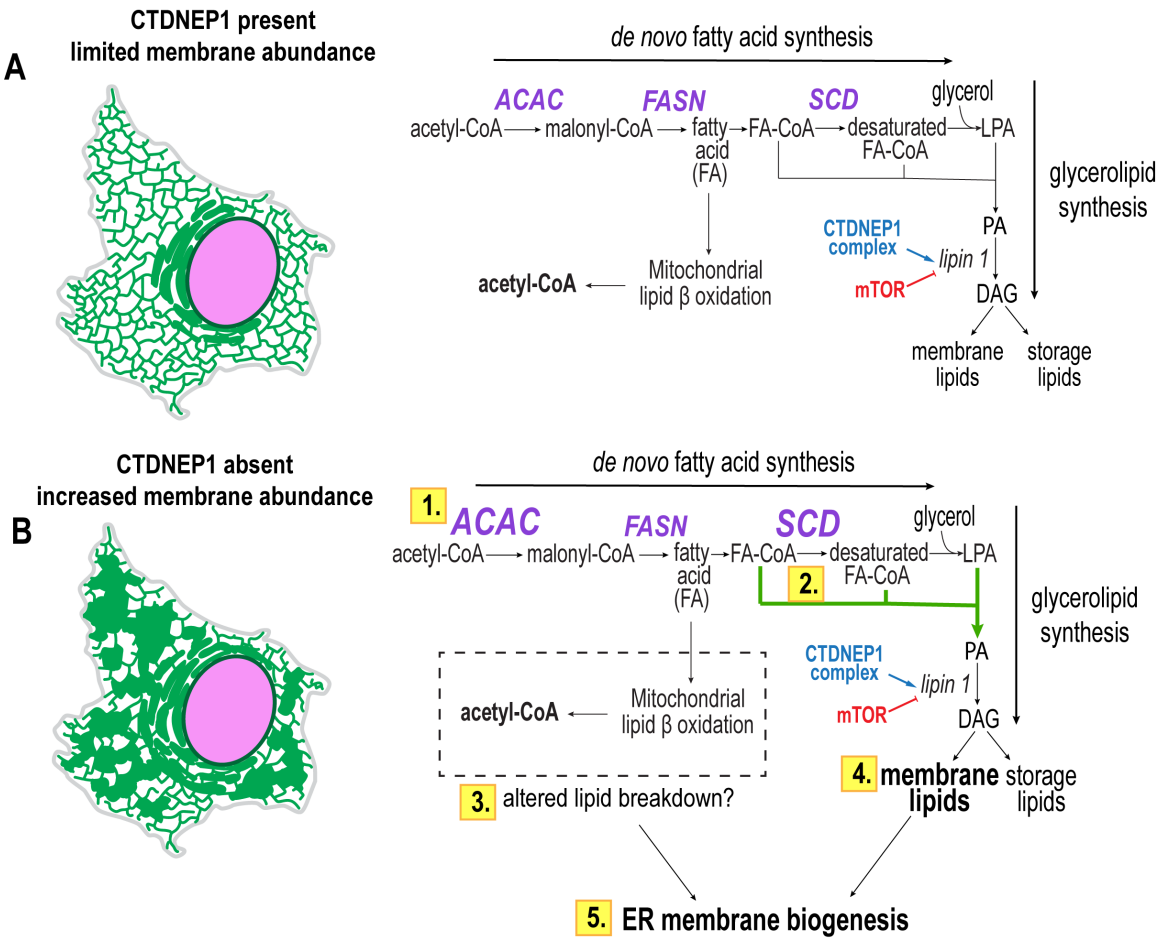

Figure 5.17 Mechanisms for expansion of ER membranes in CTDNEP1^{KO} cells

A) Schematic of showing how control of fatty acid synthesis by CTDNEP1/lipin 1 mediated by SREBP1 target gene expression can feed into ER membrane synthesis. B) Schematic showing how increased expression of SREBP1 target genes ("1."), increased flux into fatty acid and ER membrane lipid synthesis ("2.", "4."), and impacts on lipid breakdown ("3.") can lead to increased ER membrane biogenesis in cells lacking CTDNEP1 ("5.").

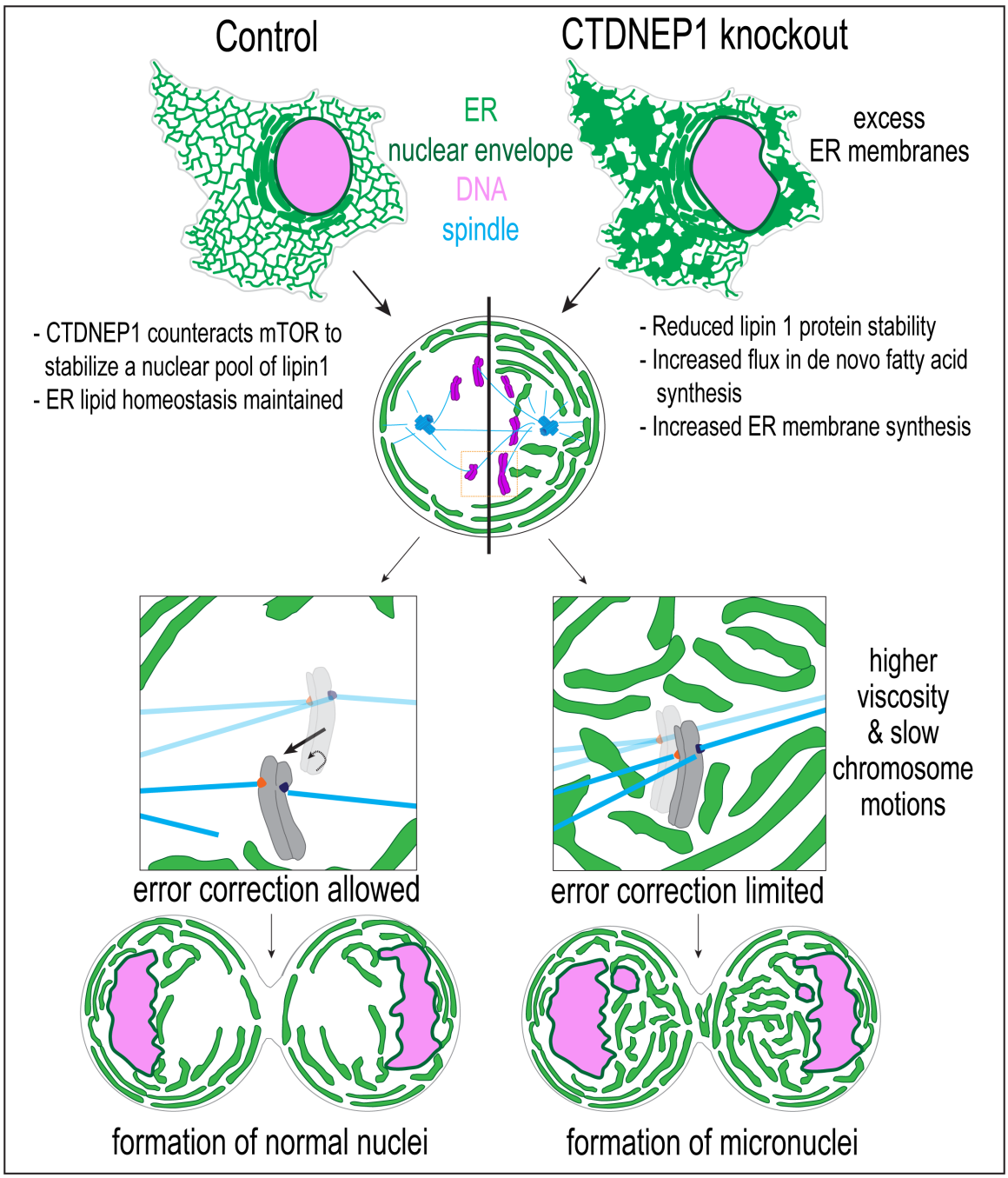

Figure 5.18 Excess membranes in CTDNEP1-depleted cells impact mitotic error correction to lead to formation of micronuclei

A) Schematic showing how excess ER membranes in CTDNEP1^{KO} cells caused by insufficient dephosphorylation of mTOR phosphorylation sites on lipin 1 disrupts mitotic error correction to lead to formation of micronuclei. Dark green = nuclear envelope; light green = ER; pink = DNA, and blue = mitotic spindle. In insets, chromosomes are gray and opposite kinetochores are orange and dark blue.

Chapter 6: Conclusions and Future Perspectives

Human CTDNEP1's role in regulating lipid synthesis, ER membrane biogenesis, and nuclear morphology

Lipid synthesis is important for organelle maintenance, cell growth, and division, yet regulation of lipid synthesis in human cells is not fully understood. This work has elucidated some of the functions of CTDNEP1 in controlling ER lipid synthesis in human cells. We have established that human CTDNEP1 restricts synthesis of PC and PE to limit ER membrane biogenesis through dephosphorylation of lipin 1 (Figure 6.1). Without CTDNEP1, lipin 1 is less able to repress SREBP-dependent fatty acid synthesis gene transcription, and flux into fatty acid and membrane lipid synthesis is increased (Figure 6.1). These mechanisms lead to the expansion of ER membranes in CTDNEP1-depleted cells.

An important future direction for determining how CTDNEP1 limits ER membrane biogenesis will be determining the mechanism for how flux into PC/PE is increased with CTDNEP1 deletion in human cells (Figure 6.1). One aspect of this regulation that is known is that Mg^{2+}-independent PAP activity is increased in CTDNEP1^{KO} U2OS cells, likely to compensate for decreased Mg^{2+}-dependent PAP activity that also occurs (Merta et al., 2021) (finding by Mitchell E. Granade). Mammalians have 3 lipin genes, and these lipins are known to compensate for each other in mice by increased expression of the other lipins when one is depleted, although this can depend on tissue specific-lipin expression (Grimsey et al., 2008; Gropler et al., 2009). While loss of CTDNEP1 can potentially limit activation all lipins, negating the effect of lipin-lipin

compensation, it is known that the PAP activities of lipin 2 and lipin 3 are unaffected by phosphoregulation (Boroda et al., 2017; Eaton et al., 2013). Thus, PAP activity of lipins 2 and 3 may continue conversion of PA to DAG in the absence of lipin 1 activation by CTDNEP1 to help shunt fatty acids into ER membrane lipids. As a whole, PAP activity not dependent on lipin 1 could contribute to increased membrane biogenesis in CTDNEP1-depleted cells (Figure 6.1).

Another possibility for how CTDNEP1 limits flux of fatty acids into ER membrane biogenesis might be regulation of CCTα activity (Figure 6.1). The increase in PC and PE in CTDNEP1^{KO} cells points to the possibility that CCTα activity may be increased with loss of lipin activity as in *A. thaliana* cells (Craddock et al., 2015). It is unclear if such activation would occur through PA activating CCTα or a more general sensing of membrane packing with increased fatty acid synthesis. Measuring CDP-choline output in CTDNEP1^{KO} cells would help determine if CCTα activity is increased to raise PC synthesis. Other possibilities for how CTDNEP1 limits the flux of fatty acids into PC and PE could be regulation of fatty acid uptake by the cell or negative regulation of other processes that lead to breakdown of lipids, like lipophagy and autophagy in general. Determining the extent of these activities and measuring expression of related genes will elucidate their involvement in control of ER membrane biogenesis by CTDNEP1 and lipin 1.

One remaining question is whether lipid breakdown is regulated by CTDNEP1/lipin 1 in human cells (Figure 6.1). It is known that lipin 1 can

positively regulate PPARα-mediated transcription to upregulate fatty acid oxidation genes in mouse liver cells (Finck et al., 2006). Lipin deficiency in humans causes symptoms that closely resemble those of fatty acid oxidation disorders (Knottnerus et al., 2018; Zeharia et al., 2008). I previously showed that PPARα binding-deficient lipin 1 can still rescue ER membrane expansion in CTDNEP1^{KO} cells (Figure 2.15). In order to determine whether CTDNEP1 limits lipin 1 activation of lipid oxidation gene transcription, future studies should test for the expression of these genes, which include fatty acid transporters and fatty acid-metabolizing enzymes, in CTDNEP1^{KO} cells and determine if overexpression can suppress ER membrane expansion.

CTDNEP1's control of nuclear morphology is also dependent on control of fatty acid synthesis— multilobed nuclear morphology in CTDNEP1^{KO} cells is suppressed by inhibiting fatty acid synthesis. Future experiments should determine to what extent nuclear envelope morphology is established during nuclear envelope reassembly as opposed to remodeling during interphase. Future experiments can also determine if there is an interaction between CTDNEP1 control of lipid synthesis and other players in establishing nuclear envelope structure, such as the nuclear lamina, nuclear sealing, and connections to the cytoskeleton.

How the study of CTDNEP1 has informed our knowledge of how membrane dynamics in mitosis are important for chromosome segregation

This work uncovers a previously unknown role for CTDNEP1 in regulating mitotic error correction to limit formation of micronuclei. We show that CTDNEP1

limits ER membrane biogenesis to restrict ER membrane abundance in mitosis (Figure 6.2). With intact CTDNEP1, ER membrane abundance is limited in interphase and mitosis, and ER membranes can properly clear from the mitotic spindle and chromosomes (Figure 6.2, “Control”). Mitotic error correction can proceed as normal, and nuclear envelope assembly ensures formation of single nuclei of the correct size and shape (Figure 6.2, “Control”). Without CTDNEP1, ER membranes are expanded due to increased membrane lipid synthesis, and ER membrane expansion persists through mitosis, when cytoplasmic viscosity is also increased (Figure 6.2, “Loss of CTDNEP1”). Consistent with findings in other organisms, expanded membranes in CTDNEP1-depleted human cells are less cleared during prometaphase. Prometaphase chromosome average velocity is also decreased, consistent with a prometaphase delay seen in other studies and corroborated in this study. Merotelic kinetochore attachment errors are less able to be corrected in CTDNEP1-depleted cells, contributing to formation of micronuclei (Figure 6.2, “Loss of CTDNEP1”). We propose that cytoplasmic viscosity and less cleared membranes limit chromosome movements, which in turn limits merotelically attached chromosomes from rotating to promote error correction, which then leads to the formation of micronuclei. Additionally, CTDNEP1-depleted cells are less able to limit membrane extensions from forming inside of nuclei during mitotic exit and to limit nuclear expansion (Figure 6.2, “Loss of CTDNEP1”). Thus, CTDNEP1 controls ER membrane biogenesis and membrane dynamics to promote mitotic error correction that limits formation of micronuclei.

Connecting lipid synthesis to chromosomal instability in cancer through CTDNEP1

Cancer cells frequently exhibit increased lipid synthesis and are prone to forming micronuclei, and these are conventionally thought to be separately occurring events. This work establishes a case in which formation of micronuclei depends on the extent of membrane lipid synthesis, with the deletion of a gene that is commonly mutated in medulloblastoma, CTDNEP1.

Our work shows that cells deleted of CTDNEP1 have upregulation of SREBP1-target fatty acid synthesis genes that are frequently upregulated in cancer. We show that increased fatty acid synthesis feeds into membrane lipid synthesis, which interferes with mitotic progression and error correction. We propose a mechanism for formation of micronuclei via improperly cleared and more abundant membranes contributing to higher cytoplasmic viscosity, all of which reduces chromosome motions to impede kinetochore attachment error correction.

CTDNEP1 truncating mutations occur frequently in Group 3 medulloblastoma, a subgroup associated with young age at presentation and poor prognosis (*CTDNEP1* frameshift, premature stop single-nucleotide variations, or splice site-altering mutations in 5% of cases) (Jones et al., 2012; Northcott et al., 2012, 2017). CTDNEP1 mutations primarily occur in the absence of known driver mutations in Group 3 medulloblastomas, including amplification of the pro-growth transcription factor MYC (Northcott et al., 2017) and homozygous tumor suppressor p53 deletion (Jones et al., 2012). At the same

time, CTDNEP1 mutations occur with loss of heterozygosity at 17p, where *CTDNEP1* and *TP53* reside (Jones et al., 2012). It is possible that loss-of-function mutations in a cell with one copy of CTDNEP1 would lead to increased lipid synthesis that supports cancer cell proliferation, along with decreased mitotic error correction leading to formation of micronuclei. These characteristics could contribute to cancer progression that leads to poor prognoses in the Group 3 medulloblastoma subgroup.

An alternative hypothesis is that CTDNEP1 could control phosphorylation of substrates besides lipin 1. CTDNEP1 was identified in *Xenopus* embryos as a gene required for neural development through negative regulation of bone morphogenic protein (BMP) signaling (Satow et al., 2002). BMP signaling in this case occurs when BMP binds to its plasma membrane receptor, which then phosphorylates Smads, which then bind other Smads and enter the nucleus to act as transcription factors for genes important for tissue development (Derynck and Zhang, 2003). Later studies implicated CTDNEP1 in limiting phospho-Smad abundance in kidney, bone, and heart tissues in *Xenopus* and mice (Darrigrand et al., 2020; Hayata et al., 2015; Sakaguchi et al., 2013). Evidence suggests that CTDNEP1 dephosphorylates Smad in *Drosophila*, but direct evidence of phosphorylation of Smads by CTDNEP1 is lacking in other organisms (Urrutia et al., 2016). The well-characterized role of CTDNEP1 in regulating lipid synthesis also needs to be ruled out in these developmental contexts, as lipid composition of membranes can impact cell signaling (Sunshine and Iruela-Arispe, 2017). CTDNEP1 does not control BMP signaling in all tissues; in mouse primordial

germ cells, CTDNEP1 does not regulate BMP/Smads (Tanaka et al., 2013). In human medulloblastomas, BMP signaling can be upregulated or downregulated, though the reason for this is unclear (Caja et al., 2015). It is possible that loss of CTDNEP1 leads to attenuation of BMP signaling that might contribute to cancer development, although the mechanism for this may not be straightforward. At the same time, we have shown that key phenotypes associated with cancer in CTDNEP1-depleted cells are suppressed with lipin 1 dephospho-mimic overexpression, which is consistent with the idea that CTDNEP1's role in cancer is more related to its role in controlling lipid synthesis. Future studies of CTDNEP1 in cancer will clarify if there are multiple roles for CTDNEP1 in controlling cancer progression.

These findings suggest the existence of a paradox between regulation of cell metabolism and chromosomal instability. Limiting membrane synthesis limits a cell's ability to proliferate, but these data show that it also appears to limit chromosomal instability, which is detrimental to cell survival at high levels (Giam and Rancati, 2015; Sansregret et al., 2017). Why do cancer cells frequently exhibit upregulation of lipid synthesis if it could confer a survival disadvantage? It is possible that this is the case merely because the benefit of increased proliferation overcomes any negative aspects of increased lipid synthesis. It has also been proposed that mechanisms that promote chromosomal instability at a low level are adaptive for cancer cells because they provide tolerable levels of chromosome missegregation that promote genetic heterogeneity (Giam and Rancati, 2015). I propose that the solution to this paradox in cancer cells lacking

functional CTDNEP1 is that cells having increased membrane lipid synthesis that can support proliferation subsequently have increased genetic heterogeneity that is adaptive for tumor progression. This conclusion strengthens the case for CTDNEP1 as a candidate tumor suppressor in Group 3 medulloblastomas.

Remaining Questions and Future Directions

We have shown that increased lipid synthesis producing excess ER membranes can change the physical properties of the cytoplasm in mitotic cells. What remains to be seen is whether cytoplasmic viscosity is also increased in interphase cells, or whether other properties of the cytoplasm are changed as well. It will be interesting to know how ER taking up more space in the cytoplasm to increase cytoplasmic viscosity impacts more cell functions, like movements of organelles and the cytoskeleton.

The fatty acid makeup of membranes in CTDNEP1-depleted cells has not been studied, as our lipidomic analysis did not include subspecies fatty acid chain information. The length and saturation of fatty acids in membrane lipids greatly impacts the physical properties of the membrane, so it will be important to determine the impact of fatty acid composition in excess membranes in cells lacking CTDNEP1. Desaturation of membrane fatty acids is associated with membrane fluidity; perhaps more Δ9-unsaturated fatty acids with SCD upregulation in CTDNEP1^{KO} cells could make expanded ER membranes more fluid and less able to be cleared to the cell periphery in mitosis.

Lipid synthesis in the ER generates membrane lipids for other organelles and performs biogenesis of peroxisomes and lipid droplets (Holthuis and Menon,

2014; Thiam et al., 2013; van der Zand et al., 2012). One remaining question is whether increased membrane biogenesis in the ER of CTDNEP1-depleted cells leads to increased size or altered composition of other organelles. Future studies should examine the appearance and function of organelles— like mitochondria, endosomes and lysosomes, peroxisomes, lipid droplets, and the plasma membrane— that derive lipids from the ER.

A major future direction for studying roles of CTDNEP1 in human cells will be to characterize CTDNEP1 structure and functions on the molecular level. One important step will be to optimize purification of CTDNEP1 for antibody synthesis and *in vitro* dephosphorylation assays. Further, another important future direction will be to determine all proteins that are dephosphorylated by CTDNEP1 by proteomic analysis. Proteins that are determined to be more phosphorylated in the absence of CTDNEP1 can be verified by *in vitro* dephosphorylation of peptides or purified proteins. If they are not directly dephosphorylated by CTDNEP1, one can determine if their dephosphorylation occurs as a result of limiting lipid synthesis by targeting lipin 1 or overexpressing/knocking down SREBP1 target genes. CTDNEP1 has a putative transmembrane domain in its N terminus; domain-mutation analyses can determine if its transmembrane domains and certain residues (outside of the active site) are important for lipin dephosphorylation, targeting to the nuclear envelope and ER, and binding with NEP1R1.

Finally, more studies should be performed to elucidate further how control of lipid synthesis controls formation of micronuclei. As mentioned previously,

tracking membranes in cells in which fatty acid synthesis has been shut off can determine if decreasing membranes in mitosis limits chromosome missegregation. Nocodazole washout leads to increased formation and persistence of merotelic attachments, but upstream of this phenomenon is delayed spindle bipolarity and possible imbalance between contributions of centrosome-nucleated and chromosome-nucleated microtubules to the spindle (Gregan et al., 2011; Silkworth and Cimini, 2012). Future experiments can determine if these upstream events can contribute to chromosome missegregation in ways other than by increasing merotelic attachments, such as by disrupting spindle architecture. Analyses of kinetochore architecture during nocodazole washout in mitotic exit in CTDNEP1^{KO} cells can confirm that lagging chromosomes are due to merotelic kinetochore attachments. These studies can also determine how many chromosomes are contained in nuclei that are not the primary nucleus in hyper-micronucleated cells. Average chromosome velocity is slower in prometaphase CTDNEP1^{KO} cells; this may reflect slower chromosome diffusion in viscous cytoplasm in the presence of uncleared membranes, but it could also reflect slower spindle microtubule motions. Further studies of live imaging of tubulin can also determine how mitotic spindle growth and movements are affected by the presence of excess ER membranes in mitotic cells depleted of CTDNEP1. These studies can cement the role of regulating membrane biogenesis in controlling chromosome segregation, which will help our understanding of how these events are misregulated in human cancers.

Conclusion

These data have implicated control of membrane lipid synthesis by the lipin 1 phosphatase CTDNEP1 to control of mitotic error correction to ensure mitotic fidelity. This finding represents the first connection between alterations in lipid synthesis that can occur in cancer and formation of micronuclei that also contribute to cancer progression. These findings and future studies will enlighten our understanding of how control of cell metabolism is orchestrated with mitotic events to allow controlled cell division.

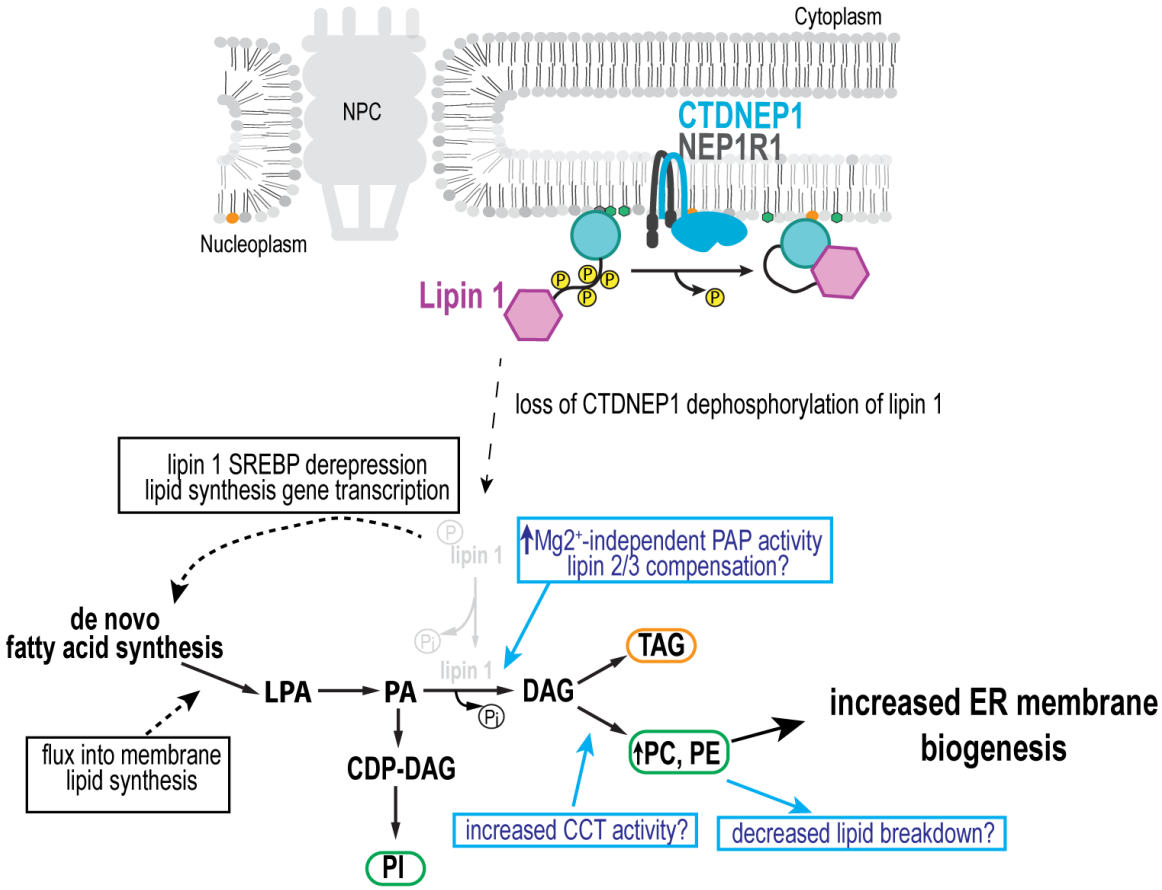

Figure 6.1 Mechanisms for increased ER membrane lipid synthesis with loss of CTDNEP1

Schematic of how CTDNEP1 control of lipin 1 at the nuclear envelope controls ER membrane biogenesis. With loss of CTDNEP1, lipin 1 is less abundant and less active, yet multiple mechanisms feed into increased PC/PE synthesis that lead to increased membrane biogenesis. Black boxes, mechanisms increasing membrane biogenesis established in this work. Blue boxes, putative mechanisms for how DAG-derived lipids are increased with less lipin 1 activity.

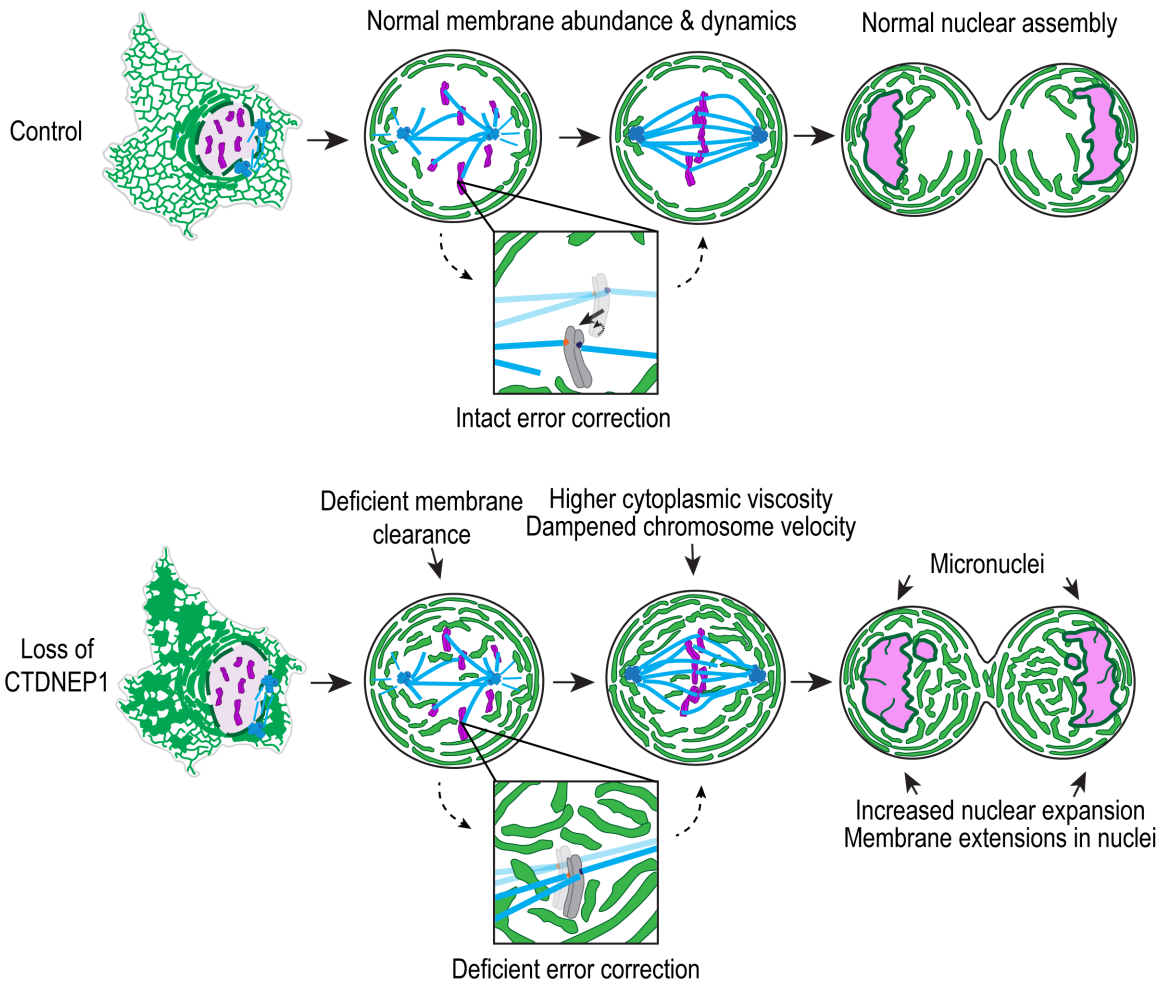

Figure 6.2 CTDNEP1 limits ER membrane abundance to promote proper nuclear assembly

Schematic for how increased ER membrane biogenesis in the absence of CTDNEP1 leads to abnormal nuclear assembly and formation of micronuclei. ER membranes, light green; nuclear envelope, dark green; Centrosomes and spindle microtubules, blue; DNA, pink.

Materials and Methods

Mammalian cell lines

U2OS and RPE-1 cells were obtained from ATCC or the source specified. Cells were grown at 37°C in 5% CO_2 in DMEM low glucose (Gibco 11885) (U2OS), or DMEM:F12+HEPES (Gibco 113300)(RPE-1) supplemented with 2 mM L-glutamine (Sigma 59202C) (RPE-1) supplemented with 10% heat inactivated FBS (F4135) and 1% antibiotic-antimycotic (Gibco 15240112). Cells were cultured without antibiotics during transfections, RNAi, and treatments for experiments. Cells were used for experiments before passage 30 (20 for RPE-1). Cells were tested for mycoplasma upon initial thaw and generation of new cell lines (Southern Biotech 13100-01), and untreated cells were continuously profiled for contamination by assessment of extranuclear DAPI/Hoechst 33258 staining.

U2OS IBB-GFP H2B-mCherry was generated by transfection of the plasmids using Lipofectamine 2000 (Thermo Fisher Scientific 11668), then plated into 10 cm dishes at ~100 cells per dish. Dishes were treated with 2 ug/ml puromycin and 400 ug/ml G418 in antibiotic-free media for 1.5-2 weeks until visible colonies of >100 cells formed. Non-overlapping colonies were isolated using sterile filter paper discs (Bel-Art F37847-0001) dipped in 0.25% trypsin-EDTA (Sigma 59428C or Gibco 25200) and applied to colonies for 30 s after washing dish with PBS. Isolated colonies were grown in 24 well plates under 1 ug/ml puromycin and 200 ug/ml G418 selection until confluent, after which colonies were imaged for fluorescence, expanded, and frozen down.

To generate U2OS GFP-Sec61β H2B-mCherry, U2OS GFP-Sec61β were transfected with H2B-mCherry-IRES-puro2v2.0 for 48 hours, then plated into 10 cm dishes at <100 cells/ml and selected with 0.5 µg/ml puromycin for 2 weeks. Colonies were trypsinized and picked with 1/8 in sterile cloning discs (Bel-Art F37847-0001) and grown to confluence in a T25 flask before imaging confirmation of marker expression.

Transfection and RNAi

Most transfections were performed with Lipofectamine 2000 (Thermo Fisher Scientific 11668) in Opti-MEM (Gibco 31985) using a 1:2 ratio of DNA:lipofectamine with DNA concentrations ranging from 0.05-0.3 µg DNA per cm^2 of growth surface. Briefly, DNA and lipofectamine were added to 10 µl OptiMEM per cm^2 of growth surface in separate borosilicate glass tubes (Thermo Fisher Scientific STT-13100-S). After 5 minutes incubation, DNA solution was added to lipofectamine solution. After 15 minutes, DNA:lipofectamine mix was added dropwise to cells plated 16-24 hrs prior to transfection in fresh antibiotic-free media (1 ml/9.6 cm^2 growth surface). Media was exchanged for antibiotic-free media after 6 hours. To increase transfection efficiency, plasmids used for live imaging were purified using the Zymopure II Plasmid Midi Prep kit, including a 10 min final elution at 56°C and use of the Zymopure endotoxin removal columns.

Transfections for lipin 1 overexpression were performed using PolyJet in vitro DNA transfection reagent (Signagen SL100688) using a 1:3 ratio of DNA:Polyjet using 0.1 µg DNA per cm^2 of growth surface. Protocol is identical to previous transfection

protocol except for using 5 µl OptiMEM per cm^2 of growth surface for mixes and no incubation before mixing reagents.

For experiments involving transient CTDNEP1 and/or NEP1R1 overexpression, pcDNA3.0 was used as an empty vector negative control. For experiments involving phenotype rescue with transient FLAG-lipin 1β construct overexpression, GFP-KDEL was used as a co-transfection marker, and untransfected cells within the same experiment were used as a negative control for effects of lipin 1β overexpression.

RNAi was performed using Dharmafect 1 (Horizon Discovery T-2001) in Opti-MEM according to the manufacturer's protocol. U2OS Sec61β/H2B-mCherry and U2OS IBB-GFP/H2B-mCherry were treated with 40 nM CTDNEP1 single siRNA (Dharmacon) or Ambion Silencer negative control 1 for 48 hours; all others were treated with 20 nM CTDNEP1 siGENOME SMARTpool or control pool #2 siRNA (Horizon Discovery) for 72 hours.

For RTN1/RTN3 knockdown, cells were treated with either 80 nM Ambion Silencer Select negative control #1 siRNA or 40 nM both Silencer Select RTN1 siRNA and Silencer Select RTN3 siRNA for 48 hours.

For SREBP1 or SCD knockdown, cells were treated with 20 nM Silencer Select negative control #1 siRNA or 20 nM Silencer Select SREBP1 or SCD siRNA for 72 hours. For SREBP1/2 knockdown, cells were treated with 40 nM Silencer Select negative control #1 siRNA or 20 nM both Silencer Select SREBP1 siRNA and Silencer Select SREBP2 siRNA for 72 hours.

RNAi knockdown efficiency was determined by qPCR or immunoblot analysis or by presence of expanded ER sheets in the RTN4^{KO} RTN1/3 knockdown.

CRISPR/Cas9 genome editing

All guide RNA sequences were designed using the online CRISPR tool http://crispr.mit.edu and reported no off-target matches. Nup160^{EN}-Halo: CACGGGATTTATTATATCGT RTN4^{KO}: CGTTCAAGTACCAGTTCGTG CTDNEP1^{EN}-GFP: GGGCATCAGACGGCATCCCA CTDNEP1^{KO}: ATGAAGTCAGGAGGCGTACC. The guide RNA sequences were synthesized as two oligos with BbsI overhangs and an additional guanidine base 5' to the protospacer sequence, and the oligos were phosphorylated with calf alkaline intestine phosphatase (New England BioLabs #M0290) and annealed by heating to 95°C and cooling to room temperature. The annealed oligos were cloned into pSPCas9(BB)-2A-Puro (PX459) v2.0 (a gift from Feng Zhang, Addgene plasmid #62988) that had been digested with BbsI-HF (New England BioLabs #R3539). For generation of KO cell lines, the vectors were transfected into U2OS cells using Lipofectamine 2000 and selected with 3 ug/ml puromycin (Invitrogen) for 48 hours. The remaining cells were grown up and gDNA isolated from the bulk population using a QiaAmp DNA Mini kit (Qiagen 51304). Genotyping was performed by sequencing and screening for indels using TIDE deconvolution (https://www.deskgen.com/landing/tide.html) (Brinkman et al., 2014). Once indels were detected in the bulk population, the cells were plated at <100 cells/ml into 10 cm dishes (RTN4^{KO}) or 96 well plates (CTDNEP1^{KO}) and grown in antibiotic-free DMEM with 10% FBS for 2 weeks. Colonies were trypsinized and picked with 1/8

in sterile cloning discs (Bel-Art) if in 10 cm dishes. Colonies were grown in 24-well plates until more than 10,000 cells could be harvested for gDNA sequencing and TIDE analysis to genotype for frameshift mutations. The RTN4^{KO} clonal cell line used in experiments showed to have -5bp deletions in >80% of alleles and 0% WT alleles as determined by TIDE deconvolution of sequencing and showed no expression of RTN4 by immunofluorescence (antigen is upstream of indel). The CTDNEP1^{KO} clonal cell line used in experiments showed to have +1 insertions in >80% of alleles and 0% WT alleles as determined by TIDE deconvolution. The homology-directed repair template for Nup160^{EN}-Halo was generated to add a 5-glycine linker and HaloTag7 sequence to the 3' end of the *NUP160* gene, fusing Halo to the C terminus of all NUP160 isoforms. The HDR template was engineered using a 4-piece Gibson assembly: 1) the vector backbone was EGFP-N1 (Clontech) amplified with oligos (listed below) so that the CMV promoter, MCS, and GFP sequence had been removed; 2) the left homology arm was an IDT gblock containing 800 bp upstream of the NUP160 stop codon with a silent mutation to the PAM sites of 1 potential guide RNA and a GGAGGCGGCGGCGGC linker and was flanked by 20-bp overhangs that overlapped with the EGFP-N1 backbone and HaloTag7; 3) HaloTag7 was amplified from Halo-N1 using oligos listed below (a silent mutation in aspartic acid was included in the forward primer to facilitate amplification of the gene); 4) the right homology arm was an IDT gblock containing 800 bp downstream of the NUP160 stop codon with 2 point mutations in the PAM sites of potential guide RNAs that was flanked by 20-bp overlap with HaloTag7 and the EGFP-N1

backbone. The CTDNEP1^{EN}-GFP homology-directed repair template was generated to add a 6-glycine linker and GFP sequence to the 3' end of the *CTDNEP1* gene, fusing GFP to the C terminus of all CTDNEP1 isoforms. The HDR template was engineered using a 4-piece Gibson assembly: 1) the vector backbone was EGFP-N1 (Clontech) amplified with oligos (listed below) so that the CMV promoter, multiple cloning site, and GFP sequences had been removed; 2) the left homology arm was an IDT gblock containing 800 bp upstream of the CTDNEP1 stop codon with silent mutations to the PAM sites of 2 potential guide RNAs and a GGTGGCGGTGGCGGTGGC linker and was flanked by 20-bp overhangs that overlapped with the EGFP-N1 backbone and GFP; 3) GFP was amplified from EGFP-N1 using oligos listed below 4) the right homology arm was an IDT gblock containing 800 bp downstream of the CTDNEP1 stop codon with 2 point mutations in the PAM sites of potential guide RNAs that was flanked by 20-bp overlap with GFP and the EGFP-N1 backbone.

To make endogenously tagged cells, the PX459v2.0 vector containing the guide sequences and the HDR templates were transfected into U2OS cells using Lipofectamine 2000 and treated with 3 ug/ml puromycin (Invitrogen) in antiobiotic-free media for 48 hours. The remaining cells were sorted for the top 1-2% of fluorescent cells (Nup160^{EN}-Halo cells were labeled with HaloTag TMR ligand (Promega). The sorted cells were plated at <100 cells/ml into 10 cm dishes, grown in antibiotic-free media for 2 weeks. Colonies were trypsinized and picked with 1/8 in sterile cloning discs (Bel-Art F37847-0001) and grown to confluence in a T75 flask, after which the gDNA was harvested using a Qiagen QiaAmp Mini kit.

For Nup160^{EN}-Halo clones, the Nup160 region was amplified with combinations of primers 1, 2, and 3 to determine correct placement, orientation, and presence of wild-type alleles in clonal cell lines. Protein lysates of the bulk and clonal populations were run on an 8% polyacrylamide gel and transferred to a nitrocellulose membrane for western blot with rabbit anti-HaloTag (Promega #G9281) to confirm that the tagged protein is full-length.

For CTDNEP1^{EN}-GFP clones, the CTDNEP1 region was amplified with the specified primer pairs to determine correct placement, orientation, and presence of wild-type alleles in clonal cell lines. Regions were additionally amplified and sequenced with the specified primers. Clone 1 used for experiments showed minimal presence of wild-type CTDNEP1 sequences in sequencing chromatograms. CTDNEP1^{EN}-GFP cells treated with 20nM of CTDNEP1 siRNA for 48 hours also show reduced nuclear envelope GFP fluorescence compared to control siRNA-treated CTDNEP1^{EN}-GFP cells (data not shown).

Plasmid generation

GFP-KDEL was modified from pDsRed2-ER (Clontech), which contains a signal peptide and ER retention sequence (KDEL), by PCR of GFP with AgeI and HindIII sites, digestion of the insert and pDeRed2 with AgeI/HindIII (NEB R0552, R3104), and ligation. CTDNEP1-HA was modified from CTDNEP1-v5-His (Han et al., 2012). pRK5 FLAG-lipin 1β 19xA PAP dead was modified from pRK5 FLAG-lipin 1β 19xA using Quickchange Mutagenesis to make the following mutations: D712E, D714E. For pRK5 FLAG-lipin 1β-NLS and -NES, the NLS of nucleoplasmin or NES of PKIα were appended to the C terminus of lipin 1β using In-Fusion (Takara Bio).

Lipidomics

Early-passage cells were counted by hemocytometer, suspended in PBS at a concentration of $3x10^6$ cells/ml, and flash frozen in liquid nitrogen. Triplicate samples were submitted for each condition. When noted, corresponding triplicate samples were lysed and protein extracted and protein concentration determined by Pierce BCA assay. Sample processing and lipidomics were performed and obtained at Lipotype GmbH. Samples were spiked with lipid class internal standards, and lipids were extracted using chloroform-methanol extraction using a Hamilton Robotics STARlet. Samples were infused using an Advion Triversa Nanomate automated nano-flow electrospray ion source with positive and negative ion mode utilized. Mass spectra were acquired using a Thermo Scientific Q-Exactive hybrid quadruple/Orbitrap mass spectrometer in MS-only mode and tandem MS mode. Lipid species were identified using LipotypeXplorer, and data was processed using Lipotype LIMS and LipotypeZoom. Lipid class pmols/mg protein was determined using protein concentration and sample volume analyzed from each replicate.

Mitotic shakeoff, micronuclei enrichment, and small molecule inhibitor treatment

For mitotic shakeoff, cells were grown to at least 50% confluence in 75 cm^2 flasks. Cells were washed with PBS or antibiotic-free media to clear debris, then flasks were whacked repeatedly on all sides and tapped on the bottom surface with a reflex hammer (DR Instruments S72118) until at least 50% of mitotic cells were

dislodged. The cell media was collected and centrifuged at 300xg for 5 min, then cells were additionally washed or plated.

For nocodazole washout, cells at 50-80% confluence in 75 cm^2 flasks were washed with 37°C PBS to clear debris and then treated with 100 ng/ml nocodazole (Sigma M1404) in antibiotic free media for 6 hours (Liu et al., 2018). Cells were subject to mitotic shakeoff without washing, then washed 3x with 37°C PBS. After the final wash, cells were plated onto acid-washed coverslips (coated with 1 ug/ml poly-D-lysine (Sigma P7886) for short-term washout) and incubated for 45 min-60 min (short-term) or 18-20 hours (long-term) before immunofluorescence processing.

For RO-3306/MPS1i micronuclei enrichment, cells were treated with 9 μM RO-3306 (Calbiochem 217699) for 19 hours, washed 7 times, then treated with 1 μM NMS-P715 (MPS1i) (Calbiochem 475949) for 18 hours before processing for immunofluorescence (Liu et al., 2018). K_i values mentioned above were obtained from Calbiochem.

For imaging cells arrested at the G2/M transition, cells in ibidi 8 well plates were treated with 9 μM RO-3306 for 18-20 hours and washed 7 times with Fluorobrite DMEM + FBS on the microscope stage, then imaged immediately.

Fatty acid synthesis inhibition and fatty acid supplementation

To inhibit fatty acid synthesis, cells were treated with 10 μM TOFA (Cayman Chem) in DMSO. Cells were treated with TOFA for 24 hours with or without fatty acid supplementation for ER and nucleus visualization or for 5-48 hours for ER

visualization over time. Cells were treated with TOFA for 48 hours for micronuclei quantification.

For fatty acid supplementation, cells were plated at a density of 200,000 cells/ml in 6 well plates. Stocks of oleic acid, linoleic acid, and palmitic acid were made in methanol and pipetted into a 50 ml conical vial, then dried with an ambient air stream. Pre-warmed DMEM containing 0.5% fatty acid-free BSA (Sigma Cat#A8806) was added to a final concentration of 25 μM palmitic acid, 50 μM oleic acid, and 25 μM linoleic acid (100 μM total fatty acid concentration; 1:2:1 ratio of palmitic:oleic:linoleic acid). The solution was incubated at 37°C for 30 min, then held to the bottom of a sonicating bath for 30 s, then incubated at 37°C for 10 min until solution was clear. FBS was added to a final concentration of 10% v/v. Cells were treated with DMEM with 10% FBS and 0.5% BSA alone or DMEM with 10% FBS 0.5% BSA, and 100 μM fatty acids with DMSO or 10 μM TOFA in DMSO for 24 hrs prior to immunofluorescence processing.

Quantitative real-time PCR

RNA was harvested using the RNeasy Mini kit (Qiagen 74104) using the manufacturer's protocol, using Qiashredder columns (Qiagen 79654) for tissue homogenization and with additional RNase-free DNase (Qiagen 79254) treatment after the first RW1 wash and subsequently adding another RW1 wash. RNA was eluted with RNAse-free water and diluted to 50 ng/μl. RNA was subject to reverse transcription using the iScript Reverse Transcription Supermix (Bio-Rad 1708840) with 400 ng RNA per reaction. The subsequent cDNA was diluted 1:5 for RT-qPCR. cDNA was analyzed for RT-qPCR using the iTaq universal SYBR Green

Supermix (Bio-Rad 1725120). Cycle threshold values were analyzed using the Δ ΔCt method. Statistical testing was performed on ΔCt values.

Immunofluorescence

Cells were washed 2x with warm PBS and fixed in 4% paraformaldehyde (+0.1% glutaraldehyde for ER structure analyses) in PBS for 15 min, permeabilized in 0.5% Triton X-100 for 5 min, then washed 3 times with PBS and blocked in 3% BSA in PBS for 30 min. Samples were transferred to a humidity chamber and incubated with primary antibodies in 3% BSA in PBS for 1 hour at room temperature with rocking. Samples were washed with PBS 3 times for 5 min, then incubated with secondary antibodies in 3% BSA in PBS for 1 hour at room temperature in the dark with rocking. Samples were then washed with PBS 3 times for 5 min in the dark. For experiments visualizing nuclear structure and/or micronuclei, cells were additionally stained with 1 µg/ml Hoechst 33258 (Thermo Fisher Scientific H3569) in PBS for 1 min followed by one PBS wash. Coverslips were mounted with ProLong Gold Antifade reagent + DAPI (Thermo Fisher P36935) and sealed with clear nail polish. For samples treated with goat primary antibodies, 5% normal donkey serum (Sigma D9663) was used in place of 3% BSA.

When indicated, cells were fixed and stained to visualize kinetochore microtubules (Thompson and Compton, 2011) by extracting in 100 mM PIPES, 1 mM $MgCl_2$, 1 mM $CaCl_2$, 0.5% Triton X-100, pH 6.8 for 4 min, then fixing in 1% glutaraldehyde in PBS for 10 min and quenched 2 times with 0.1% $NaBH_4$ in TBS for 10 min each. Cells were washed twice with 10 mM Tris, 150 mM NaCl, 10% BSA and then

stained with tubulin antibody for 1.5 hours, washed with PBS, then stained with secondary antibody for 1 hour, washed with PBS, then mounted with ProLong Gold + DAPI.

Immunoblot

Lysis buffers used were: 1% SDS in 2mM Tris-HCl pH 7.2 (RTN4^{KO}, NUP160); 1% NP-40, 150 mM NaCl, and 1 tablet/50 ml cOmplete protease inhibitor cocktail (Roche 11836170001) in 20 mM Tris pH 7.5 (calnexin, calreticulin, BiP, RTN4); or RIPA buffer (1% NP-40, 0.5% sodium deoxycholate, 0.1% SDS, 150 mM NaCl, and 1 tablet/50 ml cOmplete protease inhibitor cocktail in 25 mM Tris pH 7.4) (SREBP1, SREBP2, SCD; protein concentration determination for lipidomic analysis). Cell lysates were removed from growth surfaces by scraping with a rubber policeman after incubation in lysis buffer or by adding lysis buffer to cell pellets collected by trypsinization and centrifugation at 300xg for 5 min followed by 1-2 PBS washes. Lysates were homogenized by pushing through a 23G needle 30 times and then centrifuged at >20,000xg for 10 min at 4°C, then protein concentration was determined using the Pierce BCA Protein assay kit (Thermo Scientific 23225). 10-30 µg of lysates/lane were run on 8-15% polyacrylamide gels dependent on target size, and protein was wet transferred to 0.22 µm nitrocellulose (<100 kDa) or PVDF (>100 kDa) membranes. For SREBP and SCD knockdown assessment, Ponceau S staining was used to visualize transfer efficiency, then washed with TBS or DI water. Membranes were blocked in 5% nonfat dry milk or BSA in TBS for 1 hour. Membranes were briefly washed in TBS-0.1% Tween 20 (TBS-T) then incubated with primary antibodies in 5% milk for 1 hour at room

temperature or overnight at 4°C with rocking. Membranes were washed 3 times for 5 min in TBS-T, then incubated with anti-HRP secondary antibodies in 5% milk in TBS-T for 1 hour at room temperature with rocking. Membranes were washed 3 times for 5 min in TBS-T. Clarity or Clarity Max ECL reagent (Bio-Rad 1705060S, 1705062S) was used to visualize chemiluminescence, and images were taken with a Bio-Rad ChemiDoc or ChemiDoc XRS+ system. Exposure times of images used for analysis or presentation were maximum exposure before saturation of pixels around or within target bands.

Live cell imaging

For live imaging, cells were plated in Willco Wells 35 mm dishes (Willco Wells HBST-3522), ibidi 2 well imaging chambers (ibidi 80287) with DIC lid (ibidi 80055); or ibidi 8 well imaging chambers (ibidi 80827). Samples were imaged in a CO_2-, temperature-, and humidity-controlled Tokai Hit Stage Top Incubator. Objectives were also heated to 37°C. For CO_2-controlled imaging, the imaging media used was Fluorobrite DMEM (Gibco A1896701) supplemented with 10% FBS. U2OS IBB-GFP/H2B-mCherry and U2OS GFP-Sec61β/H2B-mCherry mitotic cells (except cells treated with RO-3306) were imaged using a custom aluminum stage insert (P. Forscher) heated to 37°C with heating tape and temperature monitored using a Physitemp thermistor (BAT7001H) and probe (IT-18), with objective heating and using 140 mM NaCl, 2.5 mM KCl, 1.8 mM $CaCl_2$, 1.0 mM $MgCl_2$, 20 mM HEPES, 15 mM glucose, pH 7.4 as the live cell imaging solution. When indicated, cells were treated with 1 μM SiR-DNA (Cytoskeleton, Inc. CY-SC007) for 1 hour prior to imaging and kept in SiR-DNA-containing live imaging media

during imaging. For STED imaging, cells were labeled with 0.5 μM 647-SiR (NEB S9102S) for 30 min at 37°C, followed by a >15 min washout at 37°C, prior to imaging.

Microscopy

Samples were imaged on an inverted Nikon Ti microscope equipped with a Yokogawa CSU-X1 confocal scanner unit with solid state 100-mW 488-nm and 50-mW 561-nm lasers, using a 60×1.4 NA plan Apo objective lens (or 10x 0.25 NA ADL objective with 1.5x magnification), and a Hamamatsu ORCA R-2 Digital CCD Camera.

Samples with SiR-DNA/GFP-KDEL, FLAG-lipin/calnexin staining, telophase nocodazole washout, SREBP depletion, or 20x images were imaged on an inverted Nikon Ti Eclipse microscope equipped with a Yokogawa CSU-W1 confocal scanner unit with solid state 100 mW 405, 488, 514, 594, 561, 594, and 640 nm lasers, using a 60x 1.4 NA plan Apo objective lens and/or 20x plan Fluor 0.75 NA multi-immersion objective lens, and a prime BSI sCMOS camera.

Images for ER sheet/nanohole visualization were imaged on a Leica SP8 gated STED 3x with a SuperK Extreme EXW-12 pulsed white light laser (excitation) and Onefive Katana-08HP pulsed 775 nm laser (depletion) with a HyD hybrid detector; imaging was performed using a 100x plan Apo 1.4 NA oil objective. SiR fluorescence was imaged with 633 nm excitation and 775 nm depletion wavelength and collected between 650-750 nm with the detector. Pixel size of STED images was 18.9 nm. STED images were processed by applying a 1.0 pixel-radius Gaussian filter.

Image analysis

Image analysis was performed using FIJI/ImageJ unless otherwise noted. For scoring of ER phenotypes, cells expressing moderate levels of GFP-KDEL with no overexpression artifacts (dense fluorescent clumps in ER or nuclei) were included for analysis. For scoring of interphase ER expansion, cells with a network of peripheral ER tubules visualized with GFP-KDEL or calnexin staining were considered “normal”, while cells with ER sheets and tubules extending into the periphery with a lack of any tubular network were considered to have “expanded ER”. Additionally, cells with the appearance of thin ER tubules, large gaps between tubules, and a smaller cluster of perinuclear ER were considered to have “reduced ER” with TOFA treatment. These phenotypes were additionally quantified with percent abundance of cytoplasmic KDEL/calnexin signal: for cells with the entire ER captured within 0.3-0.5 μm interval z stacks, 8-bit maximum intensity projections were made of the whole field of view. To ensure the different ER morphologies were all accounted for after thresholding, the 8-bit max projections were subject to unsharp masking with a radius of 2 and mask of 0.6. The max intensity projection was thresholded using the Huang threshold of object fuzziness (Huang and Wang, 1995). The cell border and nuclear border for each cell were manually traced using ER fluorescent signal, and the percent of KDEL-positive pixels per nucleus-free cell area was measured. RPE-1 ER and ER phenotypes in SCD-depleted cells were scored blindly. With SCD depletion, cells were additionally blindly scored for the presence of GFP-KDEL punctae in the perinuclear region that are brighter than the surrounding perinuclear ER.

For scoring of intracellular ER membranes in prometaphase cells, whole 75 cm^2 flasks of cells were transfected with GFP-KDEL and imaged 48 hours later after mitotic shakeoff and plating into 1 well per flask of an ibidi 8-well imaging chamber. Cells expressing GFP-KDEL in prometaphase up until metaphase (determined by DIC chromatin appearance) were imaged with 0.5 μm stacks for 20 μm total z height. 90x images of cells expressing GFP-KDEL and subject to mitotic shakeoff were blindly categorized for presence of a) no intracellular ER membranes ("cleared"), (b) few ER tubules within the cell interior ("partially cleared"); or c) large (>2 μm length) sheets and/or several tubules within the cell interior ("not cleared"). For scoring of intranuclear ER membranes in telophase nuclei, cell nuclei were scored 25 m post anaphase onset or in early G1 for presence of membrane extensions dimmer than the nuclear rim (extensions the same intensity as the nuclear rim were considered invaginations of the INM/ONM that are common in control U2OS cells). In analysis of intranuclear membrane extensions including categories, "mild" refers to cells with 1-2 extensions, while "severe" cases have several intranuclear membrane extensions.

For scoring of mitotic profiles in control and CTDNEP1^{KO} U2OS cells, 20x images of DAPI and tubulin-stained asynchronous, untreated cell populations were analyzed. For scoring of mitotic profiles in nocodazole washout (1 hour) control and CTDNEP1^{KO} U2OS cells, 60x images of DAPI and tubulin-stained cell populations were analyzed. Mitotic cells were identified by DAPI appearance as relatively bright mitotic chromatin and tubulin appearance of duplicated centrosomes and presence of mitotic spindle. Staging was performed based on

the following criteria. Prometaphase: DAPI condensed into visible chromosomes not yet aligned into single metaphase plate, centrosomes duplicated and building spindle visible (in nocodazole washout, chromosome condensation and lack of metaphase-telophase spindle features was used to score prometaphase cells due to spindle rebuilding after nocodazole treatment); Metaphase: chromosomes aligned on metaphase plate and bipolar mitotic spindle present; Anaphase: visible separation of chromosome masses with bipolar mitotic spindle that may be elongated; Telophase/cytokinesis: chromosome masses separated into two daughter cells with apparent cytokinesis and spindle midzone visible in tubulin staining; early G1: chromatin decondensed, cytokinesis nearly complete with spindle midbody present.

For quantification of micronuclei, images taken at 60x were scored for presence of micronuclei (DNA fragments encased in an emerin or calnexin-positive rim apart from main nucleus <~20% in size of the main nucleus). Severely lobulated/partitioned “hypermicronucleated” nuclei (DNA fragments/lobes apart from the main nucleus >~20% in size of the main nucleus) and micronuclei were scored through oculars or in 60x images of cells with nuclear envelope staining. Nuclei with both lobes/partitions and micronuclei were considered hypermicronucleated. For quantification of peripheral chromosome/tubulin masses in cells subjected to short-term nocodazole washout, 60x images of cells processed for immunofluorescence without non-kinetochore microtubule depolymerization were scored for the presence of chromosome masses with

microtubules extending to them that were to away to the cell periphery compared to the primary nuclei chromosome masses.

Nuclear solidity was quantified as described (Fonseca et al., 2019). Briefly, DAPI/Hoechst images were thresholded with the ImageJ default setting, then the magic wand tool was used to select segmented nuclei. Nuclei that were unable to be segmented due to poor signal:noise, adjacent nuclei touching, or presence of a micronucleus touching the main nucleus were not included in the analysis. Segmented and selected nuclei were measured using the ImageJ shape descriptors measurement metric. Data were expressed as % of nuclei with a solidity value less than the control U2OS average minus 1 standard deviation.

To quantify the percent of mitotic cell diameter that is occupied by ER membranes in cells expressing GFP-Sec61β/H2B-mCherry or GFP-KDEL/SiR-DNA, 60x image stacks of cells at anaphase onset (determined by first frame of visible chromatid separation) were obtained. Image background was subtracted using the average value of 3 boxes from surrounding the cell (but not within adjacent cells). A 10-pixel thick line was drawn encompassing the cell diameter along the metaphase plate (in the center of the dividing chromatin masses, along the division plane), and a profile plot was generated. The local maxima of theSec61β/KDEL peaks for each side of the cell was determined, and the width of the half maxima for each of the 2 Sec61β/KDEL peaks was quantified and added together. This value was divided by the diameter of the cell (determined by the bounds of the Sec61β/KDEL half maxima) to determine the % of the cell diameter occupied by

ER signal. For representation, plot profiles shown are normalized to minimum and maximum of ER and DNA signal.

For quantification of nuclear import/size during mitotic exit with CTDNEP1 RNAi in U2OS IBB-GFP/H2B/mCherry cells,15x time lapse images were taken. Cells that were not overlapping, were fully in the imaging plane in z, had bright enough signal to distinguish from background, and did not experience z drift were included for analysis. IBB background intensity was taken from the first frame of the time lapse from a box in a cell-free area and subtracted from all frames. Nuclear size over time after anaphase onset was measured using the thresholded H2B-positive regions (using imageJ default algorithm) every 30 sec 3-30 min after anaphase onset. Integrated IBB-GFP intensity was measured for the entire thresholded chromatin (H2B positive) mass every 30 sec from 3-30 min after anaphase onset. IBB values were normalized to the minimum and maximum measured values for integrated intensity and size, then divided by the value at 3 min to be expressed as fold change. Values from both nuclei per daughter cell were averaged when applicable.

To quantify lagging chromosomes in U2OS GFP-Centrin2/GFP-CENPA/mCherry-α tubulin cells, cells were imaged immediately after mitotic shakeoff. 60x image stacks encompassing the whole cell volume of late anaphase and telophase cells expressing all markers and lacking large open vacuoles (an overexpression artifact) were included for analysis. Cell images were blindly categorized as having GFP punctae apart from the segregating chromosome masses that did not have associated bright tubulin (which would indicate a Centrin2 puncta). Metaphase cell

images were taken at the same time for spindle pole-pole distance measurements. To measure spindle pole-pole distance in U2OS GFP-Centrin2/GFP-CENPA/mCherry-α tubulin cells, 60x images stacks encompassing the whole cell volume of metaphase cells that had no spindle tilt were analyzed to determine the central z plane to take measurements. A line was drawn from the center of the Centrin2 punctae (or brightest tubulin punctae if Centrin2 not expressed) and used to measure the pole-pole distance.

Statistical analysis

GraphPad Prism 8 was used for all statistical analysis. Continuous data was tested for normality using a Shapiro-Wilk test. For experimental setups in which > 10 samples (n) per experimental replicate (N) were able to be collected consistently, continuous data was measured with paired t tests of experimental replicate means. Superplot format was used for representing percent of ER-positive pixels in cytoplasm area (Lord et al., 2020). Experimental replicates of discrete data were plotted with shapes indicating separate replicates to display reproducibility, and incidences between groups (replicates pooled) were tested for significance using Fisher's exact test (2 categories) or Chi square test (>2 categories). Statistical tests used, sample sizes, definitions of n and N, and p values ($p<0.05$ as significance cutoff) are reported in figures and/or figure legends. For quantification of all data where >10 samples could be gathered within an experimental repeat, sample size calculations using the online tool (https://clincalc.com/stats/samplesize.aspx) determined the adequate sample size for number of cells to analyze for sufficient (80%) power.

Key Resources Table

Plasmid or siRNA	Source	notes
EGFP-N1	Takara Bio, Inc. 6085-1	
Halo-N1	Bewersdorf lab	
pSPCas9(BB)-2A-Puro (PX459) v2.0	Addgene #62988	
GFP-KDEL	(Merta et al., 2021) (L.K. Schroeder)	ssGFP-KDEL
SNAP-KDEL	(Schroeder et al., 2018)	
IBB-eGFP	EUROSCARF P30631	
pH2B_mCherry_IRES_puro2	Addgene 21045	
pRK5 FLAG-lipin 1β (Mm)	(Peterson et al., 2011)	Addgene #32005
pRK5 FLAG-lipin 1β 19xA	(Peterson et al., 2011)	Addgene #32007
pRK5 FLAG-lipin 1β 19xA PAP dead	(Merta et al., 2021) (M. Deline)	
pRK5 FLAG-NLS-lipin 1β	This study (S. Lee)	
pRK5 FLAG-NES-lipin 1β	This study	
CTDNEP1-HA	(Merta et al., 2021) (M. Deline)	
CTDNEP1 D67E-HA	(Merta et al., 2021) (C.L. Hu)	
FLAG-NEP1R1	(Merta et al., 2021) (M. Deline)	
CTDNEP1 custom single siRNA FWD, no modifications	Dharmacon	AGGCAGAUCCGCACGGUAA
CTDNEP1 SMARTpool siRNA	Dharmacon M-017869-00-0005	
siGENOME Non-targeting siRNA Pool #2	Dharmacon D-001206-14-05	
Silencer Negative control siRNA #1	Invitrogen AM4611	
Silencer Select negative control siRNA #1	Life Technologies 4390843	
Silencer Select Rtn1 siRNA	Life Technologies 4427037-s12378	

Silencer Select Rtn3 siRNA	Life Technologies 4427037-s20162	
Silencer Select SREBF1 (SREBP1a/c) siRNA	Life Technologies 4427038-s129	
Silencer Select SREBF2 (SREBP2) siRNA	Life Technologies 4427038-s29	
Oligo name	**Sequence**	**notes**
EGFP-N1 backbone FWD	CCTCCCCCTGAACCTGAAAC	
EGFP-N1 backbone REV	GGCTATGAACTAATGACCCCGT	
HaloTag7 FWD	ATGGACCCGAAATCGGTACT	
HaloTag7 REV	GCCGGAAATCTCTAGCGTC	
GFP FWD	ATGGTGAGCAAGGGCGAG	
GFP REV	TTACTTGTACAGCTCGTCCATGC	
Nup160^{EN}-Halo genotyping PCR FWD 1	AGCAGTTACACCTTACAGCTTG	upstream of left homology arm
Nup160^{EN}-Halo genotyping PCR REV 2	AGGACTTCCACATAATGGGG	within Nup160-Halo
Nup160^{EN}-Halo genotyping PCR REV 3	AACTCAAGAAGGGTCAAAAGGCT	downstream of right homology arm
CTDNEP1^{EN}-GFP genotyping PCR FWD 1	CCTAGATTATCCCTAGTTTGCTGTA	Upstream of left homology arm
EGFP-N1 backbone FWD	CCTCCCCCTGAACCTGAAAC	
EGFP-N1 backbone REV	GGCTATGAACTAATGACCCCGT	
HaloTag7 FWD	ATGGACCCGAAATCGGTACT	
HaloTag7 REV	GCCGGAAATCTCTAGCGTC	
GFP FWD	ATGGTGAGCAAGGGCGAG	

GFP REV	TTACTTGTACAGCTCGTCCATGC	
Nup160^{EN}-Halo genotyping PCR FWD 1	AGCAGTTACACCTTACAGCTTG	upstream of left homology arm
Nup160^{EN}-Halo genotyping PCR REV 2	AGGACTTCCACATAATGGGG	within Nup160-Halo
Nup160^{EN}-Halo genotyping PCR REV 3	AACTCAAGAAGGGTCAAAAGGCT	downstream of right homology arm
CTDNEP1^{EN}-GFP genotyping PCR FWD 1	CCTAGATTATCCCTAGTTTGCTGTA	Upstream of left homology arm
CTDNEP1^{EN}-GFP genotyping PCR REV 1	GCTGAACTTGTGGCCGTTTA	within GFP
CTDNEP1^{EN}-GFP genotyping PCR FWD 2	AAGTGAGGCACAATGGCAGT	in CTDNEP1 left homology arm
CTDNEP1^{EN}-GFP genotyping PCR REV 2	AAGGACCTAAGGCCGCTTTG	In CTDNEP1 right homology arm
CTDNEP1^{EN}-GFP genotyping sequencing FWD	GGCTGTGGGCAAATTGAACC	in CTDNEP1 left homology arm
CTDNEP1^{EN}-GFP genotyping sequencing REV	CCAGTCCTGCCTCTTCACAA	In CTDNEP1 right homology arm
Rtn4 KO genotyping sequencing FWD	TTCGTGGTCAAAAATAAAGGTGTT	
Rtn4KO genotyping sequencing REV	TCCTCATCAAACCTACCCATGTT	
CTDNEP1^{KO} genotyping sequencing FWD	CCCGGAATCGGCTAGGTAAG	
CTDNEP1^{KO} genotyping sequencing REV	AGAGGGCGATGCCATACAAG	
Hs CTDNEP1 qPCR FWD	CATTTACCTTCTGCGGAGGC	Spans exon 1
Hs CTDNEP1 qPCR REV	CACCTGGGCTAGCCGATTC	Spans exon 2 and 3

Hs GAPDH qPCR FWD	GTCTCCTCTGACTTCAACAGCG	
Hs GAPDH qPCR REV	ACCACCCTGTTGCTGTAGCCAA	
Antibody	**Source**	**notes**
Mouse α-tubulin DM1A	Millipore Sigma 05-829	1:5000 IB, 1:1000 IF
mouse α FLAG	Sigma F3165	1:4000 IB, 1:1000 IF
Rabbit α HA	Cell Signaling Technologies 3724T	1:1000 IB, 1:800 IF
Goat α Rtn4/NogoA	Santa Cruz sc-11032 (discontinued)	1:200
Mouse α RTN4	Santa Cruz sc-271878	1:200
Rabbit α-HaloTag	Promega G9281	1:1000
Rabbit α-emerin	Proteintech 10351	1:200
Rabbit anti-calnexin	Abcam Ab22595	1:1000
Rabbit anti-calreticulin	Abcam Ab2907	1:1000
Goat α GFP	Hyman lab	1:1000
Rabbit anti-PCNA	Proteintech 10205-2-AP	1:5000
Mouse anti-GAPDH	GeneTex GTX28245	1:1000-1:2000
Rabbit anti-BiP (Grp78)	Abcam Ab21685	1:400
Rabbit α SREBP1 (2A4)	Santa Cruz sc-13551X	1:250
Rabbit α SREBP2	Abcam ab30682	
Mouse anti-goat IgG-HRP	Santa Cruz sc-2354	1:2500
Goat anti mouse IgG-HRP	Thermo Fisher 31430	1:10000
Goat anti rabbit IgG-HRP	Thermo Fisher 31460	1:10000
Rhodamine RedX Donkey α mouse IgG	Jackson Immuno 715-295-150	1:250
FITC Goat α mouse IgG	Jackson Immuno 115-095-146	1:250
FITC Goat anti rabbit IgG	Jackson Immuno 111-095-003	1:250
FITC Donkey anti Goat IgG	Jackson Immuno 705-095-147	1:250
Rhodamine RedX goat anti rabbit IgG	Jackson Immuno 111-295-003	1:250

Alexa Fluor 488 Donkey anti mouse IgG	Jackson Immuno 715-545-150	1:250
Alexa Fluor 647 goat anti mouse 647	Jackson Immuno 115-605-003	1:250
Cell lines	**Source**	**notes**
U2OS	Slack lab	N/A
RPE-1	Breslow lab	N/A
U2OS GFP-Sec61β	Rapoport lab	N/A
U2OS GFP-Sec61β H2B-mCherry	(Merta et al., 2021)	N/A
U2OS lBB-GFP H2B-mCherry	This study	N/A
U2OS GFP-Centrin 2 GFP-CENPA mCherry-α tubulin	(Yu et al., 2019)	N/A
U2OS CTDNEP1^{KO}	(Merta et al., 2021)	N/A
U2OS CTDNEP1^{KO} CTDNEP1-HA^{stable}	(Merta et al., 2021) (J.W. Carrasquillo Rodríguez)	N/A
U2OS RTN4^{KO}	(Schroeder et al., 2018)	
U2OS CTDNEP1^{EN}-GFP	This study	N/A
U2OS NUP160^{EN}-Halo	(Schroeder et al., 2018)	N/A
Chemicals, Peptides, and Recombinant Proteins	**Source**	**Cat#**
Nocodazole	Sigma	Cat#M1404
RO-3306	EMD Millipore	Cat#217699
TOFA	Cayman Chemicals	Cat#10005263
NMS-P715	EMD Millipore	Cat#475949
SiR-DNA	Cytoskeleton, Inc.	Cat#CY-SC007
Puromycin HCl	Thermo Fisher	Cat#A1113803
G418	EMD Millipore	Cat#345810
Blasticidin	Sigma	Cat#R21001
Palmitic acid	Sigma	Cat#P0500
Oleic acid	Sigma	Cat#O1008
Linoleic acid	Sigma	Cat#L5900
SNAP-Cell 647-SiR	NEB	Cat# S9102S
HaloTag-TMR	Promega	Cat#G8252
Critical commercial assays	**Source**	**Cat#**
Zymopure II plasmid Midi prep kit	Zymogen	Cat#D4200

Pierce BCA Protein Assay kit	Thermo Scientific	Cat#23225
Software		
FIJI	(Schindelin et al., 2012)	https://imagej.net/Fiji
GraphPad Prism 8/9	GraphPad Software	https://www.graphpad.com/scientific-software/prism/

References

Adhikari, A. (2019). Micronuclei (MN), an important cancer biomarker. Edelweiss Cancer OA *1*, 2689–6737.

Afonso, O., Matos, I., Pereira, A.J., Aguiar, P., Lampson, M. a, and Maiato, H. (2014). Feedback control of chromosome separation by a midzone Aurora B gradient. Science *332*, 332–336.

ALJohani, A.M., Syed, D.N., and Ntambi, J.M. (2017). Insights into Stearoyl-CoA Desaturase-1 Regulation of Systemic Metabolism. Trends Endocrinol. Metab. *28*, 831–842.

Almeida, A.C., and Maiato, H. (2018). Chromokinesins. Curr. Biol. *28*, R1131–R1135.

Anderson, D.J., and Hetzer, M.W. (2007). Nuclear envelope formation by chromatin-mediated reorganization of the endoplasmic reticulum. Nat. Cell Biol. *9*, 1160–1166.

Anderson, D.J., and Hetzer, M.W. (2008). Reshaping of the endoplasmic reticulum limits the rate for nuclear envelope formation. J. Cell Biol. *182*, 911–924.

von Appen, A., Lajoie, D., Johnson, I.E., Trnka, M.J., Pick, S.M., Burlingame, A.L., Ullman, K.S., and Frost, A. (2020). LEM2 phase separation promotes ESCRT-mediated nuclear envelope reformation. Nature.

Asencio, C., Davidson, I.F., Santarella-Mellwig, R., Ly-Hartig, T.B.N., Mall, M., Wallenfang, M.R., Mattaj, I.W., and Gorjánácz, M. (2012). Coordination of kinase and phosphatase activities by Lem4 enables nuclear envelope reassembly during mitosis. Cell *150*, 122–135.

Audhya, A., Desai, A., and Oegema, K. (2007). A role for Rab5 in structuring the endoplasmic reticulum. J. Cell Biol. *178*, 43–56.

Bahmanyar, S., and Schlieker, C. (2020). Lipid and protein dynamics that shape nuclear envelope identity. Mol. Biol. Cell *31*, 1315–1323.

Bahmanyar, S., Biggs, R., Schuh, A.L., Desai, A., Müller-Reichert, T., Audhya, A., Dixon, J.E., and Oegema, K. (2014). Spatial control of phospholipid flux restricts endoplasmic reticulum sheet formation to allow nuclear envelope breakdown. Genes Dev. *28*, 121–126.

Bahr, G.F., and Beermann, W. (1954). The fine structure of the nuclear membrane in the larval salivary gland and midgut of Chironomus. Exp. Cell Res. *6*, 519–522.

Ballweg, S., Sezgin, E., Doktorova, M., Covino, R., Reinhard, J., Wunnicke, D., Hänelt, I., Levental, I., Hummer, G., and Ernst, R. (2020). Regulation of lipid saturation without sensing membrane fluidity. Nat. Commun. *11*, 1–13.

Barbosa, A.D., Sembongi, H., Su, W.-M., Abreu, S., Reggiori, F., Carman, G.M., and

Siniossoglou, S. (2015). Lipid partitioning at the nuclear envelope controls membrane biogenesis. Mol. Biol. Cell *26*, 3641–3657.
Beaudouin, J., Gerlich, D., Daigle, N., Eils, R., and Ellenberg, J. (2002). Nuclear Envelope Breakdown Proceeds by Microtubule-Induced Tearing of the Lamina. Cell *108*, 83–96.
Beck, M., Förster, F., Ecke, M., Plitzko, J.M., Melchior, F., Gerisch, G., Baumeister, W., and Medalia, O. (2004). Nuclear pore complex structure and dynamics revealed by cryoelectron tomography. Science (80-.). *306*, 1387–1390.
Ben-Sahra, I., and Manning, B.D. (2017). mTORC1 signaling and the metabolic control of cell growth. Curr. Opin. Cell Biol. *45*, 72–82.
Bharadwaj, R., and Yu, H. (2004). The spindle checkpoint, aneuploidy, and cancer. Oncogene *23*, 2016–2027.
Bigay, J., and Antonny, B. (2012). Curvature, Lipid Packing, and Electrostatics of Membrane Organelles: Defining Cellular Territories in Determining Specificity. Dev. Cell *23*, 886–895.
Bola, B., and Allan, V. (2009). How and why does the endoplasmic reticulum move ? Biochem Soc Trans *37*, 961–965.
Boroda, S., Takkellapati, S., Lawrence, R.T., Entwisle, S.W., Pearson, J.M., Granade, M.E., Mullins, G.R., Eaton, J.M., Villén, J., and Harris, T.E. (2017). The phosphatidic acid-binding, polybasic domain is responsible for the differences in the phosphoregulation of lipins 1 and 3. J. Biol. Chem. *292*, 20481–20493.
Borradaile, N.M., Han, X., Harp, J.D., Gale, S.E., Ory, D.S., and Schaffer, J.E. (2006). Disruption of endoplasmic reticulum structure and integrity in lipotoxic cell death. J. Lipid Res. *47*, 2726–2737.
Braakman, I., and Hebert, D.N. (2013). Protein folding in the endoplasmic reticulum. Cold Spring Harb. Perspect. Biol. *5*, 1–17.
Breslow, D.K. (2013). Sphingolipid homeostasis in the endoplasmic reticulum and beyond. Cold Spring Harb. Perspect. Biol. *5*, 1–16.
Brinkman, E.K., Chen, T., Amendola, M., and Van Steensel, B. (2014). Easy quantitative assessment of genome editing by sequence trace decomposition. Nucleic Acids Res. *42*, 1–8.
Bykov, V.J.N., Eriksson, S.E., Bianchi, J., and Wiman, K.G. (2018). Targeting mutant p53 for efficient cancer therapy. Nat. Rev. Cancer *18*, 89–102.
Caja, L., Bellomo, C., and Moustakas, A. (2015). Transforming growth factor β and bone morphogenetic protein actions in brain tumors. FEBS Lett. *589*, 1588–1597.
Callan, H.G., and Tomlin, S.G. (1950). Investigation of the structure of the nuclear membrane by means of the electron microscope. Exp. Stud. Amphib. Oocyte Nucl. *137*, 367–378.
Capelson, M., Doucet, C., and Hetzer, M. (2010). Nuclear Pore Complexes Guardians of the Nuclear Genome. Cold Spring Harb. Symp. Quant. Biol. *LXXV*.
Carlton, J.G., Jones, H., and Eggert, U.S. (2020). Membrane and organelle dynamics during cell division. Nat. Rev. Mol. Cell Biol. *21*, 151–166.
Caro, L.G., and Palade, G.E. (1964). Protein Synthesis, Storage, and Discharge in the Pancreatic Exocrine Cell: An Autoradiographic Study. J. Cell Biol. *20*, 473–495.
Champion, L., Pawar, S., Luithle, N., Ungricht, R., and Kutay, U. (2019). Dissociation

of membrane–chromatin contacts is required for proper chromosome segregation in mitosis. Mol. Biol. Cell *30*, 427–440.
Cheng, C., Geng, F., Cheng, X., and Guo, D. (2018). Lipid metabolism reprogramming and its potential targets in cancer. Cancer Commun. (London, England) *38*, 27.
Chiurchiù, V., Maccarrone, M., and Orlacchio, A. (2014). The role of reticulons in neurodegenerative diseases. NeuroMolecular Med. *16*, 3–15.
Choudhary, V., El Atab, O., Mizzon, G., Prinz, W.A., and Schneiter, R. (2020). Seipin and Nem1 establish discrete ER subdomains to initiate yeast lipid droplet biogenesis. J. Cell Biol. *219*.
Cimini, D. (2003). Merotelic kinetochore orientation occurs frequently during early mitosis in mammalian tissue cells and error correction is achieved by two different mechanisms. J. Cell Sci. *116*, 4213–4225.
Cimini, D., Howell, B., Maddox, P., Khodjakov, A., Degrassi, F., and Salmon, E.D. (2001). Merotelic kinetochore orientation is a major mechanism of aneuploidy in mitotic mammalian tissue cells. J. Cell Biol. *152*, 517–527.
Cimini, D., Cameron, L.A., and Salmon, E.D. (2004). Anaphase Spindle Mechanics Prevent Mis-Segregation of Merotelically Oriented Chromosomes. Curr. Biol. *14*, 2149–2155.
Cimini, D., Wan, X., Hirel, C.B., and Salmon, E.D. (2006). Aurora Kinase Promotes Turnover of Kinetochore Microtubules to Reduce Chromosome Segregation Errors. Curr. Biol. *16*, 1711–1718.
Clever, M., Funakoshi, T., Mimura, Y., Takagi, M., and Imamoto, N. (2012). The nucleoporin ELYS/Mel28 regulates nuclear envelope subdomain formation in HeLa cells. Nucleus *3*, 187–199.
Collin, P., Nashchekina, O., Walker, R., and Pines, J. (2013). The spindle assembly checkpoint works like a rheostat rather than a toggle switch. Nat. Cell Biol. *15*, 1378–1385.
Cornell, R., and Antonny, B. (2018). CCTα Commands Phospholipid Homeostasis from the Nucleus. Dev. Cell *45*, 419–420.
Cornell, R.B., and Ridgway, N.D. (2015). CTP:phosphocholine cytidylyltransferase: Function, regulation, and structure of an amphitropic enzyme required for membrane biogenesis. Prog. Lipid Res. *59*, 147–171.
Craddock, C.P., Adams, N., Bryant, F.M., Kurup, S., and Eastmond, P.J. (2015). PHOSPHATIDIC ACID PHOSPHOHYDROLASE Regulates Phosphatidylcholine Biosynthesis in Arabidopsis by Phosphatidic Acid-Mediated Activation of CTP:PHOSPHOCHOLINE CYTIDYLYLTRANSFERASE Activity. Plant Cell *27*, 1251–1264.
Crasta, K., Ganem, N.J., Dagher, R., Lantermann, A.B., Ivanova, E. V., Pan, Y., Nezi, L., Protopopov, A., Chowdhury, D., and Pellman, D. (2012). DNA breaks and chromosome pulverization from errors in mitosis. Nature *482*, 53–58.
Csordás, G., Renken, C., Várnai, P., Walter, L., Weaver, D., Buttle, K.F., Balla, T., Mannella, C.A., and Hajnóczky, G. (2006). Structural and functional features and significance of the physical linkage between ER and mitochondria. J. Cell Biol. *174*, 915–921.
Currie, E., Schulze, A., Zechner, R., Walther, T.C., and Farese, R. V. (2013). Cellular

fatty acid metabolism and cancer. Cell Metab. *18*, 153–161.
D'Angelo, M.A., and Hetzer, M.W. (2008). Structure, dynamics and function of nuclear pore complexes. Trends Cell Biol. *18*, 456–466.
Darrigrand, J.F., Valente, M., Comai, G., Martinez, P., Petit, M., Nishinakamura, R., Osorio, D.S., Renault, G., Marchiol, C., Ribes, V., et al. (2020). Dullard-mediated smad1/5/8 inhibition controls mouse cardiac neural crest cells condensation and outflow tract septation. Elife *9*, 1–25.
DeLuca, J.G., Gall, W.E., Ciferri, C., Cimini, D., Musacchio, A., and Salmon, E.D. (2006). Kinetochore Microtubule Dynamics and Attachment Stability Are Regulated by Hec1. Cell *127*, 969–982.
Derynck, R., and Zhang, Y.E. (2003). Smad-dependent and Smad-independent pathways in TGF-β family signalling. Nature *425*, 577–584.
Dick, A.E., and Gerlich, D.W. (2013). Kinetic framework of spindle assembly checkpoint signalling. Nat. Cell Biol. *15*, 1370–1377.
Donkor, J., Sariahmetoglu, M., Dewald, J., Brindley, D.N., and Reue, K. (2007). Three mammalian lipins act as phosphatidate phosphatases with distinct tissue expression patterns. J. Biol. Chem. *282*, 3450–3457.
Drozdz, M.M., and Vaux, D.J. (2017). Shared mechanisms in physiological and pathological nucleoplasmic reticulum formation. Nucleus *8*, 34–45.
Drozdz, M.M., Jiang, H., Pytowski, L., Grovenor, C., and Vaux, D.J. (2017). Formation of a nucleoplasmic reticulum requires de novo assembly of nascent phospholipids and shows preferential incorporation of nascent lamins. Sci. Rep. *7*, 1–14.
Dufourc, E.J. (2008). Sterols and membrane dynamics. J. Chem. Biol. *1*, 63–77.
Dultz, E., Zanin, E., Wurzenberger, C., Braun, M., Rabut, G., Sironi, L., and Ellenberg, J. (2008). Systematic kinetic analysis of mitotic dis- and reassembly of the nuclear pore in living cells. J. Cell Biol. *180*, 857–865.
Eaton, J.M., Mullins, G.R., Brindley, D.N., and Harris, T.E. (2013). Phosphorylation of lipin 1 and charge on the phosphatidic acid head group control its phosphatidic acid phosphatase activity and membrane association. J. Biol. Chem. *288*, 9933–9945.
Ellenberg, J., Siggia, E.D., Moreira, J.E., Smith, C.L., Presley, J.F., Worman, H.J., and Lippincott-Schwartz, J. (1997). Nuclear membrane dynamics and reassembly in living cells: targeting of an inner nuclear membrane protein in interphase and mitosis. J. Cell Biol. *138*, 1193–1206.
English, A.R., and Voeltz, G.K. (2013). Rab10 GTPase regulates ER dynamics and morphology. Nat. Cell Biol. *15*, 169–178.
Fenech, M., Kirsch-Volders, M., Natarajan, A.T., Surralles, J., Crott, J.W., Parry, J., Norppa, H., Eastmond, D.A., Tucker, J.D., and Thomas, P. (2011). Molecular mechanisms of micronucleus, nucleoplasmic bridge and nuclear bud formation in mammalian and human cells. Mutagenesis *26*, 125–132.
Finck, B.N., Gropler, M.C., Chen, Z., Leone, T.C., Croce, M.A., Harris, T.E., Lawrence, J.C., and Kelly, D.P. (2006). Lipin 1 is an inducible amplifier of the hepatic PGC-1α/PPARα regulatory pathway. Cell Metab. *4*, 199–210.
Fonseca, C.L., Malaby, H.L.H., Sepaniac, L.A., Martin, W., Byers, C., Czechanski, A., Messinger, D., Tang, M., Ohi, R., Reinholdt, L.G., et al. (2019). Mitotic

chromosome alignment ensures mitotic fidelity by promoting interchromosomal compaction during anaphase. J. Cell Biol. *218*, 1148–1163.
Fouad, Y.A., and Aanei, C. (2016). Revisiting the hallmarks of cancer. Am. J. Cancer Res. *7*, 1016–1036.
Franz, C., Walczak, R., Yavuz, S., Santarella, R., Gentzel, M., Askjaer, P., Galy, V., Hetzer, M., Mattaj, I.W., and Antonin, W. (2007). MEL-28/ELYS is required for the recruitment of nucleoporins to chromatin and postmitotic nuclear pore complex assembly. EMBO Rep. *8*, 165–172.
Friedman, J.R., DiBenedetto, J.R., West, M., Rowland, A.A., and Voeltz, G.K. (2013). Endoplasmic reticulum-endosome contact increases as endosomes traffic and mature. Mol. Biol. Cell *24*, 1030–1040.
Gehrig, K., Cornell, R.B., and Ridgway, N.D. (2008). Expansion of the Nucleoplasmic Reticulum Requires the Coordinated Activity of Lamins and CTP:Phosphocholine Cytidylyltransferase α. Mol. Biol. Cell *19*, 237–247.
Giam, M., and Rancati, G. (2015). Aneuploidy and chromosomal instability in cancer: a jackpot to chaos. Cell Div. *10*, 3.
Gibellini, F., and Smith, T.K. (2010). The Kennedy pathway-de novo synthesis of phosphatidylethanolamine and phosphatidylcholine. IUBMB Life *62*, 414–428.
Gisselsson, D. (2008). Classification of chromosome segregation errors in cancer. Chromosoma *117*, 511–519.
Golden, A., Liu, J., and Cohen-Fix, O. (2009). Inactivation of the C. elegans lipin homolog leads to ER disorganization and to defects in the breakdown and reassembly of the nuclear envelope. J. Cell Sci. *122*, 1970–1978.
Golgi, C. (1898). Intorno alla struttura della cellula nervosa. Boll Doc Med Chir Pavia *13*, 1–14.
Gorjánácz, M., and Mattaj, I.W. (2009). Lipin is required for efficient breakdown of the nuclear envelope in Caenorhabditis elegans. J. Cell Sci. *122*, 1963–1969.
Goss, V.L., Hocevar, B., Thompson, L.J., Stratton, C., Burns, D.J., and Fields, A.P. (1994). Identification of Nuclear BII Protein Kinase C as a mitotic lamin kinase. J. Biol. Chem. *269*, 19074–19080.
Goulbourne, C.N., Malhas, A.N., and Vaux, D.J. (2011). The induction of a nucleoplasmic reticulum by prelamin A accumulation requires CTP: Phosphocholine cytidylyltransferase-α. J. Cell Sci. *124*, 4253–4266.
Gregan, J., Polakova, S., Zhang, L., Tolić-Nørrelykke, I.M., and Cimini, D. (2011). Merotelic kinetochore attachment: Causes and effects. Trends Cell Biol. *21*, 374–381.
Grigoriev, I., Gouveia, S.M., Vaart, B. Van Der, Demmers, J., Smyth, J.T., Honnappa, S., Steinmetz, M.O., Putney, J.W., Hoogenraad, C.C., and Akhmanova, A. (2008). Report STIM1 Is a MT-Plus-End-Tracking Protein Involved in Remodeling of the ER. Curr. Biol. *18*, 177–182.
Grillet, M., Dominguez Gonzalez, B., Sicart, A., Pöttler, M., Cascalho, A., Billion, K., Hernandez Diaz, S., Swerts, J., Naismith, T. V., Gounko, N. V., et al. (2016). Torsins Are Essential Regulators of Cellular Lipid Metabolism. Dev. Cell *38*, 235–247.
Grimsey, N., Han, G.S., O'Hara, L., Rochford, J.J., Carman, G.M., and Siniossoglou, S. (2008). Temporal and spatial regulation of the phosphatidate phosphatases

lipin 1 and 2. J. Biol. Chem. *283*, 29166–29174.
Gropler, M.C., Harris, T.E., Hall, A.M., Wolins, N.E., Gross, R.W., Han, X., Chen, Z., and Finck, B.N. (2009). Lipin 2 is a liver-enriched phosphatidate phosphohydrolase enzyme that is dynamically regulated by fasting andobesity in mice. J. Biol. Chem. *284*, 6763–6772.
Gu, M., LaJoie, D., Chen, O.S., von Appen, A., Ladinsky, M.S., Redd, M.J., Nikolova, L., Bjorkman, P.J., Sundquist, W.I., Ullman, K.S., et al. (2017). LEM2 recruits CHMP7 for ESCRT-mediated nuclear envelope closure in fission yeast and human cells. Proc. Natl. Acad. Sci. 201613916.
Haider, A., Wei, Y.-C., Lim, K., Barbosa, A.D., Liu, C.-H., Weber, U., Mlodzik, M., Oras, K., Collier, S., Hussain, M.M., et al. (2018). PCYT1A Regulates Phosphatidylcholine Homeostasis from the Inner Nuclear Membrane in Response to Membrane Stored Curvature Elastic Stress. Dev. Cell *0*, 1–15.
Han, G.S., Wu, W.I., and Carman, G.M. (2006). The Saccharomyces cerevisiae lipin homolog is a Mg2+-dependent phosphatidate phosphatase enzyme. J. Biol. Chem. *281*, 9210–9218.
Han, S., Bahmanyar, S., Zhang, P., Grishin, N., Oegema, K., Crooke, R., Graham, M., Reue, K., Dixon, J.E., and Goodman, J.M. (2012). Nuclear envelope phosphatase 1-regulatory subunit 1 (formerly TMEM188) is the metazoan Spo7p ortholog and functions in the lipin activation pathway. J. Biol. Chem. *287*, 3123–3137.
Hanson, R.W., and Reshef, L. (2003). Glyceroneogenesis revisited. Biochimie *85*, 1199–1205.
Haraguchi, T., Koujin, T., Hayakawa, T., Kaneda, T., Tsutsumi, C., Imamoto, N., Akazawa, C., Sukegawa, J., Yoneda, Y., and Hiraoka, Y. (2000). Live fluorescence imaging reveals early recruitment of emerin, LBR, RanBP2, and Nup153 to reforming functional nuclear envelopes. J. Cell Sci. *113 (Pt 5*, 779–794.
Haraguchi, T., Kojidani, T., Koujin, T., Shimi, T., Osakada, H., Mori, C., Yamamoto, A., and Hiraoka, Y. (2008). Live cell imaging and electron microscopy reveal dynamic processes of BAF-directed nuclear envelope assembly. J. Cell Sci. *121*, 2540–2554.
Harayama, T., and Riezman, H. (2018). Understanding the diversity of membrane lipid composition. Nat. Rev. Mol. Cell Biol. *19*, 281–296.
Harris, T.E., Huffman, T.A., Chi, A., Shabanowitz, J., Hunt, D.F., Kumar, A., and Lawrence, J.C. (2007). Insulin controls subcellular localization and multisite phosphorylation of the phosphatidic acid phosphatase, lipin 1. J. Biol. Chem. *282*, 277–286.
Hatch, E.M., Fischer, A.H., Deerinck, T.J., and Hetzer, M.W. (2013). Catastrophic Nuclear Envelope Collapse in Cancer Cell Micronuclei. Cell *154*, 47.
Hayata, T., Ezura, Y., Asashima, M., Nishinakamura, R., and Noda, M. (2015). Dullard/Ctdnep1 regulates endochondral ossification via suppression of TGF-?? signaling. J. Bone Miner. Res. *30*, 318–329.
Hayward, D., Alfonso-Pérez, T., and Gruneberg, U. (2019). Orchestration of the spindle assembly checkpoint by CDK1-cyclin B1. FEBS Lett. *593*, 2889–2907.
Henry, S.M., and Hodge, L.D. (1983). Evidence for a unique profile of

phosphatidylcholine synthesis in late mitotic cells. J. Cell Biol. *97*, 166–172.
Henry, S.A., Kohlwein, S.D., and Carman, G.M. (2012). Metabolism and regulation of glycerolipids in the yeast Saccharomyces cerevisiae. Genetics *190*, 317–349.
Hetzer, M.W. (2010). The Nuclear Envelope. Online *1411*, 461–477.
Hirota, T., Lipp, J.J., Toh, B.H., and Peters, J.M. (2005). Histone H3 serine 10 phosphorylation by Aurora B causes HP1 dissociation from heterochromatin. Nature *438*, 1176–1180.
Hoepfner, D., Schildknegt, D., Braakman, I., Philippsen, P., and Tabak, H.F. (2005). Contribution of the endoplasmic reticulum to peroxisome formation. Cell *122*, 85–95.
Hofbauer, H.F., Gecht, M., Fischer, S.C., Seybert, A., Frangakis, A.S., Stelzer, E.H.K., Covino, R., Hummer, G., and Ernst, R. (2018). The molecular recognition of phosphatidic acid by an amphipathic helix in Opi1. J. Cell Biol. 1–18.
Holthuis, J.C.M., and Menon, A.K. (2014). Lipid landscapes and pipelines in membrane homeostasis. Nature *510*, 48–57.
Horton, J.D., Goldstein, J.L., and Brown, M.S. (2002). SREBPs: activators of the complete program of cholesterol and fatty acid synthesis in the liver. J. Clin. Invest. *109*, 1125–1131.
Horvath, S.E., and Daum, G. (2013). Lipids of mitochondria. Prog. Lipid Res. *52*, 590–614.
Hu, J., Shibata, Y., Voss, C., Shemesh, T., Li, Z., Coughlin, M., Kozlov, M.M., Rapoport, T. a, and Prinz, W. a (2008). Membrane proteins of the endoplasmic reticulum induce high-curvature tubules. Science *319*, 1247–1250.
Huang, L.-K., and Wang, M.-J.J. (1995). Image thresholding by minimizing the measures of fuzziness. *28*, 41–45.
Huffman, T.A., Mothe-Satney, I., and Lawrence, J.C. (2002). Insulin-stimulated phosphorylation of lipin mediated by the mammalian target of rapamycin. Proc. Natl. Acad. Sci. U. S. A. *99*, 1047–1052.
Igal, R.A. (2010). Stearoyl-coa desaturase-1: A novel key player in the mechanisms of cell proliferation, programmed cell death and transformation to cancer. Carcinogenesis *31*, 1509–1515.
Inoue, J., and Sato, R. (2013). New insights into the activation of sterol regulatory element-binding proteins by proteolytic processing. Biomol. Concepts *4*, 417–423.
Jackowski, S. (1994). Coordination of membrane phospholipid synthesis with the cell cycle. J. Biol. Chem. *269*, 3858–3867.
Jacquemyn, J., Cascalho, A., and Goodchild, R.E. (2017). The ins and outs of endoplasmic reticulum-controlled lipid biosynthesis. EMBO Rep. *18*, 1905–1921.
Jacquemyn, J., Foroozandeh, J., Vints, K., and Swerts, J. (2020). The Torsin / NEP1R1-CTDNEP1 / Lipin axis regulates nuclear envelope lipid metabolism for nuclear pore complex insertion.
Janssen, A., Burg, M. Van Der, Szuhai, K., and Kops, G.J.P.L. (2011). Chromosome Segregation Errors as a Cause of DNA Damage and Structural. *333*, 1895–1899.
Jones, D.T.W., Jäger, N., Kool, M., Zichner, T., Hutter, B., Sultan, M., Cho, Y.-J., Pugh, T.J., Hovestadt, V., Stütz, A.M., et al. (2012). Dissecting the genomic complexity underlying medulloblastoma. Nature *488*, 100–105.

Joshi, A.S., Zhang, H., and Prinz, W.A. (2017). Organelle biogenesis in the endoplasmic reticulum. Nat. Cell Biol. *19*, 876–882.
Kaminski, A., Fedorchak, G.R., and Lammerding, J. (2014). The cellular mastermind(?) - Mechanotransduction and the nucleus (Elsevier Inc.).
Karanasios, E., Han, G.S., Xu, Z., Carman, G.M., and Siniossoglou, S. (2010). A phosphorylation-regulated amphipathic helix controls the membrane translocation and function of the yeast phosphatidate phosphatase. Proc. Natl. Acad. Sci. U. S. A. *107*, 17539–17544.
Kennedy, E.P., and Weiss, S.B. (1956). The function of cytidine coenzymes in the biosynthesis of phospholipides. J Biol Chem *222*, 193–214.
Khayyo, V.I., Hoffmann, R.M., Wang, H., Bell, J.A., Burke, J.E., Reue, K., and Airola, M.V.V. (2020). Crystal structure of a lipin/Pah phosphatidic acid phosphatase. Nat. Commun. *11*, 1–11.
Kim, Y., Gentry, M.S., Harris, T.E., Wiley, S.E., Lawrence, J.C., and Dixon, J.E. (2007). A conserved phosphatase cascade that regulates nuclear membrane biogenesis. Proc. Natl. Acad. Sci. *104*, 6596–6601.
Klopfenstein, D.R., Klumperman, J., Lustig, A., Kammerer, R.A., Oorschot, V., and Hauri, H.P. (2001). Subdomain-specific localization of CLIMP-63 (p63) in the endoplasmic reticulum is mediated by its luminal α-helical segment. J. Cell Biol. *153*, 1287–1299.
Knottnerus, S.J.G., Bleeker, J.C., Wüst, R.C.I., Ferdinandusse, S., IJlst, L., Wijburg, F.A., Wanders, R.J.A., Visser, G., and Houtkooper, R.H. (2018). Disorders of mitochondrial long-chain fatty acid oxidation and the carnitine shuttle. Rev. Endocr. Metab. Disord. *19*, 93–106.
Knowles, D.G., Lee, J., Taneva, S.G., and Cornell, R.B. (2019). Remodeling of the interdomain allosteric linker upon membrane binding of CCTα pulls its active site close to the membrane surface. J. Biol. Chem. *294*, 15531–15543.
Koh, Y.K., Lee, M.Y., Kim, J.W., Kim, M., Moon, J.S., Lee, Y.J., Ahn, Y.H., and Kim, K.S. (2008). Lipin1 is a key factor for the maturation and maintenance of adipocytes in the regulatory network with CCAAT/enhancer-binding protein α and peroxisome proliferator-activated receptor γ2. J. Biol. Chem. *283*, 34896–34906.
Kuhajda, F.P., Jenner, K., Wood, F.D., Hennigar, R.A., Jacobs, L.B., Dick, J.D., and Pasternack, G.R. (1994). Fatty acid synthesis: A potential selective target for antineoplastic therapy. Proc. Natl. Acad. Sci. U. S. A. *91*, 6379–6383.
Kumar, D., Golchoubian, B., Belevich, I., Jokitalo, E., and Schlaitz, A.L. (2019). REEP3 and REEP4 determine the tubular morphology of the endoplasmic reticulum during mitosis. Mol. Biol. Cell *30*, 1377–1389.
Kuniyasu, K., Iemura, K., and Tanaka, K. (2019). Delayed chromosome alignment to the spindle equator increases the rate of chromosome missegregation in cancer cell lines. Biomolecules *9*, 1–17.
Lagrutta, L.C., Montero-Villegas, S., Layerenza, J.P., Sisti, M.S., García De Bravo, M.M., and Ves-Losada, A. (2017). Reversible nuclear-lipid-droplet morphology induced by oleic acid: A link to cellular-lipid metabolism. PLoS One *12*, 1–25.
Laurell, E., Beck, K., Krupina, K., Theerthagiri, G., Bodenmiller, B., Horvath, P., Aebersold, R., Antonin, W., and Kutay, U. (2011). Phosphorylation of Nup98 by multiple kinases is crucial for NPC disassembly during mitotic entry. Cell *144*,

539–550.
Layerenza, J.P., González, P., García De Bravo, M.M., Polo, M.P., Sisti, M.S., and Ves-Losada, A. (2013). Nuclear lipid droplets: A novel nuclear domain. Biochim. Biophys. Acta - Mol. Cell Biol. Lipids *1831*, 327–340.
Lee, K.K., Haraguchi, T., Lee, R.S., Koujin, T., Hiraoka, Y., and Wilson, K.L. (2001). Distinct functional domains in emerin bind lamin A and DNA-bridging protein BAF. 4567–4573.
Leeuw, R. De, Gruenbaum, Y., and Medalia, O. (2018). Nuclear Lamins : Thin Filaments with Major Functions. Trends Cell Biol. *28*, 34–45.
Leibowitz, M.L., Zhang, C.-Z., and Pellman, D. (2015). Chromothripsis: A New Mechanism for Rapid Karyotype Evolution. Annu. Rev. Genet. 1–29.
Lénárt, P., Rabut, G., Daigle, N., Hand, A.R., Terasaki, M., and Ellenberg, J. (2003). Nuclear envelope breakdown in starfish oocytes proceeds by partial NPC disassembly followed by a rapidly spreading fenestration of nuclear membranes. *160*, 1055–1068.
Levental, K.R., Surma, M.A., Skinkle, A.D., Lorent, J.H., Zhou, Y., Klose, C., Chang, J.T., Hancock, J.F., and Levental, I. (2017). W-3 Polyunsaturated Fatty Acids Direct Differentiation of the Membrane Phenotype in Mesenchymal Stem Cells To Potentiate Osteogenesis. Sci. Adv. *3*, 1–16.
Levy, D.L., and Heald, R. (2010). Nuclear Size Is Regulated by Importin α and Ntf2 in Xenopus. Cell *143*, 288–298.
Liu, G.H., and Gerace, L. (2009). Sumoylation regulates nuclear localization of lipin-1α in neuronal cells. PLoS One *4*, 1–10.
Liu, S., Kwon, M., Mannino, M., Yang, N., Renda, F., Khodjakov, A., and Pellman, D. (2018). Nuclear envelope assembly defects link mitotic errors to chromothripsis. Nature.
Loewen, C.J.R., Gazpar, M.L., Jesch, S.A., Delon, C., Ktistakis, N.T., Henry, S.A., and Levine, T.P. (2004). Phospholipid metabolism regulated by a transcription factor sensing phosphatidic acid. Science (80-.). *304*, 1644–1647.
Lord, S.J., Velle, K.B., Dyche Mullins, R., and Fritz-Laylin, L.K. (2020). SuperPlots: Communicating reproducibility and variability in cell biology. J. Cell Biol. *219*.
Lorent, J.H., Levental, K.R., Ganesan, L., Rivera-Longsworth, G., Sezgin, E., Doktorova, M., Lyman, E., and Levental, I. (2020). Plasma membranes are asymmetric in lipid unsaturation, packing and protein shape. Nat. Chem. Biol.
Lu, L., Ladinsky, M.S., and Kirchhausen, T. (2009). Cisternal Organization of the Endoplasmic Reticulum during Mitosis. Mol. Biol. Cell *20*, 3471–3480.
Lu, L., Ladinsky, M.S., and Kirchhausen, T. (2011). Formation of the postmitotic nuclear envelope from extended ER cisternae precedes nuclear pore assembly. J. Cell Biol. *194*, 425–440.
Lunt, S.Y., and Vander Heiden, M.G. (2011). Aerobic Glycolysis: Meeting the Metabolic Requirements of Cell Proliferation. Annu. Rev. Cell Dev. Biol. *27*, 441–464.
Ma, H., Qian, W., Bambouskova, M., Collins, P.L., Porter, S.I., Byrum, A.K., and Zhang, R. (2020). Barrier-to-Autointegration Factor 1 Protects against a Basal. Am. Soc. Microbiol. *11*, 1–15.
Macaulay, C., Meier, E., and Forbes, D.J. (1995). Differential Mitotic Phosphorylation

of Proteins of the Nuclear Pore Complex. J. Biol. Chem. *270*, 254–262.
Maciejowski, J., Li, Y., Bosco, N., Campbell, P.J., and De Lange, T. (2015). Chromothripsis and Kataegis Induced by Telomere Crisis. Cell *163*, 1641–1654.
MacKenzie, K.J., Carroll, P., Martin, C.A., Murina, O., Fluteau, A., Simpson, D.J., Olova, N., Sutcliffe, H., Rainger, J.K., Leitch, A., et al. (2017). CGAS surveillance of micronuclei links genome instability to innate immunity. Nature *548*, 461–465.
Mall, M., Walter, T., Gorjánácz, M., Davidson, I.F., Ly-Hartig, T.B.N., Ellenberg, J., and Mattaj, I.W. (2012). Mitotic lamin disassembly is triggered by lipid-mediated signaling. J. Cell Biol. *198*, 981–990.
Mazzarello, P. (1999). A unifying concept: The history of cell theory. Nat. Cell Biol. *1*, E13–E15.
van Meer, G., Voelker, D.R., and Feigenson, G.W. (2008). Membrane lipids: Where they are and how they behave. Nat. Rev. Mol. Cell Biol. *9*, 112–124.
Merta, H., Carrasquillo Rodriguez, J.W., Anjur-Dietrich, M.I., Granade, M.E., Vitale, T., Harris, T.E., Needleman, D., and Bahmanyar, S. (2021). A CTDNEP 1-Lipin 1-mTOR Regulatory Network Restricts ER Membrane Biogenesis to Enable Chromosome Motions Necessary for Mitotic Fidelity. bioRxiv doi: doi.org/10.1101/2021.03.02.433553
Michot, C., Hubert, L., Brivet, M., De Meirleir, L., Valayannopoulos, V., Müller-Felber, W., Venkateswaran, R., Ogier, H., Desguerre, I., Altuzarra, C., et al. (2010). LPIN1 gene mutations: A major cause of severe rhabdomyolysis in early childhood. Hum. Mutat. *31*, 1564–1573.
Mitchell, J.M., Mansfeld, J., Capitanio, J., Kutay, U., and Wozniak, R.W. (2010). Pom121 links two essential subcomplexes of the nuclear pore complex core to the membrane. J. Cell Biol. *191*, 505–521.
Molitor, T.P., and Traktman, P. (2014). Depletion of the protein kinase VRK1 disrupts nuclear envelope morphology and leads to BAF retention on mitotic chromosomes. Mol. Biol. Cell *25*, 891–903.
Mukherjee, R.N., Sallé, J., Dmitrieff, S., Nelson, K.M., Oakey, J., Minc, N., and Levy, D.L. (2020). The Perinuclear ER Scales Nuclear Size Independently of Cell Size in Early Embryos. Dev. Cell *54*, 395-409.e7.
Murate, M., and Kobayashi, T. (2016). Revisiting transbilayer distribution of lipids in the plasma membrane. Chem. Phys. Lipids *194*, 58–71.
Musacchio, A. (2015). The Molecular Biology of Spindle Assembly Checkpoint Signaling Dynamics. Curr. Biol. *25*, R1002–R1018.
Nicolson, G.L. (2014). The Fluid - Mosaic Model of Membrane Structure: Still relevant to understanding the structure, function and dynamics of biological membranes after more than 40 years. Biochim. Biophys. Acta - Biomembr. *1838*, 1451–1466.
Nikolouzakis, T.K., Stivaktakis, P.D., Apalaki, P., Kalliantasi, K., Sapsakos, T.M., Spandidos, D.A., Tsatsakis, A., Souglakos, J., and Tsiaoussis, J. (2019). Effect of systemic treatment on the micronuclei frequency in the peripheral blood of patients with metastatic colorectal cancer. Oncol. Lett. *17*, 2703–2712.
Nixon-Abell, J., Obara, C.J., Weigel, A. V., Li, D., Legant, W.R., Xu, C.S., Pasolli, H.A., Harvey, K., Hess, H.F., Betzig, E., et al. (2016). Increased spatiotemporal resolution reveals highly dynamic dense tubular matrices in the peripheral ER. Science (80-.). *354*.

Northcott, P.A., Shih, D.J.H., Peacock, J., Garzia, L., Sorana Morrissy, A., Zichner, T., Stútz, A.M., Korshunov, A., Reimand, J., Schumacher, S.E., et al. (2012). Subgroup-specific structural variation across 1,000 medulloblastoma genomes. Nature *487*, 49–56.

Northcott, P.A., Buchhalter, I., Morrissy, A.S., Hovestadt, V., Weischenfeldt, J., Ehrenberger, T., Gröbner, S., Segura-Wang, M., Zichner, T., Rudneva, V.A., et al. (2017). The whole-genome landscape of medulloblastoma subtypes. Nature *547*, 311–317.

O'Hara, L., Han, G.S., Sew, P.C., Grimsey, N., Carman, G.M., and Siniossoglou, S. (2006). Control of phospholipid synthesis by phosphorylation of the yeast lipin Pah1p/Smp2p Mg2+-dependent phosphatidate phosphatase. J. Biol. Chem. *281*, 34537–34548.

Ohsaki, Y., Kawai, T., Yoshikawa, Y., Cheng, J., Jokitalo, E., and Fujimoto, T. (2016). PML isoform II plays a critical role in nuclear lipid droplet formation. J. Cell Biol. *212*, 29–38.

Olmos, Y., Hodgson, L., Mantell, J., Verkade, P., and Carlton, J.G. (2015). ESCRT-III controls nuclear envelope reformation. Nature *522*, 236–239.

Orphanides, G., and Reinberg, D. (2002). A Unified Theory of Gene Expression Review. *108*, 439–451.

Orso, G., Pendin, D., Liu, S., Tosetto, J., Moss, T.J., Faust, J.E., Micaroni, M., Egorova, A., Martinuzzi, A., McNew, J. a, et al. (2009). Homotypic fusion of ER membranes requires the dynamin-like GTPase atlastin. Nature *460*, 978–983.

Otsuka, S., Steyer, A.M., Schorb, M., Hériché, J.K., Hossain, M.J., Sethi, S., Kueblbeck, M., Schwab, Y., Beck, M., and Ellenberg, J. (2018). Postmitotic nuclear pore assembly proceeds by radial dilation of small membrane openings. Nat. Struct. Mol. Biol. *25*, 21–28.

Ottaviano, Y., and Gerace, L. (1985). Phosphorylation of the nuclear lamins during interphase and mitosis. J. Biol. Chem. *260*, 624–632.

Palade, G.E. (1952). The fine structure of mitochondria. Anat. Rec. *114*, 427–451.

Palade, G.E. (1956). The endoplasmic reticulum. J. Biophys. Biochem. Cytol. *2*, 85–98.

Palade, G.E., and Siekevitz, P. (1956). Pancreatic Microsomes: An Integrated Morphological and Biochemical Study. J Biophys. Biochem Cytol *2*, 671–690.

Paludan, S.R., and Bowie, A.G. (2013). Review Immune Sensing of DNA. Immunity *38*, 870–880.

Pampalona, J., Roscioli, E., Silkworth, W.T., Bowden, B., Genescà, A., Tusell, L., and Cimini, D. (2016). Chromosome bridges maintain kinetochore-microtubule attachment throughout mitosis and rarely break during anaphase. PLoS One *11*, 1–17.

Pelosi, M., Testet, E., Le Lay, S., Dugail, I., Tang, X., Mabilleau, G., Hamel, Y., Madrange, M., Blanc, T., Odent, T., et al. (2017). Normal human adipose tissue functions and differentiation in patients with biallelic LPIN1 inactivating mutations. J. Lipid Res. *58*, 2348–2364.

Penfield, L., S, R., E, S., A, L., MS, M., A, A., T, M.-R., and S, B. (2020). Regulated lipid synthesis and LEM2/CHMP7 jointly control nuclear envelope closure. J. Cell Biol. *Epub ahead*.

Peter, M., Nakagawa, J., Dorée, M., Labbé, J., and Nigg, E. (1990). In Vitro Disassembly of the Nuclear Lamina and M Phase-Specific Phosphorylation of Lamins by cdc2 Kinase-. Cell *61*, 591–602.
Péterfy, M., Phan, J., Xu, P., and Reue, K. (2001). Lipodystrophy in the fld mouse results from mutation of a new gene encoding a nuclear protein, lipin. Nat. Genet. *27*, 121–124.
Péterfy, M., Phan, J., and Reue, K. (2005). Alternatively spliced lipin isoforms exhibit distinct expression pattern, subcellular localization, and role in adipogenesis. J. Biol. Chem. *280*, 32883–32889.
Peterson, T.R., Sengupta, S.S., Harris, T.E., Carmack, A.E., Kang, S.A., Balderas, E., Guertin, D.A., Madden, K.L., Carpenter, A.E., Finck, B.N., et al. (2011). mTOR complex 1 regulates lipin 1 localization to control the SREBP pathway. Cell *146*, 408–420.
Phan, J., Péterfy, M., and Reue, K. (2004). Lipin expression preceding peroxisome proliferator-activated receptor-γ is critical for adipogenesis in vivo and in vitro. J. Biol. Chem. *279*, 29558–29564.
Phillips, M.J., and Voeltz, G.K. (2015). Structure and function of ER membrane contact sites with other organelles. Nat. Rev. Mol. Cell Biol. *17*.
Pietrocola, F., Galluzzi, L., Bravo-San Pedro, J.M., Madeo, F., and Kroemer, G. (2015). Acetyl coenzyme A: A central metabolite and second messenger. Cell Metab. *21*, 805–821.
Poirier, C.C., Zheng, Y., and Iglesias, P.A. (2010). Mitotic membrane helps to focus and stabilize the mitotic spindle. Biophys. J. *99*, 3182–3190.
Porter, K.R., Claude, A., and Fullam, E.F. (1945). A study of tissue culture cells by electron microscopy: Methods and preliminary observations. J. Exp. Med. *81*, 233–246.
Puhka, M., Vihinen, H., Joensuu, M., and Jokitalo, E. (2007). Endoplasmic reticulum remains continuous and undergoes sheet-to-tubule transformation during cell division in mammalian cells. J. Cell Biol. *179*, 895–909.
Puhka, M., Joensuu, M., Vihinen, H., Belevich, I., and Jokitalo, E. (2012). Progressive sheet-to-tubule transformation is a general mechanism for endoplasmic reticulum partitioning in dividing mammalian cells. Mol. Biol. Cell *23*, 2424–2432.
Ramezanpour, M., Lee, J., Taneva, S.G., Peter Tieleman, D., and Cornell, R.B. (2018). An auto-inhibitory helix in CTP: Phosphocholine cytidylyltransferase hijacks the catalytic residue and constrains a pliable, domain-bridging helix pair. J. Biol. Chem. *293*, 7070–7084.
Rapoport, T.A. (2007). Protein translocation across the eukaryotic endoplasmic reticulum and bacterial plasma membranes. Nature *450*, 663–669.
Rashid, T., Nemazanyy, I., Paolini, C., Tatsuta, T., Crespin, P., Villeneuve, D., Brodesser, S., Benit, P., Rustin, P., Baraibar, M.A., et al. (2019). Lipin1 deficiency causes sarcoplasmic reticulum stress and chaperone-responsive myopathy. EMBO J. *38*, 1–21.
Ren, H., Federico, L., Huang, H., Sunkara, M., Tracy Drennan, M.A.F., Smyth, S.S., and Morris*, A.J. (2010). A Phosphatidic Acid Binding/Nuclear Localization Motif Determines Lipin1 Function in Lipid Metabolism and Adipogenesis. Mol. Biol. Cell *21*, 3171–3181.

Ribatti, D. (2018). An historical note on the cell theory. Exp. Cell Res. *364*, 1–4.
Rodríguez-Feo, J.A., Puerto, M., Fernández-Mena, C., Verdejo, C., Lara, J.M., Díaz-Sánchez, M., Álvarez, E., Vaquero, J., Marín-Jiménez, I., Bañares, R., et al. (2015). A new role for reticulon-4B/NOGO-B in the intestinal epithelial barrier function and inflammatory bowel disease. Am. J. Physiol. - Gastrointest. Liver Physiol. *308*, 981–993.
Rodriguez Sawicki, L., Garcia, K.A., Corsico, B., and Scaglia, N. (2019). De novo lipogenesis at the mitotic exit is used for nuclear envelope reassembly/expansion. Implications for combined chemotherapy. Cell Cycle *18*, 1646–1659.
Romanauska, A., and Köhler, A. (2018). The Inner Nuclear Membrane Is a Metabolically Active Territory that Generates Nuclear Lipid Droplets. Cell 1–16.
Sakaguchi, M., Sharmin, S., Taguchi, A., Ohmori, T., Fujimura, S., Abe, T., Kiyonari, H., Komatsu, Y., Mishina, Y., Asashima, M., et al. (2013). The phosphatase Dullard negatively regulates BMP signalling and is essential for nephron maintenance after birth. Nat. Commun. *4*, 1398.
Samwer, M., Schneider, M.W.G., Hoefler, R., Schmalhorst, P.S., Jude, J.G., Zuber, J., and Gerlich, D.W. (2017). DNA Cross-Bridging Shapes a Single Nucleus from a Set of Mitotic Chromosomes. Cell *170*, 956-972.e23.
Sansregret, L., Patterson, J.O., Dewhurst, S., López-García, C., Koch, A., McGranahan, N., Chao, W.C.H., Barry, D.J., Rowan, A., Instrell, R., et al. (2017). APC/C dysfunction limits excessive cancer chromosomal instability. Cancer Discov. *7*, 218–233.
Santos-Rosa, H., Leung, J., Grimsey, N., Peak-Chew, S., and Siniossoglou, S. (2005). The yeast lipin Smp2 couples phospholipid biosynthesis to nuclear membrane growth. EMBO J. *24*, 1931–1941.
Satow, R., Chan, T., and Asashima, M. (2002). Molecular cloning and characterization of dullard: a novel gene required for neural development. Biochem Biophys Res Commun *295*, 85–91.
Schellhaus, A.K., De Magistris, P., and Antonin, W. (2015). Nuclear Reformation at the End of Mitosis. J. Mol. Biol. *428*, 1962–1985.
Schindelin, J., Arganda-Carreras, I., Frise, E., Kaynig, V., Longair, M., Pietzsch, T., Preibisch, S., Rueden, C., Saalfeld, S., Schmid, B., et al. (2012). Fiji: an open-source platform for biological-image analysis. Nat. Methods *9*, 676–682.
Schlaitz, A.L., Thompson, J., Wong, C.L., Yates, J., and Heald, R. (2013). REEP3/4 ensure endoplasmic reticulum clearance from metaphase chromatin and proper nuclear envelope architecture. Dev. Cell *26*, 315–323.
Schmitz, M.H.A., Held, M., Janssens, V., Hutchins, J.R.A., Hudecz, O., Ivanova, E., Goris, J., Trinkle-Mulcahy, L., Lamond, A.I., Poser, I., et al. (2010). Live-cell imaging RNAi screen identifies PP2A-B55alpha and importin-beta1 as key mitotic exit regulators in human cells. Nat. Cell Biol. *12*, 886–893.
Schooley, A., Vollmer, B., and Antonin, W. (2012). Building a nuclear envelope at the end of mitosis: Coordinating membrane reorganization, nuclear pore complex assembly, and chromatin de-condensation. Chromosoma *121*, 539–554.
Schroeder, L.K., Barentine, A.E.S., Merta, H., Schweighofer, S., Zhang, Y., Baddeley, D., Bewersdorf, J., and Bahmanyar, S. (2018). Dynamic nanoscale

morphology of the ER surveyed by STED microscopy. J. Cell Biol. *218*, jcb.201809107.
Schwarz, D.S., and Blower, M.D. (2015). The endoplasmic reticulum: structure, function and response to cellular signaling. Cell. Mol. Life Sci. *73*, 79–94.
Schweigreiter, R., Stasyk, T., Contarini, I., Frauscher, S., Oertle, T., Klimaschewski, L., Huber, L.A., and Bandtlow, C.E. (2007). Phosphorylation-regulated cleavage of the reticulon protein Nogo-B by caspase-7 at a noncanonical recognition site. Proteomics *7*, 4457–4467.
Schweizer, N., Weiss, M., and Maiato, H. (2014). The dynamic spindle matrix. Curr. Opin. Cell Biol. *28*, 1–7.
Schweizer, N., Pawar, N., Weiss, M., and Maiato, H. (2015). An organelle-exclusion envelope assists mitosis and underlies distinct molecular crowding in the spindle region. J. Cell Biol. *210*, 695–704.
Seifried, A., Schultz, J., and Gohla, A. (2013). Human HAD phosphatases: Structure, mechanism, and roles in health and disease. FEBS J. *280*, 549–571.
Semenova, N., Bosnjak, M., Markelc, B., Znidar, K., Cemazar, M., and Heller, L. (2019). Multiple cytosolic DNA sensors bind plasmid DNA after transfection. Nucleic Acids Res. *47*, 10235–10246.
Sezgin, E., Levental, I., Mayor, S., and Eggeling, C. (2017). The mystery of membrane organization: Composition, regulation and roles of lipid rafts. Nat. Rev. Mol. Cell Biol. *18*, 361–374.
Shibata, Y., Shemesh, T., Prinz, W.A., Palazzo, A.F., Kozlov, M.M., and Rapoport, T.A. (2010). Mechanisms determining the morphology of the peripheral ER. Cell *143*, 774–788.
Shimano, H., and Sato, R. (2017). SREBP-regulated lipid metabolism: Convergent physiology-divergent pathophysiology. Nat. Rev. Endocrinol. *13*, 710–730.
Shimizu, K., Fukushima, H., Ogura, K., Lien, E.C., Nihira, N.T., Zhang, J., North, B.J., Guo, A., Nagashima, K., Nakagawa, T., et al. (2017). The SCFβ-TRCP E3 ubiquitin ligase complex targets Lipin1 for ubiquitination and degradation to promote hepatic lipogenesis. Sci. Signal. *10*.
Siekevitz, P., and Palade, G.E. (1960). A cyto-chemical study on the pancreas of the guinea pig. V. In vivo incorporation of leucine-1-C14 into the chymotrypsinogen of various cell fractions. J Biophys. Biochem Cytol *7*, 619–630.
Silkworth, W.T., and Cimini, D. (2012). Transient defects of mitotic spindle geometry and chromosome segregation errors. Cell Div. *7*, 1–8.
Singer, S.J., and Nicolson, G.L. (1975). The fluid mosaic model of the structure of cell membranes. Science (80-.). *175*, 720–731.
Siniossoglou, S., Santos-Rosa, H., Rappsilber, J., Mann, M., and Hurt, E. (1998). A novel complex of membrane proteins required for formation of a spherical nucleus. EMBO J. *17*, 6449–6464.
Skinner, B.M., and Johnson, E.E.P. (2017). Nuclear morphologies: their diversity and functional relevance. Chromosoma *126*, 195–212.
Smyth, J.T., Beg, A.M., Wu, S., Putney, J.W., and Rusan, N.M. (2012). Phosphoregulation of STIM1 leads to exclusion of the endoplasmic reticulum from the mitotic spindle. Curr. Biol. *22*, 1487–1493.
Sołtysik, K., Ohsaki, Y., Tatematsu, T., Cheng, J., and Fujimoto, T. (2019). Nuclear

lipid droplets derive from a lipoprotein precursor and regulate phosphatidylcholine synthesis. Nat. Commun. *10*.
Sołtysik, K., Ohsaki, Y., Tatematsu, T., Cheng, J., Maeda, A., Morita, S., and Fujimoto, T. (2020). Nuclear lipid droplets form in the inner nuclear membrane in a seipin-independent manner. *220*.
Song, L., Liu, Z., Hu, H.H., Yang, Y., Li, T.Y., Lin, Z.Z., Ye, J., Chen, J., Huang, X., Liu, D.T., et al. (2020). Proto-oncogene Src links lipogenesis via lipin-1 to breast cancer malignancy. Nat. Commun. *11*.
Sosa, B.A., Kutay, U., and Schwartz, T.U. (2013). Structural insights into LINC complexes. Curr. Opin. Struct. Biol. *23*, 285–291.
Soto, M., Raaijmakers, J.A., Bakker, B., Spierings, D.C.J., Lansdorp, P.M., Foijer, F., and Medema, R.H. (2017). p53 Prohibits Propagation of Chromosome Segregation Errors that Produce Structural Aneuploidies. Cell Rep. *19*, 2423–2431.
Soto, M., García-Santisteban, I., Krenning, L., Medema, R.H., and Raaijmakers, J.A. (2018). Chromosomes trapped in micronuclei are liable to segregation errors. J. Cell Sci. *131*.
Storck, E.M., Özbalci, C., and Eggert, U.S. (2018). Lipid Cell Biology: A Focus on Lipids in Cell Division. Annu. Rev. Biochem. *87*, 839–869.
Sunshine, H., and Iruela-Arispe, M.L. (2017). Membrane lipids and cell signaling. Curr. Opin. Lipidol. *28*, 408–413.
Tanaka, S.S., Nakane, A., Yamaguchi, Y.L., Terabayashi, T., Abe, T., Nakao, K., Asashima, M., Steiner, K.A., Tam, P.P.L., and Nishinakamura, R. (2013). Dullard/Ctdnep1 Modulates WNT Signalling Activity for the Formation of Primordial Germ Cells in the Mouse Embryo. PLoS One *8*.
Tange, Y., Hirata, A., and Niwa, O. (2002). An evolutionarily conserved fission yeast protein, Ned1, implicated in normal nuclear morphology and chromosome stability, interacts with Dis3, Pim1/RCC1 and an essential nucleoporin. J. Cell Sci. *115*, 4375–4385.
Terasaki, M., Campagnola, P., Rolls, M.M., Stein, P.A., Ellenberg, J., Hinkle, B., and Slepchenko, B. (2001). A New Model for Nuclear Envelope Breakdown. Mol. Biol. Cell *12*, 503–510.
Thaller, D.J., Tong, D., Marklew, C.J., Ader, N.R., Mannino, P.J., Borah, S., King, M.C., Ciani, B., and Lusk, C.P. (2021). Direct binding of ESCRT protein Chm7 to phosphatidic acid – rich membranes at nuclear envelope herniations. *220*.
Thiam, A.R., Farese, R. V., and Walther, T.C. (2013). The biophysics and cell biology of lipid droplets. Nat. Rev. Mol. Cell Biol. *14*, 775–786.
Thompson, S.L., and Compton, D.A. (2011). Chromosome missegregation in human cells arises through specific types of kinetochore-microtubule attachment errors. Proc. Natl. Acad. Sci. *108*, 17974–17978.
Tong, L. (2005). Acetyl-coenzyme A carboxylase: Crucial metabolic enzyme and attractive target for drug discovery. Cell. Mol. Life Sci. *62*, 1784–1803.
Tsai, P.L., Zhao, C., Turner, E., and Schlieker, C. (2016). The Lamin B receptor is essential for cholesterol synthesis and perturbed by disease-causing mutations. Elife *5*, 1–26.
Tseng, L.C., and Chen, R.H. (2011). Temporal control of nuclear envelope assembly

by phosphorylation of lamin B receptor. Mol. Biol. Cell *22*, 3306–3317.
Turgay, Y., Champion, L., Balazs, C., Held, M., Toso, A., Gerlich, D.W., Meraldi, P., and Kutay, U. (2014). SUN proteins facilitate the removal of membranes from chromatin during nuclear envelope breakdown. J. Cell Biol. *204*, 1099–1109.
Ugrankar, R., Liu, Y., Provaznik, J., Schmitt, S., and Lehmann, M. (2011). Lipin Is a Central Regulator of Adipose Tissue Development and Function in Drosophila melanogaster. Mol. Cell. Biol. *31*, 1646–1656.
Ulbert, S., Platani, M., Boue, S., and Mattaj, I.W. (2006). Direct membrane protein-DNA interactions required early in nuclear envelope assembly. J. Cell Biol. *173*, 469–476.
Ungricht, R., and Kutay, U. (2017). Mechanisms and Functions of Nuclear Envelope Remodelling. Nat. Publ. Gr.
Urrutia, H., Aleman, A., and Eivers, E. (2016). Drosophila Dullard functions as a Mad phosphatase to terminate BMP signaling. Nat. Publ. Gr. 1–9.
Vance, J.E. (2015). Phospholipid Synthesis and Transport in Mammalian Cells. Traffic *16*, 1–18.
Vergnes, L., Chin, R.G., De Vallim, T.A., Fong, L.G., Osborne, T.F., Young, S.G., and Reue, K. (2016). SREBP-2-deficient and hypomorphic mice reveal roles for SREBP-2 in embryonic development and SREBP-1c expression. J. Lipid Res. *57*, 410–421.
Vietri, M., Schink, K.O., Campsteijn, C., Wegner, C.S., Schultz, S.W., Christ, L., Thoresen, S.B., Brech, A., Raiborg, C., and Stenmark, H. (2015). Spastin and ESCRT-III coordinate mitotic spindle disassembly and nuclear envelope sealing. Nature *522*, 231–235.
Vietri, M., Schultz, S.W., Bellanger, A., Jones, C.M., Petersen, L.I., Raiborg, C., Skarpen, E., Pedurupillay, C.R.J., Kjos, I., Kip, E., et al. (2020). Unrestrained ESCRT-III drives micronuclear catastrophe and chromosome fragmentation. Nat. Cell Biol. *22*, 856–867.
Voeltz, G.K., Prinz, W.A., Shibata, Y., Rist, J.M., and Rapoport, T.A. (2006). A class of membrane proteins shaping the tubular endoplasmic reticulum. Cell *124*, 573–586.
Wang, C., Xu, C., Sun, M., Luo, D., Liao, D. fang, and Cao, D. (2009). Acetyl-CoA carboxylase-α inhibitor TOFA induces human cancer cell apoptosis. Biochem. Biophys. Res. Commun. *385*, 302–306.
Wang, H., Becuwe, M., Housden, B.E., Chitraju, C., Porras, A.J., Graham, M.M., Liu, X.N., Thiam, A.R., Savage, D.B., Agarwal, A.K., et al. (2016a). Seipin is required for converting nascent to mature lipid droplets. Elife *5*, 1–28.
Wang, H., Peng, B., Pandita, R.K., Engler, D.A., Matsunami, R.K., Xu, X., Hegde, P.M., Butler, B.E., Pandita, T.K., Mitra, S., et al. (2017). Aurora kinase B dependent phosphorylation of 53BP1 is required for resolving merotelic kinetochore-microtubule attachment errors during mitosis. Oncotarget *8*, 48671–48687.
Wang, S., Romano, F.B., Field, C.M., Mitchison, T.J., and Rapoport, T.A. (2013). Multiple mechanisms determine ER network morphology during the cell cycle in Xenopus egg extracts. J. Cell Biol. *203*, 801–814.
Wang, S., Tukachinsky, H., Romano, F.B., and Rapoport, T.A. (2016b). Cooperation

of the ER-shaping proteins atlastin, lunapark, and reticulons to generate a tubular membrane network. Elife *5*, 1–29.
Waterman-Storer, C.M., and Salmon, E.D. (1998). Endoplasmic reticulum membrane tubules are distributed by microtubules in living cells using three distinct mechanisms. Curr. Biol. *8*, 798–807.
Watson, M.L. (1955). The nuclear envelope: its structure and relation to cytoplasmic membranes. J Biophys. Biochem Cytol *1*, 257–270.
Watt, M.J., Hoy, A.J., Muoio, D.M., and Coleman, R.A. (2012). Distinct roles of specific fatty acids in cellular processes: Implications for interpreting and reporting experiments. Am. J. Physiol. - Endocrinol. Metab. *302*, 15–17.
Williams, D.B. (2006). Beyond lectins: The calnexin/calreticulin chaperone system of the endoplasmic reticulum. J. Cell Sci. *119*, 615–623.
Yalçın, B., Zhao, L., Stofanko, M., O'Sullivan, N.C., Kang, Z.H., Roost, A., Thomas, M.R., Zaessinger, S., Blard, O., Patto, A.L., et al. (2017). Modeling of axonal endoplasmic reticulum network by spastic paraplegia proteins. Elife *6*, 1–27.
Yamashita, A., Hayashi, Y., Nemoto-Sasaki, Y., Ito, M., Oka, S., Tanikawa, T., Waku, K., and Sugiura, T. (2014). Acyltransferases and transacylases that determine the fatty acid composition of glycerolipids and the metabolism of bioactive lipid mediators in mammalian cells and model organisms. Prog. Lipid Res. *53*, 18–81.
Yang, L., Guan, T., and Gerace, L. (1997). Integral membrane proteins of the nuclear envelope are dispersed throughout the endoplasmic reticulum during mitosis. J. Cell Biol. *137*, 1199–1210.
Yu, C.H., Redemann, S., Wu, H.Y., Kiewisz, R., Yoo, T.Y., Conway, W., Farhadifar, R., Müller-Reichert, T., and Needleman, D. (2019). Central-spindle microtubules are strongly coupled to chromosomes during both anaphase A and anaphase B. Mol. Biol. Cell *30*, 2503–2514.
Yue, L., McPhee, M.J., Gonzalez, K., Charman, M., Lee, J., Thompson, J., Winkler, D., Cornell, R.B., Pelech, S., and Ridgway, N.D. (2020). Differential dephosphorylation of CTP:phosphocholine cytidylyltransferase upon translocation to nuclear membranes and lipid droplets. Mol. Biol. Cell *31*, mbcE20010014.
van der Zand, A., Gent, J., Braakman, I., and Tabak, H.F. (2012). Biochemically distinct vesicles from the endoplasmic reticulum fuse to form peroxisomes. Cell *149*, 397–409.
Zeharia, A., Shaag, A., Houtkooper, R.H., Hindi, T., de Lonlay, P., Erez, G., Hubert, L., Saada, A., de Keyzer, Y., Eshel, G., et al. (2008). Mutations in LPIN1 Cause Recurrent Acute Myoglobinuria in Childhood. Am. J. Hum. Genet. *83*, 489–494.
Zhang, P., and Reue, K. (2017). Lipin proteins and glycerolipid metabolism: Roles at the ER membrane and beyond. Biochim. Biophys. Acta - Biomembr. *1859*, 1583–1595.
Zhang, C.Z., Spektor, A., Cornils, H., Francis, J.M., Jackson, E.K., Liu, S., Meyerson, M., and Pellman, D. (2015). Chromothripsis from DNA damage in micronuclei. Nature *522*, 179–184.
Zhang, P., Takeuchi, K., Csaki, L.S., and Reue, K. (2012). Lipin-1 phosphatidic phosphatase activity modulates phosphatidate levels to promote peroxisome proliferator-activated receptor γ (PPARγ) gene expression during adipogenesis.

J. Biol. Chem. *287*, 3485–3494.
Zoni, V., Shinoda, W., and Vanni, S. (2020). Seipin accumulates and traps diacylglycerols and triglycerides in its ring-like structure. BioRxiv.